Nonresonant interactions in nonlinear dynamical systems

A thesis submitted in fulfilment of the requirements

for the degree of Doctor of Philosophy

by

Tandel Dhananjaykumar Devchandbhai

19105268

Department of Mechanical Engineering

INDIAN INSTITUTE OF TECHNOLOGY KANPUR

September 2024

Certificate

It is certified that the work contained in this thesis entitled **"Nonresonant interactions in nonlinear dynamical systems"** by **Tandel Dhananjaykumar Devchandbhai** has been carried out under our supervision and that it has not been submitted elsewhere for a degree.

Pankaj Wahi
Professor
Mechanical Engineering
I.I.T. Kanpur

Anindya Chatterjee
Professor
Mechanical Engineering
I.I.T. Kanpur

September, 2024

Declaration

This is to certify that the thesis titled **"Nonresonant interactions in nonlinear dynamical systems"** has been authored by me. It presents the research conducted by me under the supervision of **Dr. Pankaj Wahi** and **Dr. Anindya Chatterjee**.

To the best of my knowledge, it is an original work, both in terms of research content and narrative, and has not been submitted elsewhere, in part or in full, for a degree. Further, due credit has been attributed to the relevant state-of-the-art and collaborations with appropriate citations and acknowledgments, in line with established norms and practices.

Tandel Dhananjaykumar Devchandbhai
Roll No. 19105268
Mechanical Engineering Department
Indian Institute of Technology Kanpur
September, 2024

D.D. Tandel

Abstract

Name of the student: **Tandel Dhananjaykumar Devchandbhai** Roll No: **19105268**

Degree for which submitted: **PhD** Department: **ME Department**

Thesis title: **Nonresonant interactions in nonlinear dynamical systems**

Thesis supervisors: **Dr. Pankaj Wahi** and **Dr. Anindya Chatterjee**

Month and year of thesis submission: **September 2024**

In nonlinear vibrations, studies involving two frequencies with special rational relationships appear routinely. These include studies incorporating various resonances. For example, in the study of a harmonically forced Duffing oscillator, 1:1, 1:3 and 3:1 ratios of the forcing frequency and the natural frequency of the system are highlighted, which correspond to primary, subharmonic and superharmonic resonances, respectively. In the classical Mathieu equation, the 2:1 parametric resonance remains a key aspect of investigation. Further, in two degree of freedom systems, rationally related frequencies of coupled oscillators receive significant attention and are called internal resonances. However, in practice, such resonances may be difficult to achieve or maintain when parameters are varied. In this context we observe that studies involving two frequencies with no simple rational relationship are limited in number. In this thesis, we deviate from the usual resonant case and present four studies involving nonresonant interactions relevant to engineering applications.

In the first problem, we explore vibration stabilization using a light nonresonant limit cycle oscillator. The motivation is that many vibrating systems, over some ranges of parameter values, exhibit a single unstable mode. Adding a small resonant secondary system to the unstable system is a well-known stabilization strategy. In this study, we show that even a nonresonant secondary system, if equipped with a limit cycle of its own, can stabilize the unstable mode of the primary system. The primary system is modeled here as a

linear spring block system with negative damping. The secondary system is a van der Pol oscillator well known for its limit cycle behavior. Smallness of the latter's parameters allows use of the method of multiple scales. The resulting slow amplitude equations decouple from the phases and a two-dimensional system is obtained. The secondary system's amplitude evolves faster than that of the primary system, which simplifies analysis. A parameter-dependent transformation casts the system in a canonical form with a single free parameter $c_1 > 0$ in addition to the small perturbation parameter. The canonical phase portrait involves two key straight lines. When $c_1 < 4$, these lines intersect and a separatrix passes through that intersection. Solutions on one side of the separatrix show quenching of the primary instability with limit cycle oscillation of the secondary system. Solutions on the other side of the separatrix show significant oscillations of the primary system at its natural frequency, with the secondary limit cycle being quenched. When $c_1 > 4$, stabilization fails for all initial conditions. In summary, for the case of a negatively damped oscillator interacting with a small nonresonant secondary limit cycle oscillator, this study shows stabilization, provides a pair of canonical equations with one free parameter, and presents a complete qualitative characterization of the dynamics.

In the second problem, we investigate nonresonant interactions between a linear system and a light double limit cycle oscillator. As a possible physical realization or as demonstration of reasonableness, we point to a mass on a moving belt system. In addition to limit cycle oscillations, this frictional system offers other regimes of operation, i.e., double limit cycle and globally stable equilibrium. A frictional oscillator with such behavior constitutes the secondary oscillator in the second problem of this thesis. The primary system remains the same linear spring-mass-dashpot system with negative damping, representing a linearly unstable mode of a structure. As before, the secondary system can act as an untuned stabilizer for this unstable mode. Using the method of multiple scales, we obtain decoupled amplitude and phase evolution equations. Only the amplitude equations need to be examined to elucidate the dynamics. These amplitude evolution equations are further simplified using a parameter-dependent transformation. We find that the system's qualitative dynamics depends only on *two* nondimensional parameters ν and c_1, where ν

decides the regime of operation of the secondary oscillator. We identify boundaries in this parameter space between regimes corresponding to different qualitative dynamics. The corresponding phase portraits allow us to identify system parameters that can offer conditional or unconditional stabilization of the primary system. For this second problem, we find that conditional stabilization is feasible even for $c_1 > 4$ when the secondary oscillator operates in the regime of double limit cycle response. The corresponding basin of attraction shrinks in size for larger instability of the primary oscillator (or larger c_1). Finally, complete stabilization can be achieved for $c_1 < 4$ wherein the secondary oscillator operates in the regime of a globally stable equilibrium.

In the third problem examined in this thesis, we explore tool-chatter suppression using a nonresonant limit cycle absorber. A key point is that in regenerative tool chatter in turning operations, the bifurcation to instability is generally subcritical. Consequently, when stability is lost (usually due to a large depth of cut), vibrations grow quickly and immediately involve loss of contact between the tool and workpiece. If the bifurcation was supercritical instead, then a small foray into instability would produce small vibrations, and a small retreat to stability would remain possible. With this motivation, we study complete suppression of the *subcritical* instability of machine-tool chatter using a light, nonresonant, limit cycle absorber. The absorber's nonresonant nature means it does not require precise tuning, which is a practical advantage. In the present work, a familiar model for regenerative tool vibrations is the primary system and a van der Pol oscillator models the secondary system. Linear analysis of steady cutting yields the Hopf bifurcation boundary. Asymptotic approximations are developed for different segments of the stability boundary, and used in the subsequent multiple scales analysis. Amplitude evolution equations thus obtained are recast into a canonical form. *Three* nondimensional parameters govern the system and its variety of qualitative behaviors. A key finding from the present work is that parameters of the secondary system can always be chosen to ensure a supercritical bifurcation along the entire stability lobe. Larger incursions into the linearly unstable regime yield dynamics that depend on the magnitude of perturbation. Interestingly, unstable oscillations can occur without loss of contact, although still-larger depths of cut can eventually cause separation. Predictions from the multiple scales approximations match full numerical results from DDE-BIFTOOL, including the possibility of a turning point bifurcation leading to large amplitude vibrations. Admittedly, some of these unstable large amplitude solutions will be invalidated by tool separation, the study of which is left for future work.

In the final problem, we depart from mechanical systems and study the parametrically excited dynamics of a trapped ion in a mass spectrometer with no simple rational relationship between the secular frequency (characterizing the ion's motion) and the frequency of parametric forcing. Under the action of both the usual quadrupolar RF as well as dipolar DC excitation, the governing equation, derived from electrostatic field calculations for realistic geometries, takes the form of an inhomogeneous Mathieu equation with a constant along with a quadratic term on the right hand side. An early paper by Plass examined the case without the quadratic term on the right hand side, using the method of variation of parameters. Here we note a significantly simpler particular solution than used by Plass, include the quadratic term, and develop a second order averaging based approximation without assuming 2:3 or any other resonance. The averaging results show that a particular underlying simple periodic solution is stable. We then show that a two-frequency approximation matches that solution well for practical purposes. Finally, we present and validate an easy iterative calculation for obtaining that two-frequency solution, and quantify the effect of the quadratic nonlinearity.

To summarize, this thesis presents four studies wherein two frequencies important in the dynamics do not have any rational relationship, i.e., the frequencies are nonresonant. In three of the studies, we consider nonresonant coupled mechanical oscillators and do not assume any internal resonance. These studies contribute towards the design of nonresonant vibration absorbers. In the final study, we investigate a parametrically excited system relevant to quadrupole ion traps, where we do not assume any rational relationship between the forcing frequency and the system's secular frequency. This study provides some useful insights for an analyst working on a mass spectrometer.

Acknowledgements

I am thankful to Prof. Anindya Chatterjee and Prof. Pankaj Wahi for advising me on this wonderful journey.

I admire Prof. Chatterjee's remarkable insights on problems spanning wide areas. The way he explains anything very clearly and systematically always puts me in awe. His class-room lectures many times felt like talks that esteemed speakers give on an honored platform. A line to students of ME351A resonated with me: 'if I were distributing money, you would be listening carefully; just because I am distributing knowledge, and knowledge is below money in your value system, you are not listening!'. Once he told me on writing: 'think of each word as a drop of your blood; use it after due thought'. One more, from when there was a murmur in the classroom: 'we are working now': what is called *yoga* in my opinion, i.e., to join something intensely. The work ethic I have learnt from him is going to help me throughout my life. Thanking him by words does not seem enough. Guru-dakshina system of ancient times was really worth performing. Simply put, I will remain indebted.

Prof. Wahi has been very supportive and kind to me. I credited his course on nonlinear vibrations, which was unfortunately interrupted by COVID. He gave us computer assignments that were useful in staying engaged during that tough time. Attending NODYCON in Italy and ICTAM in South Korea with him were memorable events of my life. I appreciate his way of engaging in the research problem of a student and thoroughly examining results. I remember, in one of the slow-flows I computed, one term was appearing that was not present in other cases. He didn't accept it, and later I found a mistake in my Maple code! That is the fun part of research: we think that we have got the results but in reality those may be wrong. I hope I will be more alert in the future. Earlier in the same problem, I did something in one way but he insisted that this can be done in a better way, and finally, we could achieve that. Apart from technical matters, I admire his down to earth personality. I am very grateful to him for silently changing my attitude.

I am thankful to Prof. A. K. Mohanty for technical help in one of the problems of this thesis. He shared references to understand working principles of a quadrupole ion trap. I enjoyed studying this system. We have coauthored a research paper on that work. I am also thankful to Prof. C. S. Upadhyay for coauthoring a different paper on work that is not reported in this thesis. I have been benefited from his NPTEL course on FEM. His PhD student Dr. V. Murari was my M.Tech. supervisor. I am happy to have this old connection with him.

I am thankful to Prof. Bhaskar Dasgupta. I got a chance to serve as a TA in his courses: theory of machines during a regular semester and optimization during summer semester. I am grateful to him for providing me some learning opportunities. I am thankful to Prof. S. S. Gupta, Prof. Ishan Sharma, Prof. Anupam Saxena, Prof. Malay Das, Prof. N. S. Vyas, and Prof. C. Chindam for their teaching. I thank Prof. Anurag Gupta, Prof. Dipayan Mukherjee, Prof. Ushasi Roy and Prof. Manjesh Singh for their support and encouragement. I thank Prof. Mohit Law and Prof. Akhilesh Mimani for being my doctoral committee members. I thank other professors of our department for their general support through many departmental roles. I thank Prof. Devlina Chatterjee for her encouragement and support as well. Finally, I thank all my school and college teachers for their continuous encouragement and support, because they were essential parts of my journey.

I thank the department's office members for their help. They have been very kind to us all the time. Special thanks to Shobhit Ji for smoothly processing all our requests. I thank Gyanendra Ji for helping with ME352A lab work. I did that as a TA two times. I thank Ramlakhan Ji for his help during my journey. Around the building, I thank security guards, gardeners and sanitation workers for providing us with a safe and healthy environment. Thanks to canteen members and other service providers in the campus for their services. Many thanks to CC members, library members, LHC office, hall and other office staff for their non-stop services, processing and cooperation. Thanks to IWD staff. Notable among other resolved complaints, they repaired my hostel room cupboard's drawer by installing a new one because termites had spoiled the old drawer. I cannot forget our Mess workers. Hall-7 food is nice. I will miss the kindness of one worker who offers us garama-garam extra roti.

Thanking our parents is never enough. I am thankful to my father for aligning me towards study. I remember he took me to a book stall and I was free to buy any story book. He has never ever scolded me. On the other hand, when I was even younger, my mother used to hit me sometimes to send me to school. I am very thankful to her for that discipline at the right time. It is my mother's will and prayer that has brought me to this stage. It fills my heart with immense gratitude when I think about their hard-work for my betterment.

My Bhai and Bhabhi have always supported me for higher education. I remember my Bhabhi preparing tiffin early in the mornings during my school days. She is the one whom I first approach in any difficulty. Bhai is very caring. They used to keep things secret that would disturb my focus. Their support and encouragement have kept me going. I thank my sister for being available whenever I needed her. I know that she will stand by my side in all circumstances. My relatives always supported me. Many offered to provide financial help whenever needed. I wish to mention Natu Masa and Leela Masi here. My Masi, who was a school teacher, paid significant attention to my development. She even took me to her home when I got into the high school in the town. I believe that the study oriented environment I received at their home has had an immense impact on my career. It prepared me for the long journey ahead. I am indebted to my Masi for this. She would have been very proud today. I dedicate this thesis to her.

Coming to my friends, I thank my close friends of my PhD days: Manish, Sudhir, Kapil, Bharat, Arjun-da, Amit, Sushant, Sunil, PK, Nitish, Sushil, Prasenjit, Naisarg, Rajkumar, Pramod, Ramkishor, Shivam, Pratibha, Prachi. I will never forget our beloved friend and senior Kavindra. I thank other friends whom I met here: Devang, Vinay, Vishal, Himanshu, Mukul, Retam, Ronald. I thank my seniors Vaibhav, Krishnan, Arindam, Aningi, Ankur, Sumit, Santanu, Shivam, Sankalp, Bidhayak, Ashutosh, Nikhil, Sandeep, Manoj, Rohit, Deepankar. Special thanks to Vaibhav, Krishnan and Bidhayak for all discussions and help. I thank my hall mates Sunil, Shrey, Ankit; my juniors: Abhishek, Kush, Gourav, Shubham, Randhir, Akash, Subhadeep, Tanuj, Pavan, Saurabh, Bishal, Ashish; and other friends: Shivanshu, Abhishek, Dhiraj, Junaid. I have had a good time with them. I thank my lab mates: Riju, Pritam, Soumyabrata, Ravi, Saurabh, Shubham, Abhimanyu, Abdul Hannan, Kundan, Vinoba, Saurav, Saranya, Arun, Susheel, Ajay, Sayma, Qurat. I wish to mention some representative names from other friend circles whose company I enjoy a lot and they are ready to help me anytime: MTech friends: Ashutosh, Abhimanyu, Shubham, Shivam, Richa, Shikha, Deepak, Anoop, Dhaval; BTech friends: Sudhir, Ujas, Raas, Divyesh, Bhumi, Amit, Rupesh, Rishabh, Rajan, Vaibhav; school friends: Rajan, Parimal, Smit, Chirag, A1, Ronit; village friends: Vishal, Guddu, Jaimeen, Tarang, Jay, Riki, Dhiraj, Harshil, Sagar, Dhaval, Kunjan; TON, Akki, Jignesh, Jenish, Aniket, Kenish. Apologies to many many others whose names I haven't mentioned.

Finally, I consider myself a spiritual seeker. That surely has helped me stay calm and to persist during my journey. I thank revered teachers Swami Vivekananda, Pandurang

Shashtri Ji, Swami Sarvapriyananda, Rupert Spira and many others for their wonderful teachings on the subject. Finally, I thank Lord Krishna who takes care of me a lot. While doing research, one frequently gets stuck and there are chances of regrettable errors. From where do those insights come? From where does the help come? To close in short, I quote a line by Shri Pandurang Shashtri Ji: ‘God does not work for you, he works with you.’

This section has made me experience a wave of gratitude. I am finding that so many have directly or indirectly helped me in this journey. Thank you very much again to everyone for their support, kindness and love. May my Lord gives you all good health and happiness.

Contents

List of Figures

List of Tables

Abbreviations

EOM	**E**quation **O**f **M**otion
ODE	**O**rdinary **D**ifferential **E**quation
TMD	**T**uned **M**ass **D**amper
NES	**N**onlinear **E**nergy **S**ink
NLTVA	**N**on**L**inear **T**uned **V**ibration **A**bsorber
VI-NES	**V**ibro **I**mpact **NES**
IDVA	**I**nerter-based **D**ynamic **V**ibration **A**bsorber
LCO	**L**imit **C**ycle **O**scillator
QIT	**Q**uadrupole **I**on **T**rap

List of Publications

Publications from Thesis

1. Paper 1: Vibration stabilization by a nonresonant secondary limit cycle oscillator (Nonlinear Dynamics, *10.1007/s11071-022-08145-4*).
2. Paper 2: Quadrupole ion trap with dipolar DC excitation: motivation, nonlinear dynamics, and simple formulas (Nonlinear Dynamics, *10.1007/s11071-023-08706-1*).
3. Paper 3: Ensuring supercritical Hopf bifurcation in tool chatter using a nonresonant limit cycle absorber (Journal of Sound and Vibration, *10.1016/j.jsv.2025.118958*).

Others

1. Paper 1: Design charts for hydraulic twister based aircraft arrester gear (Mechanics Based Design of Structures and Machines, *10.1080/15397734.2023.2288184*).

Dedicated to

Leela Masi

Chapter 1

Introduction

This thesis presents some studies on nonresonant interactions in nonlinear mechanical systems.

1.1 Motivation

A Google Scholar search for ‘resonant vibration’ shows 14,10,000 results, whereas it shows 33,500 results for ‘nonresonant vibration’. These numbers informally suggest that there are less than three studies on nonresonant vibrations for every 100 studies on resonant vibrations. The significant focus on resonant interactions is expected as they produce strong interactions in the system dynamics. For example, when a child pumps a swing, he/she changes the length of the swing (thereby, changes the moment of inertia) by raising and lowering the center of mass of his/her body at the lowest and the highest positions, respectively [1]. Here, the length change (external parametric excitation) and the swing oscillation frequencies are in a 2:1 relation, inducing a 2:1 parametric resonance. Such rational relations between frequency components characterize resonant interactions. For an externally excited system, studies incorporating rational relations between the frequency of external excitation and the natural frequency of the system are routine, e.g., 1:1 primary, 1:3 subharmonic and 3:1 superharmonic resonances in the harmonically forced Duffing oscillator are well explored. Even for multi degrees of freedom systems, coupled oscillators with rationally related frequencies have received significant attention. These are called internally resonant systems. Interestingly, a Google Scholar search for 'internal resonance' yields 40,30,000 results! This shows how frequent these resonant interaction studies are.

In this thesis, we deviate from the usual resonant considerations and investigate a few problems where important frequency components do not have special simple rational relationships and are, therefore, nonresonant. When these frequencies are widely spaced, the interaction is known as 0:1 resonance which has been studied earlier [2]. However, the interaction of non-widely spaced modes, as considered in the present thesis, has not received significant attention in the literature to the best of our knowledge. We next discuss the specific contexts of the problems studied in this thesis.

1.1.1 Towards untuned passive vibration stabilizers

Primarily, vibration suppression techniques are of two types: active and passive. Active strategies involve a direct application of strong actuators. These are bulky and costly. Passive strategies, on the other hand, sometimes utilize a small secondary system which is attached to a relatively large primary system. A tuned mass damper (TMD) is an example of a passive absorber used for vibration mitigation in buildings (e.g. Taipei 101), transmission line cables (known as Stockbridge dampers), machine tools, etc. Here the word 'tuned' highlights the fact that the natural frequency of the TMD is matched with that of the structure which requires vibration suppression. Thus, the TMD interacts with the structure resonantly to provide effective vibration suppression. However, in practice, resonance cannot always be maintained under parameter variations. For example, if a boring bar is gripped at different locations, its effective length and natural frequency may change significantly, and a TMD may be rendered less effective. Researchers utilise system nonlinearities to increase the working frequency range of the TMD. However, in most studies, resonant interactions remain pivotal. We will present a relevant literature review later in this thesis.

A vibration absorber that does not require resonant interaction will not require precise tuning and hence may remain effective over a larger range of natural frequencies of the primary system. That motivates us to undertake nonresonant interaction studies involving two oscillators with $\mathcal{O}(1)$ nonresonant frequencies, where the relatively light secondary oscillator works as a passive absorber. For the primary oscillator, we consider a single unstable mode of a system [3–5] that can exhibit large amplitude oscillations without any external force. If the nonresonant secondary oscillator stabilizes the mode, we will have an untuned stabilizer that does not require precise tuning to operate.

Here, we note the study by Singla and Chatterjee [3], where they showed stabilization of an unstable mode using a light, lightly damped, untuned whirling pendulum. The whirling pendulum offers exactly constant amplitude (length of the pendulum) oscillations of the pendulum mass at all whirling frequencies. A limit cycle oscillator offers a preferred amplitude and can oscillate at various frequencies, and it also eliminates the need for a whirling component. This motivates our secondary limit cycle oscillator for the stablization of an unstable primary system. In this thesis, we will investigate three such nonresonant systems in detail.

1.1.2 Quadrupole ion trap (QIT) with dipolar DC excitation

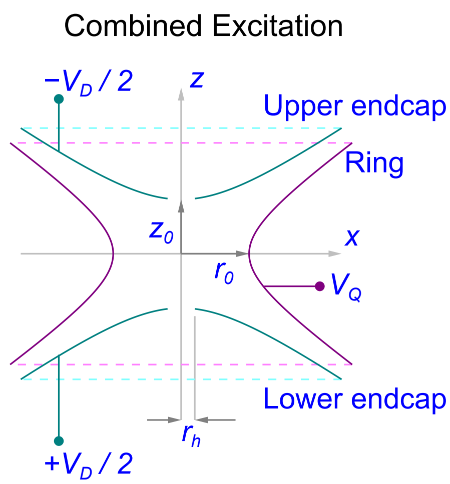

FIGURE 1.1: Cross section of an axisymmetric QIT with combined quadrupolar and dipolar excitations. This figure is provided by Prof. A. K. Mohanty, IISc Bengaluru.

The other nonresonant interaction study in this thesis is relevant to quadrupole ion traps (QITs) [6]. Paul traps or Ion traps utilize a dynamic electric field to trap charged particles. Figure 1.1 depicts the combined quadrupolar and dipolar excitations in an axisymmetric QIT. Traditional ion traps utilize quadrupolar excitation where the end-cap electrodes are grounded and the ring electrode is given an AC sinusoidal input. The added dipolar DC excitation V_D in Fig. 1.1 is used for collision induced dissociation and for breaking large ions into small fragments. The associated dipolar field has been considered constant in earlier studies [7]. However, the presence of holes in the end-caps disturbs the dipolar field near the trap center. A separate analysis shows that the variation of the field is approximately parabolic over a large portion of the trap. Thus, the governing equation of motion of the ion in a QIT with combined excitation takes the form of a classical Mathieu equation perturbed with a constant inhomogeneous term and a small quadratic nonlinearity. This equation has not been investigated earlier to our knowledge. Because we are interested in nonresonant interactions in this thesis, we investigate the governing equation for nonresonant secular frequencies, i.e., away from resonant values 1, 2/3, etc. Insights from the study may be useful to analysts working on mass spectrometers.

We note that nonresonant interactions are not limited to these areas. For example, energy harvesting [8] and viscosity measurement [9] are some other applications that can involve nonresonant interactions. Here, we limit this thesis to the above described problems.

Finally, we note that resonant interactions are captured using first-order analyses, whereas nonresonant interactions require higher-order analyses in general because the interaction is weaker. In this thesis, we present second-order analyses of problems under investigation. An advantage in the analysis of nonresonant interactions is that the evolution of system amplitudes is independent of phases. This simplifies the analysis by reducing the dimension of the resulting slow flow. Finally, and satisfyingly, unifying phase portraits can cover the complete system dynamics.

1.2 A broader literature review and objectives of the thesis

As indicated, two types of nonresonant interactions are studied in this thesis. First, in view of passive vibration suppression, we study the interaction of two coupled oscillators with nonresonant natural frequencies. Second, for exploring the nonresonant operating regime of a parametrically excited system, we investigate the system for no special rational relationship between the parametric forcing frequency and the system's secular frequency (the dominant component within its multifrequency response). Because these various studies are independent, we present their detailed literature reviews in their respective chapters. Here, we highlight how our study is different from many others.

For nonresonant interaction studies of coupled oscillators, we consider a primary unstable system coupled with a secondary nonresonant limit cycle oscillator, where the latter is modelled using the van der Pol oscillator. Many studies are available related to the van der Pol oscillator coupled to either the van der Pol, the Duffing or some other oscillator. For this reason, we have conducted a broader literature review and categorized many such articles based on their focus of study.

We have found 40 papers, of which 39 of them were published between 1980 and 2022. These papers each have the van der Pol oscillator coupled to either the van der Pol oscillator or some other oscillator. These papers are included in this thesis as references [10–49]. These references can be grouped in various ways depending on which aspect of their contribution we wish to focus on. Each such grouping serves to emphasize how our work is different.

Many of these papers involve two coupled oscillators that are resonant, i.e., the natural frequencies are close. From our 40 references, it turns out that references [10, 13–31] are in this first category. Since our two oscillators have frequencies that are *not close*, we do not fall in this category of *resonant* coupled oscillators.

Another way to classify the papers is to identify those (27 out of 40) where the two oscillators' inertia terms are of equal or nearly equal magnitude, and their coupled dynamics, which may be weakly or strongly nonlinear, are then examined. References [11–27, 31–40] fall in this category. We do not fall in this category because our motivation is an *untuned vibration stabilizer* where the added system is necessarily small compared to the primary system, and it still affects the dynamics.

Another way to group some papers is to note those wherein two oscillators, by *mathematical design*, are capable of having perfectly synchronized solutions. In abstract first-order form, if we have

$$\dot{x} = f(x) + g(x, y) \quad \text{and} \quad \dot{y} = f(y) + g(y, x),$$

then $x = y$ is a possible solution satisfying

$$\dot{x} = f(x) + g(x, x).$$

Whether that phase-locked solution is stable or not then becomes important. If it is stable, the basin of attraction is important, and so on. Out of the 40, 9 papers fall in this category [14, 16–18, 21, 23, 24, 27, 31]. Since our two oscillators do not have this form, our study does not fall into this category.

Then there are coupled van der Pol and Duffing systems, for which some papers study the dynamics near 1:1 resonance [26, 29, 34, 41, 42], phase-locked motions [34, 39], or assume comparable inertia [12, 26, 27, 34, 37–39]. As explained above, our study is very different from these papers. There are also studies of coupled van der Pol and Duffing systems that involve 1:2 or 1:3 resonances: see [43–46]. We focus on *nonresonant* interactions and so we do not fall in this category.

We note that nonresonant interactions were studied in [36–38], but there the inertias of the two oscillators were the same (as noted above), and they reported decoupled amplitude dynamics of the coupled oscillators, while our results with disparate inertias show a potentially useful coupled dynamics. Therefore we differ from those papers.

Finally, for parameter values that are not small and where analytical progress was limited, numerical or experimental approaches have been used [32, 35, 39, 47–49] to observe nonlinear responses like multistability and chaotic solutions. Our study is not in this category.

In this way, there is at least one key difference, and usually more than one key difference, between our study and these 40 papers. This completes our broader literature review for Chapters 2 and 3 (and Chapter 4 to some extent) highlighting the main characteristics of the coupled oscillators studied in the present thesis as being *nonresonant* and *having disparate inertias*. A detailed literature review relevant for Chapters 2 and 3 in the context of passive vibration suppression is presented in Chapter 2.

Next, we investigate a system where the secondary limit cycle oscillator is attached to a primary system of machine tool vibrations in Chapter 4. The motivation is to examine the secondary system's effectiveness in altering the subcritical nature of bifurcation in the primary system [50]. The advantage gained by altering the nature of bifurcation is the indication of loss of stability, as with supercritical Hopf bifurcation stable limit cycles will appear instead of sudden large amplitude solutions in case of subcritical Hopf bifurcation. Linear absorbers [51–57] including TMD do not succeed in altering the nature of bifurcation. Various other absorbers have been studied including nonlinear [60–62], nonsmooth [63–67], and actuation based [58, 59, 68, 69] absorbers. Our study of Chapter 4 differs from these papers in that we have a *nonresonant* attachment which can exhibit self-excited oscillations. Further, nonlinear absorber studies have reported only partial success in altering the nature of bifurcation over a stability lobe [60–62]. Here, we demonstrate the change of the nature of bifurcation for a complete stability lobe.

For the final nonresonant interaction study relevant to a QIT with dipolar DC excitation, we will show in Chapter 5 that the governing nondimensional equation is

$$\zeta'' + \varepsilon^2 \eta \zeta' - 2q\cos(2\xi)\zeta = \mu\left(1 + \varepsilon\zeta^2\right),$$

which is a nonlinear inhmogeneous Mathieu equation with a constant along with a quadratic term on the right hand side. If the amplitude of the parametric term in the Mathieu equation is small, i.e., q is small, then the direct application of perturbation methods is routine

[70–77], where studies [73–75] involve external periodic forcing instead of a constant term. Studies [78–83] incorporate large q. However, analyses in these studies consider near-resonant situations. To the best of our knowledge, no formal averaging-based or similar analysis has been reported for a weakly nonlinear Mathieu equation with a non-time-varying inhomogeneous term and large q under a nonresonant scenario.

With this background, the main objectives of the thesis can be stated as the following:

1. To study stabilization dynamics of a linear unstable mode coupled with a light non-resonant secondary limit cycle oscillator,
2. To investigate the efficacy of a nonresonant limit cycle oscillator in altering the nature of bifurcation in a nonlinear system of machine tool vibrations, and
3. To explore nonresonant operation of a QIT in the presence of a practically relevant nonlinearity.

1.3 Organization of this thesis

In Chapter 2, we study vibration stabilization using a light nonresonant limit cycle oscillator. We consider a single unstable mode of a system as a primary system and model it using a single degree of freedom linear spring-mass-damper system, where the negative damping represents the instability [5]. Adding a small resonant oscillator is a well-known stabilization strategy. Here, we implement a nonresonant limit cycle oscillator for stabilization. We use the well-known van der Pol oscillator to model the secondary limit cycle oscillator. The smallness of this oscillator allows the introduction of a small perturbation parameter. Then the governing equations of the coupled system are investigated using the method of multiple scales. The resulting slow amplitude equations decouple from the phases and a two-dimensional system is obtained. The secondary system's amplitude evolves faster than that of the primary system, which simplifies analysis. A parameter-dependent transformation casts the system in a canonical form with a single free parameter $c_1 > 0$ in addition to the small perturbation parameter. c_1 denotes the ratio of viscous damping in the primary and secondary oscillators. Two canonical phase portraits corresponding to $0 < c_1 < 4$ and $c_1 > 4$ are presented. These phase portraits unify the system dynamics and help to elaborate the nonresonant dynamics of the coupled system in an asymptotic limit, for any combination of system parameters and initial conditions. Further, these phase portraits indicate that $c_1 < 4$ is required to achieve conditional stabilization of the primary system. When $c_1 > 4$, stabilization fails for all initial conditions. This work has been published as [84].

In Chapter 3, an additional quartic nonlinearity is added to the quadratic van der Pol damping term of the secondary oscillator. The motivation for this lies in the search for a mechanical system that can offer limit cycle oscillations. Here, a model for mass on a moving belt system is a conceptual potential choice. In addition to a limit cycle behavior, this system offers double limit cycle and globally stable equilibrium solutions resulting from a subcritical Hopf bifurcation followed by a fold bifurcation. These additional response regimes in the secondary oscillator can be incorporated using a quartic term. Here again, the primary oscillator is a linear, negatively damped system representing an unstable mode. The nonresonant interactions in the coupled system are investigated using the method of multiple scales. The simplified amplitude slow flows indicate that two nondimensional parameters c_1 and ν now govern the system's nonresonant dynamics. Here, ν denotes the ratio of the coefficients of the quartic and quadratic nonlinearities in the secondary oscillator. We identify the bifurcation boundaries in the parameter plane and present amplitude phase portraits to elaborate the system dynamics for different parameter combinations. We find that conditional stabilization is feasible for $c_1 > 4$ when the secondary oscillator operates in the regime of double limit cycle response. The corresponding basin of attraction shrinks in size for larger instability. Finally, complete stabilization is achieved for $c_1 < 4$ when the secondary oscillator operates in the regime of globally stable equilibrium, whereas stabilization fails for $c_1 > 4$.

In Chapter 4, we consider a time-delayed model for regenerative tool-chatter vibrations as the primary system, where the corresponding nonlinear model is known to exhibit subcritical bifurcation which is catastrophic in nature. We again attach a light, *nonresonant*, limit cycle oscillator to suppress this instability. Note that the traditional solution of attaching a TMD to the primary system does not alter the nature of bifurcation and the earlier literature utilizing nonlinearities has reported supercritical bifurcation only for limited segments of the second stability lobe. In this study, we establish supercriticality for the complete lobe. We first find asymptotic approximations for various segments of the linear stability boundary and then utilize those expressions in the multiple scales analyses. The obtained amplitude slow flows are then transformed into simpler forms which indicate that three nondimensional parameters govern the system and its variety of qualitative behaviors. Parameters of the secondary system can always be chosen to ensure a supercritical bifurcation along the entire stability lobe. Larger incursions into the linearly unstable regime yield dynamics that depend on the magnitude of perturbation. DDE-BIFTOOL results support our findings and assist in revealing a turning point bifurcation. The chapter concludes with a discussion of parameter selection to ensure supercriticality for the complete second stability lobe.

In Chapter 5, we turn to a nonresonant interaction study related to dipolar DC excitation in QITs. The governing equation of the ion's motion in such a QIT takes the form of a classical Mathieu equation perturbed with an $\mathcal{O}(1)$ constant and a small quadratic nonlinearity. We present a simple form of a particular solution for the unperturbed inhomogeneous Mathieu equation. Then we implement nonresonant version of the method of higher order averaging, where we assume absence of resonance and allow secular frequencies away from resonant values, e.g., 1, 2/3, etc. The final slow flows transform to a simple form and establish the stability of the simple particular solution. We then show that a two-frequency approximation matches that solution well for practical purposes. Finally, we present and validate an easy iterative calculation for obtaining that two-frequency solution, and quantify the effect of the quadratic nonlinearity. This work has been published recently [85] and was done in collaboration with Prof. Atanu Mohanty of IISc Bengaluru.

Finally, Chapter 6 ends the thesis with some concluding discussion.

Chapter 2

Vibration stabilization by a nonresonant secondary limit cycle oscillator

In this chapter, we study nonresonant interactions between a linear unstable system and a light limit cycle oscillator. We begin with an introduction to the problem in the context of vibration stabilization and present relevant literature. Subsequently, we write governing equations, introduce scaling and implement the method of multiple scales. Thus obtained amplitude slow flows are then transformed into a simple canonical form and investigated for fixed points and their stability, where we present two key phase portraits covering the system dynamics. We detail various responses of the coupled system and finally conclude the chapter. This work has been published as [84].

2.1 Introduction

Stabilization of unstable vibration modes is an important engineering problem. Structures exposed to aerodynamic loading can experience flutter instability. High tension transmission lines exposed to winds can show what is called a galloping instability. Long, flexible members of machine tools, like boring bars, can display undesirable oscillations while cutting. Here we consider a single mode of such a weakly unstable structure as our primary system and model it as a linear spring-mass oscillator with, for simplicity, negative linear viscous damping. There is no persistent external excitation. Our aim is to counteract the negative damping and stabilize the mode.

Our main novelty in this work is that we do not use resonance, because that requires precise tuning. We are interested in a stabilizer that does not require precise tuning.

To that end, we consider attaching a small secondary system to the primary system, wherein the secondary system's natural frequency is *not close* to that of the primary system, i.e., the secondary system is untuned. Additionally, the secondary system has its own nonlinear active behavior that we model using the well known van der Pol oscillator. In this way, the small and light secondary system has a tendency to vibrate at one frequency, while the more massive primary system has a tendency to vibrate at another frequency altogether. The aim of our investigation is to seek new analytical criteria, with proper numerical support, for conditions under which the instability in the primary system is suppressed. If we succeed, then we will have found a new kind of vibration stabilizer which is robust under parameter uncertainty, because precise tuning of the frequency is not needed. The price paid will be the active excitation of the secondary system: but this will not require feedback of the primary system state.

When we try to stabilize vibrations, we can do it with passive damping which is not tuned at all, and is effective over a large range of frequencies. However, it has the disadvantage that, for a large structure, a physically large damper may be needed. Another option is active control where we measure the state of the system and feed back something to an actuator, where again, a physically large actuator may be needed. In contrast, if we use passive dynamic methods, we may have a tuned vibration absorber, and it can be extremely effective in some cases. However, the parameters of the stabilized system must then remain within a narrow range. For example, if a boring bar is gripped at different locations, its effective length and natural frequency may change too much, and a tuned vibration absorber will then be less effective. In contrast to the above approaches, in this work, we seek something that does not require *precise* tuning, is physically small, and still is effective over a larger range of natural frequencies of the primary oscillator, i.e., it does not require a resonant interaction to work. We emphasize that the resonant case, when it works, works very well. However, when resonance cannot be maintained due to parameter variations, a nonresonant stabilizer can be considered. We note that in the present study, although we envisage the use of active means to produce a limit cycle oscillation in the secondary system, it is less demanding than using direct feedback on the primary system because the secondary system size and actuator size are both expected to be small. Detailed modeling of the physical mechanisms used to produce the secondary limit cycle is left to future work. In the present study, we work out the basic academic theory.

In our two-degree-of-freedom system, both modes have negative damping in the linearized equations. So there will essentially be a contest between two instabilities. Since the secondary system is small, its effect will only be felt if the initial conditions for the primary system are small as well. However, as we will show, significant regimes of desirable behavior may be possible for initial conditions of usefully large size.

2.2 Literature review

The broad context in which we present our work is as follows. Traditional tuned mass dampers (TMDs) are well known passive absorbers in the vibrations research community. Improvements in TMD have continued long after its introduction by Frahm in 1911 [86]. The advantage of passive vibration absorbers is that they do not require any external power source. However, TMDs have the disadvantage of being effective only in a narrow frequency range. Researchers continue to design and improve vibration absorbers effective over a wider range of frequencies. Ibrahim [87] has documented the history of passive vibration absorbers. With an introduction of nonlinearity in TMDs, nonlinear vibration absorbers (NVAs) or nonlinear energy sinks (NESs) have gained attention as potential candidates to replace TMDs. While they involve challenges like multivaluedness (or multiple steady state behaviors) and instability in some cases, NESs can offer the advantage of having a broader working frequency range than TMDs. Ding and Chen [88] have reviewed NES designs and applications.

Since our primary structure is a linear spring-mass oscillator while our secondary oscillator is nonlinear, we specifically mention some articles in which an NES is attached to a linear oscillator. Gatti [89] considered an NES with a linear and cubic spring nonlinearity and viscous damping attached to a damped linear spring-mass system subjected to harmonic forcing. Using frequency response analysis, tuning conditions were presented to apply the NES as an absorber or a neutralizer depending on the forcing frequency, considering the hardening and softening characteristics of the cubic spring. Although the attenuation observed for the desired forcing frequency remained similar to that using a linear attachment, bandwidth improvement was recognized. Starosvetsky and Gendelman [90] investigated an NES with nonlinear damping and a pure cubic spring element attached to a linear spring-mass system under periodic forcing. They showed that the introduction of damping nonlinearity could annihilate undesirable nonlinear effects, i.e., extending the amplitude of forcing over which the NES is effective. Zhu *et al.* [91] studied a two-degree-of-freedom system with nonlinear spring and damper elements in primary and secondary systems, where the latter is excited. Using frequency response curves, they showed that increasing the secondary oscillator's nonlinear spring and damping coefficients improves attenuation while increasing the primary system's nonlinear parameters serves when a nondimensional forcing frequency (defined therein) is below unity. It is important to note that these studies related to the enhancement of TMDs and NESs have focused on vibration mitigation of periodically forced structures. Attempts towards suppression of self-excited oscillations can be found in [92], [93] and [94]. Verhulst [92] studied quenching of self-excited oscillations in the van der Pol and Rayleigh oscillators by coupling another oscillator. As a tuning methodology, coupling parameters were chosen such that the stable periodic solution of the self-excited oscillator became unstable. For strong interaction, quenching of relaxation oscillations was attempted, and design recommendations were given. Lee *et al.*

[93] investigated the efficacy of an NES with essentially nonlinear cubic spring and viscous damping in suppressing limit cycle oscillations of the van der Pol oscillator for grounded and ungrounded configurations. They showed that elimination of the limit cycle of the primary structure is attainable. Habib and Kerschen [94] studied mitigation of limit cycles in the van der Pol-Duffing oscillator. The attached nonlinear tuned vibration absorber (NLTVA) has linear and cubic spring elements with viscous damping. The optimum value of the frequency ratio of the linear parts of both oscillators was close to unity, i.e., tuning was needed. Additional benefits from nonlinearity were noted.

We now focus our literature review to some papers that specifically included linear viscous negative damping in the primary oscillator. Such papers include many that refer to flow-induced vibrations. Passive vibration absorbers for flow-induced vibrations have been studied for decades: see the review paper by Wang *et al.* [95]. Nasrabadi *et al.* [96] studied design of an NES for vibration suppression of a cantilever cylinder under cross-flow. They achieved significant reduction in the vibration amplitude of the cylinder. Guo *et al.* [97] studied the suppression of limit cycle oscillation of a linear extensible cable. They showed that an NES can raise the wind speed needed for initiation of galloping. The role of attachment location was studied as well. Qin *et al.* [98] studied models of a transmission line with one through three degrees of freedom. The secondary system was a pendulum, and the roles of length, mass, and damping were studied. Tuning was found to be beneficial. Dai *et al.* [99] studied the use of an NES to suppress fluid-induced vibrations of a single degree of freedom (SDOF) system. It was found that damping plays a strong role, and a stronger nonlinear stiffness can limit response amplitudes more effectively. Shirude *et al.* [4] also studied an essentially nonlinear vibration stabilizer for a negatively damped SDOF system. They used informal harmonic balance based averaging to obtain both steady state responses and stability information. The stabilizer was found to be effective for some range of parameter values, and precise tuning was not needed. In all the papers referred to in this paragraph, the response of the secondary system, whether it is weakly or strongly nonlinear, and tuned or untuned, was essentially at the natural frequency of the primary system.

In a rather different approach from those above, Singla and Chatterjee [3] studied a negatively damped linear system coupled with a light whirling viscously damped pendulum driven by a small steady torque. In the stabilized regime, the pendulum frequency was *not tuned* to the primary oscillator. The method of multiple scales, carried out to second-order, gave an analytical stability criterion which was then supported by numerics. Post-instability behavior was also studied, but is not relevant to the present work. The whirling pendulum system differs from other NESs in that it has constant amplitude and specific untuned frequency. That paper [3] motivates our present work, where we incorporate the preferred amplitude approximately and are able to eliminate the need for a whirling pendulum component.

Finally, we acknowledge papers [100–102] which, although not identical to our work, share some philosophical similarities. Chatterjee [100] considered linear control actuation of a secondary oscillator coupled to a self-excited primary system with nonlinear damping. Given absorber parameters including the absorber's natural frequency, optimum feedback gains were found. It was noted that higher absorber frequencies gave greater robustness. Since the primary system is nonlinearly self-excited and the feedback parameters are both linear and based on inertial position and velocity of the absorber mass, the system deviates from ours. Additionally, the total dynamics in [100] could not be reduced to a simple one-parameter form as we will present here. Mondal and Chatterjee [101] applied resonant nonlinear feedback control to suppress self-excited oscillations in a single-mode nonlinear model of a beam. The velocity measurement from the beam was fed to a second-order filter (which is essentially a damped harmonic oscillator), and then the filtered velocity (which is essentially the velocity of that secondary oscillator) was used to provide feedback control. Here also, the primary system was self-excited and nonlinear; and eventually the optimum frequency of the secondary system was found to be equal to the natural frequency of the original system, i.e., the optimum system was resonant. Third, we come to the work of Gattulli *et al.* [102]. This work has somewhat greater relevance to our work, as will become clearer below. The work of [102] is discussed in greater detail in sections 2.3 and 2.6. Finally, we acknowledge that many studies are available related to the van der Pol oscillator coupled to either the van der Pol, the Duffing or some other oscillator. For this reason, we have conducted a broader literature review and categorized many such articles based on their focus of study in Chapter 1. We conclude our literature review here by highlighting the main characteristics of the stabilizer proposed in the present study as being *light, nonresonant* and *self-excited*.

2.3 Equations of motion

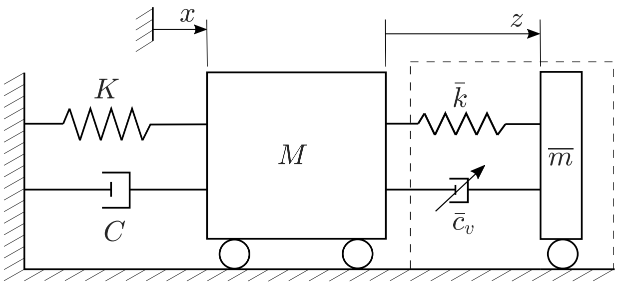

FIGURE 2.1: Schematic of the coupled system.

Figure 2.1 shows a schematic of the system considered in this chapter. We consider a primary oscillator with mass M, spring stiffness K and viscous damping coefficient C. A negative value of C represents instability in the primary structure. The attached van der Pol (sometimes called "vdP") oscillator has mass $\overline{m}$, linear spring stiffness $\bar{k}$ and nonlinear damping coefficient $\bar{c}_v$, while x and z denote the absolute and relative displacements of the primary and secondary systems, respectively. The equations of motion (EOMs) are

$$M\ddot{x} + C\dot{x} + Kx - \bar{k}z - \bar{c}_v\dot{z}(z^2 - 1) = 0, \tag{2.1}$$

$$\overline{m}(\ddot{z} + \ddot{x}) + \bar{k}z + \bar{c}_v\dot{z}(z^2 - 1) = 0, \tag{2.2}$$

By either choice of units or a preliminary nondimensionalization, we can set $M = 1$ and $K = 1$ to obtain

$$\ddot{x} + \widetilde{C}\dot{x} + x - \tilde{k}z - \tilde{c}_v\dot{z}(z^2 - 1) = 0,$$

$$\widetilde{m}(\ddot{z} + \ddot{x}) + \tilde{k}z + \tilde{c}_v\dot{z}(z^2 - 1) = 0,$$

where $\widetilde{C}$, $\widetilde{m}$, $\tilde{c}_v$ and $\tilde{k}$ are nondimensional parameters given by

$$\widetilde{C} = \frac{C}{\sqrt{MK}}, \quad \widetilde{m} = \frac{\overline{m}}{M}, \quad \tilde{c}_v = \frac{\bar{c}_v}{\sqrt{MK}}, \quad \tilde{k} = \frac{\bar{k}}{K}. \tag{2.3}$$

Note that the nondimensional time sets the natural frequency of the primary oscillator to unity. Now, we introduce a small bookkeeping parameter ε and write

$$\widetilde{C} = \varepsilon c, \quad \widetilde{m} = \sqrt{\varepsilon}\, m, \quad \tilde{c}_v = \varepsilon c_v \quad \text{and} \quad \tilde{k} = \sqrt{\varepsilon}\, k, \tag{2.4}$$

The parameters c, m, c_v and k are understood to be $\mathcal{O}(1)$. We will not refer to the unscaled quantities any more. The EOMs take the form

$$\begin{aligned} &\ddot{x} + \varepsilon c\dot{x} + x - \sqrt{\varepsilon}\, kz - \varepsilon c_v \dot{z}(z^2 - 1) = 0, \\ &\sqrt{\varepsilon}\, m(\ddot{z} + \ddot{x}) + \sqrt{\varepsilon}\, kz + \varepsilon c_v \dot{z}(z^2 - 1) = 0. \end{aligned}$$

We define

$$\omega_p{}^2 = \frac{k}{m} \quad \text{and} \quad \gamma = \frac{c_v}{m} \tag{2.5}$$

for convenience, obtaining

$$\ddot{x} + \varepsilon c\dot{x} + x - \sqrt{\varepsilon}\, m\omega_p{}^2 z - \varepsilon m\gamma \dot{z}(z^2 - 1) = 0, \tag{2.6}$$

$$\ddot{z} + \ddot{x} + \omega_p{}^2 z + \sqrt{\varepsilon}\, \gamma \dot{z}(z^2 - 1) = 0. \tag{2.7}$$

We will study Eqs. (2.6) and (2.7) using the method of multiple scales in the next section.

We are now in a position to discuss the work of Gattulli *et al.* [102], who studied the effect of a tuned mass damper (TMD) on a single degree of freedom model of a bluff body undergoing galloping. Their nondimensionalized equations (Eq. (4) in [102]) are

$$\begin{aligned} &\ddot{q}_1 + 2\xi\dot{q}_1 + 2\mu\gamma\xi_t(\dot{q}_1 - \dot{q}_2) + q_1 + \mu\gamma^2(q_1 - q_2) = \delta\frac{A_3}{U}\dot{q}_1^3, \\ &\ddot{q}_2 + 2\gamma\xi_t(\dot{q}_2 - \dot{q}_1) + \gamma^2(q_2 - q_1) = 0. \end{aligned}$$

Writing $z = q_2 - q_1$, we obtain

$$\begin{aligned}
&\ddot{q}_1 + 2\xi\dot{q}_1 - 2\mu\gamma\xi_t\dot{z} + q_1 - \mu\gamma^2 z = \delta\frac{A_3}{U}\dot{q}_1^3, \\
&\ddot{q}_1 + \ddot{z} + 2\gamma\xi_t\dot{z} + \gamma^2 z = 0.
\end{aligned}$$

We note that the parameter values mentioned in [102] are $2\xi = -0.1356$ and $\delta\dfrac{A_3}{U} = -0.0033$ with $\delta = 4.7\times 10^{-4}, A_3 = -421, U \sim 60$. Because the RHS in the first equation is small for the reported parameter values, and it only modifies the damping, we drop it to obtain

$$\begin{aligned}
&\ddot{q}_1 + 2\xi\dot{q}_1 - 2\mu\gamma\xi_t\dot{z} + q_1 - \mu\gamma^2 z = 0, \\
&\ddot{q}_1 + \ddot{z} + 2\gamma\xi_t\dot{z} + \gamma^2 z = 0.
\end{aligned}$$

Now, to connect with our system, we introduce a van der Pol term instead of the linear damping term, to obtain

$$\begin{aligned}
&\ddot{q}_1 + 2\xi\dot{q}_1 - 2\mu\gamma\xi_t(z^2-1)\dot{z} + q_1 - \mu\gamma^2 z = 0, \\
&\ddot{q}_1 + \ddot{z} + 2\gamma\xi_t(z^2-1)\dot{z} + \gamma^2 z = 0.
\end{aligned}$$

The above equations match our Eqs. (2.6) and (2.7) if we rename the parameters appropriately. In this way, it is clear that if the van der Pol term is achieved using relatively small components and active control, then the results of our study are relevant to practical systems studied by other researchers in the nonlinear dynamics community. In fact, the authors of [102] continued with a study of the above system after including a $z^2\dot{z}$ term in [10], which makes the connection with the van der Pol oscillator more direct. However, in [10], the two oscillators were resonant, while in our system they are not resonant.

We now return to an analysis of our equations.

2.4 Multiple scales analysis

The method of multiple scales is an asymptotic method which transforms an ordinary differential equation into a partial differential equation by considering different time scales to be independent variables within an assumed functional form [103, 104]. The method has been regularly applied to a wide variety of engineering and physics problems. The reader may also refer to the review paper by Cartmell *et al.* [105] to appreciate features of the method in the context of weakly nonlinear mechanical systems. Here we apply multiple scales analysis up to second-order to obtain good approximations for the system dynamics. The intermediate expressions are lengthy but can be handled by the computer algebra package Maple, and the final evolution equations are simple and easy to interpret.

The reader may note that, although the multiple scales method presents a seemingly unified approach to a large variety of problems, there may be important differences in the detailed applications to different classes of problems. In terms of the analytical treatment of resonant versus nonresonant interactions, such is indeed the case. When we have a resonant system, we use a detuning parameter. And usually, first-order multiple scales or first-order averaging will give us a useful slow flow. However, when we do nonresonant analysis, usually we have to go to second order to obtain a nontrivial term, and the slow flows obtained are not at all easy to predict from intuition. The expressions dealt with are much longer as well, but it is possible to handle them using symbolic algebra packages. For these reasons, in principle, in detail, and in the magnitude of calculations involved, the resonant and the nonresonant analyses are quite different.

2.4.1 Initial setup

We let $\mu = \sqrt{\varepsilon}$ and rewrite Eqs. (2.6) and (2.7) as

$$\ddot{x} + \mu^2 c\dot{x} + x - \mu m {\omega_p}^2 z - \mu^2 m\gamma \dot{z}(z^2 - 1) = 0,$$

$$\ddot{z} + \ddot{x} + {\omega_p}^2 z + \mu\gamma\, \dot{z}(z^2 - 1) = 0.$$

We introduce multiple time scales $T_0 = t, T_1 = \mu t$ and $T_2 = \mu^2 t$; and then expand $x = X_0 + \mu X_1 + \mu^2 X_2$ and $z = Z_0 + \mu Z_1 + \mu^2 Z_2$. Substituting these expansions into the above equations, we obtain at $\mathcal{O}(1)$

$$\frac{\partial^2}{\partial {T_0}^2} X_0(T_0, T_1, T_2) + X_0(T_0, T_1, T_2) = 0, \tag{2.8}$$

$$\frac{\partial^2}{\partial {T_0}^2} Z_0(T_0, T_1, T_2) + {\omega_p}^2 Z_0(T_0, T_1, T_2) + \frac{\partial^2}{\partial {T_0}^2} X_0(T_0, T_1, T_2) = 0. \tag{2.9}$$

Solving Eq. (2.8) for X_0, we obtain

$$X_0(T_0, T_1, T_2) = R(T_1, T_2) \sin(T_0 + \phi(T_1, T_2)). \tag{2.10}$$

In the above, R denotes the $\mathcal{O}(1)$ amplitude of the primary oscillator. We substitute the above $X_0(T_0, T_1, T_2)$ into Eq. (2.9) and obtain

$$\frac{\partial^2}{\partial {T_0}^2} Z_0(T_0, T_1, T_2) + {\omega_p}^2 Z_0(T_0, T_1, T_2) - R(T_1, T_2) \sin(T_0 + \phi(T_1, T_2)) = 0. \tag{2.11}$$

We solve Eq. (2.11) for Z_0 and obtain

$$Z_0(T_0, T_1, T_2) = Q(T_1, T_2) \sin(\omega_p T_0 + \psi(T_1, T_2)) - \frac{R(T_1, T_2) \sin(T_0 + \phi(T_1, T_2))}{(1 - {\omega_p}^2)}, \tag{2.12}$$

where the first term with new slowly-evolving variables $Q(T_1, T_2)$ and $\psi(T_1, T_2)$ is a complementary solution, and the second term is the particular integral. From the latter, $\omega_p \neq 1$, i.e., $m \neq k$ (by Eq. (2.5)) in the van der Pol oscillator, is an obvious requirement for the analysis to proceed. We recall that $(x + z)$ is the absolute displacement of the secondary oscillator. By Eqs. (2.10) and (2.12), Q denotes the $\mathcal{O}(1)$ amplitude of $z + \dfrac{x}{1 - \omega_p^2}$. When the primary system is stabilized, i.e., x is small or even zero, Q represents the amplitude of the secondary oscillator. In what follows, we suppress the (T_0, T_1, T_2) dependence of already-introduced quantities for compact representation.

2.4.2 Intermediate details

Although the method of multiple scales is well known, here the presence of two frequencies makes some things somewhat new. For completeness, details are presented in this subsection and analysis of the slow dynamics proceeds in the next subsection.

Proceeding as usual, we obtain at $\mathcal{O}(\mu)$

$$\frac{\partial^2 X_1}{\partial {T_0}^2} + X_1 + \left(2\frac{\partial R}{\partial T_1}\right)\cos(T_0+\phi) + \left(-2\frac{\partial \phi}{\partial T_1} + \frac{m{\omega_p}^2}{1-{\omega_p}^2}\right) R\sin(T_0+\phi) - m{\omega_p}^2 Q\sin(\omega_p T_0+\psi) = 0, \quad (2.13)$$

and

$$\begin{aligned}\frac{\partial^2 Z_1}{\partial {T_0}^2} + {\omega_p}^2 Z_1 + \frac{\partial^2 X_1}{\partial {T_0}^2} + \frac{\omega_p}{4(1-{\omega_p}^2)^2}\Bigg(\gamma(1-{\omega_p}^2)^2 Q^3 \\ + 2\gamma(R^2 - 2(1-{\omega_p}^2)^2)Q + 8(1-{\omega_p}^2)^2\frac{\partial Q}{\partial T_1}\Bigg)\cos(\omega_p T_0+\psi) \\ - 2Q\omega_p\frac{\partial \psi}{\partial T_1}\sin(\omega_p T_0+\psi) - \frac{1}{4(1-{\omega_p}^2)^3}\Bigg(2\gamma(1-{\omega_p}^2)^2 Q^2 R \\ + \gamma(R^2 - 4(1-{\omega_p}^2)^2)R + 8(1-{\omega_p}^2)^2{\omega_p}^2\frac{\partial R}{\partial T_1}\Bigg)\cos(T_0+\phi) \\ + \frac{2R{\omega_p}^2}{(1-{\omega_p}^2)}\frac{\partial \phi}{\partial T_1}\sin(T_0+\phi) + \frac{\gamma(2-\omega_p)QR^2}{4(1-{\omega_p}^2)^2}\cos(2T_0-\omega_p T_0+2\phi-\psi) \\ + \frac{\gamma R^3}{4(1-{\omega_p}^2)^3}\cos(3T_0+3\phi) + \frac{\gamma(1+2\omega_p)Q^2 R}{4(1-{\omega_p}^2)}\cos(T_0+2\omega_p T_0+\phi+2\psi) \\ - \frac{1}{4}\gamma\omega_p Q^3\cos(3\omega_p T_0+3\psi) - \frac{\gamma(2+\omega_p)QR^2}{4(1-{\omega_p}^2)^2}\cos(2T_0+\omega_p T_0+2\phi+\psi) \\ + \frac{\gamma(1-2\omega_p)Q^2 R}{4(1-{\omega_p}^2)}\cos(T_0-2\omega_p T_0+\phi-2\psi) = 0. \quad (2.14)\end{aligned}$$

To eliminate secular terms in Eq. (2.13), assuming ω_p is not close to $1/3$ for reasons that will be clear below, we require

$$2\frac{\partial R}{\partial T_1} = 0, \quad (2.15)$$

and

$$\left(-2\frac{\partial \phi}{\partial T_1} + \frac{m{\omega_p}^2}{1-{\omega_p}^2}\right) R = 0. \quad (2.16)$$

Because $R \neq 0$ in general, by Eqs. (2.15) and (2.16), we conclude

$$R(T_1, T_2) = R(T_2), \tag{2.17}$$

and

$$\frac{\partial \phi}{\partial T_1} = \frac{m{\omega_p}^2}{2(1-{\omega_p}^2)}. \tag{2.18}$$

We incorporate the conclusions (2.17) and (2.18) into Eq. (2.13), and obtain

$$\frac{\partial^2 X_1}{\partial {T_0}^2} + X_1 - m{\omega_p}^2 Q \sin(\omega_p T_0 + \psi) = 0. \tag{2.19}$$

Solving Eq. (2.19) for X_1, we obatin

$$X_1(T_0, T_1, T_2) = \frac{m{\omega_p}^2}{1-{\omega_p}^2} Q \sin(\omega_p T_0 + \psi), \tag{2.20}$$

where we have dropped the complementary solution because we are not solving an initial value problem and Eq. (2.10) contains the complementary solution already. We substitute the solution for X_1, i.e., Eq. (2.20), into Eq. (2.14) and obtain

$$\begin{aligned}\frac{\partial^2 Z_1}{\partial {T_0}^2} + {\omega_p}^2 Z_1 + \frac{\omega_p}{4(1-{\omega_p}^2)^2}\Bigg(&\gamma(1-{\omega_p}^2)^2 Q^3 + 2\gamma(R^2 - 2(1-{\omega_p}^2)^2)Q \\ &+ 8(1-{\omega_p}^2)^2 \frac{\partial Q}{\partial T_1}\Bigg)\cos(\omega_p T_0 + \psi) - \left(2\frac{\partial \psi}{\partial T_1} + \frac{m{\omega_p}^3}{(1-{\omega_p}^2)}\right)\omega_p Q \sin(\omega_p T_0 + \psi) \\ &- \frac{1}{4(1-{\omega_p}^2)^3}\Bigg(2\gamma(1-{\omega_p}^2)^2 Q^2 R + \gamma(R^2 - 4(1-{\omega_p}^2)^2)R \\ &+ 8(1-{\omega_p}^2)^2{\omega_p}^2 \frac{\partial R}{\partial T_1}\Bigg)\cos(T_0 + \phi) + \frac{2R{\omega_p}^2}{(1-{\omega_p}^2)}\frac{\partial \phi}{\partial T_1}\sin(T_0 + \phi)\end{aligned}$$

$$
\begin{aligned}
&+\frac{\gamma R^3}{4(1-{\omega_p}^2)^3}\cos(3T_0\ +\ 3\phi)\ +\ \frac{\gamma(1+2\omega_p)Q^2R}{4(1-{\omega_p}^2)}\cos(T_0\ +\ 2\omega_pT_0\ +\ \phi\ +\ 2\psi)\\
&\qquad -\frac{1}{4}\gamma\omega_pQ^3\cos(3\omega_pT_0+3\psi)+\frac{\gamma(1-2\omega_p)Q^2R}{4(1-{\omega_p}^2)}\cos(T_0-2\omega_pT_0+\phi-2\psi)\\
&\qquad\qquad -\frac{\gamma(2+\omega_p)QR^2}{4(1-{\omega_p}^2)^2}\cos(2T_0+\omega_pT_0+2\phi+\psi)\\
&\qquad\qquad +\frac{\gamma(2-\omega_p)QR^2}{4(1-{\omega_p}^2)^2}\cos(2T_0-\omega_pT_0+2\phi-\psi)=0.
\end{aligned}
\tag{2.21}
$$

To eliminate secular terms in Eq. (2.21), we require

$$
\frac{\omega_p}{4(1-{\omega_p}^2)^2}\left(\gamma(1-{\omega_p}^2)^2Q^3+2\gamma(R^2-2(1-{\omega_p}^2)^2)Q+8(1-{\omega_p}^2)^2\frac{\partial Q}{\partial T_1}\right)=0,
\tag{2.22}
$$

and

$$
\left(2\frac{\partial\psi}{\partial T_1}+\frac{m{\omega_p}^3}{(1-{\omega_p}^2)}\right)\omega_pQ=0.
\tag{2.23}
$$

Because $Q\neq 0$ in general, by Eqs. (2.22) and (2.23), we find

$$
\frac{\partial Q}{\partial T_1}=-\frac{\gamma\left((Q^2-4)(1-{\omega_p}^2)^2+2R^2\right)}{8(1-{\omega_p}^2)^2}Q,
\tag{2.24}
$$

and

$$
\frac{\partial\psi}{\partial T_1}=-\frac{m{\omega_p}^3}{2(1-{\omega_p}^2)}.
\tag{2.25}
$$

We incorporate the conclusions (2.24) and (2.25) into Eq. (2.21), and obtain

$$
\begin{aligned}
&\frac{\partial^2Z_1}{\partial {T_0}^2}+{\omega_p}^2Z_1-\frac{1}{4(1-{\omega_p}^2)^3}\Bigg(2\gamma(1-{\omega_p}^2)^2Q^2R\\
&\qquad\qquad +\gamma(R^2-4(1-{\omega_p}^2)^2)R+8(1-{\omega_p}^2)^2{\omega_p}^2\frac{\partial R}{\partial T_1}\Bigg)\cos(T_0+\phi)\\
&\qquad +\frac{2R{\omega_p}^2}{(1-{\omega_p}^2)}\frac{\partial\phi}{\partial T_1}\sin(T_0+\phi)-\frac{\gamma(2+\omega_p)QR^2}{4(1-{\omega_p}^2)^2}\cos(2T_0+\omega_pT_0+2\phi+\psi)\\
&\qquad +\frac{\gamma R^3}{4(1-{\omega_p}^2)^3}\cos(3T_0+3\phi)+\frac{\gamma(2-\omega_p)QR^2}{4(1-{\omega_p}^2)^2}\cos(2T_0-\omega_pT_0+2\phi-\psi)
\end{aligned}
$$

$$
-\frac{1}{4}\gamma\omega_p Q^3\cos(3\omega_p T_0 + 3\psi) + \frac{\gamma(1+2\omega_p)Q^2 R}{4(1-{\omega_p}^2)}\cos(T_0 + 2\omega_p T_0 + \phi + 2\psi) \\
+ \frac{\gamma(1-2\omega_p)Q^2 R}{4(1-{\omega_p}^2)}\cos(T_0 - 2\omega_p T_0 + \phi - 2\psi) = 0. \quad (2.26)
$$

We can now solve Eq. (2.26) for Z_1. The expression for Z_1, being of minor interest, is provided in Appendix A. Proceeding further, we obtain the $\mathcal{O}(\mu^2)$ equations of the form

$$
L_1 = 0 \quad \text{and} \quad L_2 = 0, \quad (2.27)
$$

where L_1 and L_2 are long expressions also provided in Appendix A. Eliminating secular terms from the equation $L_1 = 0$, we obtain

$$
\frac{\partial R}{\partial T_2} = \left[-\frac{c}{2} - \frac{m\gamma\left(2(Q^2-2)(1-{\omega_p}^2)^2 + R^2\right)}{8(1-{\omega_p}^2)^4}\right]R, \quad (2.28)
$$

and

$$
\frac{\partial \phi}{\partial T_2} = -\frac{m^2{\omega_p}^4(1+3{\omega_p}^2)}{8(1-{\omega_p}^2)^3}. \quad (2.29)
$$

Equation (2.28) governs the evolution of R. We incorporate Eqs. (2.28) and (2.29) into the equation $L_1 = 0$ and solve the resulting equation for X_2. The expression for X_2 is provided in Appendix A. We substitute the solution for X_2 into the equation $L_2 = 0$ and eliminate secular terms therein. We obtain

$$
\frac{\partial Q}{\partial T_2} = \left[\frac{m\gamma{\omega_p}^2\left((Q^2-4)(2-{\omega_p}^2)(1-{\omega_p}^2)^2 + 2R^2(2+{\omega_p}^2)\right)}{8(1-{\omega_p}^2)^4}\right]Q, \quad (2.30)
$$

and

$$
\frac{\partial \psi}{\partial T_2} = -\frac{7\gamma^2}{256\omega_p}Q^4 + \frac{\gamma^2}{8\omega_p}(Q^2-1) + \frac{\gamma^2(3{\omega_p}^2-2)}{64\omega_p(1-{\omega_p}^2)^5}R^4 \\
- \frac{\gamma^2(21{\omega_p}^4 - 14{\omega_p}^2 + 1)}{16\omega_p(1-9{\omega_p}^2)(1-{\omega_p}^2)^3}Q^2R^2 + \frac{\gamma^2}{8\omega_p(1-{\omega_p}^2)^2}R^2 + \frac{m^2{\omega_p}^5({\omega_p}^2+3)}{8(1-{\omega_p}^2)^3}. \quad (2.31)
$$

The fourth term on the right hand side of Eq. (2.31) indicates a 1:3 internal resonance, which we have avoided as our primary interest is in non-resonant interactions. As stated earlier, therefore, we simply assume $\omega_p \neq \frac{1}{3}$ in the present analysis.

2.4.3 Slow amplitude equations

We note that the evolution Eqs. (2.24), (2.28) and (2.30) for the amplitudes R and Q are independent of the phases ϕ and ψ. This is because the system is autonomous and nonresonant. For stabilization of the block, the amplitudes R and Q are of primary interest. Therefore, we do not need the ϕ and ψ evolution Eqs. (2.18), (2.25), (2.29) and (2.31) any more.

Further, the evolution of Q given by Eq. (2.24) dominates while Eq. (2.30) provides only a tiny correction, because T_2 is a slower time scale than T_1. Therefore, we may drop Eq. (2.30) while considering the evolution of Q. We are then left with two first-order equations, Eqs. (2.24) and (2.28). Recalling $T_1 = \mu t$ and $T_2 = \mu^2 t$ with $\mu = \sqrt{\varepsilon}$, we will work with

$$\frac{\mathrm{d}Q}{\mathrm{d}T_1} = -\frac{\gamma\left((Q^2-4)(1-{\omega_p}^2)^2+2R^2\right)}{8(1-{\omega_p}^2)^2}Q + \mathcal{O}(\mu), \tag{2.32}$$

and

$$\frac{\mathrm{d}R}{\mathrm{d}T_1} = \mu\left[-\frac{c}{2} - \frac{m\gamma\left(2(Q^2-2)(1-{\omega_p}^2)^2+R^2\right)}{8(1-{\omega_p}^2)^4}\right]R. \tag{2.33}$$

Figure 2.2 compares two numerical solutions of Eqs. (2.6) and (2.7) with those of Eqs. (2.32) and (2.33). Although the primary system is negatively damped in both cases, with $c < 0$, Figs. 2.2(a) and 2.2(b) demonstrate suppression and growth respectively. The match between the multiple scales solution (or slow amplitude equations) and full integration is seen to be very good. We now study the slow amplitude equations more systematically.

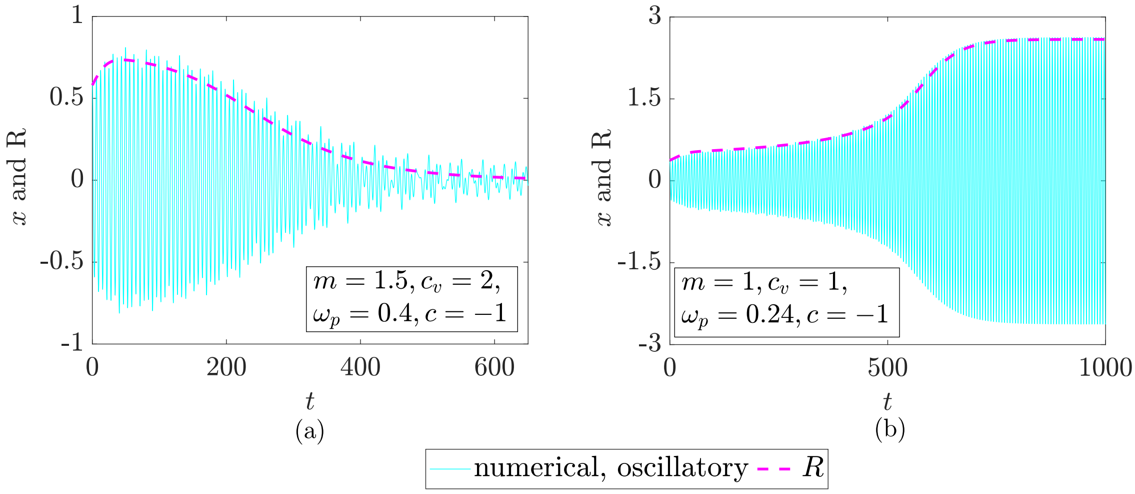

FIGURE 2.2: Comparison of numerical solution of Eqs. (2.6) and (2.7) with that of Eqs. (2.32) and (2.33). $\varepsilon = 0.01$ in all cases. Subplots (a) and (b) demonstrate decaying and limit cycle solutions of the primary oscillator, respectively. Initial conditions for (a) are $x(0) = 0.6, \dot{x}(0) = 0, z(0) = 0, \dot{z}(0) = 0, R(0) = 0.58, Q(0) = 0.7143$, and for (b) are $x(0) = 0.35, \dot{x}(0) = 0, z(0) = 0, \dot{z}(0) = 0, R(0) = 0.375, Q(0) = 0.3964$.

2.5 Canonical form

We now adopt a parameter-dependent transformation, including an $\mathcal{O}(1)$ stretching of the time T_1, to simplify the slow flow Eqs. (2.32) and (2.33) into a unifying form. Writing $(1 - {\omega_p}^2)^2 = w$, we set

$$Q^2 = S \quad \text{and} \quad R^2 = wP \tag{2.34}$$

to obtain

$$\frac{\mathrm{d}S}{\mathrm{d}T} = \mp (S + 2P - 4)\, S + \mathcal{O}(\bar{\mu}), \tag{2.35}$$

$$\frac{\mathrm{d}P}{\mathrm{d}T} = \mp \bar{\mu}\, (2S + P - 4 - c_1)\, P, \tag{2.36}$$

where

$$c_1 = -\frac{4cw}{m\gamma}, \quad \bar{\mu} = \frac{\mu m}{w}, \tag{2.37}$$

and the T indicates that we have absorbed the $\mathcal{O}(1)$ factor of $\dfrac{|\gamma|}{4}$ into T_1. The $\mp$ sign reflects the sign of γ, with the negative being taken for $\gamma > 0$.

Based on the goals of this chapter, we consider $\gamma > 0$, i.e., the negative sign in the $\mp$

options above. It may be noted in Eq. (2.37) that our main interest is in $c < 0$ (primary system negatively damped) and $\gamma > 0$ (secondary system has a stable untuned limit cycle), and so we are mainly interested in $c_1 > 0$. However, from a dynamic systems viewpoint, if the primary system is changed to positively damped and the secondary system's limit cycle oscillator also has its nonlinear damping reversed[1] then c_1 will remain unchanged while the positive sign will be adopted in the $\mp$ options above, leading to the same phase portrait with flow directions reversed. With these observations, in what follows, we will take the negative sign in the $\mp$ options above.

With the above motivation we finally write our main equations in canonical form, as obtained *via* the second-order multiple scales analysis:

$$\frac{\mathrm{d}S}{\mathrm{d}T} = -\left(S + 2P - 4\right) S + \mathcal{O}(\bar{\mu}), \tag{2.38}$$

$$\frac{\mathrm{d}P}{\mathrm{d}T} = -\bar{\mu}\left(2S + P - 4 - c_1\right) P, \tag{2.39}$$

with $0 < \bar{\mu} \ll 1$ and $c_1 > 0$. In the above, S and P correspond to the squares of the secondary and primary oscillators' amplitudes respectively.

Equations (2.38) and (2.39) are simpler than Eqs. (2.32) and (2.33). For $\bar{\mu}$ sufficiently small, the single physical parameter c_1 governs the qualitative dynamics of the system. Interestingly, recalling $c_v = m\gamma$ from Eq. (2.5), we see that c_1 is superficially independent of the secondary oscillator's mass m. Of course, the foregoing analysis assumes that there is indeed an $\mathcal{O}(1)$ mass m. The effect of m is retained in the frequency ω_p which in turn determines w.

2.6 Final slow amplitude dynamics

We now use Eqs. (2.38) and (2.39) to examine the dynamics on the first quadrant of the P-S plane. We first note that the S dynamics is typically much faster than the P

[1]Upon changing the sign of γ, small solutions for that oscillator would be stable, large solutions would be unbounded, and there would be an unstable limit cycle.

dynamics. Accordingly, for the overall qualitative dynamics, we neglect the small $\mathcal{O}(\bar{\mu})$ term in Eq. (2.38), because retaining it would change the resulting phase portrait only slightly, at the cost of more complicated expressions and less clear insight. Comparisons with full numerical solutions of the original equations will support this simplification.

We also note that P and S axes form invariant manifolds: $S = 0$ yields dynamics purely on the P-axis, and vice versa.

On examining dynamics on the P-axis, by Eq. (2.39), we find an unstable point $P = 0$ and a stable point $P = 4 + c_1$. Further, by Eq. (2.38), it is easy to see that $S = 0$ is unstable for $P = 0$ and stable for $P = 4 + c_1$. Hence, the fixed points $(S = 0, P = 0)$ and $(0, 4 + c_1)$ are unstable and stable nodes, respectively.

Similarly, on the S-axis, by Eq. (2.38), we find an unstable fixed point $S = 0$ and a stable fixed point $S = 4$. By Eq. (2.39), for $S = 4$, stability of $P = 0$ requires $c_1 < 4$. Hence, the fixed point $(4, 0)$ is a stable node if $c_1 < 4$, and a saddle if $c_1 > 4$. Further, by Eqs. (2.38) and (2.39), the fourth and final fixed point is at the intersection of the straight lines

$$S + 2P - 4 = 0, \quad \text{and} \quad 2S + P - 4 - c_1 = 0. \tag{2.40}$$

For $c_1 > 4$, the above lines do not intersect in the first quadrant. Therefore, the fourth fixed point exists for $0 < c_1 < 4$.

From the above, we conclude that the system dynamics has two qualitatively different regimes: $0 < c_1 < 4$ and $c_1 > 4$. The canonical form of our equations allows us to reach this far quite easily. We now study these two regimes separately.

2.6.1 Dynamics for $0 < c_1 < 4$

Recalling Eq. (2.40), the fourth fixed point named (S^*, P^*) is at

$$S^* = \frac{2}{3}(2 + c_1), \quad P^* = \frac{1}{3}(4 - c_1). \tag{2.41}$$

The stability of (S^*, P^*) is governed by the eigenvalues of a Jacobian matrix of the form

$$\mathbf{D} = \begin{bmatrix} -S^* + \mathcal{O}(\bar{\mu}) & -2S^* + \mathcal{O}(\bar{\mu}) \\ -2\bar{\mu}P^* & -\bar{\mu}\left(S^* - c_1\right) \end{bmatrix}, \tag{2.42}$$

where $\mathcal{O}(\bar{\mu})$ terms in the first row have been suppressed for simplicity. To obtain the eigenvalues of $\mathbf{D}$, we can solve the characteristic equation

$$\det(\mathbf{D} - \lambda\mathbf{I}) = 0.$$

But we can use asymptotic arguments to make progress through simpler expressions. The characteristic equation takes the form

$$(S^* + \lambda)\lambda + \mathcal{O}(\bar{\mu}) = 0. \tag{2.43}$$

Thus, one eigenvalue is

$$\lambda_1 = -S^* + \mathcal{O}(\bar{\mu})$$

and the other one is $\mathcal{O}(\bar{\mu})$. Consistent with these, we also note that $\mathrm{tr}(\mathbf{D}) = -S^* + \mathcal{O}(\bar{\mu})$. The product of the eigenvalues is

$$\det(\mathbf{D}) = \bar{\mu}\left(S^* - c_1\right) S^* - 4\bar{\mu}P^*S^* + \mathcal{O}\left(\bar{\mu}^2\right).$$

Dropping the higher order small term and factoring out the known eigenvalue of $-S^*$, we find using Eq. (2.41) that the other eigenvalue is

$$\lambda_2 = -\bar{\mu}\left(S^* - 4P^* - c_1\right) = \bar{\mu}(4 - c_1) > 0$$

to leading order. Thus, the fixed point given by Eq. (2.41) is a saddle.

We next find the corresponding eigenvectors of λ_1 and λ_2, given by

$$(\mathbf{D} - \lambda\mathbf{I})\mathbf{X} = \mathbf{0}, \tag{2.44}$$

where $\mathbf{X} = \{x_1,\, x_2\}^T$. For $\lambda = \lambda_1$, the second row in Eq. (2.44) yields

$$-2\bar{\mu}P^* x_1 - (\bar{\mu}\,(S^* - c_1) - S^*)x_2 = 0,$$

whence, x_2 is $\mathcal{O}(\bar{\mu})$. Hence, to $\mathcal{O}(1)$, the eigenvector corresponding to λ_1 is $\{1,\, 0\}^T$. For $\lambda = \lambda_2$, the second row in Eq. (2.44) yields

$$x_1 + 2x_2 = 0$$

at leading order, where we have substituted for P^* and S^* from Eq. (2.41). This means the eigenvector corresponding to λ_2 is $\{2,\, -1\}^T$. Graphically, the eigenvector corresponding to λ_1 (stable direction) is horizontal, and the eigenvector corresponding to λ_2 (unstable direction) is along a line like EF in Fig. 2.3(a).

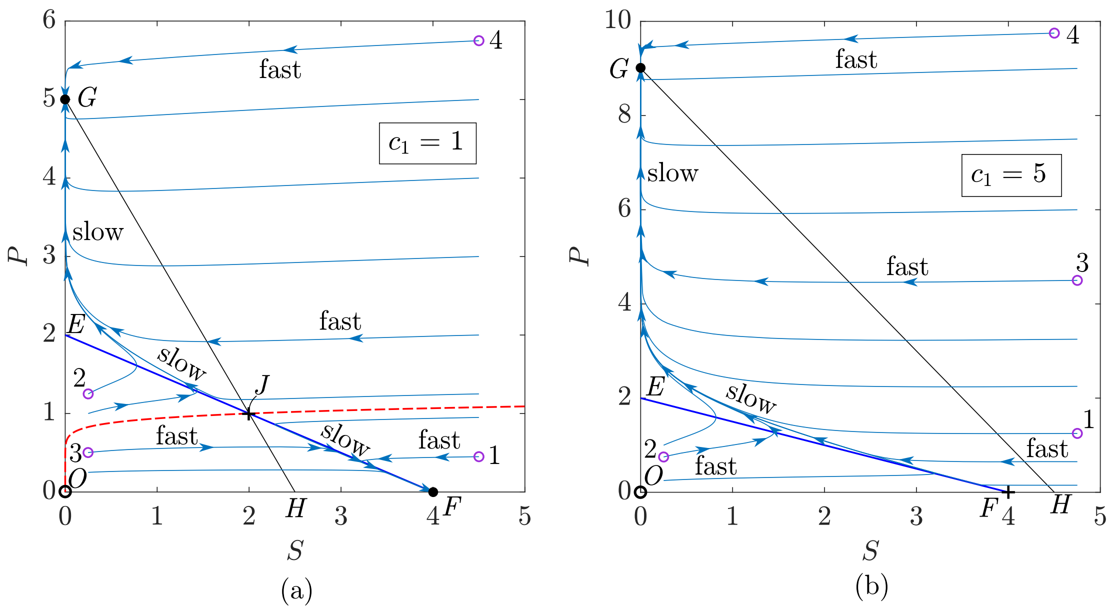

FIGURE 2.3: Phase portraits for (a) $0 < c_1 < 4$ and (b) $c_1 > 4$. $\bar{\mu} = 0.05$ in both cases. Trajectories starting from different initial conditions are obtained by numerical integration of Eq. (2.39) along with Eq. (2.38) with the small $\mathcal{O}(\bar{\mu})$ term dropped.

Figure 2.3(a) shows a phase portrait for $c_1 = 1$, which is representative of the case $0 < c_1 < 4$. Here, solid circles denote stable nodes, hollow circles denote unstable nodes and plus signs denote saddles. The fixed points are: (i) $O(0, 0)$, unstable node, (ii) $F(4, 0)$, stable node, (iii) $G(0, 4 + c_1)$, stable node, and (iv) $J(S^*, P^*)$, saddle. Nearly-horizontal trajectories depict much faster evolution of S than P, as expected by the smallness of $\bar{\mu}$. Near the saddle, trajectories rapidly approach the unstable eigenvector and then turn to move more slowly and approximately along the unstable eigenvector direction, i.e., line EF. Trajectories toward F follow the line EF all the way, while trajectories towards E veer off to approach G on the vertical axis. The dashed (red) line is a separatrix that divides the plane into two regions: trajectories going to G and going to F. The separatrix was obtained numerically by reversing the flow from the saddle point with a tiny perturbation in the stable eigenvector direction, i.e., horizontal direction. This separatrix depicts the nature and extent of the vibration stabilization achieved. For initial conditions below the separatrix, the primary system is stabilized and the secondary system's limit cycle is established. For initial conditions above the separatrix, the primary system wins the contest, the secondary system's limit cycle is quenched, and the nonlinear damping of the secondary system serves to limit the oscillation amplitudes of the otherwise-linear primary system. As c_1 increases towards 4, the point H moves towards F, the separatrix moves downward, and the basin of attraction of the stabilized primary system shrinks in size. Recalling the definition of c_1 in Eq. (2.37), we see that c_1 is smaller if the negative damping level c of the primary system is smaller, if the strength of the van der Pol term γ is bigger, and if the untuned frequency ω_p of the secondary system is closer to unity. Note that with resonance at $\omega_p = 1$, the present analysis breaks down; ω_p should not be too close to unity for the stabilization strategy considered in this work.

2.6.2 Dynamics for $c_1 > 4$

Figure 2.3(b) shows a phase portrait for $c_1 = 5$. The fixed points are: (i) $O(0, 0)$, unstable node, (ii) $F(4, 0)$, saddle, and (iii) $G(0, 4 + c_1)$, stable node. The intersection point J of the foregoing case has disappeared. The basin of attraction of stabilized motions of the primary system has shrunk to zero and then disappeared. Essentially all trajectories go to node G. As discussed above, the value of c_1 can be made smaller by increasing γ

or letting ω_p be closer to unity, but the upper limit of the present stabilization strategy, asymptotically for small μ, is analytically clear from the canonical equations: $c_1 = 4$.

We note that responses like in Fig. 2.3 are typical for systems with nonresonant double Hopf bifurcations: see [11, 12, 102, 106] and also [107]. Therefore, Fig. 2.3 resembles some plots in these studies, e.g., see Fig. 4 in [102], Fig. 2 in [11], Fig. 2 in [12] and Fig. 5 in [106]. However, in contrast to those studies, in the present work, we consider a specific parameter regime where one oscillator is much less massive than the other; where the secondary oscillator is destabilized with feedback to produce a limit cycle; and where the slow flow carried up to second-order is found to be such that everything can be expressed in terms of a single nondimensional parameter in canonical equations. In this way, our study makes significant new contributions although in a more narrow application area.

2.6.3 Using Rayleigh damping

It is interesting at this stage to consider a different form of nonlinear damping. As an alternative to the nonlinear damping of the van der Pol oscillator, we can use the Rayleigh damping term. Using that term, the governing equations take the form

$$\begin{aligned}
&\ddot{x} + x + \mu^2 c\dot{x} - \mu\, m\, \omega_p^2\, z - \mu^2\, m\gamma\, \dot{z}\,(\dot{z}^2 - 1) = 0,\\
&\ddot{z} + \ddot{x} + \omega_p^2\, z + \mu\gamma\, \dot{z}\,(\dot{z}^2 - 1) = 0.
\end{aligned}$$

where we refer the reader to Section 2.3 for nomenclature and details of variables and parameters. Following the method detailed in Section 2.4, and using the transformation

$$Q^2 = \frac{S}{\omega_p^2}, \quad R^2 = wP,$$

we finally obtain

$$\frac{\mathrm{d}S}{\mathrm{d}T} = -\left(S + 2P - \frac{4}{3}\right) S + \mathcal{O}(\bar{\mu}), \tag{2.45}$$

$$\frac{\mathrm{d}P}{\mathrm{d}T} = -\bar{\mu}\left(2S + P - \frac{4}{3} - \frac{c_1}{3}\right) P, \tag{2.46}$$

where

$$T = \frac{3\gamma}{4} T_1, \quad \bar{\mu} = \frac{\mu m}{w}, \quad c_1 = -\frac{4cw}{m\gamma}.$$

Equations (2.45) and (2.46) can be compared with Eqs. (2.38) and (2.39). They are essentially identical with only the divisor 3 being new here. The above equations indicate a saddle

$$S^* = \frac{2}{9}(2 + c_1), \quad P^* = \frac{1}{9}(4 - c_1).$$

The equation for P^* indicates that the stabilization criterion remains identical to what was found earlier using the van der Pol term, i.e., $c_1 < 4$.

2.6.4 Parameter c_1 in terms of system parameters

We have observed that the nondimensional parameter c_1 governs the qualitative dynamics of the system. To reconnect with the original physical variables we note that, by Eqs. (2.3), (2.4), (2.5) and (2.37),

$$c_1 = -4\,\frac{C}{\bar{c}_v}\left(1 - \frac{\omega^2}{\Omega^2}\right)^2, \tag{2.47}$$

where $C < 0$ and $\bar{c}_v > 0$ are in Eq. (2.1), and where Ω and ω are the natural frequencies of the primary and secondary oscillators respectively. We recall the stabilization criterion $c_1 < 4$, and that lower c_1 gives a larger stabilization regime. Finally, we emphasize that $\omega \neq \Omega$ in our analysis. By Eq. (2.47), the following interpretations can now be made. Higher values of $\omega < \Omega$ lower the demand on $\bar{c}_v$. For example, with $\omega \sim 0.4\Omega$, $\bar{c}_v$ is required to be higher than $0.84^2 C \approx 0.7C$. In comparison, with $\omega \sim 0.85\Omega$, $\bar{c}_v$ is required to be higher than merely $0.077C$. Conversely, with the same $\bar{c}_v$, relatively larger ω can help to stabilize larger negative damping C. Always, by selecting high enough $\bar{c}_v$, we can achieve $c_1 < 4$, i.e.,

$$- \frac{C}{\bar{c}_v}\left(1 - \frac{\omega^2}{\Omega^2}\right)^2 < 1. \tag{2.48}$$

However, as emphasized repeatedly in this thesis, precise near-resonant tuning ($\omega \approx \Omega$) is assumed to be absent. This allows the same stabilization system to continue working even under a change in operating parameters that changes Ω.

We next discuss system responses in terms of the original variables. In particular, we will demonstrate that widely different sets of parameter values corresponding to the same c_1 and $\bar{\mu}$ follow the same phase portrait.

2.6.5 Responses in terms of original variables

Recalling the transformations to variables P and S adopted in Eq. (2.34) from the amplitude variables Q and R introduced within the multiple scales analysis, we now present numerical solutions of the original Eqs. (2.6) and (2.7) and the slow amplitude Eqs. (2.32) and (2.33) in Figs. 2.4–2.7. These numerical solutions show an excellent qualitative match between the $\mathcal{O}(1)$ dynamics and the full numerical solutions; and they also show a small mismatch (as expected) when the leading order term in the solution goes to zero, because the next term in the expansion still remains nonzero. For a sizeable range of parameter values, in particular, it will be seen that the phase portraits obtained from the canonical equations yield accurate and useful insight into the dynamics of the original system.

These four Figs. 2.4–2.7 are arranged as follows. In each figure, the two subplots on the left correspond to a single set of parameter values corresponding to particular values of c_1 and $\bar{\mu}$, as well as one set of initial conditions; and the two subplots on the right correspond to a different set of parameter values corresponding to the *same* values of c_1 and $\bar{\mu}$, along with a different set of initial conditions. The upper subplots show the numerical solution for x, whose slowly varying amplitude is to be compared with the variable R; and the lower subplots show the numerically obtained values of $z + \dfrac{x}{1-\omega_p^2}$, whose slowly varying amplitude is to be compared with Q. In this way, the direct correspondence between the original oscillatory solutions and the slow amplitude solutions can be easily seen. The unifying role of the canonical equations is demonstrated as well. Individual details for the different figures, including initial conditions, are provided below.

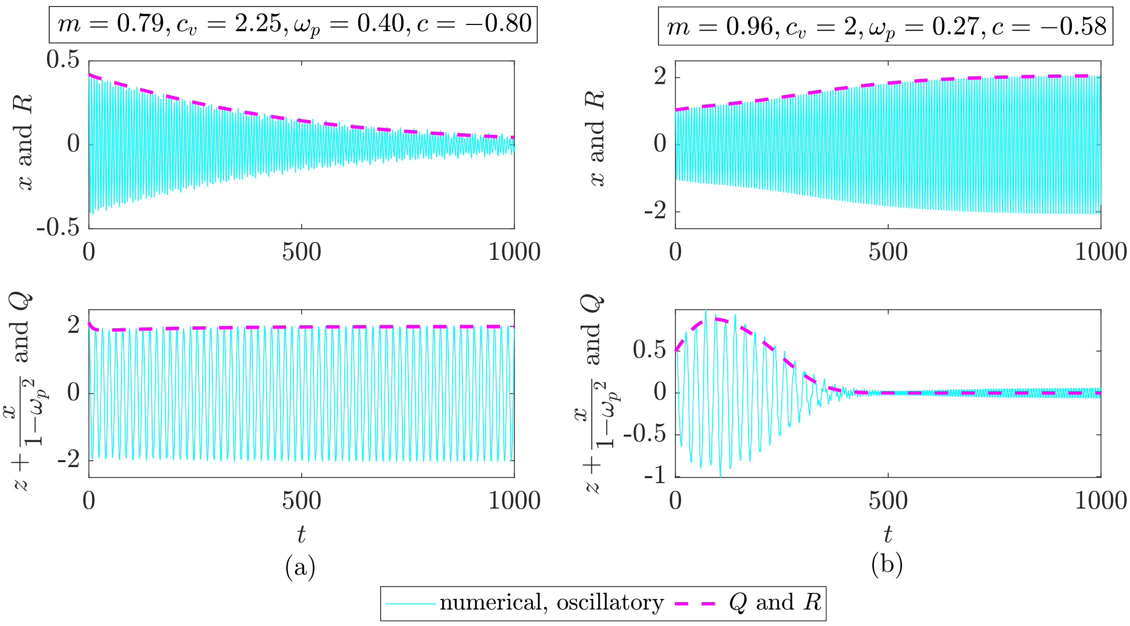

FIGURE 2.4: Numerical solutions of Eqs. (2.6) and (2.7) and Eqs. (2.32) and (2.33). For upper (respectively, lower) subplots, the dashed magenta line shows solutions for R (respectively, Q). For left and right subplots, initial conditions match points 1 and 2 respectively in Fig. 2.3(a). $\varepsilon = 0.002$, $c_1 = 1$ and $\bar{\mu} = 0.05$ in all cases.

Initial conditions in Figs. 2.4(a) and 2.4(b) respectively correspond to the points marked 1 and 2 in Fig. 2.3(a). Figure 2.3(a) shows that the trajectory from initial condition 1 moves to the point $F(4, 0)$. The corresponding response in Fig. 2.4(a) shows that the primary system amplitude decays to a small value (upper plot), and the secondary system settles to a limit cycle with amplitude 2 (lower plot).

For the trajectory from initial condition 2 in Fig. 2.3(a), S initially grows up to about 0.77 and then decays. The corresponding response in Fig. 2.4(b) initially grows to about $\sqrt{0.77} = 0.88$ and then decays (recall that $Q = \sqrt{S}$, Eq. (2.34)). In this solution the limit cycle of the secondary oscillator is quenched. The upper plot confirms the predicted steady nonzero oscillation of the primary system.

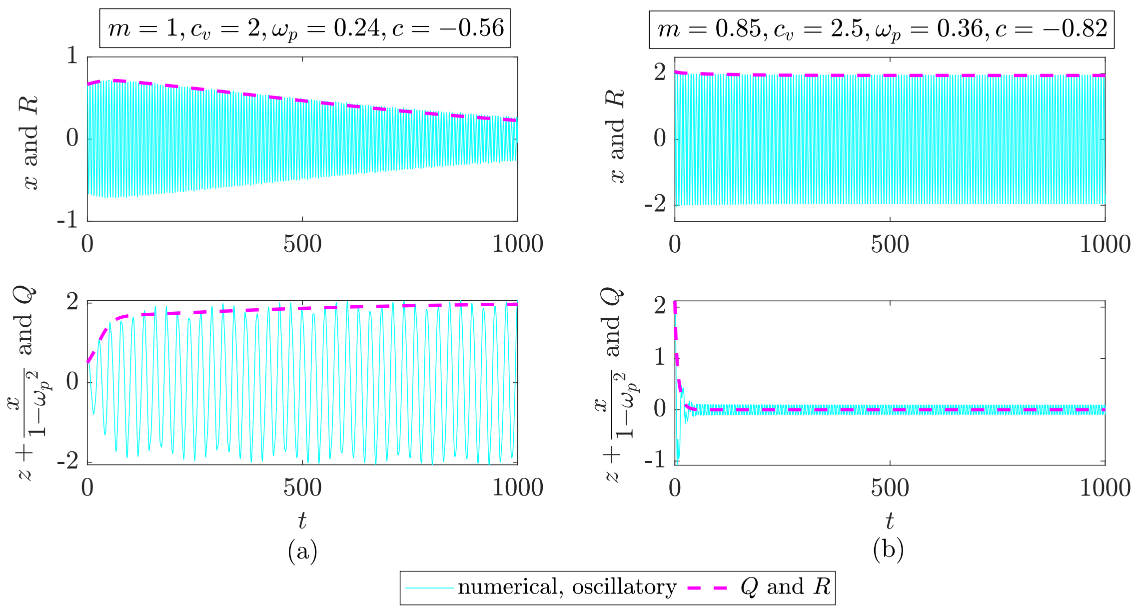

FIGURE 2.5: Numerical solutions of Eqs. (2.6) and (2.7) and Eqs. (2.32) and (2.33). For upper (respectively, lower) subplots, the dashed magenta line shows solutions for R (respectively, Q). For left and right subplots, initial conditions match points 3 and 4 respectively in Fig. 2.3(a). $\varepsilon = 0.002$, $c_1 = 1$ and $\bar{\mu} = 0.05$ in all cases.

Next, see Fig. 2.5. Initial conditions in Figs. 2.5(a) and 2.5(b) correspond to the points marked 3 and 4 respectively in Fig. 2.3(a). In Fig. 2.3(a), for the trajectory from initial condition 3, P decays and S shows rapid initial growth followed by a slower increase. Figure 2.5(a), on the left, shows the corresponding responses in the original variables. The upper subplot shows the decaying response of the primary system. In the lower subplot we see the fast initial growth in the secondary system's response followed by a slow approach to amplitude 2.

The trajectory from initial condition 4, in Fig. 2.3(a), goes to $G(0, 5)$ with a rapid decay in S. Correspondingly in Fig. 2.5(b), the upper subplot shows a steady oscillation while the lower subplot shows a rapid decay in amplitude. The secondary system's limit cycle is quenched for this initial condition, although the parameters are the same.

Similarly, consider Figs. 2.6 and 2.7. In these figures, $\varepsilon = 0.002$, $c_1 = 5$, and $\bar{\mu} = 0.05$. The initial conditions for Figs. 2.6(a), 2.6(b), 2.7(a) and 2.7(b) correspond to the points 1, 2, 3 and 4 respectively in Fig. 2.3(b). In the upper subplots of these two figures, we observe that the primary system stabilizes to a limit cycle because all trajectories in Fig. 2.3(b) finally merge to $G(0,9)$. The limit cycle amplitude is $3(1-{\omega_p}^2)$ in these figures. The decay in the secondary oscillator's response is consistent with the corresponding trajectories in Fig. 2.3(b). In particular, the relatively lower frequency (ω_p) of oscillations in the decaying portions of the lower subplots may be noted: after the decay is complete, the remaining oscillations are at the frequency of the primary oscillator, which is itself seen in the upper subplots.

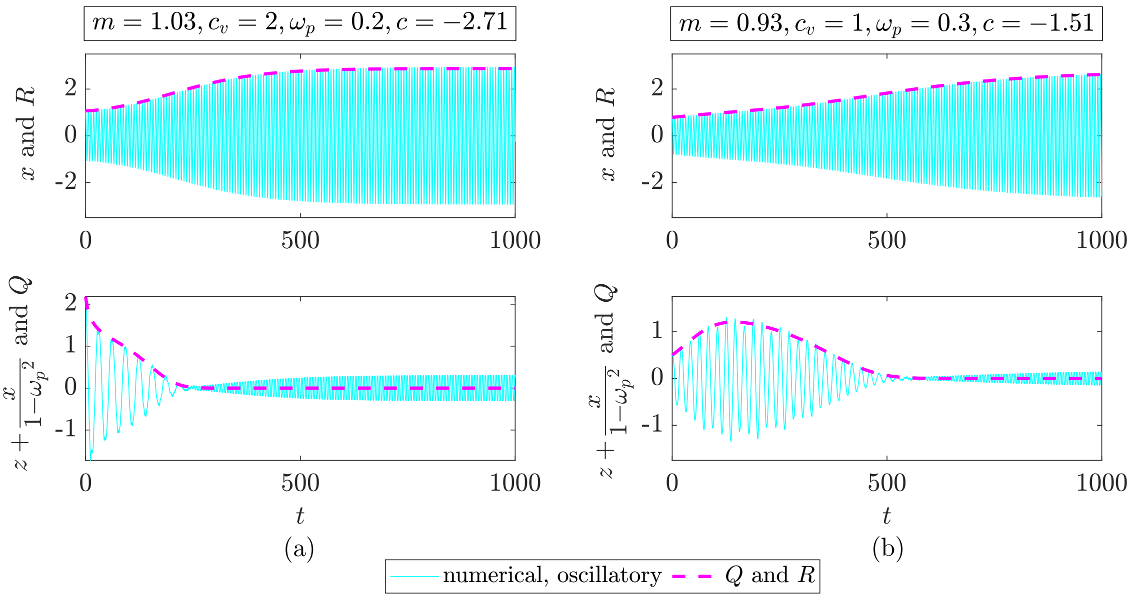

FIGURE 2.6: Numerical solutions of Eqs. (2.6) and (2.7) and Eqs. (2.32) and (2.33). For upper (respectively, lower) subplots, the dashed magenta line shows solutions for R (respectively, Q). For left and right subplots, initial conditions match points 1 and 2 respectively in Fig. 2.3(b). $\varepsilon = 0.002$, $c_1 = 5$ and $\bar{\mu} = 0.05$ in all cases.

For the trajectory from initial condition 1, the slow decay of S in Fig. 2.3(b) correlates with the secondary oscillator's response in the lower plot of Fig. 2.6(a). For the trajectory from initial condition 2, we notice that S initially grows upto about 1.46 and then decays. The lower plot in Fig. 2.6(b) confirms this increase-decrease evolution of the secondary oscillator's response. Further, for trajectories from initial conditions 3 and 4 in Fig. 2.3(b), we notice the rapid initial decay of S. The lower subplots in the corresponding Figs. 2.7(a) and 2.7(b) show rapid initial decay in the secondary oscillator's response. As mentioned above, the remaining oscillations in the lower subplots, most clearly seen in Fig. 2.7(b), are due to $\mathcal{O}(\mu)$ terms in the multiple scales expansion that have not been incorporated in the plots: see the expression for Z_1 in Appendix A.

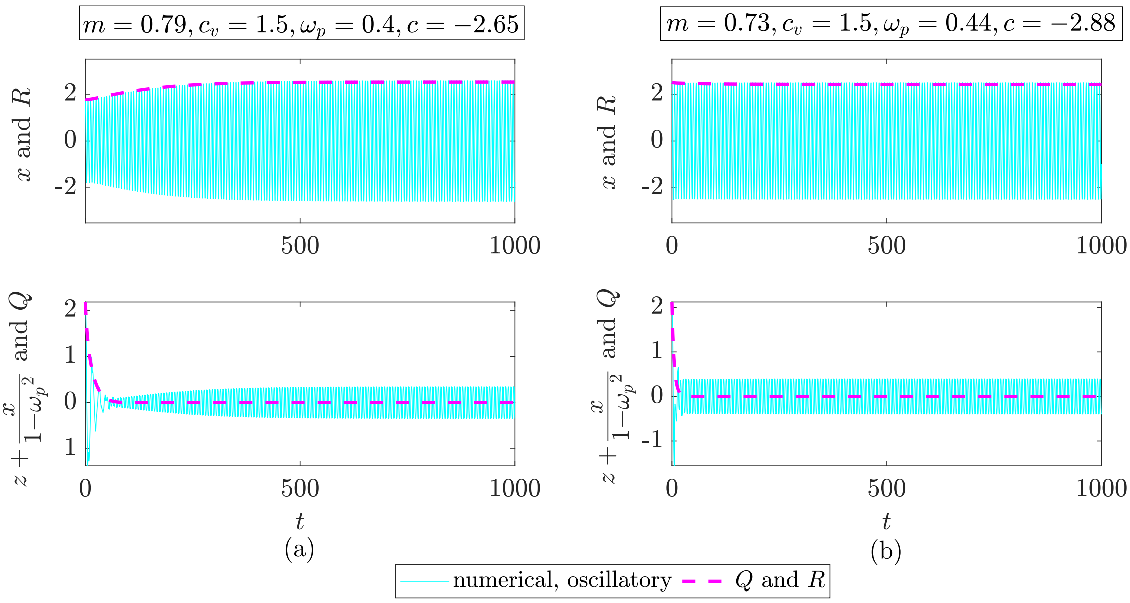

FIGURE 2.7: Numerical solutions of Eqs. (2.6) and (2.7) and Eqs. (2.32) and (2.33). For upper (respectively, lower) subplots, the dashed magenta line shows solutions for R (respectively, Q). For left and right subplots, initial conditions match points 3 and 4 respectively in Fig. 2.3(b). $\varepsilon = 0.002$, $c_1 = 5$ and $\bar{\mu} = 0.05$ in all cases.

In this way, through Figs. 2.4–2.7, it is seen that the slow dynamics captured by the second-order multiple scales analysis does a good job of capturing the qualitative behavior of quenching of the primary oscillator's unstable vibrations. Moreover, the phase portraits obtained from our canonical equations (2.38) and (2.39) give a simple and clear picture of the separatrix that lies between persistence and quenching of the primary unstable mode.

We note that although the results presented in this study consider $\omega_p < 1$, it is not necessary for the validity of our analysis. The main requirement is that different terms treated as $\mathcal{O}(1)$ in the analysis should be reasonably comparable to 1. If they are significantly bigger or significantly smaller than 1, extremely small ε may be required before we get a good match. Figure 2.8 shows the comparison for $\omega_p = 1.15$ (> 1) and different ε, demonstrating the asymptotic nature of solutions.

We end this chapter by recalling that the solutions for x and z have been assumed to be $\mathcal{O}(1)$ with respect to $0 < \varepsilon \ll 1$. Numerical solutions show that if initial conditions for x (the unstable primary mode) are taken large enough, then solutions to the original Eqs. (2.6) and (2.7) can be unbounded. Recalling that $\gamma = c_v/m$ in Eqs. (2.6) and (2.7),

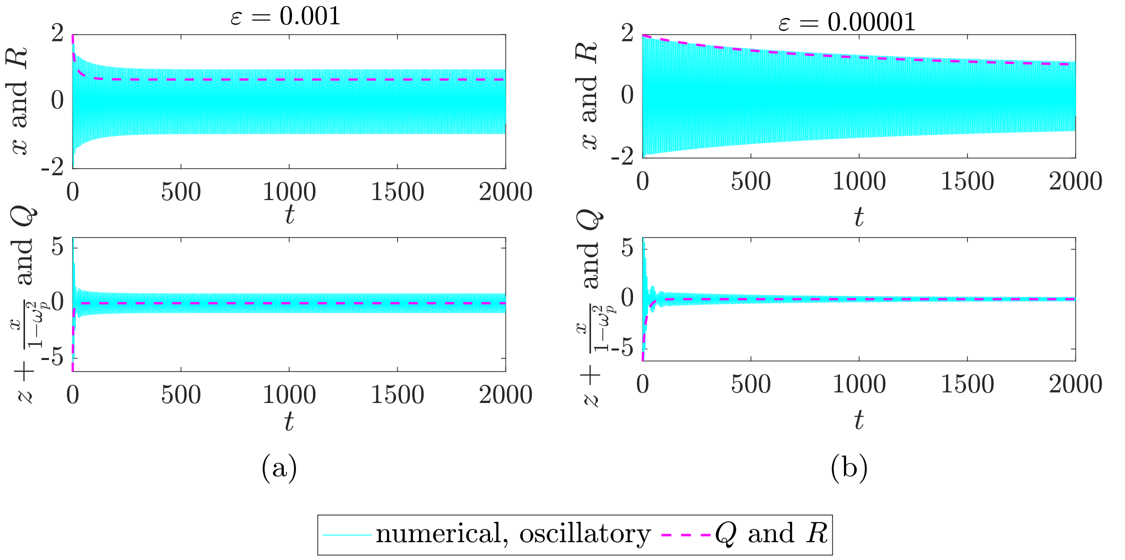

FIGURE 2.8: Comparison of responses by numerical integration of the original system equations (2.6) and (2.7) and slow flow equations (2.32) and (2.33) for $\omega_p > 1$. The system parameters are $m = 1, \omega_p = 1.15, c = -1$ and $c_v = 2$. The initial conditions are taken as $x(0) = 2, \dot{x}(0) = 0, z(0) = 0, \dot{z}(0) = 0, R(0) = 2, Q(0) = -6.2016$.

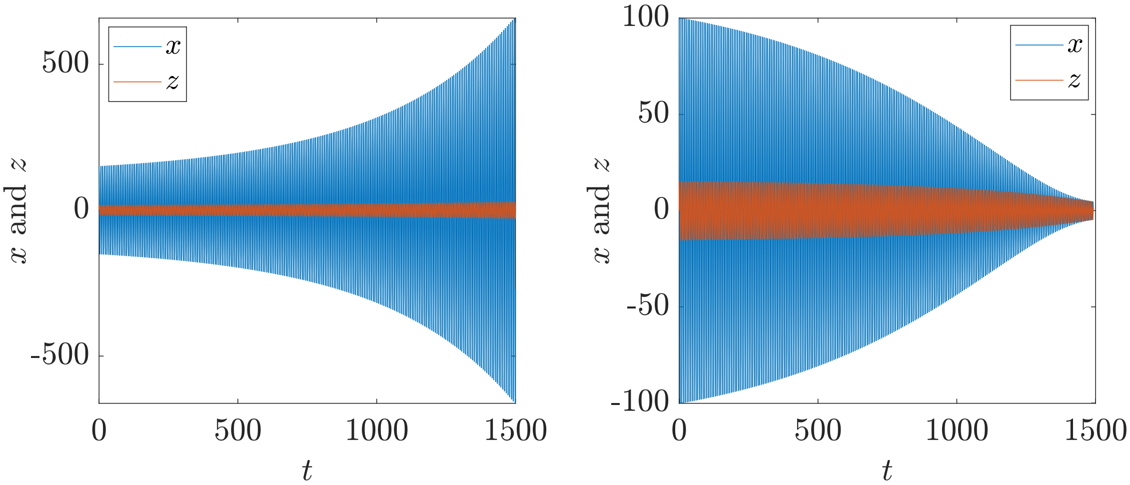

FIGURE 2.9: Responses for large initial conditions for x. Parameters are the same as in Fig. 2.7(a). Left: initial x-amplitude 150. Right: initial x-amplitude 100.

and using the parameters of Fig. 2.7(a), we present two large-x solutions in Fig. 2.9. Such failure of a nonlinear stabilizer at large amplitudes of the primary unstable oscillator is not surprising: see, e.g., [3]. For such large-amplitude regimes the solution approach adopted in this chapter, namely multiple scales based on treating x as $\mathcal{O}(1)$, is inappropriate. If such a regime is considered interesting, analysis using a different strategy may be undertaken in future work. For this study, we simply note that extremely large amplitudes render our approximations invalid.

2.7 Conclusions

In this chapter, we have studied the interaction between a weakly unstable and linear primary oscillator with an attached, small, secondary oscillator with its own nonresonant limit cycle. The practical motivation for studying such an untuned or nonresonant secondary oscillator is that precise tuning of physical parameters is no longer needed, and the stabilizer may remain effective even if system parameters drift to some extent.

The system studied is autonomous: there is no external forcing, and the goal is simply to render the primary mode of vibration stable. Since we have explicitly assumed there is no resonance, when we use the method of multiple scales and introduce amplitude and phase variables, a significant simplification occurs. The slow amplitude equations of the primary and secondary system decouple, and the phases of these two oscillators have no effect on the qualitative behavior of the system. The resulting two-dimensional phase portrait can be further simplified by a parameter-dependent change of variables which yields what we think is the simplest possible form for the slow flow, with one small perturbation parameter and only one $\mathcal{O}(1)$ system parameter, $c_1 > 0$. In particular, stabilization is possible for $c_1 < 4$. In the phase plane, the transformed coordinates lie in the first quadrant only. For $c_1 < 4$, a single separatrix divides the first quadrant into two regions. Solutions in one region display a quenching of the secondary oscillator's limit cycle along with a steady oscillation of the primary system. Solutions in the second region display a quenching of the unstable primary mode, along with a steady oscillation of the secondary system. As c_1 approaches 4, the second region shrinks in size and vanishes in the limit.

Future work may explore practical implementations of such a stabilizing device, as well as the possibility of stabilizing more than one unstable mode with a single additional oscillator. Note that if precise tuning of frequencies is needed, it is in general not possible to stabilize two modes of different frequencies using a single added stabilizing oscillator.

In this way, we hope that our present analytical study of nonresonant modal interactions may lead to both new research as well as applications.

One way to realise a limit cycle oscillator based vibration stabilizer for the primary system is to consider a physical system which undergoes a Hopf bifurcation and operate it in the linearly unstable regime. Depending on the operating conditions the Hopf bifurcation could be either subcritical or supercritical in nature. In order to consider the possibility of a limit cycle oscillator which undergoes a subcritical bifurcation operating in the linearly stable regime wherein there is an unstable limit cycle surrounding the stable equilibrium which is further surrounded by a large amplitude stable limit cycle, we next consider nonresonant interactions between a linear system and a light double limit cycle oscillator.

Chapter 3

Nonresonant interactions between a linear system and a light double limit cycle oscillator

In the previous chapter, we investigated the interaction between a linearly unstable system and a light limit cycle oscillator. A mass on a moving belt system is a potential choice to realize stable limit cycle oscillations. However, in addition to stable limit cycles, this system offers other regimes of operation, mainly, globally stable equilibrium and double limit cycles. This chapter considers a secondary oscillator with these regimes of operation and explores its nonresonant interactions with the linear unstable system.

This chapter proceeds as follows. We first motivate our study by recalling a mass on a moving belt system. We then introduce the coupled system, where the primary system is a single degree of freedom negatively damped spring-mass-damper oscillator and the secondary system is a light weakly nonlinear oscillator that can exhibit double limit cycle and globally stable equilibrium solutions, resembling the additional response regimes of a mass on a moving belt system. We write governing equations and implement the method of multiple scales following the previous chapter. The resulting slow flow equations are transformed into a simpler form and subsequently studied for fixed points and stability.

The simplified slow flows reveal that two nondimensional parameters govern the system dynamics. Bifurcation boundaries are identified in the parameter plane separating parameter domains of different qualitative behavior. We detail the bifurcation structure using amplitude phase portraits and identify parameter domains that provide basins of attraction corresponding to the stabilized primary oscillator. We supplement the details with an animation [108] demonstrating the evolution of the phase portraits with changing system parameters.

3.1 Introduction

In the previous chapter, we showed conditional stabilization of an unstable mode by a light limit cycle oscillator. A mass on a moving belt system is a potential choice for the physical realization of limit cycle oscillations. However, this oscillator involves other regimes of operation depending on the friction model. Two famous friction models are polynomial and exponential. Corresponding bifurcation diagrams (with belt velocity v_b as a parameter) are depicted in Fig. 3.1, see [109] for more details. For the polynomial friction model (left figure), bifurcation is supercritical and stable limit cycles exist in the linearly unstable regime whereas the equilibrium is globally stable in the linearly stable regime. Whereas, for the exponential friction model, subcritical bifurcation exists, where the unstable branch turns around and yields large amplitude stable limit cycles. Thus, we obtain three possible regimes of operation in this model as shown in Fig. 3.1, where regimes 1-2-3 correspond to regimes of stable limit cycle, double limit cycle and globally stable equilibrium, respectively. These cover the response regimes for the polynomial friction model. In the present study, we consider a secondary oscillator that can exhibit all three response regimes, where we model it using archetypical mathematical terms for convenience. The primary system remains identical to that in the previous chapter, i.e., linear and negatively damped.

The study by Hu and Habib [110] is closely related to the present work, where they investigated the suppression of friction-induced vibrations using a TMD. In [110], the primary system is the mass on a moving belt system and the attached small system (TMD) is linear and positively damped. Thus, that system is almost the reverse of the present system.

We next present the governing equations of motion for the present system.

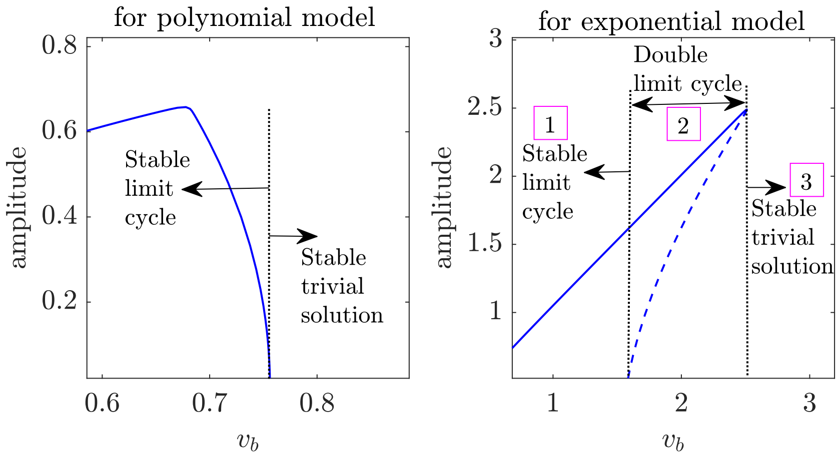

FIGURE 3.1: Single and double limit cycle responses by different friction models.

3.2 Governing equations

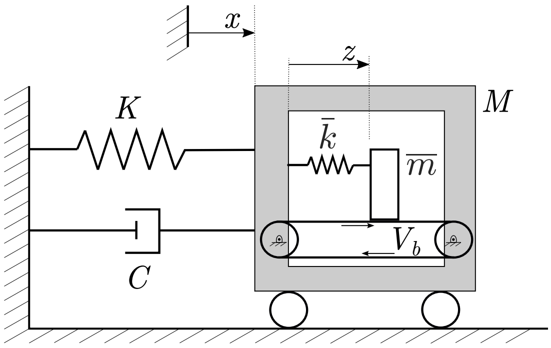

FIGURE 3.2: Schematic of the present system, where we use an archetypical mathematical model for three response regimes of the mass on a moving belt system.

The coupled system under investigation consists of a negatively damped linear spring-mass-damper oscillator as a primary system and a small mass on a moving belt system as a secondary system. Figure 3.2 shows the schematic of the system. The negative damping in the primary system represents the instability and our interest is in the stabilization of this system. As noted earlier, the mass on a moving belt system possesses three regimes of operation: single limit cycle response in regime-1, double limit cycle response in regime-2 and globally stable equilibrium in regime-3 (see Fig. 3.1). We use an archetypical model to depict these responses of the secondary oscillator. Studies incorporating an actual model for the mass on a moving belt system can be undertaken in the future. Now, the van der Pol oscillator depicts the regime-1 behavior and is utilized in Chapter-2. Here, we modify the van der Pol oscillator by adding a quartic nonlinear term to the quadratic term of the van der Pol damping to include the response regimes 2 and 3. Following [84] or equivalently the previous chapter for notations, the governing equations of motion (EOMs) for the coupled system take the form

$$M\ddot{x} + C\dot{x} + Kx - \bar{k}z + \bar{c}_v\dot{z}(\nu z^4 - \beta z^2 + 1) = 0,$$
$$\overline{m}(\ddot{x} + \ddot{z}) + \bar{k}z - \bar{c}_v\dot{z}(\nu z^4 - \beta z^2 + 1) = 0,$$

where we note the added quartic term in the van der Pol damping of the secondary oscillator. The coefficients of nonlinear terms, i.e., ν and β, qualitatively capture the effect of belt velocity, characterizing the regimes of operation. For $\nu = 0$ and $\bar{c}_v > 0$, the system reduces to that studied in [84] where the secondary oscillator exhibits regime-1 response. $\bar{c}_v < 0$ and $\nu > 0$ can yield responses corresponding to regimes 2 and 3. Note that, in regime 2 of double limit cycle response, an unstable limit cycle is surrounded by a large amplitude stable limit cycle, and the equilibrium is stable. We nondimensionalize the EOMs by setting $M = 1, K = 1$ and $\beta = 1$. Further, adopting the scaling used in the earlier work [84], we set

$$C = \mu^2 c, \quad \overline{m} = \mu\, m, \quad \bar{c}_v = \mu^2 c_v, \quad \bar{k} = \mu\, k,$$

where μ is a small bookkeeping parameter. Finally, the EOMs take the form

$$\ddot{x} + \mu^2 c\dot{x} + x - \mu m\omega_p^2 z + \mu^2 m\gamma\dot{z}(\nu z^4 - z^2 + 1) = 0, \tag{3.1}$$
$$\ddot{x} + \ddot{z} + \omega_p^2 z - \mu\gamma\dot{z}(\nu z^4 - z^2 + 1) = 0, \tag{3.2}$$

where we have defined $\omega_p^2 = \dfrac{k}{m}$ and $\gamma = \dfrac{c_v}{m}$ for convenience. Note that $\gamma < 0$ for response regimes 2 and 3. We explore Eqs. (3.1) and (3.2) using the method of multiple scales in the next section.

3.3 Multiple scales result and transformation

In this section, Eqs. (3.1) and (3.2) are treated using the method of multiple scales. We omit details of the method as it is identical to that reported in [84] (or the previous chapter), and only mention important equations of the methodology. Note that we do not assume any internal resonance.

We use timescales

$$T_0 = t, \quad T_1 = \mu t \quad \text{and} \quad T_2 = \mu^2 t,$$

and expand

$$x = X_0 + \mu X_1 + \mu^2 X_2,$$
$$z = Z_0 + \mu Z_1 + \mu^2 Z_2,$$

where (T_0, T_1, T_2) dependence of the variables is suppressed for convenience. Omitting details, the first order solutions are

$$X_0 = R\sin(T_0 + \phi), \tag{3.3}$$

$$Z_0 = Q\sin(\omega_p T_0 + \psi) - \frac{R\sin(T_0 + \phi)}{(1 - \omega_p^2)}, \tag{3.4}$$

where R, ϕ, Q and ψ are new slowly varying functions evolving at timescales (T_1, T_2). The final amplitude slow flow equations are found to be

$$\frac{\partial Q}{\partial T_1} = \frac{\gamma}{16(1-\omega_p^2)^4}\left[(1-\omega_p^2)^4\{\nu Q^4 - 2Q^2 + 8\} + 2(1-\omega_p^2)^2\{3\nu Q^2 - 2\}R^2 + 3\nu R^4\right]Q, \tag{3.5}$$

$$\frac{\partial R}{\partial T_2} = \left[-\frac{c}{2} + \frac{m\gamma}{16(1-\omega_p^2)^6}\Big((1-\omega_p^2)^4\{3\nu Q^4 - 4Q^2 + 8\} + 2(1-\omega_p^2)^2\{3\nu Q^2 - 1\}R^2 + \nu R^4\Big)\right]R, \tag{3.6}$$

where the evolution equations for ϕ and ψ have been dropped because the above amplitude evolution equations are independent of phases, and our interest is in the stabilization of the primary system. Figures 3.3 and 3.4 compare numerical solutions obtained by numerical integration of the original Eqs. (3.1) and (3.2) and the slow flow Eqs. (3.5) and (3.6). The match is excellent although we dropped the second order correction $\frac{\partial Q}{\partial T_2}$. For a small amplitude initial condition, Fig. 3.3 shows that the primary oscillator is stabilized and the secondary oscillator approaches a limit cycle. Whereas for a large amplitude initial condition, Fig. 3.4 shows that the primary oscillator approaches a limit cycle and the free response of the secondary oscillator is quenched.

Equations (3.5) and (3.6) are further simplified using a parameter-dependent transformation [84]. Writing

$$(1-\omega_p^2)^2 = w, \quad Q^2 = S \quad \text{and} \quad R^2 = wP,$$

we obtain

$$\frac{\mathrm{d}S}{\mathrm{d}T} = -\left[\{\nu S^2 - 2S + 8\} + 2\{3\nu S - 2\}P + 3\nu P^2\right]S + \mathcal{O}(\bar{\mu}), \tag{3.7}$$

$$\frac{\mathrm{d}P}{\mathrm{d}T} = -\bar{\mu}\left[\{3\nu S^2 - 4S + 8\} + 2\{3\nu S - 1\}P + \nu P^2 - 2c_1\right]P, \tag{3.8}$$

where

$$c_1 = \frac{4cw}{m\gamma}, \quad \bar{\mu} = \frac{\mu m}{w}, \quad T = -\frac{\mu\gamma}{8}t. \tag{3.9}$$

Note that a negative sign in T is retained because $\gamma < 0$ for operating regimes 2 and

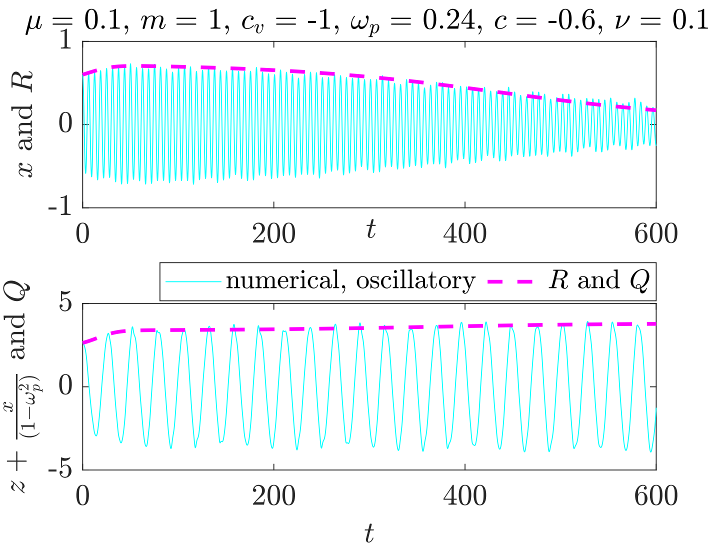

FIGURE 3.3: Comparison of numerical solutions obtained by numerical integration of the original Eqs. (3.1)-(3.2) and the slow flow Eqs. (3.5)-(3.6). The initial conditions are $x(0) = 0.6, \dot{x}(0) = 0, z(0) = 2, \dot{z}(0) = 0, R(0) = 0.6, Q(0) = 2.6367$. Here, the primary oscillator is stabilized, and the secondary oscillator approaches a limit cycle.

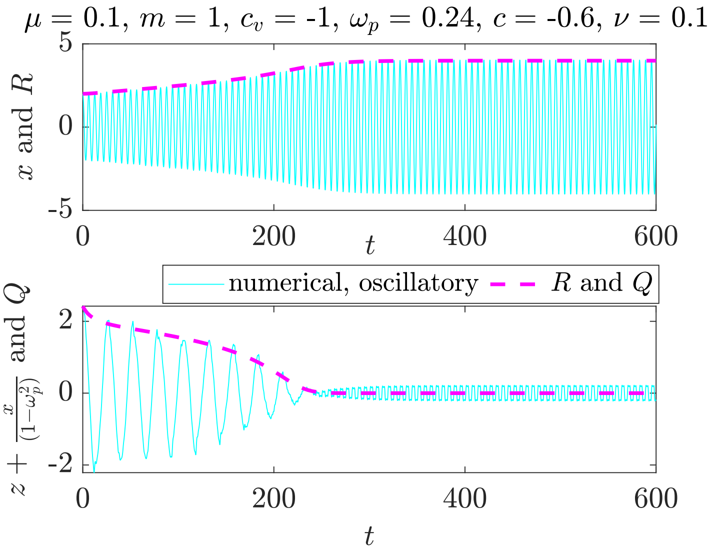

FIGURE 3.4: Comparison of numerical solutions obtained by numerical integration of the original Eqs. (3.1)-(3.2) and the slow flow Eqs. (3.5)-(3.6). The initial conditions are $x(0) = 2, \dot{x}(0) = 0, z(0) = 0.3, \dot{z}(0) = 0, R(0) = 2, Q(0) = 2.4222$. Here, the primary oscillator approaches a limit cycle, and the free response of the secondary oscillator is quenched.

3. Further, $c_1 > 0$ is of practical interest because $c < 0$ represents the instability in the primary system. For $\nu = 0$, Eqs. (3.7) and (3.8) yield the equations reported in the previous chapter [84] which correspond to regime-1 operation of the secondary oscillator. When the secondary oscillator works in regimes 2 and 3, the present slow flows reveal that two parameters c_1 and ν govern the qualitative dynamics of the system. Here, c_1 represents the ratio of damping in the primary and the secondary systems, and ν represents the ratio of the quartic and the quadratic terms in the nonlinear damping of the secondary system. We further investigate the slow flow Eqs. (3.7) and (3.8) in the next section.

3.4 Dynamics of the amplitude slow flows

In this section, we explore first order amplitude evolution equations (3.7) and (3.8) for fixed points and their stability. For easy reference, we categorize fixed points of the system as those on the P-S axes and those not on the axes. Further, we use the notation (S, P) to denote a point on the P-S plane. Recall that $P \geq 0$ and $S \geq 0$.

3.4.1 Fixed points on the P-S axes

Here, (0, 0) is a fixed point. By Eqs. (3.7) and (3.8), fixed points on the P-axis ($S = 0$) satisfy

$$\nu P^2 - 2P + 8 - 2c_1 = 0. \tag{3.10}$$

Solving the above, we obtain

$$P_{1,2} = \frac{1 \pm \sqrt{1 - \nu(8 - 2c_1)}}{\nu}, \tag{3.11}$$

representing the fixed points $(0, P_1)$ and $(0, P_2)$ for $\pm$, respectively. Fixed points on the S-axis ($P = 0$) satisfy

$$\nu S^2 - 2S + 8 = 0, \tag{3.12}$$

solving which, we obtain

$$S_{1,2} = \frac{1 \pm \sqrt{1-8\nu}}{\nu} \tag{3.13}$$

representing the fixed points $(S_1, 0)$ and $(S_2, 0)$ for $\pm$, respectively. Thus, we obtain five fixed points that lie on the axes: (i) (0,0), (ii) $(0, P_1)$, (iii) $(0, P_2)$, (iv) $(S_1, 0)$ and (v) $(S_2, 0)$. By Eq. (3.11), the curve in the c_1-ν plane which separates the domain of existence of $P_{1,2}$ is

$$1 - \nu(8 - 2c_1) = 0, \tag{3.14}$$

and by Eq. (3.13), the curve in the c_1-ν plane which separates the domain of existence of $S_{1,2}$ is

$$1 - 8\nu = 0. \tag{3.15}$$

These will be useful later.

3.4.2 Fixed points not on the axes

By Eqs. (3.7) and (3.8), fixed points with non-zero S and P satisfy

$$\{\nu S^2 - 2S + 8\} + 2\{3\nu S - 2\}P + 3\nu P^2 = 0,$$
$$\{3\nu S^2 - 4S + 8\} + 2\{3\nu S - 1\}P + \nu P^2 - 2c_1 = 0.$$

After some algebraic manipulation, we obtain

$$P = -\frac{(8\nu S^2 - 10S - 6c_1 + 16)}{2(6\nu S - 1)} \tag{3.16}$$

and

$$a_1 S^4 + a_2 S^3 + a_3 S^2 + a_4 S + a_5 = 0, \tag{3.17}$$

where

$$a_1 = 80\nu^3, \quad a_2 = -128\nu^2, \quad a_3 = -48c_1\nu^2 - 256\nu^2 + 88\nu,$$
$$a_4 = 128\nu - 24, \quad a_5 = -36c_1^2\nu + 192c_1\nu - 256\nu - 16c_1 + 32,$$

where again, we assume $(6\nu S - 1) \neq 0$ and require $P \geq 0$. The above equations result in four fixed points that can be evaluated numerically for given ν and c_1.

TABLE 3.1: Jacobian and its eigenvalues at fixed points with $S = 0$ or $P = 0$.

Fixed point	Jacobian	Eigenvalues
(0,0)	$-\begin{bmatrix} 8 & 0 \\ 0 & \bar{\mu}(8-2c_1) \end{bmatrix}$	-8, $-\bar{\mu}(8-2c_1)$
$(0, P_{1,2})$	$-\begin{bmatrix} 2P+6c_1-16 & 0 \\ 2\bar{\mu}P(3\nu P-2) & 2\bar{\mu}P(\nu P-1) \end{bmatrix}_{(0,P_{1,2})}$	$-(2P_{1,2}+6c_1-16)$, $\mp 2\bar{\mu}P_{1,2}(\sqrt{1-\nu(8-2c_1)})$
$(S_{1,2}, 0)$	$-\begin{bmatrix} 2S(\nu S-1) & 2S(3\nu S-2) \\ 0 & \bar{\mu}(2S-2c_1-16) \end{bmatrix}_{(S_{1,2},0)}$	$\mp 2S_{1,2}(\sqrt{1-8\nu})$, $-\bar{\mu}(2S_{1,2}-2c_1-16)$

3.4.3 Stability of fixed points

Stability of fixed points with zero S or P (of Section 3.4.1) is depicted in Table 3.1 by their Jacobians and corresponding eigenvalues. Note that the negative sign of the $\mp$ sign in the eigenvalues corresponds to P_1 or S_1. Similarly, the positive sign of the $\mp$ sign in the eigenvalues corresponds to P_2 or S_2. Useful information observed from the table are as follows.

1. The origin changes stability at
$$c_1 = 4. \tag{3.18}$$
Further, by Eq. (3.11), P_2 (that is smaller than P_1) coalesces with the origin at $c_1 = 4$, resulting in a bifurcation.

2. $P_{1,2}$ changes stability at $2P_{1,2} + 6c_1 - 16 = 0$. Substituting for $P_{1,2}$ by Eq. (3.11), we obtain

$$-36c_1^2\nu + 192c_1\nu - 256\nu - 16c_1 + 32 = 0. \tag{3.19}$$

By Eq. (3.17), the above equation is identical to $a_5 = 0$. Hence, on this curve, a fixed point with non-zero S and P merges with one of the P-axis roots $(0, P_{1,2})$, resulting in a change of stability of those roots.

3. $S_{1,2}$ changes stability at $2S_{1,2} - 2c_1 - 16 = 0$. Substituting for $S_{1,2}$ by Eq. (3.13), we obtain

$$(-c_1\nu - 8\nu + 1)^2 + 8\nu - 1 = 0. \tag{3.20}$$

Equation (3.16) with $P = 0$ and $S = S_{1,2}$ (by Eq. (3.13)) yields the same equation. Further, Eq. (3.17) is satisfied by the corresponding expressions. Therefore, on this curve, a fixed point with non-zero S and P meets one of the S-axis roots $(S_{1,2}, 0)$, resulting in the change of stability of those roots.

4. The other eigenvalues with $\mp$ sign vanish for $P_2 = 0$ or $S_2 = 0$. By Eqs. (3.10) and (3.12), P_2 meets the origin when $c_1 = 4$ whereas S_2 does not meet the origin. The stability of the origin has already revealed this. The other multiplied terms under square roots refer to Eqs. (3.14) and (3.15), i.e., curves separating domains of the existence of $P_{1,2}$ and $S_{1,2}$ in the c_1-ν plane.

Stability of a fixed point with non-zero S and P can be determined by a Jacobian

$$-\begin{bmatrix} 2S(\nu S - 1 + 3\nu P) & 2S(3\nu S - 2 + 3\nu P) \\ 2\bar{\mu}P(3\nu S - 2 + 3\nu P) & 2\bar{\mu}P(3\nu S - 1 + \nu P) \end{bmatrix}, \tag{3.21}$$

evaluated at that fixed point. As we evaluate these fixed points numerically, the corresponding eigenvalues of the Jacobian are also determined numerically, revealing the stability of these fixed points. Here, the corresponding eigen-directions are useful to plot separatrices in phase portraits presented later.

The change in stability of non-zero roots can occur by two means. Either these roots meet other roots on the axes or these roots meet the other among them, i.e., repeated non-zero roots. The former has been already explored. For the latter, we seek numerical estimation of the corresponding bifurcation boundary in the c_1-ν plane. For a given ν, we formulate the problem in 5 unknowns: σ, σ_1, σ_2, p and c_1, where (σ, p) denotes the repeated (S, P) root, and σ_1 and σ_2 denote S-coordinates of the remaining roots. By Eq. (3.17), we write

$$a_1 S^4 + a_2 S^3 + a_3 S^2 + a_4 S + a_5 = (S - \sigma)^2 (S - \sigma_1)(S - \sigma_2), \tag{3.22}$$

and by Eq. (3.16),

$$2(6\nu\sigma - 1)p = -(8\nu\sigma^2 - 10\sigma - 6c_1 + 16). \tag{3.23}$$

Equation (3.23) helps to avoid roots with equal S and unequal P. Equation (3.22) yields 4 equations. Including Eq. (3.23), we solve 5 equations numerically and accept a positive solution of $\sigma, \sigma_1, \sigma_2$ and p. We then extend the solution using the arc-length continuation technique and obtain the required bifurcation boundary in the c_1-ν plane. Crossing this boundary results in the emergence or annihilation of two fixed points that are not on the axes, denoting a saddle-node bifurcation. This will be shown using phase portraits in the next section.

With that, we have obtained all fixed points of the system and corresponding bifurcation boundaries in the c_1-ν plane. Figure 3.5 shows the parameter plane where we have labelled the bifurcation boundaries as A_1 to A_6; see Table 3.2 for the corresponding details. We have also marked the number of fixed points that exist for different domains of the parameter plane. This will guide our explanation of the system dynamics in the next section.

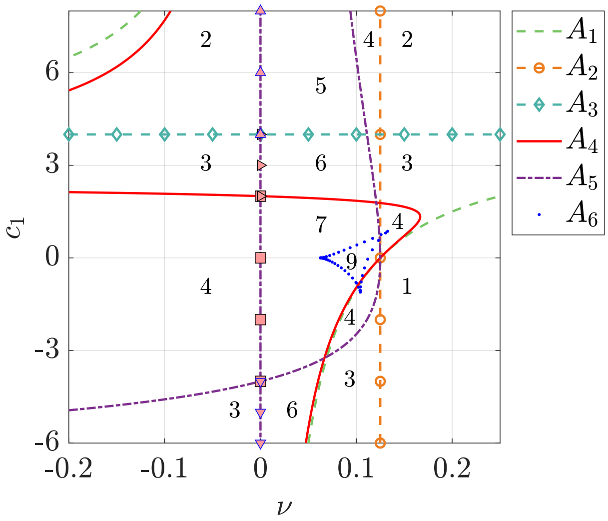

FIGURE 3.5: Bifurcation boundaries and the number of fixed points in the c_1-ν plane. See Table 3.2 for the expressions of various curves in the figure. Markers on the $\nu = 0$ axis represent corresponding dynamics. The number of fixed points on the $\nu = 0$ axis is the same as those in the nearby $\nu < 0$ regime.

TABLE 3.2: Summary of bifurcation boundaries.

Curve label in Fig. 3.5	Expression	Represents
A_1	$1 - \nu(8 - 2c_1) = 0$	existence of $P_{1,2}$
A_2	$1 - 8\nu = 0$	existence of $S_{1,2}$
A_3	$c_1 = 4$	coalescence of P_2 with the origin
A_4	$-36c_1^2\nu + 192c_1\nu - 256\nu - 16c_1 + 32 = 0$	coalescence of a non-zero fixed point with P-axis
A_5	$(-c_1\nu - 8\nu + 1)^2 + 8\nu - 1 = 0$	coalescence of a non-zero fixed point with S-axis
A_6	obtained numerically	coalescence of non-zero fixed points

3.5 Complete dynamics for regimes 1, 2 and 3

We recall that when the secondary oscillator operates in regime-1 (with $\nu = 0$), it exhibits stable limit cycle oscillations and the corresponding coupled system's nonresonant dynamics have already been explored in our earlier work [84]. The other operating regimes of the secondary oscillator are governed by the parameter ν. For $0 < \nu < 0.125$, the secondary oscillator operates in regime 2 and possesses a double limit cycle response. For $\nu > 0.125$, the secondary oscillator operates in regime 3 and possesses a globally stable equilibrium solution. c_1 is the other parameter governing the coupled system dynamics. In this section, we present phase portraits corresponding to various domains of the c_1-ν plane (shown in Fig. 3.5), representing unified system dynamics. Figure 3.6(a) shows the phase portrait with all 9 fixed points. Here, solid circles denote stable nodes, hollow circles denote unstable nodes and plus signs denote saddles. Red-dotted lines in the figure show separatrices found numerically by perturbing the flow around fixed points in the eigendirections, where we have altered the flow direction to find a stable direction of a saddle as in [84]. The parameter combination for the phase portrait in Fig. 3.6(a) can be traced to the domain with 9 fixed points in the c_1-ν plane of Fig. 3.5 (the region inside A_6). This phase portrait represents the unified dynamics for that parameter domain. We next discuss various phase portraits in detail depending on the range of ν. We recall that $c_1 > 0$ is of practical interest for stabilization. Figures 3.6, 3.7 and 3.8 show phase portraits corresponding to different regimes of c_1-ν plane for $c_1 > 0$. Using these phase portraits, we spot regimes of parameter combination that provide basins of attraction for the stabilization of the primary oscillator.

3.5.1 When the secondary oscillator operates in regime-2

Here, $0 < \nu < 0.125$ and the uncoupled secondary oscillator exhibits double limit cycles. Figure 3.6 shows phase portraits for the $c_1 > 0$ domains between $\nu = 0$ and A_5 in Fig. 3.5. These phase portraits exhibit 9, 7, 6 and 5 fixed points. In Figs. 3.6(a), (b) and (c), there exists a basin of attraction for the stable origin. Thus, stabilization is possible by using the corresponding parameter domains of Fig. 3.5. Note that a stable fixed point on the S-axis also leads to the stabilized primary oscillator, where the secondary oscillator exhibits limit cycle oscillations. Thus, the corresponding basin of attraction is also important. Figures 3.6(a), (b) and (c) possess that basin of attraction as well. Here, the parameter domains corresponding to these phase portraits operate when $c_1 < 4$. For $c_1 > 4$, Fig. 3.6(d)

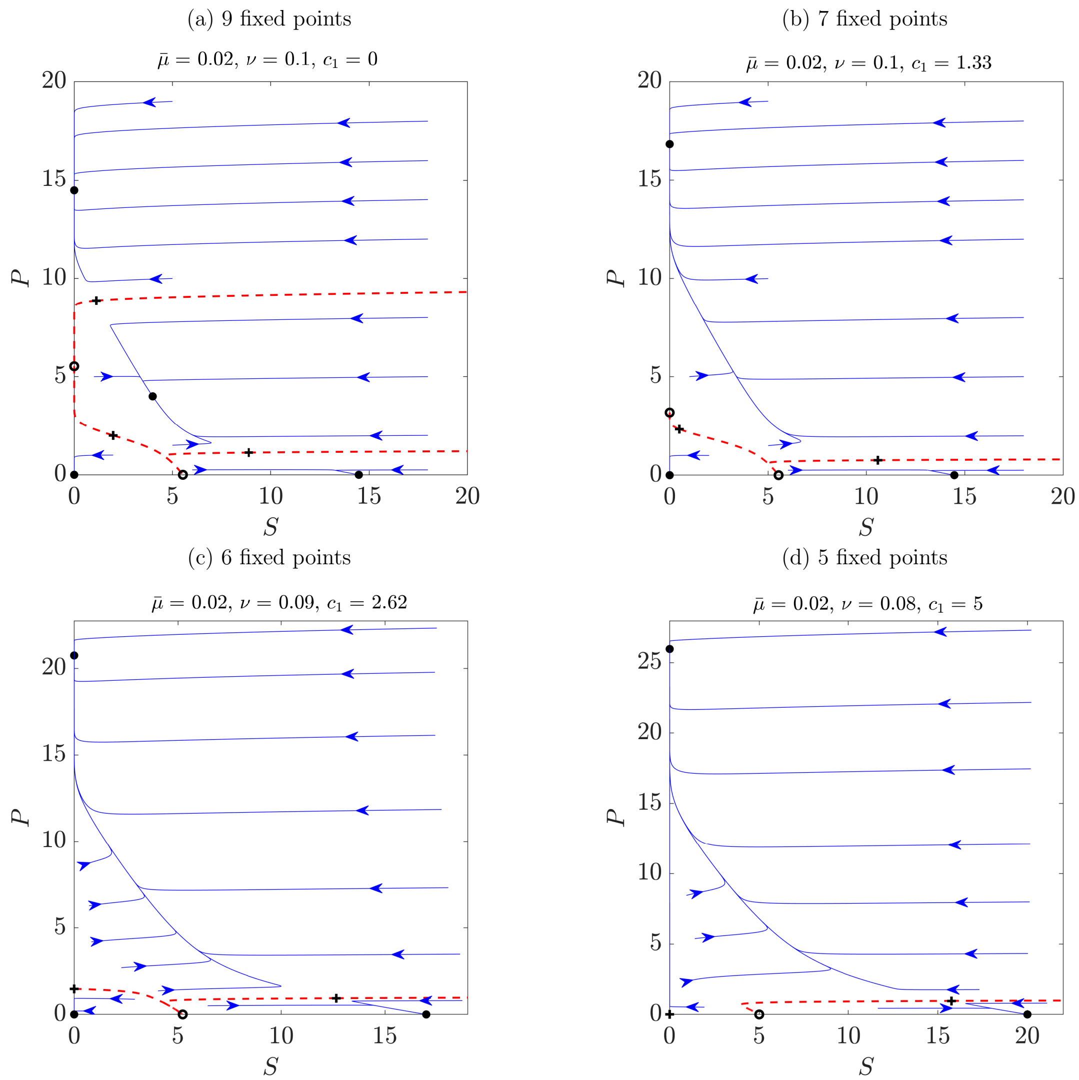

FIGURE 3.6: Phase portraits with 9, 7, 6 and 5 fixed points for $c_1 > 0$ regime of Fig. 3.5 (between $\nu = 0$ and A_5).

shows the phase portrait with 5 fixed points, where the basin of attraction that yields the stabilized primary oscillator with limit cycle oscillations of the secondary oscillator is available. We note that, in [84], stabilization was not possible for $c_1 > 4$. Here, no such threshold is found, and the phase portrait with 5 fixed points continues to provide the basin of attraction for larger negative damping. However, this basin of attraction shrinks in size as c_1 decreases.

The bifurcation among these phase portraits can also be elaborated. To begin with, consider the phase portrait with 9 fixed points, i.e., Fig. 3.6(a), which corresponds to the

c_1-ν region covered by the dotted curve A_6 in Fig. 3.5. As c_1 increases, we cross A_6 and two fixed points with non-zero S-P are merged and annihilated leaving 7 fixed points and resulting in the phase portrait depicted in Fig. 3.6(b). With further increase in c_1, we cross A_4 (Fig. 3.5) where the fixed point with non-zero S-P meets the P-axis root $(0, P_2)$. Entering the regime with 6 fixed points, the stability of $(0, P_2)$ changes and we obtain the phase portrait depicted in Fig. 3.6(c). Finally, crossing A_3 ($c_1 = 4$) in Fig. 3.5, the fixed point $(0, P_2)$ vanishes after merging with the origin. The origin changes its stability and we obtain Fig. 3.6(d) having 5 fixed points.

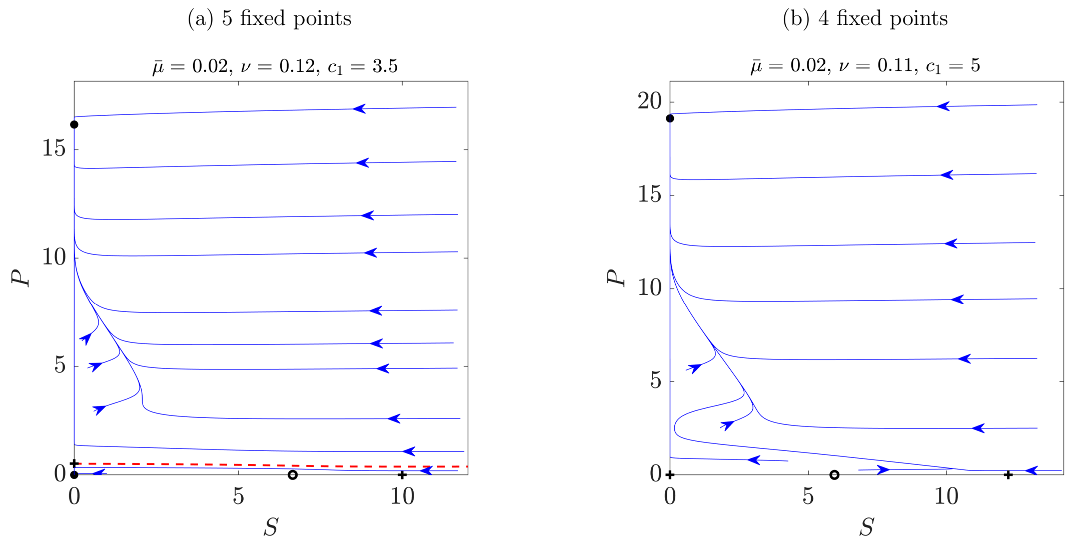

FIGURE 3.7: Phase portraits with 5 and 4 fixed points for $c_1 > 0$ regime between curves A_2 and A_5 in Fig. 3.5.

For $0 < \nu < 0.125$ and $c_1 > 0$, domains between curves A_2 and A_5 in Fig. 3.5 exhibit 4 and 5 fixed points (labelled and not labelled in the figure, respectively). Figure 3.7 shows corresponding phase portraits. For $c_1 < 4$, the phase portrait with 5 fixed points exhibits a small basin of attraction for complete stabilization. For $c_1 > 4$, the phase portrait with 4 fixed points does not possess any useful basin of attraction. Thus, the corresponding parameter regime shall be avoided. Here, the bifurcation is clear: $(0, P_2)$ merges with the origin changing its stability as c_1 increases.

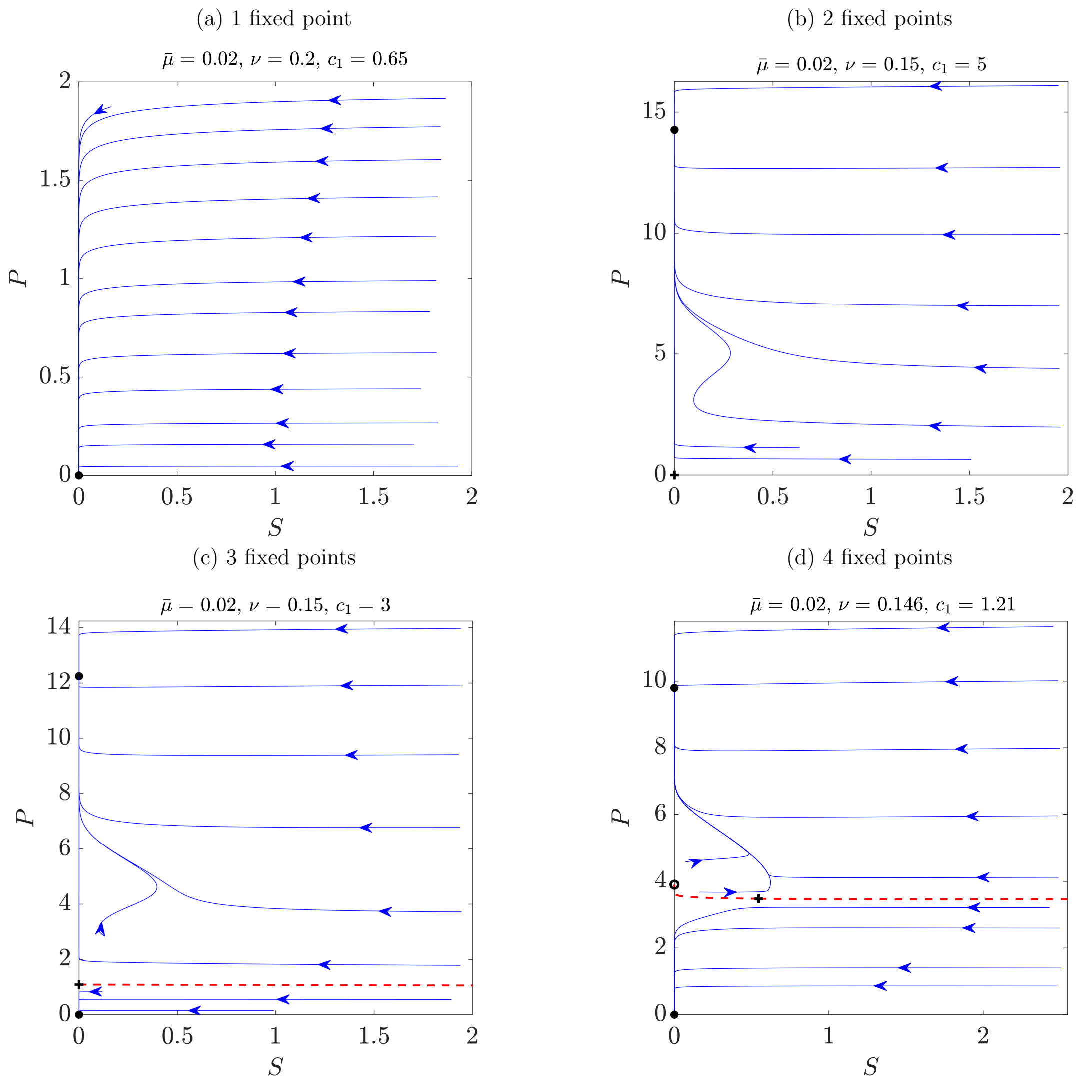

FIGURE 3.8: Phase portraits with 1, 2, 3 and 4 fixed points for $c_1 > 0$ regime of Fig. 3.5, where $\nu > 0.125$.

3.5.2 When the secondary oscillator operates in regime-3

For $\nu > 0.125$, the secondary oscillator possesses the globally stable trivial solution. Thus, the fixed points on the S-axis vanish. Corresponding phase portraits depicted in Fig. 3.8 possess 1, 2, 3 or 4 fixed points for the correspondingly labelled c_1-ν domains of Fig. 3.5. Phase portraits with 1, 3 and 4 fixed points possess the stable origin; see Figs. 3.8(a), (c) and (d). Hence, those phase portraits provide a useful basin of attraction corresponding to the stabilization of the system. Figure 3.8(a) possesses the origin as the only stable fixed point. Thus, we here achieve unconditional stabilization, where all initial conditions lead to complete quenching. This corresponds to $c_1 < 4$ and large ν. Note that, in Fig. 3.5, curve A_1 asymptotically meets curve A_3 ($c_1 = 4$). Finally, the phase portrait with two fixed points depicted in Fig. 3.8(b) possesses the only stable node on the P-axis. Thus, no stabilization is possible for $c_1 > 4$ and $\nu > 0.125$. Thus, in contrast to general expectation, larger ν does not necessarily help in achieving stabilization. From the foregoing analyses, it is a double limit cycle response (regime-2) that provides a useful basin of attraction for $c_1 > 4$ or larger instability.

To explain the bifurcation scenario for Fig. 3.8, we begin with the phase portrait with 2 fixed points, i.e., Fig. 3.8(b). With a decrease in c_1, we cross $c_1 = 4$ and obtain Fig. 3.8(c) with 3 fixed points; the origin's stability has changed and the fixed point $(0, P_2)$ has emerged. Depending on the value of ν, if we cross A_4 in Fig. 3.5, a fixed point with non-zero P-S emerges and $(0, P_2)$ changes its stability (Fig. 3.8(d)). Crossing A_1 with a further decrease in c_1 results in the coalescence and disappearance of the fixed points on the P-axis leading to the simplest phase portrait with the origin as the only stable fixed point (Fig. 3.8(a)).

3.5.3 Other regimes

That leaves the parameter domain with $\nu < 0$. Figure 3.9 shows corresponding phase portraits for completeness. Here, a small basin of attraction for the stable origin exists except when c_1 is large. The existence of unbounded solutions makes this parameter domain practically less interesting. The phase portraits for $\nu < 0$ also explain the dynamics on the $\nu = 0$ axis. Note that phase portraits for $\nu < 0$ and $c_1 < 0$ match those presented in [84] with flow directions reversed.

Finally, we present an animation [108] depicting phase portraits alongside the c_1-ν parameter plane. That helps to visualise the bifurcation among various boundaries presented in Fig. 3.5. For completeness, another animation [108] is presented depicting the dynamics for $c_1 < 0$ and $\nu > 0$. This concludes our investigation.

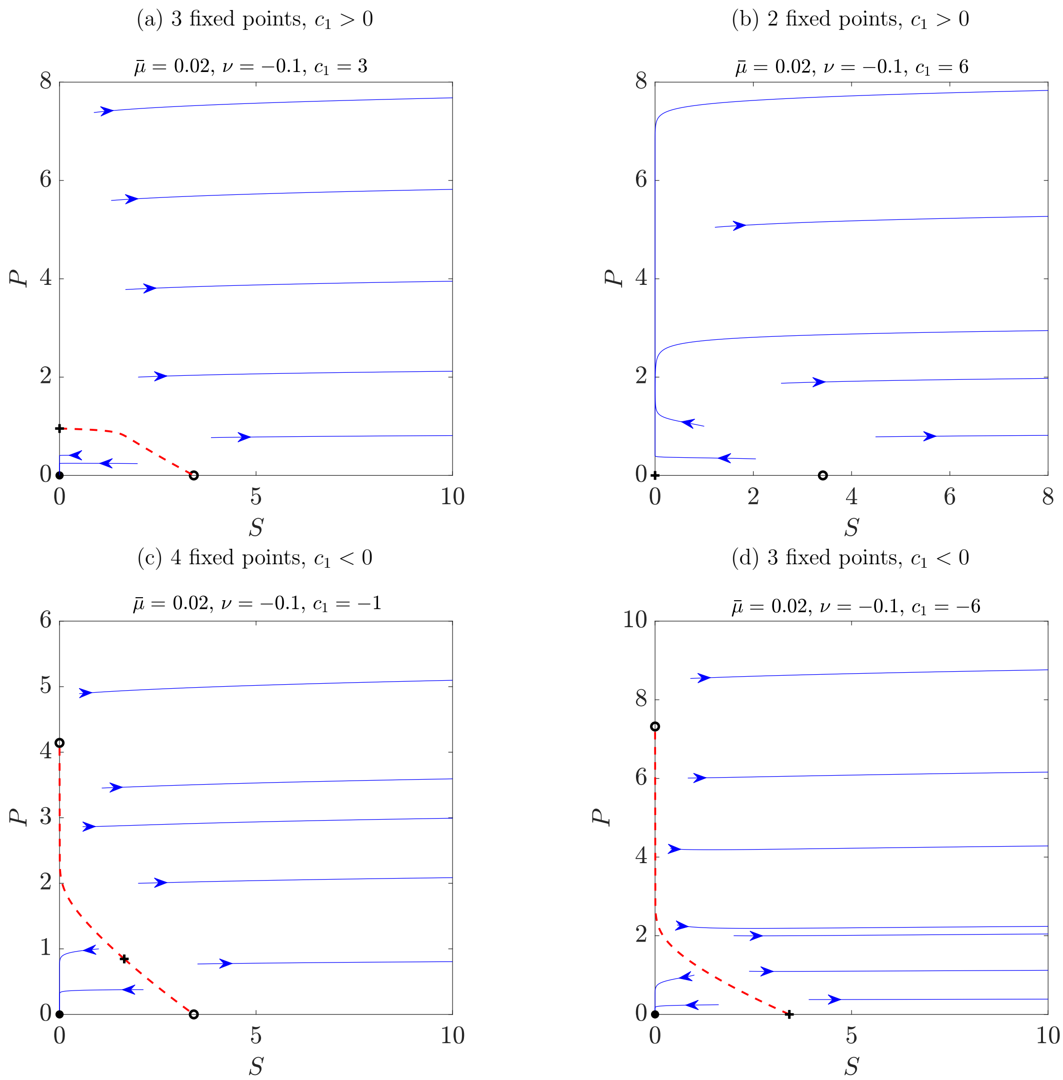

FIGURE 3.9: Phase portraits for $\nu < 0$ regime that also represent the dynamics on the $\nu = 0$ axis.

3.6 Conclusions

In this chapter, we have investigated nonresonant interactions between a primary linear system and a secondary, light, weakly nonlinear, double limit cycle oscillator. For the negatively damped linear system, the double limit cycle oscillator can work as an untuned passive stabilizer. A single limit cycle oscillator has been shown to provide conditional stabilization in our previous chapter. Our search for the physical realization of the limit cycle oscillator drove us to a mass on a moving belt system. In addition to a stable limit cycle response, this system offers other regimes of operation: a double limit cycle response and a globally stable equilibrium. In the present study, a modified van der Pol oscillator resembling these responses characterizes the secondary oscillator, where a quartic nonlinear term is added to the quadratic term of the van der Pol damping.

Using the method of multiple scales, we find amplitude slow flows that are independent of phases. After the transformation to a simple form, the slow flows reveal that two nondimensional parameters govern the system dynamics, i.e., ν and c_1. ν denotes the ratio of the coefficients of quartic and quadratic nonlinearities, and c_1 denotes a frequency ratio-dependent ratio of damping in the primary and secondary oscillators. Further investigating the slow flow, we find bifurcation boundaries in the c_1-ν plane and elaborate the system dynamics using amplitude phase portraits. We find that conditional stabilization is theoretically possible for $c_1 > 4$ or larger negative damping compared to that provided by a single limit cycle oscillator. Even though the corresponding basin of attraction shrinks in size for larger negative damping in the primary system. Further, we observe that larger ν or globally stable response ($\nu > 0.125$) of the secondary system does not help in this regime of $c_1 > 4$. It is the double limit cycle response ($0 < \nu < 0.125$) that is useful. We note that $\nu > 0.125$ offers the regime of unconditional stabilization for $c_1 < 4$.

Having studied the efficacy of the limit cycle oscillator based secondary oscillator working in either of its operating regimes as a possible stabilizer of an unstable primary system, we next move to a more practical application where the primary system is nonlinear and possesses a subcritical Hopf bifurcation. Since our secondary system is nonlinear, it has the potential to interact with the nonlinearity of the primary system and alter the nature of bifurcation of the primary system. It is this aspect of the limit cycle oscillator based vibration absorber which is studied in our next chapter wherein the delayed nonlinear model of tool vibrations is taken as a primary system which is coupled with a light nonresonant limit cycle oscillator working in regime-1.

Chapter 4

Ensuring supercritical Hopf bifurcation in tool chatter using a limit cycle absorber

In this chapter, we study nonresonant interactions between a single mode of a machine tool and a light limit cycle oscillator. The uncoupled machine tool system exhibits regenerative tool chatter instability of subcritical or catastrophic nature. We establish in this study that the nonresonant light limit cycle oscillator can change the nature of instability to supercritical or non-catastrophic. The chapter proceeds as follows. We begin with the introduction and relevant literature review in Section 4.1 where we notice novelty of the present study. We then introduce the coupled system and write its governing equations in Section 4.2. We perform linear stability analysis and develop the corresponding asymptotic approximations in Section 4.3. We then numerically demonstrate in Section 4.4 that the system with a TMD exhibits subcritical bifurcation whereas the present system with a limit cycle oscillator exhibits supercritical bifurcation. We proceed to implement the method of multiple scales in Section 4.5 to investigate the bifurcation structure around Hopf points with expressions developed in Section 4.3. We simplify and thoroughly investigate the resulting slow flows in Section 4.6, and elaborate the dynamics over the complete second stability lobe in Section 4.7. Section 4.8 finally concludes the chapter.

4.1 Introduction

Machine tool vibrations adversely affect the surface finish and tool life. One of the main cause of such vibrations is the regenerative effect wherein the vibratory state of the system from one revolution earlier affects the current chip thickness and the cutting forces on the system. This model of the machine tool system loses stability above a limiting depth of cut via a Hopf bifurcation. The nature of this bifurcation is largely known to be subcritical or catastrophic [50]. This limits the operational depth of cut for a given rotational speed of the workpiece without encountering tool chatter. Thus, stabilization strategies are needed to increase the workable depth of cut and convert the nature of bifurcation to supercritical so as to obtain better productivity. In this chapter, we demonstrate that a secondary limit cycle absorber can ensure a supercritical bifurcation for the tool chatter model.

Primarily, stabilization strategies are active or passive. In an active arrangement, control law-based direct actuation is used, while in a passive arrangement, the primary structure is modified with a view to enhance its dissipation characteristics. One of the most popular ways of achieving this is through a tuned mass damper or a tuned vibration absorber wherein a secondary system is attached to the primary system with the vibration characteristics of the two systems tuned to each other. The attached system in the case of a primary machine tool system can be light and, under proper parameter selection, can increase the stability limit and suppress the subcritical instability. Both active and passive strategies have advantages and limitations: the former is effective but costly, while the latter is cheaper but requires precise tuning for efficient operation. For a passive absorber, tuning can be lost by changes in system parameters. For example, gripping a long boring bar at different lengths results in different fundamental frequencies. Here, tuned absorbers require proper parameter adjustment based on the altered natural frequency. If that is not done, and the nature of bifurcation remains subcritical, tool vibrations may grow, resulting in a system failure. Thus, untuned stabilizers are needed that can alter the bifurcation scenario to non-catastrophic (supercritical) ones and provide efficient operation without precise tuning. In the present work, we implement a light, nonresonant, limit cycle oscillator as a passive stabilizer. The limit cycle oscillator is linearly unstable and possesses an energy source. The energy input required is small because the oscillator is light. Further, being nonresonant, it does not require precise tuning. Moreover, the implementation will be easy if it does not require the machine tool system's state feedback to attain a limit cycle. From a dynamics perspective, the secondary oscillator's stable limit cycle can interact with the unstable limit cycle of the uncoupled primary system to yield an unconditionally stable response. Further advantageous would be the nature of bifurcation turned to non-catastrophic or supercritical. We uncover relevant dynamics in the present study.

Chatter suppression by different passive absorbers has been investigated earlier. A linear tuned mass damper (TMD) is well-known among them. Tarng *et al.* [51] applied a traditional tuning strategy where they tuned the natural frequency of the absorber to that of the machine tool system and showed improvement in the stability limit. Sims [52] noted that the limiting depth of cut is inversely proportional to the real part of the system's frequency response function (FRF). They found useful tuning expressions following Den Hartog's equal peak method. Later, Miguélez *et al.* [53] improved those expressions following a local analysis. Notably, a factor linearly dependent on a mass ratio was introduced. Rubio *et al.* [54] proposed further improvement in the results of [52] and [53], where they incorporated the primary system's damping and maximized the minimum value of the real part of the frequency response function. In a related work, Patel *et al.* [55] incorporated rotational effects while designing the tuned mass absorber for a slender boring bar and tuning was achieved by maximizing the limiting depth of cut directly. As is evident from the above, these studies were focused on finding tuning rules. Moradi *et al.* [56] studied a tuned mass absorber attached to a cantilever boring bar where they minimized free-end deflection of the beam. They reported that the optimum parameters depended on chatter frequency and cutting force position. In general, a TMD requires precise tuning to work effectively. Therefore, if the tuning is lost, undesirable oscillations may arise because of a drop in the stability limit. Patel *et al.* [57] studied a hybrid damper utilizing an eddy current damper in conjunction with a TMD. They found that the hybrid damper helps to retain the effectiveness of a TMD when detuned. Then there are inerter-based dynamic vibration absorbers (IDVAs) used by Dogan *et al.* [58, 59], where an actuator mimics an inerter by providing a force proportional to the relative acceleration of the absorber mass. Dogan *et al.* [58] studied different configurations of IDVAs theoretically and reported relevant experimentation in [59]. In [58], they found that tuned IDVA can provide a larger stability margin than a dynamic vibration absorber tuned using Sims's formulae. However, in the end, a linear absorber does not alter the nature of the bifurcation.

Nonlinear oscillators have also been explored as alternative absorbers to control the nature of bifurcation. Gourc *et al.* [60] studied the dynamics of a cutting tool coupled with a nonlinear energy sink (NES) that possesses essential cubic stiffness nonlinearity. They showed that the system mainly exhibits three types of responses: complete suppression, stable limit cycle oscillation and relaxation oscillation. Nankali *et al.* [61] also studied regenerative chatter suppression using an NES. They demonstrated improvement in the stability boundary with an increased mass ratio. Further, they identified regimes in a parameter plane for the three types of responses mentioned above, with the fourth being no suppression. Later, Habib *et al.* [62] considered a linear stiffness along with the cubic stiffness component, obtaining a nonlinear tuned vibration absorber (NLTVA). Using the method of multiple scales, they showed that hardening or softening nonlinearity can change the nature of bifurcation to supercritical for some range of rotational speeds. In these studies, the attached oscillators are positively damped or linearly stable. In contrast, the attached oscillator in the present study (the limit cycle oscillator) is linearly unstable. Hence, the present system is significantly different from the nonlinear absorbers studied earlier.

There have been studies involving non-smooth nonlinear vibration absorbers for controlling machine tool chatter. Edhi and Hoshi [63] studied a friction damper in which a small mass is attached to a boring bar using a magnet. Energy dissipation primarily occurs due to the friction opposing relative motion at the interface. The simple technique does not require tuning and has been found to be effective in the suppression of high-frequency chatter. Wang *et al.* [64] added an element to a linear TMD that consists of a linear spring and a dry friction element in series, and tuned the spring stiffness and the normal reaction to obtain efficient performance of this nonlinear TMD. Wang [65] further examined this system using the method of harmonic balance. They reported the variation in optimum parameters with mass ratio. This shows that if tuning is lost, multiple components of an absorber require adjustment. Gourc *et al.* [66] investigated vibro-impact NES (VI-NES) for chatter suppression. They reported the capability of VI-NES to limit large amplitude machine tool oscillations in an unstable regime. Further, Iklodi *et al.* [67] investigated vibro-impact TMD in light of space constraints during the implementation of a TMD in a boring bar. They demonstrated that the system can undergo large amplitude oscillation under an impulsive perturbation even for a parameter combination corresponding to a stable regime. We note that friction and impact dampers differ significantly from a limit cycle oscillator because of the non-smoothness which introduces multiple co-existing solutions and hence, lowers the reliability of the desired performance.

Some researchers have considered absorbers which are augmented by actuators or active components. These are popularly called active dynamic absorbers. Tewani *et al.* [68] considered a lumped parameter model of a boring bar and attached an active dynamic absorber with piezoelectric pushers for actuation. Depending on the control law used for the actuation, they found significant improvement in the stability limit compared to passive absorbers. Sahu *et al.* [69] compared different actuation strategies for an active damper and found that direct velocity feedback strategy is the most effective. To change the nature of bifurcation, researchers have applied nonlinear feedback in active methods, e.g., Nayfeh and Nayfeh [111] considered cubic velocity feedback. Similar nonlinear elements in active dynamic absorbers could be an attractive solution and have been tried by several researchers [112, 113]. However, they were focused on suppressing forced vibrations of either a parametrically-excited system [112] or self-excited system [113]. Recently, Tandel *et al.* [84] explored use of a secondary limit cycle oscillator to conditionally control self-excited oscillations in a linear negatively damped structure. One realization of the secondary limit cycle oscillator is through an active actuator while it can also be realized using a passive absorber with an energy input without any sensor based feedback. In this work, we use the limit cycle oscillator based vibration absorber of [84] to suppress the subcritical delay-induced Hopf instability of the tool chatter model.

To summarize, no study in the authors' knowledge has considered an untuned limit cycle oscillator to mitigate machine tool vibrations as has been considered in the current work. The goal of this study is to ensure a supercritical bifurcation for the tool chatter model along with obtaining an improvement in the linear stability boundary to the best extent possible. The forthcoming analysis will uncover these aspects. To begin with, we write the governing equations of motion for the system considered in this work in the next section.

4.2 Governing equations

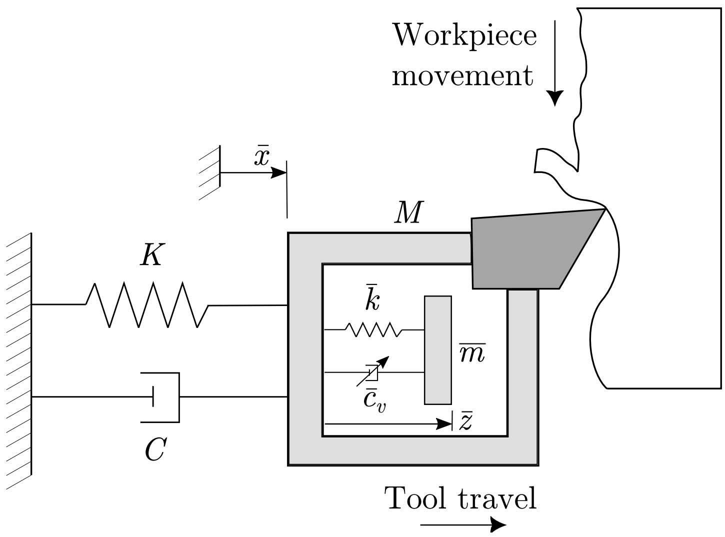

FIGURE 4.1: Schematic of the present system.

Figure 4.1 shows a schematic of the present system. Here, a primary system with mass M, linear stiffness K and viscous damping C models the dominant mode of vibration of the machine tool whose relative position from the steady cutting condition is denoted as $\bar{x}$. For the variable cutting force component acting upon the primary system due to this departure from steady cutting, we use a power series expression in terms of the chip thickness variation $(\bar{x} - \bar{x}_{\bar{\tau}})$ where $\bar{\tau}$ denotes time period of one revolution of the rotating workpiece; see the work of Kalmár-Nagy *et al.* [50] for more details. The novelty of the present work is the attached secondary oscillator with its own limit cycle. As shown in the figure, it has mass $\overline{m}$, linear stiffness $\bar{k}$, and linear and nonlinear damping parameters $\bar{c}_v$ and $\bar{\beta}$ (not shown in the figure), respectively. $\bar{z}$ denotes its relative position from the primary system.

Following [50] and [84], the governing equations of motion of the coupled system are

$$M\ddot{\bar{x}} + C\dot{\bar{x}} + K\bar{x} + \bar{k}_1(\bar{x} - \bar{x}_{\bar{\tau}}) - \frac{\bar{k}_1}{8f_0}\left((\bar{x} - \bar{x}_{\bar{\tau}})^2 - \frac{5}{12f_0}(\bar{x} - \bar{x}_{\bar{\tau}})^3\right) \\ - \bar{k}\bar{z} - \bar{c}_v\dot{\bar{z}}(\bar{\beta}\bar{z}^2 - 1) = 0, \quad (4.1)$$

and

$$\overline{m}(\ddot{\bar{x}} + \ddot{\bar{z}}) + \bar{k}\bar{z} + \bar{c}_v\dot{\bar{z}}(\bar{\beta}\bar{z}^2 - 1) = 0, \quad (4.2)$$

where $\bar{k}_1$ is the cutting force coefficient and f_0 is the steady-state chip thickness. We now nondimensionalize these equations. For length nondimensionalization, we use $\bar{x} = \dfrac{12f_0}{5}x$ and $\bar{z} = \dfrac{12f_0}{5}z$, and obtain

$$M\ddot{x} + C\dot{x} + Kx + \bar{k}_1\left(x - x_{\bar{\tau}}\right) - \frac{3}{10}\bar{k}_1\left((x - x_{\bar{\tau}})^2 - (x - x_{\bar{\tau}})^3\right) \\ - \bar{k}z - \bar{c}_v\dot{z}\left(\tilde{\beta}z^2 - 1\right) = 0, \quad (4.3)$$

and

$$\overline{m}\left(\ddot{x} + \ddot{z}\right) + \bar{k}z + \bar{c}_v\dot{z}\left(\tilde{\beta}z^2 - 1\right) = 0, \quad (4.4)$$

where $\tilde{\beta} = \dfrac{144}{25} f_0^2 \bar{\beta}$. With $\tilde{t} = \omega_n t$ as the nondimensional time, the above equations take the form

$$M\omega_n^2 \ddot{x} + C\omega_n \dot{x} + Kx + \bar{k}_1 \left(x - x_{\bar{\tau}}\right) - \frac{3}{10}\bar{k}_1 \left(\left(x - x_{\bar{\tau}}\right)^2 - \left(x - x_{\bar{\tau}}\right)^3\right) - \bar{k}z - \bar{c}_v \omega_n \dot{z} \left(\tilde{\beta} z^2 - 1\right) = 0, \quad (4.5)$$

and

$$\overline{m}\omega_n^2 \left(\ddot{x} + \ddot{z}\right) + \bar{k}z + \bar{c}_v \omega_n \dot{z} \left(\tilde{\beta} z^2 - 1\right) = 0. \quad (4.6)$$

Finally, defining

$$\widetilde{m} = \frac{\overline{m}}{M}, \quad \widetilde{C} = \frac{C}{M\omega_n}, \quad p = \frac{\bar{k}_1}{M\omega_n^2}, \quad \omega_p^2 = \frac{\bar{k}}{\overline{m}\omega_n^2}, \quad \tilde{c}_v = \frac{\bar{c}_v}{M\omega_n}, \quad (4.7)$$

we obtain the nondimensional equations of motion as

$$\ddot{x} + \widetilde{C}\dot{x} + x + p\left(x - x_\tau\right) - \frac{3p}{10}\left(\left(x - x_\tau\right)^2 - \left(x - x_\tau\right)^3\right) - \widetilde{m}\omega_p^2 z - \tilde{c}_v \dot{z}\left(\tilde{\beta} z^2 - 1\right) = 0, \quad (4.8)$$

and

$$\left(\ddot{x} + \ddot{z}\right) + \omega_p^2 z + \frac{\tilde{c}_v}{\widetilde{m}} \dot{z}\left(\tilde{\beta} z^2 - 1\right) = 0. \quad (4.9)$$

Considering that the attached system is light and lightly damped and that the primary system is also lightly damped, we introduce the scaling

$$\widetilde{m} = \varepsilon\, m, \quad \tilde{c}_v = \varepsilon^2\, c_v, \quad \text{and} \quad \widetilde{C} = \varepsilon^2\, c, \quad (4.10)$$

where ε is a small bookkeeping parameter. Further, in the secondary oscillator's damping, we expect $\tilde{\beta} z^2$ to interact at the same order with $\mathcal{O}(1)$ negative damping. Therefore, for small z of $\mathcal{O}(\varepsilon)$, we introduce $\tilde{\beta} = \dfrac{\beta}{\varepsilon^2}$. Finally, we define $\gamma = \dfrac{c_v}{m}$ to obtain

$$\ddot{x} + \varepsilon^2\, c\,\dot{x} + x + p\,(x - x_\tau) - \frac{3}{10}p\left((x - x_\tau)^2 - (x - x_\tau)^3\right) \\ - \varepsilon\, m\, \omega_p^2\, z - m\,\gamma\,\dot{z}\left(\beta z^2 - \varepsilon^2\right) = 0, \quad (4.11)$$

and

$$\ddot{x} + \ddot{z} + \omega_p^2\, z + \frac{1}{\varepsilon}\gamma\,\dot{z}\left(\beta z^2 - \varepsilon^2\right) = 0. \quad (4.12)$$

Equations (4.11) and (4.12) are treated in the upcoming sections. We first find the linear stability boundary of our coupled system in the next section.

4.3 Linear stability analysis

For the linear stability analysis, we drop nonlinear terms in Eqs. (4.11) and (4.12) and obtain

$$\ddot{x} + \varepsilon^2\, c\,\dot{x} + x + p\,(x - x_\tau) - \varepsilon\, m\, \omega_p^2\, z + \varepsilon^2\, m\,\gamma\,\dot{z} = 0, \quad (4.13)$$

and

$$\ddot{x} + \ddot{z} + \omega_p^2\, z - \varepsilon\,\gamma\,\dot{z} = 0. \quad (4.14)$$

Substituting $x = Ae^{\lambda t}$ and $z = Be^{\lambda t}$ in the above equations and writing in a matrix form, we obtain

$$\begin{bmatrix} \lambda^2 + \varepsilon^2 c\lambda + 1 + p - p\,\mathrm{e}^{-\lambda\,\tau} & \varepsilon^2\gamma\,\lambda\, m - \varepsilon\, m{\omega_p}^2 \\ \lambda^2 & -\varepsilon\,\gamma\,\lambda + \lambda^2 + {\omega_p}^2 \end{bmatrix} \begin{bmatrix} A \\ B \end{bmatrix} = \begin{bmatrix} 0 \\ 0 \end{bmatrix}. \quad (4.15)$$

For a nontrivial solution of A and B, the determinant of the coefficient matrix should be zero. This yields the characteristic equation

$$\begin{aligned} &-\varepsilon^2\gamma\,\lambda^3 m - c\,\varepsilon^3\gamma\,\lambda^2 + \varepsilon\,\lambda^2\,m\,{\omega_p}^2 + c\,\varepsilon^2\lambda^3 + c\,\varepsilon^2{\omega_p}^2\lambda - \varepsilon\,\gamma\,\lambda^3 \\ &\qquad - \varepsilon\,\gamma\,\lambda\,p + \lambda^4 + \lambda^2{\omega_p}^2 - \varepsilon\,\gamma\,\lambda + \lambda^2 p + {\omega_p}^2\,p + \varepsilon\,\gamma\,\lambda\,p\,\mathrm{e}^{-\lambda\,\tau} \\ &\qquad\qquad + \lambda^2 + {\omega_p}^2 - \lambda^2\,p\,\mathrm{e}^{-\lambda\,\tau} - {\omega_p}^2 p\,\mathrm{e}^{-\lambda\,\tau} = 0. \end{aligned} \tag{4.16}$$

At a Hopf boundary, $\lambda = \mathrm{I}\omega$. We substitute this in the above characteristic equation and separate the real and imaginary parts to obtain the following two equations

$$\begin{aligned} &c\,\varepsilon^3\gamma\,\omega^2 - \varepsilon\,\omega^2 m{\omega_p}^2 + \sin(\omega\,\tau)\,\varepsilon\,\gamma\,\omega\,p + \omega^4 - \omega^2{\omega_p}^2 \\ &\qquad - \omega^2 p + {\omega_p}^2 p - \omega^2 + {\omega_p}^2 + \left(\omega^2 - {\omega_p}^2\right) p\cos(\omega\,\tau) = 0, \end{aligned} \tag{4.17}$$

and

$$\begin{aligned} &- c\,\varepsilon^2\omega^3 + c\,\varepsilon^2\omega\,{\omega_p}^2 + \varepsilon\,\gamma\,\omega^3 - \varepsilon\,\gamma\,\omega\,p - \varepsilon\,\gamma\,\omega \\ &\qquad + \cos(\omega\,\tau)\,\varepsilon\,\gamma\,\omega\,p + \varepsilon^2\gamma\,\omega^3 m + \left({\omega_p}^2 - \omega^2\right) p\sin(\omega\,\tau) = 0. \end{aligned} \tag{4.18}$$

We solve Eqs. (4.17) and (4.18) numerically and obtain bifurcation boundaries shown by solid curves in Fig. 4.2. We obtain analytical approximations for these boundaries as follows. We assume

$$p_{cr} = \bar{p} + \varepsilon p_1 + \varepsilon^2 p_2 + \mathcal{O}(\varepsilon^3), \tag{4.19}$$

$$\tau_{cr} = \bar{\tau} + \varepsilon\tau_1 + \varepsilon^2\tau_2 + \mathcal{O}(\varepsilon^3), \tag{4.20}$$

and substitute the above in Eqs. (4.17) and (4.18). At $\mathcal{O}(1)$, we obtain

$$(\omega - \omega_p)\,(\omega + \omega_p)\left(\cos(\omega\,\bar{\tau})\,\bar{p} + \omega^2 - \bar{p} - 1\right) = 0, \tag{4.21}$$

$$-\sin(\omega\,\bar{\tau})\,\bar{p}\,(\omega - \omega_p)\,(\omega + \omega_p) = 0. \tag{4.22}$$

Based on the value of ω, various approximations are obtained as elaborated next.

4.3.1 Case-1: $\omega \nrightarrow \omega_p, \omega \nrightarrow 1$

By Eqs. (4.21) and (4.22), for ω not close to ω_p and $\omega \neq 1$, we find

$$\bar{p} = \frac{\omega^2 - 1}{2}, \quad \sin(\omega\bar{\tau}) = 0 \quad \text{and} \quad \cos(\omega\,\bar{\tau}) = -1. \tag{4.23}$$

Solving $\mathcal{O}(\varepsilon)$ and $\mathcal{O}(\varepsilon^2)$ equations, we obtain

$$p_1 = -\frac{m\,\omega^2\,{\omega_p}^2}{2\left(\omega^2 - {\omega_p}^2\right)}, \quad p_2 = 0, \tag{4.24}$$

$$\tau_1 = 0, \quad \text{and} \quad \tau_2 = \frac{2\left(-m\,\gamma\,\omega^4 + c\omega^4 - 2\,c\omega^2{\omega_p}^2 + c{\omega_p}^4\right)}{\left(\omega - \omega_p\right)^2\left(\omega + \omega_p\right)^2\left(\omega - 1\right)\left(\omega + 1\right)}. \tag{4.25}$$

4.3.2 Case-2: $\omega \to \omega_p$

For ω close to ω_p, we introduce a detuning parameter ω_2 and write $\omega = \omega_p + \varepsilon\omega_2$. $\mathcal{O}(1)$ Eqs. (4.21) and (4.22) are now satisfied. The $\mathcal{O}(\varepsilon)$ equations are

$$\omega_p\,\left(-m{\omega_p}^3 + \sin\left(\omega_p\,\bar{\tau}\right)\gamma\,\bar{p} + 2\,\cos\left(\omega_p\,\bar{\tau}\right)\omega_2\,\bar{p} + 2\,{\omega_p}^2\omega_2 - 2\,\omega_2\,\bar{p} - 2\,\omega_2\right) = 0, \tag{4.26}$$

$$-\,\omega_p\,\left(2\,\sin\left(\omega_p\,\bar{\tau}\right)\omega_2\,\bar{p} - \cos\left(\omega_p\,\bar{\tau}\right)\gamma\,\bar{p} - \gamma\,{\omega_p}^2 + \gamma\,\bar{p} + \gamma\right) = 0. \tag{4.27}$$

Solving the above two equations, we obtain

$$\bar{p} = \frac{\begin{aligned}&\left(m^2{\omega_p}^6 - 4\,m{\omega_p}^5\omega_2 + \gamma^2{\omega_p}^4 + 4\,{\omega_p}^4{\omega_2}^2 + 4\,m{\omega_p}^3\omega_2 - 2\,\gamma^2{\omega_p}^2\right.\\ &\qquad\qquad\left. - 8\,{\omega_p}^2{\omega_2}^2 + \gamma^2 + 4\,{\omega_2}^2\right)\end{aligned}}{2\,\left(-2\,m{\omega_p}^3\omega_2 + \gamma^2{\omega_p}^2 + 4\,{\omega_p}^2{\omega_2}^2 - \gamma^2 - 4\,{\omega_2}^2\right)}, \tag{4.28}$$

$$\cos\left(\omega_p\,\bar{\tau}\right) = -\frac{-2\,m{\omega_p}^3\omega_2 + \gamma^2{\omega_p}^2 + 4\,{\omega_p}^2{\omega_2}^2 - \gamma^2\bar{p} - 4\,{\omega_2}^2\bar{p} - \gamma^2 - 4\,{\omega_2}^2}{\bar{p}\,\left(\gamma^2 + 4\,{\omega_2}^2\right)}, \tag{4.29}$$

$$\sin\left(\omega_p\,\bar{\tau}\right) = \frac{\gamma\,{\omega_p}^3 m}{\bar{p}\,\left(\gamma^2 + 4\,{\omega_2}^2\right)}. \tag{4.30}$$

Proceeding further at $\mathcal{O}(\varepsilon^2)$ and $\mathcal{O}(\varepsilon^3)$, we find higher order correction terms p_1, p_2, τ_1 and τ_2; see Appendix B for corresponding expressions. By Eq. (4.28), $\bar{p} \to \infty$ as the denominator goes to zero, and that yields the approximation for the corresponding ω_2 or ω.

4.3.3 Case-3: $\omega \to 1$

For ω close to 1, we introduce detuning parameters ω_3 and ω_4 to write $\omega = 1+\varepsilon\omega_3+\varepsilon^2\omega_4$. The $\mathcal{O}(1)$ equations take the form

$$-\bar{p}\,(\omega_p - 1)\,(\omega_p + 1)\,(\cos(\bar{\tau}) - 1) = 0, \tag{4.31}$$

$$\sin(\bar{\tau})\,\bar{p}\,(\omega_p - 1)\,(\omega_p + 1) = 0. \tag{4.32}$$

The above equations are satisfied if $\bar{p} = 0$ or $\bar{\tau} = 2N\pi$, where N is an integer. Accordingly, we can have three sub-cases as detailed below.

4.3.3.1 Case-3a: $\bar{p} = 0$, $\bar{\tau} = (2N + 1)\pi$

With $\bar{p} = 0$ and $p_1 \neq 0$, we obtain $\sin(\bar{\tau}) = 0$ and $\cos(\bar{\tau}) = -1$. This implies $\bar{\tau} = (2N+1)\pi$. Further, we obtain

$$p_1 = \frac{m{\omega_p}^2 + 2\,\omega_3\,{\omega_p}^2 - 2\,\omega_3}{2\,({\omega_p}^2 - 1)}. \tag{4.33}$$

Corresponding p_2, τ_1 and τ_2 are provided in Appendix C. Note that ω_3 is a free parameter here. Hence, we need not consider ω_4, i.e., $\omega = 1 + \varepsilon\omega_3$.

4.3.3.2 Case-3b: $\bar{p} = 0$, $p_1 = 0$

Along with $\bar{p} = 0$, if we consider $p_1 = 0$ as well, then $\bar{\tau}$ remains indeterminate and serves as the free parameter, and we obtain

$$\omega_3 = -\frac{m{\omega_p}^2}{2\left({\omega_p}^2 - 1\right)}, \tag{4.34}$$

$$p_2 = -\frac{c{\omega_p}^4 - 2\,c{\omega_p}^2 - \gamma\,m + c}{\left({\omega_p}^2 - 1\right)^2 \sin\left(\bar{\tau}\right)}, \tag{4.35}$$

and

$$\begin{aligned}\omega_4 = \Big(&3\,m^2{\omega_p}^6 \sin\left(\bar{\tau}\right) + 4\,\cos\left(\bar{\tau}\right) c{\omega_p}^6 + m^2{\omega_p}^4 \sin\left(\bar{\tau}\right) - 4\,c{\omega_p}^6 - 12\,\cos\left(\bar{\tau}\right) c{\omega_p}^4 \\ &- 4\,\cos\left(\bar{\tau}\right)\gamma\,m{\omega_p}^2 + 12\,c{\omega_p}^4 + 12\,\cos\left(\bar{\tau}\right) c{\omega_p}^2 + 4\,\gamma\,m{\omega_p}^2 + 4\,\cos\left(\bar{\tau}\right)\gamma\,m \\ &-12\,c{\omega_p}^2 - 4\,\cos\left(\bar{\tau}\right) c - 4\,\gamma\,m + 4\,c\Big)\Big/\Big(8\,\left({\omega_p}^2 - 1\right)^3 \sin\left(\bar{\tau}\right)\Big).\end{aligned} \tag{4.36}$$

Note that since $\bar{\tau}$ is the free parameter, τ_1 and τ_2 are not required and accordingly set to zero.

4.3.3.3 Case-3c: $\bar{\tau} = 2N\pi$

With $\bar{\tau} = 2N\pi$, $\bar{p}$ remains indeterminate and serves as the free parameter, and we obtain

$$\omega_3 = -\frac{m{\omega_p}^2}{2\left({\omega_p}^2 - 1\right)} \quad \text{and} \quad \tau_1 = \frac{m{\omega_p}^2\bar{\tau}}{2({\omega_p}^2 - 1)}. \tag{4.37}$$

The next order corrections are found to be

$$\omega_4 = \frac{m^2{\omega_p}^4\left(3\,{\omega_p}^2 + 1\right)}{8\left({\omega_p}^6 - 3\,{\omega_p}^4 + 3\,{\omega_p}^2 - 1\right)}, \tag{4.38}$$

$$\tau_2 = -\frac{\begin{aligned}\big(m^2{\omega_p}^6\bar{p}\,\bar{\tau} + 3\,m^2{\omega_p}^4\bar{p}\,\bar{\tau} + 8\,c{\omega_p}^6 - 24\,c{\omega_p}^4 - 8\,\gamma\,m{\omega_p}^2 \\ +24\,c{\omega_p}^2 + 8\,\gamma\,m - 8\,c\big)\end{aligned}}{8\bar{p}\,\left({\omega_p}^6 - 3\,{\omega_p}^4 + 3\,{\omega_p}^2 - 1\right)}. \tag{4.39}$$

Here, p_1 and p_2 are not required.

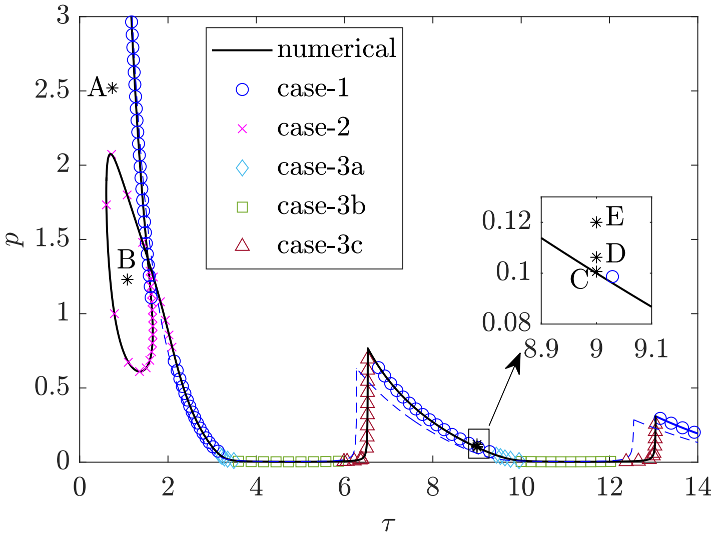

FIGURE 4.2: Stability lobes for the coupled system with analytical approximations along various segments. Here, $\varepsilon = 0.05, m = 1, c = 2, c_v = 2, \omega_p = 1.573$. The dotted curve shows the stability lobes for the uncoupled damped primary system.

Figure 4.2 shows the numerically obtained stability boundary along with that obtained by the above approximations for the parameter set $\varepsilon = 0.05, m = 1, c = 2, c_v = 2, \omega_p = 1.573$. The approximations are capturing the boundary well in the various segments. The arbitrarily chosen value of $\omega_p = 1.573$ represents an untuned or nonresonant scenario. We note that $\omega_p > \omega$ is needed for improvement in linear stability boundary, i.e., $p_1 > 0$ (Eq. (4.24)) of case-1, where τ_2 (Eq. (4.25)) being $\mathcal{O}(\varepsilon^2)$ correction, plays a minor role. The choice of $\omega_p = 1.573$ ensures $p_1 > 0$ for this segment of the second stability lobe. The blue-dash curve in Fig. 4.2 shows the stability lobes for the uncoupled damped primary oscillator. The improvement for case-1 (present system) is noticed. However, the boundaries corresponding to the present system have shifted to the right. This is evident from the expression for τ_1 of case-3c. For this τ_1 to be negative, $\omega_p < 1$ is required. However, branches turn and become complicated for $\omega_p < 1$. We observe that reducing the value of c_v helps avoid turning. Not getting into these complications, we continue with $\omega_p = 1.573$ in the rest of the present study.

We note that using Sims' expressions [52] for tuning the linear negative damping does not help, although the real part of the frequency response function that Sims has treated for equal troughs, involves the square of the secondary oscillator's damping (see Eq. (6) of that paper). Therefore, a different approach is required for tuning the limit cycle oscillator. Our preliminary search for optimum parameters based on maximizing the minimum p did not yield any useful results. Hence, the improvement in the stability boundary using this negatively damped or unstable secondary oscillator may not be very impressive. However, the change in the nature of bifurcation that we will reveal later in this chapter is certainly noticeable in our opinion. In the present study, the secondary oscillator is linearly unstable. Here, limit cycle oscillations of this oscillator can stabilize the primary system. Hence, the coupled system can be linearly unstable, meaning that a pair of eigenvalues may already exist in the right half plane without showing tool chatter. Therefore, to better understand the tool chatter dynamics for different portions of the stability diagram, we next present some numerical solutions.

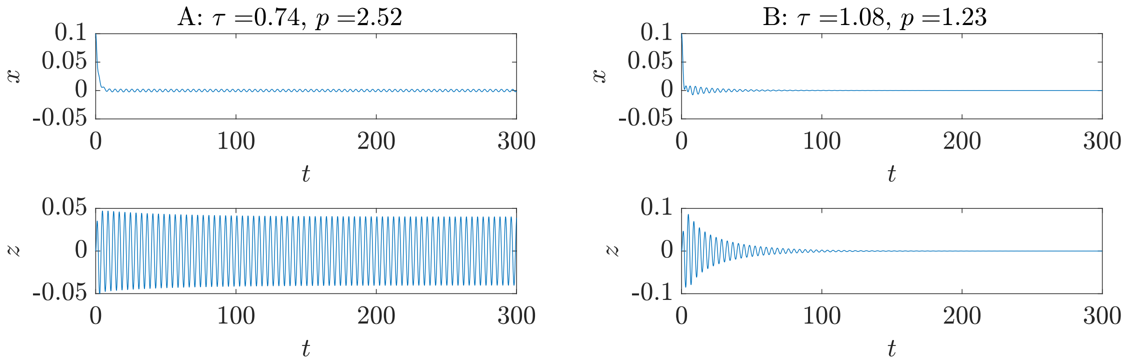

FIGURE 4.3: Numerical solutions corresponding to points A and B. Initial conditions for both the figures are $x(\eta) = 0.1\cos(\eta), \dot{x}(\eta) = -0.1\sin(\eta), z(\eta) = 0, \dot{z}(\eta) = 0, \eta \in [-\tau, 0]$.

4.4 Numerical results: stability and supercriticality

Here, we present numerical solutions corresponding to different regimes represented by points marked A to E in the stability diagram (Fig. 4.2). Corresponding responses along with labels are shown in Figs. 4.3 and 4.4, where the upper plot in each figure shows the response of the primary oscillator and the lower plot shows that of the secondary oscillator. From Fig. 4.3, we can note that the primary oscillator is stable in regions represented by

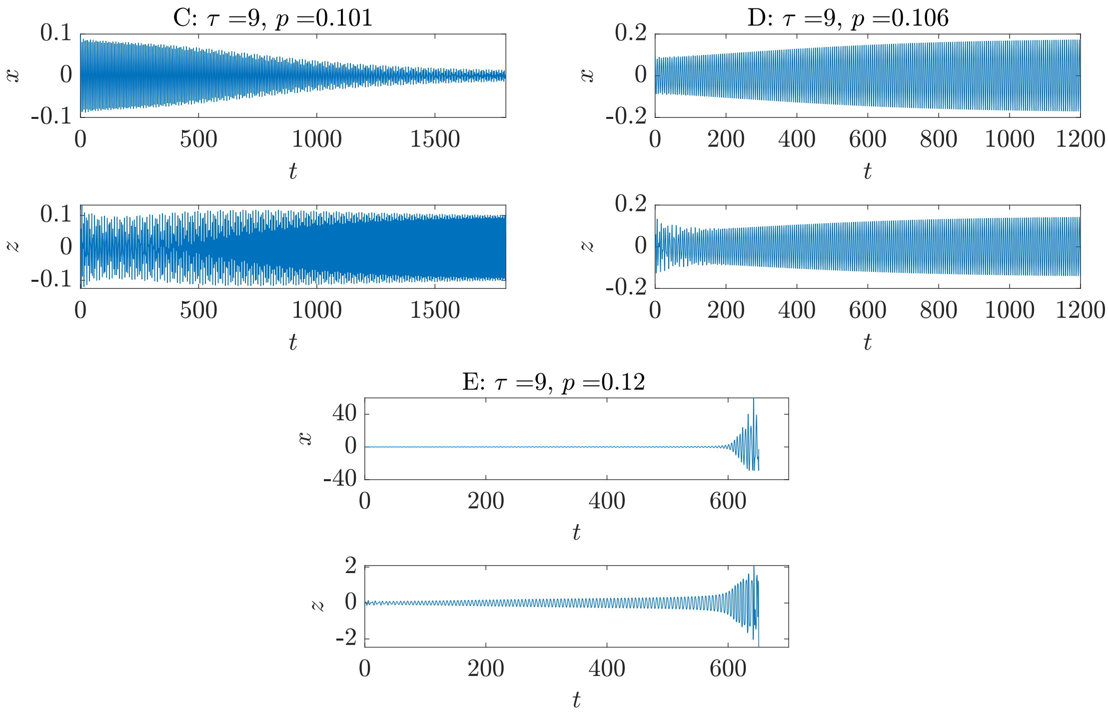

FIGURE 4.4: Numerical solutions near the stability boundary in the unstable regime; for C, D and E shown in Fig. 4.2. Initial conditions for all the figures are $x(\eta) = 0.1\cos(\eta), \dot{x}(\eta) = -0.1\sin(\eta), z(\eta) = 0, \dot{z}(\eta) = 0, \eta \in [-\tau, 0]$.

A and B. Note that due to the negative damping in the secondary oscillator, its equilibrium solution is generally unstable. However, for the point B, the coupling between the two oscillators stabilizes the secondary oscillator thereby denoting an equilibrium for the coupled system which is linearly stable. For regions corresponding to A, the secondary oscillator approaches a limit cycle, indicating linear instability of the coupled system. In this region, the primary oscillator shows a small amplitude response at the frequency of the secondary oscillator and this is not tool chatter.

Figure 4.4 shows some responses for parameters post the stability boundary corresponding to the tool chatter instability. For point C which is close to the stability boundary, we observe that the primary oscillator still gets stabilized (i.e., no tool chatter) even though the equilibrium of the coupled system has become unstable to small perturbations in both the primary and the secondary oscillator direction. Then marching slightly forward in the unstable regime, the primary oscillator starts to show limit cycle oscillations as shown for the simulation corresponding to D in Fig. 4.4. The post-bifurcation small amplitude bounded response of the primary oscillator in Fig. 4.4 indicates a supercritical bifurcation. That, in turn, hints elimination of bistability in the stable regime and these results further suggest possible bistability in the linearly unstable region. Further deep inside the unstable regime, the system begins to show unbounded responses as shown for E. In this simulation, the tool chatter amplitude has become sufficiently large that the tool gets into self-interruption. However, the current model does not accommodate self-interruption and hence, blows up. Inclusion of self-interruption as in [114] will result in bounded tool chatter for the point E as well.

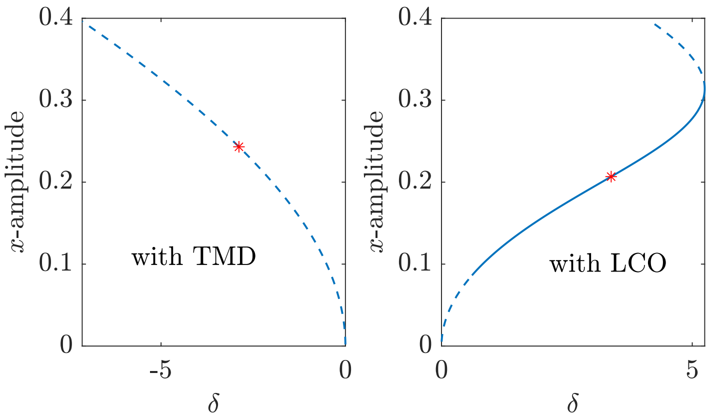

FIGURE 4.5: Bifurcation diagrams obtained using DDE-BIFTOOL [115, 116] for a system with TMD (left figure) and the present system with a limit cycle oscillator (right figure) for $\tau_{cr} = 9$ and $p = p_{cr} + \varepsilon^2\delta$, where the red stars denote the initiation of loss of contact. Here, solid and dotted lines respectively represent stable and unstable solutions. The initial unstable branch for the system with a limit cycle oscillator denotes a stabilized primary oscillator with limit cycle oscillations of the secondary oscillator. Parameter values for the system with limit cycle oscillator are $\varepsilon = 0.05, m = 1, c = 2, c_v = 2, \beta = 1, \omega_p = 1.573$. To simulate the system with TMD, we use $\varepsilon = 0.05, m = 1, c = 2, c_v = -5.542, \beta = 0, \omega_p = 1.037$.

We note that a system with a linear TMD has a subcritical Hopf bifurcation for the tool chatter model and hence, exhibits bistability in the linearly stable regime. We compare the bifurcation structure for a system with a linear TMD and the present system (with a limit cycle oscillator as the absorber) in Fig. 4.5 for $\tau_{cr} = 9$, where δ denotes detuning in p, i.e.,

$$p = p_{cr} + \varepsilon^2\delta,$$

where again p_{cr} is the value of p at the Hopf point and is obtained numerically. Parameters for the TMD are selected following Sims' expressions [52]. The bifurcation diagrams are obtained using the Matlab package DDE-BIFTOOL [115, 116]. Solid and dashed lines in the figure represent stable and unstable limit cycles, respectively. The present system exhibits supercritical bifurcation, demonstrating the dynamical advantage that the limit cycle oscillator can offer. The initial unstable part of the supercritical branch represents a stabilized primary oscillator. The multiple scales analysis of the next section will further disclose this aspect. Note that solutions above the red stars exhibit a negative depth of cut, i.e., $x - x_\tau < -\frac{5}{12}$ based on the chosen nondimensionalization. This defines the region of bistability in the linearly stable regime [117]. Because of the supercritical bifurcation, the loss of contact occurs after the system loses stability, and hence, the bistable region in the linearly stable region is completely eliminated by the limit cycle oscillator. The present study is limited to responses where the loss of contact does not occur. For such small amplitude oscillations, we examine the bifurcation scenario analytically using the method of multiple scales in the next section. As noted in the section on linear stability, we have different asymptotic approximations for the different portions of the linear stability boundary and accordingly, the method of multiple scales analysis for the different portions of the stability boundaries will be different. We first start with case-1 wherein both p_{cr} and τ_{cr} can be obtained in terms of the tool chatter frequency as the parameter.

4.5 The method of multiple scales for case-1

In this section, we present the multiple scales analysis for a perturbation around a Hopf point of case-1. The multiple scales treatment of a delayed system have been reported earlier, e.g., see [109, 118–121]. Here, the analysis is slightly different from earlier studies as we consider the Hopf point in an expanded form that is derived in section 4.3. With the detuning parameter δ, we write

$$p = \bar{p} + \varepsilon p_1 + \varepsilon^2 \delta, \tag{4.40}$$

$$\tau = \bar{\tau} + \varepsilon^2 \tau_2, \tag{4.41}$$

where $\bar{p}$, $\bar{\tau}$, p_1 and τ_2 are given by Eqs. (4.23) to (4.25) for case-1. Note that the above implies that $\tau_{cr} = \bar{\tau} + \varepsilon^2\tau_2$ with $p_{cr} = \bar{p} + \varepsilon p_1$. We introduce timescales $T_0 = t, T_1 = \varepsilon t$ and $T_2 = \varepsilon^2 t$, and use the expansions

$$x = \varepsilon X_0(T_0, T_1, T_2) + \varepsilon^2 X_1(T_0, T_1, T_2) + \varepsilon^3 X_2(T_0, T_1, T_2),$$
$$z = \varepsilon Z_0(T_0, T_1, T_2) + \varepsilon^2 Z_1(T_0, T_1, T_2) + \varepsilon^3 Z_2(T_0, T_1, T_2),$$

restraining our analysis to small amplitude oscillations. Following [109, 118–121], we note

$$t - \tau = T_0 - \tau, \quad \varepsilon(t - \tau) = T_1 - \varepsilon\tau, \quad \varepsilon^2(t - \tau) = T_2 - \varepsilon^2\tau,$$

and write the delayed term x_τ as

$$\begin{aligned} x_\tau = x(t-\tau) = \varepsilon X_0(T_0 - \tau, T_1 - \varepsilon\tau, T_2 - \varepsilon^2\tau) + \varepsilon^2 X_1(T_0 - \tau, T_1 - \varepsilon\tau, T_2 - \varepsilon^2\tau) \\ + \varepsilon^3 X_2(T_0 - \tau, T_1 - \varepsilon\tau, T_2 - \varepsilon^2\tau)\,. \end{aligned} \tag{4.42}$$

Now substituting for τ from Eq. (4.41) and a Taylor series expansion about $\varepsilon = 0$ yields

$$\begin{aligned} x_\tau = \varepsilon X_0\left(T_0 - \bar{\tau}, T_1, T_2\right) + \varepsilon^2 \Bigg(-\bar{\tau}\,\frac{\partial}{\partial T_1} X_0\left(T_0 - \bar{\tau}, T_1, T_2\right) \\ + X_1\left(T_0 - \bar{\tau}, T_1, T_2\right)\Bigg) + \varepsilon^3 \Bigg(\frac{1}{2}\,\bar{\tau}^2 \frac{\partial^2}{\partial T_1^2} X_0\left(T_0 - \bar{\tau}, T_1, T_2\right) \\ -\tau_2\,\frac{\partial}{\partial T_0} X_0\left(T_0 - \bar{\tau}, T_1, T_2\right) - \bar{\tau}\,\frac{\partial}{\partial T_2} X_0\left(T_0 - \bar{\tau}, T_1, T_2\right) \\ -\bar{\tau}\frac{\partial}{\partial T_1} X_1\left(T_0 - \bar{\tau}, T_1, T_2\right) + X_2\left(T_0 - \bar{\tau}, T_1, T_2\right)\Bigg) + \mathcal{O}\left(\varepsilon^4\right). \end{aligned} \tag{4.43}$$

Substituting the above expansions in Eqs. (4.11) and (4.12), we obtain at $\mathcal{O}(\varepsilon)$

$$\frac{\partial^2}{\partial {T_0}^2} X_0(T_0, T_1, T_2) + X_0(T_0, T_1, T_2) + \bar{p}\left(X_0(T_0, T_1, T_2) - X_0(T_0 - \bar{\tau}, T_1, T_2)\right) = 0, \tag{4.44}$$

and

$$\frac{\partial^2}{\partial {T_0}^2} Z_0(T_0, T_1, T_2) + {\omega_p}^2 Z_0(T_0, T_1, T_2) + \frac{\partial^2}{\partial {T_0}^2} X_0(T_0, T_1, T_2) = 0. \tag{4.45}$$

Equation (4.44) is the governing equation of the uncoupled undamped primary system. Note that $(\bar{\tau}, \bar{p})$ by Eq. (4.23) corresponds to a Hopf point for that system with ω denoting the chatter frequency [122]. Therefore, we write the corresponding solution as

$$X_0(T_0, T_1, T_2) = R(T_1, T_2) \sin\left(\omega T_0 + \phi(T_1, T_2)\right), \tag{4.46}$$

where the newly introduced slowly varying functions $R(T_1, T_2)$ and $\phi(T_1, T_2)$ denote the amplitude and phase of the primary system response, respectively. Substituting the solution for $X_0(T_0, T_1, T_2)$ in Eq. (4.45), we solve for $Z_0(T_0, T_1, T_2)$ and obtain

$$\begin{aligned} Z_0(T_0, T_1, T_2) = Q(T_1, T_2) \sin(\omega_p T_0 + \psi(T_1, T_2)) \\ + \frac{\omega^2}{(\omega_p^2 - \omega^2)} R(T_1, T_2) \sin(\omega T_0 + \phi(T_1, T_2)), \end{aligned} \tag{4.47}$$

where the first term is a complimentary solution and the second term is a particular integral. At the next order, i.e., $\mathcal{O}(\varepsilon^2)$, we obtain

$$\begin{aligned} \frac{\partial^2 X_1}{\partial {T_0}^2} + 2\, \frac{\partial^2 X_0}{\partial T_0 \partial T_1} + X_1 + \bar{p} \left(X_1 - X_{1\bar{\tau}} + \frac{\partial\, X_{0\bar{\tau}}}{\partial T_1}\, \bar{\tau} \right) \\ + p_1\, (X_0 - X_{0\bar{\tau}}) - \frac{3}{10}\, \bar{p}\, (X_0 - X_{0\bar{\tau}})^2 - m{\omega_p}^2 Z_0 = 0, \end{aligned} \tag{4.48}$$

and

$$\frac{\partial^2 Z_1}{\partial {T_0}^2} + {\omega_p}^2 Z_1 + 2\, \frac{\partial^2 Z_0}{\partial T_0 \partial T_1} + \gamma \left(\frac{\partial Z_0}{\partial T_0} \right) \left(\beta\, Z_0^2 - 1\right) + \frac{\partial^2 X_1}{\partial {T_0}^2} + 2\, \frac{\partial^2 X_0}{\partial T_0 \partial T_1} = 0, \tag{4.49}$$

where we have suppressed (T_0, T_1, T_2) dependence of variables. Substituting Eqs. (4.46) and (4.47) into Eq. (4.48) and removing secular terms, namely coefficients of $\sin(\omega T_0 + \phi)$ and $\cos(\omega T_0 + \phi)$, we find that

$$\frac{\partial R}{\partial T_1} = 0 \quad \text{and} \quad \frac{\partial \phi}{\partial T_1} = 0, \tag{4.50}$$

where $p_1 = -\frac{m\,\omega^2\,\omega_p^2}{2(\omega^2-\omega_p^2)}$ from the linear stability analysis is used. We incorporate conclusion (4.50) into Eq. (4.48) and obtain

$$\frac{\partial^2 X_1}{\partial {T_0}^2} + X_1 + \bar{p}\,\left(X_1 - X_{1\bar{\tau}}\right) - \frac{3}{5}\,\bar{p}\,R^2 - m{\omega_p}^2 Q\sin(\omega_p T_0 + \psi) + \frac{3}{5}\,\bar{p}\,R^2\,\cos(2\omega T_0 + 2\phi) = 0. \quad (4.51)$$

Because X_0 already contains the complementary solution, only a particular solution for X_1 is of interest. Following [118], we consider

$$X_1 = A_1 + A_2\sin(\omega_p T_0) + A_3\cos(\omega_p T_0) + A_4\sin(2\omega T_0) + A_5\cos(2\omega T_0)\,. \quad (4.52)$$

We substitute the above expression into Eq. (4.51), simplify the resulting equation, and coefficients of trigonometric terms and a T_0-independent term are equated to zero to yield five equations for the five unknowns. We solve those equations for A_i $(i = 1, 2, 3, 4, 5)$ and obtain

$$A_1 = \frac{3}{5}\,\bar{p}\,R^2, \quad (4.53)$$

$$A_2 = \frac{\left(-m{\omega_p}^4 + m{\omega_p}^2\bar{p} + m{\omega_p}^2\right)Q\cos\left(\psi\right) - Qm{\omega_p}^2\bar{p}\cos\left(\omega_p\,\bar{\tau} + \psi\right)}{\left(2\,{\omega_p}^2\bar{p} - 2\,\bar{p}^2 - 2\,\bar{p}\right)\,\cos\left(\omega_p\,\bar{\tau}\right) + {\omega_p}^4 - 2\,{\omega_p}^2\bar{p} - 2\,{\omega_p}^2 + 2\,\bar{p}^2 + 2\,\bar{p} + 1}, \quad (4.54)$$

$$A_3 = \frac{\left(-m{\omega_p}^4 + m{\omega_p}^2\bar{p} + m{\omega_p}^2\right)Q\sin\left(\psi\right) - Qm{\omega_p}^2\bar{p}\sin\left(\omega_p\,\bar{\tau} + \psi\right)}{\left(2\,{\omega_p}^2\bar{p} - 2\,\bar{p}^2 - 2\,\bar{p}\right)\cos\left(\omega_p\,\bar{\tau}\right) + {\omega_p}^4 - 2\,{\omega_p}^2\bar{p} - 2\,{\omega_p}^2 + 2\,\bar{p}^2 + 2\,\bar{p} + 1}, \quad (4.55)$$

$$A_4 = -\,\frac{3\,\bar{p}\,R^2\sin\left(2\,\phi\right)}{20\,\omega^2 - 5}, \quad (4.56)$$

$$A_5 = \frac{3\bar{p}\,R^2\cos\left(2\,\phi\right)}{20\,\omega^2 - 5}. \quad (4.57)$$

From the expression for A_4, we note that the results are only valid for $\omega \neq 0.5$ which is generally true since chatter frequencies are typically greater than the fundamental natural frequency. Similarly, a careful analysis of the denominator of A_2 yields that it vanishes at $\omega = \omega_p$. Since these results have been obtained for case-1 for which $\omega \neq \omega_p$, this situation never arises as well. We now turn to find Z_1. We substitute solutions obtained so far, that are X_0, Z_0 and X_1, into Eq. (4.49) and find secular terms as coefficients of $\sin(\omega_p\,T_0 + \psi)$

and $\cos(\omega_p T_0 + \psi)$. These secular terms lead to

$$\frac{\partial Q}{\partial T_1} = \left[\frac{\gamma}{2} - \frac{\beta\gamma}{8}Q^2 - \frac{\beta\,\gamma\,\omega^4}{4\left(\omega^2-\omega_p^2\right)^2}R^2 \right.$$
$$\left. -\frac{1}{2}\frac{m{\omega_p}^3\bar{p}\,\sin(\omega_p\,\bar{\tau})}{\left(\left(2\,{\omega_p}^2\bar{p}-2\,\bar{p}^2-2\,\bar{p}\right)\,\cos(\omega_p\,\bar{\tau})+{\omega_p}^4-2\,{\omega_p}^2\bar{p}-2\,{\omega_p}^2+2\,\bar{p}^2+2\,\bar{p}+1\right)}\right] Q, \quad (4.58)$$

$$\frac{\partial \psi}{\partial T_1} = \frac{1}{2}\,\frac{\left(\cos(\omega_p\,\bar{\tau})\,\bar{p}+{\omega_p}^2-\bar{p}-1\right)m{\omega_p}^3}{\left(2\,{\omega_p}^2\bar{p}-2\,\bar{p}^2-2\,\bar{p}\right)\,\cos(\omega_p\,\bar{\tau})+{\omega_p}^4-2\,{\omega_p}^2\bar{p}-2\,{\omega_p}^2+2\,\bar{p}^2+2\,\bar{p}+1}. \quad (4.59)$$

Substituting the above equations along with X_0, Z_0 and X_1 into Eq. (4.49) and solving the resulting equation, we obtain Z_1. Expression for Z_1 is lengthy and therefore presented in Appendix D.

Proceeding further, $\mathcal{O}(\varepsilon^3)$ equations are

$$\begin{aligned}
&\frac{\partial^2 X_2}{\partial {T_0}^2} + 2\,\frac{\partial^2 X_1}{\partial T_1 \partial T_0} + 2\,\frac{\partial^2 X_0}{\partial T_2 \partial T_0} + \frac{\partial^2 X_0}{\partial {T_1}^2} + c\frac{\partial X_0}{\partial T_0} + X_2 \\
&\quad + \bar{p}\left(X_2 - \frac{1}{2}\,\frac{\partial^2 X_{0\bar{\tau}}}{\partial T_1^2}\bar{\tau}^2 + \frac{\partial X_{0\bar{\tau}}}{\partial T_0}\tau_2 + \frac{\partial X_{0\bar{\tau}}}{\partial T_2}\bar{\tau} + \frac{\partial X_{1\bar{\tau}}}{\partial T_1}\bar{\tau} - X_{2\bar{\tau}}\right) \\
&\quad + p_1\left(X_1 + \frac{\partial X_{0\bar{\tau}}}{\partial T_1}\bar{\tau} - X_{1\bar{\tau}}\right) + \delta\,\left(X_0 - X_{0\bar{\tau}}\right) \\
&\quad - \frac{3}{10}\,\bar{p}\left(2\,\left(X_0 - X_{0\bar{\tau}}\right)\left(X_1 + \frac{\partial X_{0\bar{\tau}}}{\partial T_1}\bar{\tau} - X_{1\bar{\tau}}\right) - \left(X_0 - X_{0\bar{\tau}}\right)^3\right) \\
&\quad - \frac{3}{10}\,p_1\,\left(X_0 - X_{0\bar{\tau}}\right)^2 - m{\omega_p}^2 Z_1 - m\gamma\left(\frac{\partial Z_0}{\partial T_0}\right)\left(\beta\,Z_0^2 - 1\right) = 0, \quad (4.60)
\end{aligned}$$

and

$$\begin{aligned}
&\frac{\partial^2 Z_2}{\partial {T_0}^2} + {\omega_p}^2 Z_2 + \frac{\partial^2 X_2}{\partial {T_0}^2} + 2\,\frac{\partial^2 X_1}{\partial T_1 \partial T_0} + 2\,\frac{\partial^2 X_0}{\partial T_2 \partial T_0} + \frac{\partial^2 X_0}{\partial {T_1}^2} + 2\,\frac{\partial^2 Z_1}{\partial T_1 \partial T_0} + 2\,\frac{\partial^2 Z_0}{\partial T_2 \partial T_0} \\
&\quad + \frac{\partial^2 Z_0}{\partial {T_1}^2} + 2\,\gamma\left(\frac{\partial Z_0}{\partial T_0}\right)\beta\,Z_0 Z_1 + \gamma\left(\frac{\partial Z_1}{\partial T_0} + \frac{\partial Z_0}{\partial T_1}\right)\left(\beta\,Z_0^2 - 1\right) = 0. \quad (4.61)
\end{aligned}$$

We substitute so far obtained X_0, Z_0, X_1 and Z_1 into Eq. (4.60), and remove secular terms from the resulting equation. That yields

$$\frac{\partial R}{\partial T_2} = -\frac{1}{\left(\bar{p}^2\bar{\tau}^2 + 4\,\omega^2\right)}\left[\frac{\beta\,\gamma\,m\omega^6 Q^2}{\left(\omega^2-\omega_p^2\right)^2} + \frac{\beta\gamma\,m\omega^{10}R^2}{2\left(\omega^2-\omega_p^2\right)^4} - \frac{9\bar{p}^2\bar{\tau}R^2 + 10\,\bar{p}\,\bar{\tau}\delta}{5}\right]R, \tag{4.62}$$

and

$$\frac{\partial \phi}{\partial T_2} = \frac{\bar{\tau}\,\bar{p}\,\beta\,\gamma\,m\omega^5\,Q^2}{2\,\left(\bar{p}^2\bar{\tau}^2+4\,\omega^2\right)\left(\omega^2-\omega_p^2\right)^2} + \frac{\omega^9\bar{p}\,\gamma\,m\bar{\tau}\,\beta\,R^2}{4\,\left(\bar{p}^2\bar{\tau}^2+4\,\omega^2\right)\left(\omega^2-\omega_p^2\right)^4} + \frac{18\,\bar{p}\,\omega\,R^2 + 20\,\omega\,\delta}{5\,\left(\bar{p}^2\bar{\tau}^2+4\,\omega^2\right)}. \tag{4.63}$$

The procedure can be followed to obtain next order evolution equations for Q and ψ that are $\frac{\partial Q}{\partial T_2}$ and $\frac{\partial \psi}{\partial T_2}$. However, Eq. (4.58) governs the dynamics of Q at T_1 timescale. Because T_1 is faster than T_2, evolution of Q is dominated by $\frac{\partial Q}{\partial T_1}$. Therefore, we only consider Eq. (4.58) for the evolution of Q and drop $\frac{\partial Q}{\partial T_2}$ from our analysis. Equation (4.62) governs the dynamics of R. Note that the amplitude evolution equations, i.e., Eqs. (4.58) and (4.62) are independent of phases. Therefore, to study the stabilization dynamics, we focus on amplitude evolution equations only [84]. Advantageously, our analysis of the infinite-dimensional delay differential equation has reduced to a two-dimensional amplitude plane of the ODEs.

We compare responses from numerical integration of the original equations (4.11) and (4.12) and slow flow Eqs. (4.58) and (4.62) in Figs. 4.6 and 4.7. Here, initial conditions for R and Q are chosen based on values of system variables at $t = 0$ by the initial function. As discussed in Appendix B of [123], slow flows only capture the dynamics on the slow manifold, and hence, initial conditions for slow flows should correspond to a point where the full solution converges to the slow manifold. Figures 4.6 and 4.7 show that the present slow flows capture the dynamics. Note that δ is positive in Figs. 4.6 and 4.7. Figure 4.6 shows post-bifurcation stabilization and Fig. 4.7 depicts supercritical bifurcation with an increase in δ. We further investigate Eqs. (4.58) and (4.62) in upcoming sections.

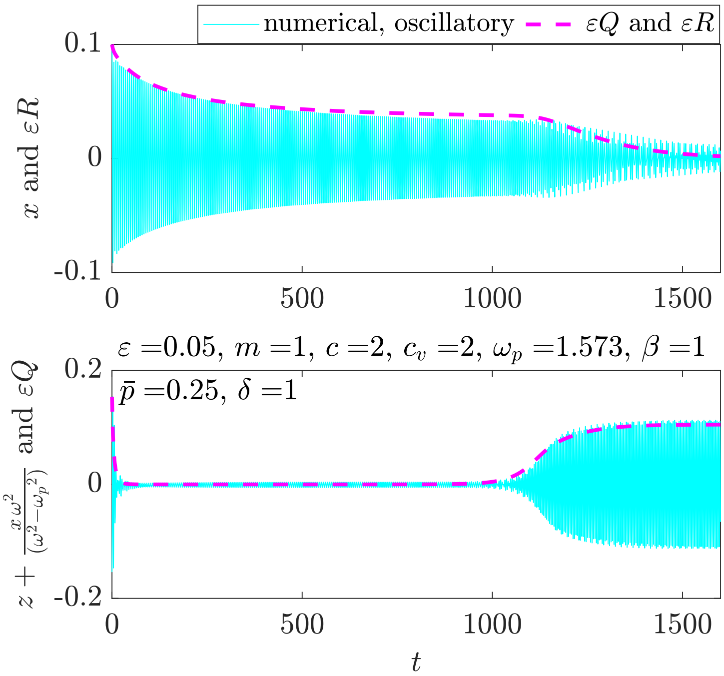

FIGURE 4.6: Comparison of the responses obtained from numerical integration of the original Eqs. (4.11) and (4.12) and slow flow Eqs. (4.58) and (4.62). This figure also demonstrates the primary system's post-bifurcation stabilization. Here, $\bar{\tau} = 3\pi/\omega$ ($\omega^2 = 2\bar{p}+1$) and initial conditions are $x(\eta) = 0.1\cos(1.225\eta), \dot{x}(\eta) = -0.1225\sin(1.225\eta), z(\eta) = 0, \dot{z}(\eta) = 0, \eta \in [-\tau, 0]$. By Eqs. (4.46) and (4.47), $R(0) = 2$, $Q(0) = 3.079$; see [123] for relevant discussion on initial conditions. Note $c_1 = -4.411, c_2 = 0.897, c_3 = -1.082$; explained later.

4.6 Simplified amplitude equations and associated dynamics

Following [84], Eqs. (4.58) and (4.62) can be transformed into simpler form using a transformation

$$R^2 = \frac{\left(\omega^2 - {\omega_p}^2\right)^2}{\omega^4} P \quad \text{and} \quad Q^2 = S,$$

where P and S are new variables representing squares of the primary and secondary oscillators' amplitudes, respectively. Here, $P \geq 0$ and $S \geq 0$. Final amplitude evolution equations take the form

$$\frac{\partial S}{\partial T_1} = -\frac{\beta\gamma}{4}\left(S + 2P + c_1\right) S, \tag{4.64}$$

$$\frac{\partial P}{\partial T_2} = -\frac{4\beta\,\gamma\, m\omega^6}{\left(\omega^2 - \omega_p^2\right)^2 w}\left(c_2 P + 2S + c_3\right) P, \tag{4.65}$$

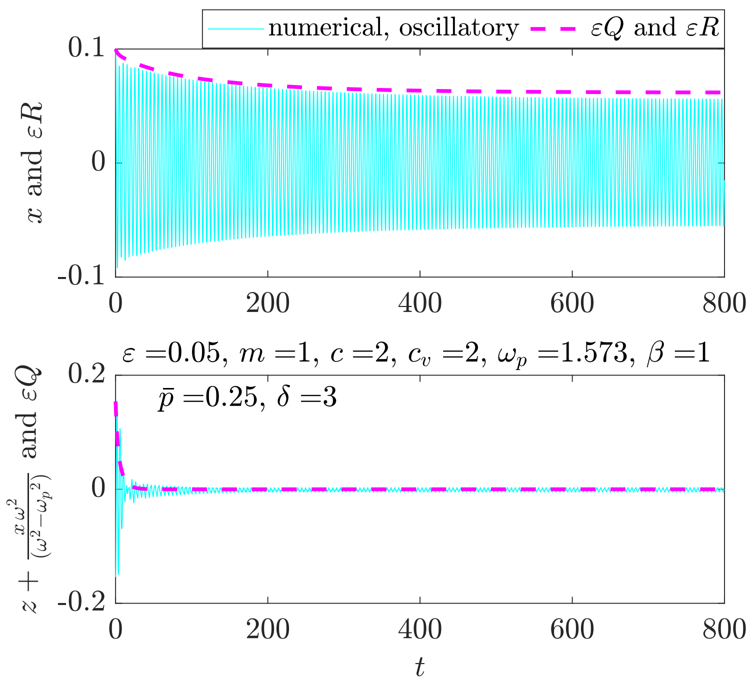

FIGURE 4.7: Comparison of the responses obtained from numerical integration of the original Eqs. (4.11) and (4.12) and slow flow Eqs. (4.58) and (4.62). This figure also demonstrates supercritical bifurcation with an increase in δ: the stable primary system of Fig. 4.6 now approaches a limit cycle. Here, $\bar{\tau} = 3\pi/\omega$ ($\omega^2 = 2\bar{p}+1$) and initial conditions are $x(\eta) = 0.1\cos(1.225\eta), \dot{x}(\eta) = -0.1225\sin(1.225\eta), z(\eta) = 0, \dot{z}(\eta) = 0, \eta \in [-\tau, 0]$. By Eqs. (4.46) and (4.47), $R(0) = 2$, $Q(0) = 3.079$. Note $c_1 = -4.411, c_2 = 0.897, c_3 = -3.247$; explained later.

where

$$w = \left(\omega^4\bar{\tau}^2 - 2\,\omega^2\bar{\tau}^2 + 16\,\omega^2 + \bar{\tau}^2\right), \tag{4.66}$$

$$c_1 = -\frac{4}{\beta} - \frac{4}{\beta\gamma}\frac{{\omega_p}^3 m\sin\left(\omega_p\,\bar{\tau}\right)\left(\omega^2-1\right)}{\Big(\left(\omega^2-1\right)\left(\omega^2-2\,{\omega_p}^2+1\right)\cos\left(\omega_p\,\bar{\tau}\right) - \omega^4 + 2\,\omega^2{\omega_p}^2 - 2\,{\omega_p}^4 + 2\,{\omega_p}^2 - 1\Big)}, \tag{4.67}$$

$$c_2 = 1 - \left(\frac{9\left(\omega^2-\omega_p^2\right)^4\bar{\tau}\,\left(\omega^2-1\right)^2}{10\beta\,\gamma\,m\omega^{10}}\right), \tag{4.68}$$

$$c_3 = -\frac{2\left(\omega^2-\omega_p^2\right)^2\left(\omega^2-1\right)\bar{\tau}\,\delta}{\beta\,\gamma\,m\omega^6}. \tag{4.69}$$

By Eqs. (4.64) and (4.65), we obtain

$$\frac{\mathrm{d}S}{\mathrm{d}T} = -\left(S + 2P + c_1\right) S + \mathcal{O}(\bar{\mu}), \tag{4.70}$$

$$\frac{\mathrm{d}P}{\mathrm{d}T} = -\bar{\mu}\left(c_2 P + 2S + c_3\right) P, \tag{4.71}$$

where T and $\bar{\mu}$ are defined as

$$T = \frac{\beta\gamma}{4} T_1 \quad \text{and} \quad \bar{\mu} = \frac{16\varepsilon\, m\omega^6}{\left(\omega^2 - \omega_p^2\right)^2 w}. \tag{4.72}$$

We consider $\beta > 0, \gamma > 0$ in the present study. We investigate the above system of two nonlinear differential equations in detail, starting with fixed points.

4.6.1 Fixed points and their stability

The system of two first order differential Eqs. (4.70) and (4.71) has four fixed points: (i) $(0, 0)$, (ii) $(-c_1, 0)$, (iii) $(0, -c_3/c_2)$ and (iv) (S^*, P^*), where

$$S^* = \frac{2c_3 - c_1c_2}{c_2 - 4} \quad \text{and} \quad P^* = \frac{2c_1 - c_3}{c_2 - 4}. \tag{4.73}$$

Stability of these fixed points can be determined by finding corresponding Jacobians and its eigenvalues. Table 4.1 shows those eigenvalues, where leading order approximations [84] are presented for (S^*, P^*).

We here point out two important facts related to (S^*, P^*): one related to its existence and the other related to its stability. First note that $c_2 \le 1$ by Eq. (4.68). Now, by Eq. (4.73), (S^*, P^*) exists if

$$2c_1 - c_3 < 0 \quad \text{and} \quad 2c_3 - c_1c_2 < 0,$$

or

$$2c_1 < c_3 \quad \text{and} \quad 2c_3 < c_1c_2,$$

or

$$c_1 < \frac{c_1 c_2}{4}.$$

For $c_1 > 0$, the above condition violates $c_2 \leq 1$. Therefore, we require $c_1 < 0$ for (S^*, P^*) to exist. Note that $(-c_1, 0)$ also exists with $c_1 < 0$. Thus, we find that if (S^*, P^*) exists, $(-c_1, 0)$ exists as well. Next, if $P^* > 0$ then $2c_1 - c_3 < 0$. Hence, by Table 4.1, the Jacobian at (S^*, P^*) has one positive and one negative eigenvalues. Therefore, when this fixed point exists, it is a saddle. These observations have implications when we present feasible phase portraits in the next subsection.

TABLE 4.1: Fixed points and eigenvalues of corresponding Jacobians for the system of equations (4.70) and (4.71), where leading order terms are presented for (S^*, P^*).

Fixed point	$(0, 0)$	$(-c_1, 0)$	$(0, -c_3/c_2)$	(S^*, P^*)
Eigenvalues of the Jacobian	$-c_1$ $-\bar{\mu}\, c_3$	c_1 $\bar{\mu}(2c_1 - c_3)$	$\dfrac{2c_3 - c_1 c_2}{c_2}$ $\bar{\mu}\, c_3$	$-S^*$ $-\bar{\mu}(2c_1 - c_3)$

4.6.2 Feasible phase portraits

Schematics of all the feasible phase portraits are depicted in Fig. 4.8 where a stable fixed point is shown by a solid circle, a saddle by a plus sign and an unstable node by a hollow circle. These phase portraits are labelled 'a' to 'l' for easy reference. The arrangement of phase portraits in the c_1-c_2 plane depicts a bifurcation structure that is explained later. Conditions corresponding to each phase portrait are listed in Table 4.2. Reasoning for the finite number of feasible phase portraits is based on the existence of the number of fixed points and their stability, where we refer to Table 4.1 to comment on the stability of fixed points. A reader may skip this part and jump to the bifurcation structure detailed in the next subsection. Here, we continue with our investigation.

4.6.2.1 All four fixed points exist

Here, $c_1 < 0, S^* > 0$ and $P^* > 0$. There are two cases for a fixed point on the P-axis to exist: (i) $c_3 < 0$ and $c_2 > 0$ and (ii) $c_3 > 0$ and $c_2 < 0$.

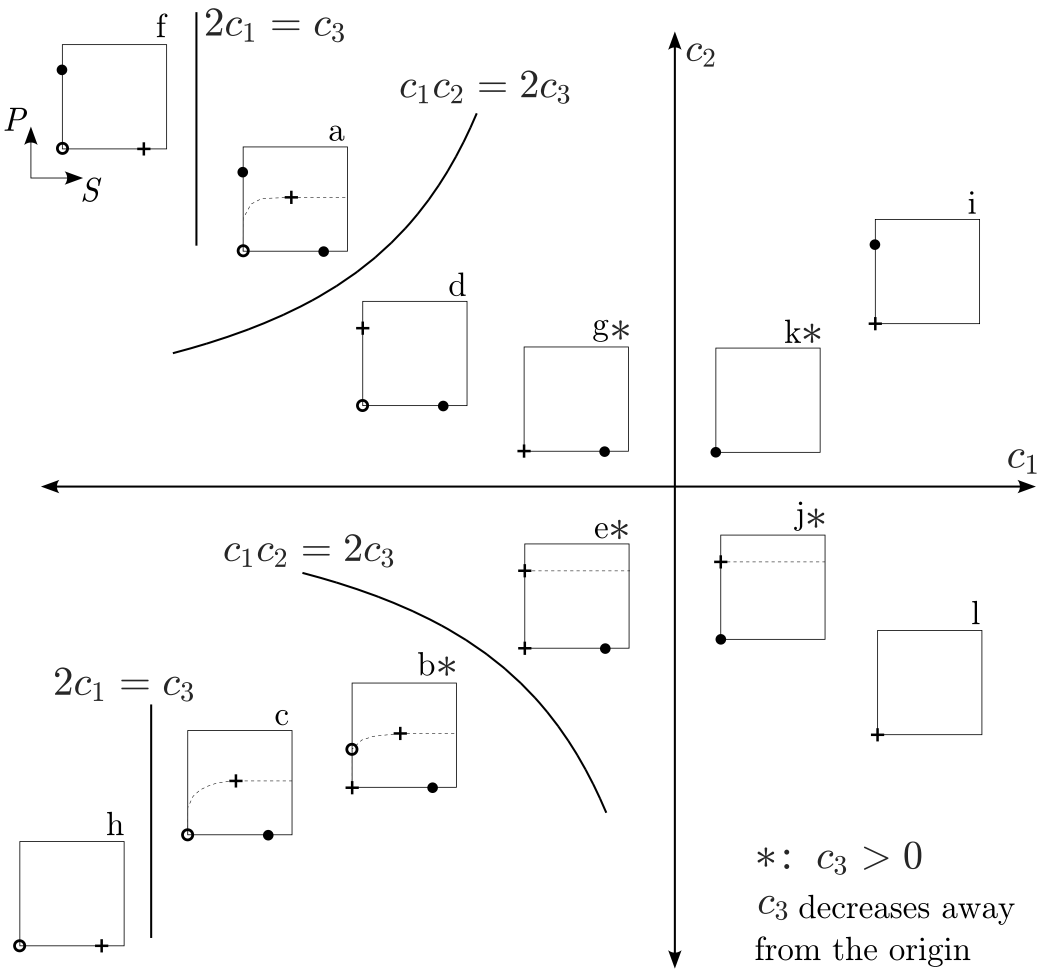

FIGURE 4.8: Schematic depicting feasible phase portraits and bifurcation scenarios: a solid circle denotes a stable fixed point, a plus sign denotes a saddle, and a hollow circle denotes an unstable node. Note that phase portraits are labelled based on the number of fixed points in them: 'a-b' has four, 'c-d-e-f' has three, 'g-h-i-j' has two and 'k-l' has a single fixed point. Curves $c_1c_2 = 2c_3$ and $2c_1 = c_3$ are bifurcation boundaries between phase portraits on either side of it. Conditions and examples of parameter combinations corresponding to these phase portraits are provided in Table 4.2.

For case (i), $c_1 < 0$ and $c_3 < 0$ indicates that the origin is an unstable fixed point. $P^* > 0$ indicates that $2c_1 - c_3 < 0$. Hence, $(-c_1, 0)$ is a stable fixed point. Now, $S^* > 0$ indicates $2c_3 - c_1c_2 < 0$. Therefore, $(0, -c_3/c_2)$ is also a stable fixed point. Finally, as discussed earlier, (S^*, P^*) is a saddle. Thus, we obtain phase portrait 'a' of Fig. 4.8.

For case (ii), $c_1 < 0$ and $c_3 > 0$ indicates that the origin is a saddle. Because $P^* > 0$, $(-c_1, 0)$ is again a stable fixed point. By $S^* > 0$ and $c_2 < 0$, $(0, -c_3/c_2)$ is now an unstable fixed point. Finally, (S^*, P^*) is a saddle. Thus, we obtain phase portrait 'b' of Fig. 4.8.

We have reported the above and upcoming cases with their conditions in Table 4.2. In what follows, we omit detailing stability since it is easy to infer using Tables 4.1 and 4.2.

TABLE 4.2: Conditions and examples of parameter combinations corresponding to phase portraits in Fig. 4.8.

Figure	$c_1 < 0$	$c_2 < 0$	$c_3 < 0$	$2c_3 < c_1c_2$	$2c_1 < c_3$	(c_1, c_2, c_3), e.g.
(a)	✓	×	✓	✓	✓	$(-1, 1/2, -1)$
(b)	✓	✓	×	✓	✓	$(-3, -1, 1)$
(c)	✓	✓	✓	✓	✓	$(-3, -1, -1)$
(d)	✓	×	✓	×	✓	$(-5, 1/2, -1)$
(e)	✓	✓	×	×	✓	$(-1, -1, 1)$
(f)	✓	×	✓	✓	×	$(-1, 1/2, -3)$
(g)	✓	×	×	×	✓	$(-1, 1/2, 1)$
(h)	✓	✓	✓	✓	×	$(-1/4, -1, -1)$
(i)	×	×	✓	✓	×	$(1, 1/2, -1)$
(j)	×	✓	×	×	×	$(1, -1, 1)$
(k)	×	×	×	-	-	$(1, 1/2, 1)$
(l)	×	✓	✓	-	-	$(3, -1, -1)$

4.6.2.2 Three fixed points exist

Because $(-c_1, 0)$ exists when (S^*, P^*) exists, there are two combinations of fixed points that yield phase portraits with three fixed points including the origin: (i) $(-c_1, 0)$ and $(0, -c_3/c_2)$ and (ii) $(-c_1, 0)$ and (S^*, P^*).

For case (i), there are again two cases for $(0, -c_3/c_2)$ to exist: (1a) $c_3 > 0$ and $c_2 < 0$ and (1b) $c_3 < 0$ and $c_2 > 0$. Then, for both of them, there are three cases for (S^*, P^*) not to exist, i.e., $S^* < 0$, $P^* < 0$ or both. Both (S^*, P^*) being negative is unimportant since the physical space is the first quadrant, and the third quadrant can be approached from the second or fourth quadrants, not affecting the system dynamics.

For case (1a), i.e., $c_3 > 0$ and $c_2 < 0$, these cases lead to the following.

1. $S^* < 0$ and $P^* > 0$

   We obtain phase portrait 'e' of Fig. 4.8.

2. $S^* > 0$ and $P^* < 0$

   $2c_1 > c_3$ contradicts $c_1 < 0, c_3 > 0$. Hence, this case is infeasible.

For case (1b), i.e., $c_3 < 0$ and $c_2 > 0$, we obtain the following.

1. $S^* < 0$ and $P^* > 0$

   Phase portrait 'd' of Fig. 4.8 depicts the dynamics.

2. $S^* > 0$ and $P^* < 0$

   We obtain the phase portrait 'f' of Fig. 4.8.

Now, recall case (ii) with fixed points $(-c_1, 0)$ and (S^*, P^*). Here,

$$S^* > 0, \quad P^* > 0 \quad \text{imply} \quad 2c_3 < c_1 c_2, \quad 2c_1 < c_3, \quad \text{respectively.}$$

Now, $(0, -c_3/c_2)$ does not exist in two cases where c_2 and c_3 have the same sign. If both are positive, then $2c_3 < c_1 c_2$ is violated because $c_1 < 0$. The other case then leads to the phase portrait 'c' with a parameter set satisfying

$$c_1 < 0, \quad c_2 < 0, \quad c_3 < 0, \quad 2c_3 < c_1 c_2, \quad 2c_1 < c_3.$$

Thus, we obtain four phase portraits (c-d-e-f) that consist of three fixed points.

4.6.2.3 Two fixed points exist

There are three possibilities as one of the three, i.e., $(-c_1, 0)$, $(0, -c_3/c_2)$ and (S^*, P^*), should exist with the origin. However, (S^*, P^*) does not exist without $(-c_1, 0)$. Hence, there are two possibilities: either $(-c_1, 0)$ or $(0, -c_3/c_2)$ exist.

Depending on the feasibility, we obtain four phase portraits (g-h-i-j) with two fixed points. Complete reasoning for this case is provided in Appendix E to avoid repetitiveness.

4.6.2.4 Single fixed point exists

Only $(0, 0)$ exists. $(-c_1, 0)$ does not exist when $c_1 > 0$. That in turn vanishes (S^*, P^*). The remaining fixed point $(0, -c_3/c_2)$ does not exist when c_2 and c_3 have the same sign.

For positive c_2 and c_3, the origin is a stable fixed point and we obtain phase portrait 'k'. Then, for negative c_2 and c_3, we obtain phase portrait 'l' where the origin is a saddle. Thus, we obtain two phase portraits (k-l) with a single fixed point.

We have obtained twelve feasible phase portraits shown in Fig. 4.8 covering the system dynamics. We next examine the corresponding bifurcation structure.

4.6.3 Understanding the bifurcation structure

To depict the bifurcation scenario, we have arranged phase portraits in Fig. 4.8 in the c_1-c_2 plane such that c_3 decreases as we move away from the origin of the plane. By Eq. (4.69), decrease in c_3 denotes increase in the detuning parameter δ for $\omega > 1$.

In the second quadrant of the c_1-c_2 plane, positive c_3 yields phase portrait 'g': complete stabilization with limit cycle oscillations of a secondary oscillator. Decreasing c_3 to a negative value leads to phase portrait 'd' where a saddle is born on the P-axis. Note that complete stabilization is retained. With further decrease in c_3, we cross $2c_3 = c_1c_2$ and obtain phase portrait 'a', where a saddle on the P-axis has become stable, and a new fixed point (S^*, P^*) has emerged. We obtain conditional stabilization for the primary oscillator: initial conditions inside the basin of attraction for the stable node on the S-axis lead to stabilization. With an even further decrease in c_3, we approach $c_3 = 2c_1$, and the size of the basin of attraction reduces. Upon crossing this boundary, the saddle (S^*, P^*) merges with the stable node on the S-axis, resulting in the phase portrait 'f' where the only stable node available is on the P-axis. The primary oscillator cannot be stabilized now. However, it approaches limit cycle oscillations which has some advantage over the unbounded response of the uncoupled primary oscillator for small detuning. Here, the subcritical bifurcation has changed to supercritical.

We now turn to the third quadrant of the c_1-c_2 plane. For large positive c_3, phase portrait 'e' has a stable node on the S-axis. A saddle on the P-axis limits the stabilization. Hence, we achieve bistability here. As we decrease c_3, we approach $2c_3 = c_1c_2$. Crossing this boundary, a saddle on the P-axis undergoes bifurcation; it becomes unstable and gives birth to a saddle (S^*, P^*). Decreasing c_3 to a negative value, the unstable node on the P-axis merges with the origin, yielding it unstable. The primary system retains bistability. Decreasing c_3 further, we cross $c_3 = 2c_1$ and obtain phase portrait 'h'. The basin of attraction has vanished, leaving no stable node. The system becomes unstable leading to unbounded solutions. Bounded solutions can only be obtained by incorporating self-interruption [114] which has been left for future studies.

For the first and fourth quadrants of the c_1-c_2 plane, we find that a sign change in c_3 causes bifurcation. In the first quadrant, the stable origin loses its stability and the stable node is born on the P-axis. Since the primary oscillator shows a bounded response, the bifurcation is supercritical. In the fourth quadrant, the primary system loses bistability, and the system becomes completely unstable indicating a subcritical bifurcation. Again, bounded solutions require incorporation of self-interruption.

The bifurcation investigation above reveals that the first and second quadrant of the c_1-c_2 plane yield supercritical bifurcation. Hence, the secondary oscillator's parameters should ensure

$$c_2 = 1 - \left(\frac{9\left(\omega^2 - \omega_p^2\right)^4 \bar{\tau}\, \left(\omega^2 - 1\right)^2}{10\beta\, \gamma\, m\omega^{10}} \right) > 0, \tag{4.74}$$

for advantageous performance. Among the phase portraits in the first and second quadrants with $c_3 < 0$, 'd' is the most desirable since it offers complete stabilization. By Table 4.2, corresponding parameter set should satisfy

$$c_1 < 0, c_2 > 0, c_3 < 0, 2c_3 > c_1 c_2, 2c_1 < c_3. \tag{4.75}$$

The next favourable phase portrait is 'a', where conditional stabilization is possible. The condition $2c_3 > c_1 c_2$ is violated here. Note that this corresponds to further incursion in the unstable regime. Then we are left with phase portraits 'f' and 'i'. These two have a similar steady-state response: the primary system approaches a limit cycle, and the secondary oscillator's free response gets quenched. In the next section, we will explore the bifurcation scenario along the complete second stability lobe.

4.7 Dynamics along the complete second stability lobe

Based on our multiple scales analysis presented earlier, which is valid for a segment captured by case-1 in Fig. 4.2 where $\omega > 1$, a choice of $\omega_p = 1.573$ along with $\beta = 1$ ensures $c_2 > 0$ for the portion $\omega > 1$ of the second lobe as shown in Fig. 4.9. Therefore, the bifurcation is supercritical along this segment. As can be seen from Fig. 4.9, c_1 is negative throughout this portion, and hence, the second quadrant of the c_1-c_2 plane in Fig. 4.8 describes the bifurcation structure.

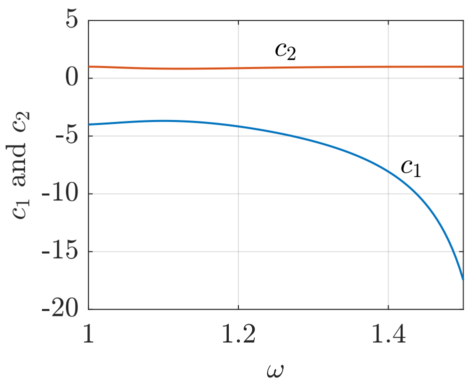

FIGURE 4.9: For $1 < \omega < \omega_p$, $c_1 < 0$ and $c_2 > 0$. Hence, the bifurcation along the case-1 segment of the second lobe is supercritical, and it follows the second quadrant of the c_1-c_2 plane in Fig. 4.8. Here, $\varepsilon = 0.05, m = 1, c = 2, c_v = 2, \beta = 1, \omega_p = 1.573$.

The remaining segment of the second stability lobe in Fig. 4.2 involves cases 3a, 3b and 3c of section 4.3, all of which correspond to $\omega \approx 1$. For those segments, we investigate the bifurcation scenario using the method of multiple scales as elaborated for case-1, but with modified expressions for p and τ. We directly present simplified amplitude evolution equations, omitting details of the analytical treatment for brevity. Note that, for case-2, the primary oscillator provides resonant forcing to the secondary oscillator at the leading order. Hence, corresponding scaling and the multiple scales treatment requires special attention. We do not explore that here. To our benefit, the second lobe is majorly captured by other cases for the present choice of ω_p. Out of which, case-1 is explored earlier and results for the other cases are presented next.

4.7.1 Results for the multiple scales treatment for $\omega \approx 1$

In what follows, R and Q denotes leading order amplitudes as stated in Eqs. (4.46) and (4.47) with $\omega = 1$. Further, the transformed coordinates are

$$P = \frac{R^2}{(\omega_p^2 - 1)^2} \quad \text{and} \quad S = Q^2.$$

Finally, δ denotes corresponding detuning parameter.

4.7.1.1 Case-3a

Recall section 4.3.3.1. We introduce an $\mathcal{O}(\varepsilon)$ detuning in τ; write

$$\tau = \bar{\tau} + \varepsilon\tau_1 + \varepsilon^2\tau_2 + \varepsilon\delta, \tag{4.76}$$

and obtain the final amplitude evolution equations as

$$\frac{\partial S}{\partial T_1} = -\frac{\beta\gamma}{4}\left(S + 2P + c_1\right) S, \tag{4.77}$$

$$\frac{\partial P}{\partial T_2} = -\frac{\beta\,\gamma\,m}{4\left(\omega_p^2 - 1\right)^2}\left(P + 2S + c_3\right) P, \tag{4.78}$$

where

$$c_1 = -\frac{4}{\beta}, \tag{4.79}$$

$$c_3 = -\frac{2\left(m{\omega_p}^2 + 2\,{\omega_p}^2\omega_3 - 2\,\omega_3\right)\left(\omega_p^2 - 1\right)\delta}{\beta\,\gamma\,m}. \tag{4.80}$$

4.7.1.2 Case-3b

Recalling section 4.3.3.2, where $\bar{\tau}$ is indeterminate, we write

$$p = \varepsilon^2 p_2 + \varepsilon^2\delta,$$

and obtain

$$\frac{\partial S}{\partial T_1} = -\frac{\beta\gamma}{4}\left(S + 2P + c_1\right)S, \tag{4.81}$$

$$\frac{\partial P}{\partial T_2} = -\frac{\beta\,\gamma\,m}{4\left(\omega_p^2 - 1\right)^2}\left(P + 2S + c_3\right)P, \tag{4.82}$$

with

$$c_1 = -\frac{4}{\beta}, \tag{4.83}$$

$$c_3 = \frac{4\,\delta\sin(\bar\tau)\left(\omega_p^2 - 1\right)^2}{\beta\,\gamma\,m}. \tag{4.84}$$

4.7.1.3 Case-3c

By section 4.3.3.3, $\bar p$ is indeterminate. We perturb τ; write

$$\tau = \bar\tau + \varepsilon\tau_1 + \varepsilon^2\tau_2 - \varepsilon^2\delta,$$

and obtain

$$\frac{\partial S}{\partial T_1} = -\frac{\beta\gamma}{4}\left(S + 2P + c_1\right)S, \tag{4.85}$$

$$\frac{\partial P}{\partial T_2} = -\frac{\beta\,\gamma\,m}{\left(\bar p^2\bar\tau^2 + 4\right)\left(\omega_p^2 - 1\right)^2}\left(P + 2S + c_3\right)P, \tag{4.86}$$

with

$$c_1 = -\frac{4}{\beta} + \frac{4}{\beta\gamma}\frac{m{\omega_p}^3\bar p\,\sin\left(\omega_p\,\bar\tau\right)}{\left(2\bar p({\omega_p}^2 - \bar p - 1)\cos\left(\omega_p\,\bar\tau\right) + 2\,\bar p^2 + {\omega_p}^4 - 2\,{\omega_p}^2\bar p - 2\,{\omega_p}^2 + 2\,\bar p + 1\right)}, \tag{4.87}$$

$$c_3 = -\frac{4\bar p\,\delta\left(\omega_p^2 - 1\right)^2}{\beta\,\gamma\,m}. \tag{4.88}$$

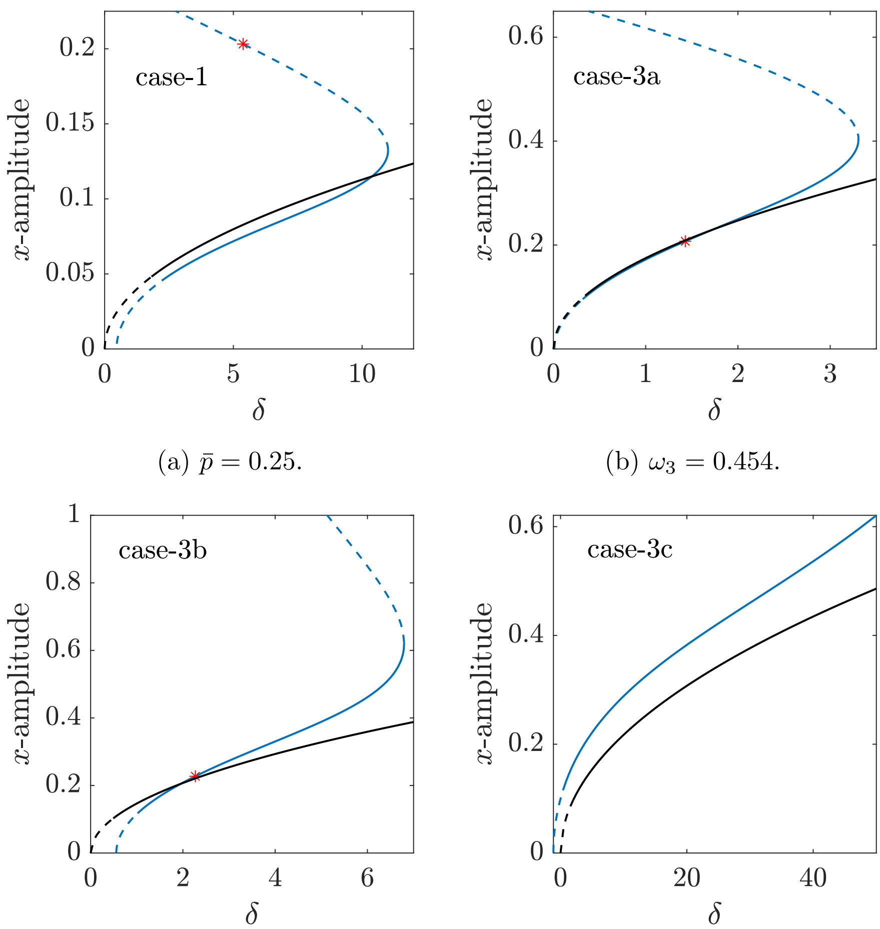

(a) $\bar{p} = 0.25$.

(b) $\omega_3 = 0.454$.

(c) $\bar{\tau} = 10.568$.

(d) $\bar{p} = 0.2$.

FIGURE 4.10: Comparison of bifurcation boundaries obtained using DDE-BIFTOOL [115, 116] (blue) and the multiple scales (black) results for all four cases corresponding to the second stability lobe. Red stars denote the initiation of loss of contact. x-amplitude from a DDE-BIFTOOL result is calculated using a point from the solution trajectory and applying $x = R\sin(\phi)$ and $\dot{x} = R\omega\cos(\phi)$. Parameter values are $\varepsilon = 0.05, m = 1, c = 2, c_v = 2, \beta = 1, \omega_p = 1.573$. For case-1 and case-3b, δ is detuning in p_{cr}. For cases 3a and 3c, δ is detuning in τ_{cr}. See sections 4.3 and 4.7.1 for definitions of some parameters mentioned here.

It can be noted from the above slow flow equations that $c_2 = 1$ for all these cases. Hence, all of them involve a supercritical bifurcation. We next verify these analytical findings by comparing the bifurcation diagrams obtained from the method of multiple scales (blue lines) for all the four cases corresponding to the second stability lobe against bifurcation diagrams obtained using DDE-BIFTOOL [115, 116] (black lines) in Fig. 4.10. Solid and dashed lines represent stable and unstable solutions, respectively. The match for case-1 and case-3a are good. The mismatch for cases 3b and 3c is because of the largeness of $\mathcal{O}(\varepsilon^3)$

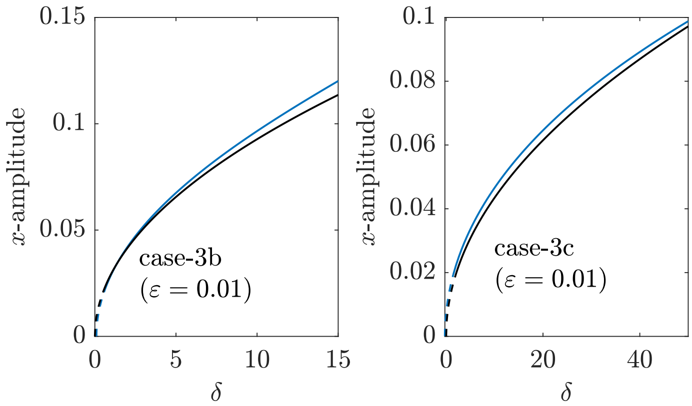

FIGURE 4.11: Comparison of DDE-BIFTOOL [115, 116] (blue) and the multiple scales (black) results for cases 3b and 3c for small ε, demonstrating asymptotic validity of the present analytical results.

correction in the Hopf point. That is evident from the difference in the value of δ at which periodic solution emerges, where DDE-BIFTOOL results are also obtained using $\mathcal{O}(\varepsilon^2)$ approximations of the Hopf points. We present Fig. 4.11 showing the match for cases 3b and 3c for small ε and demonstrate the asymptotic validity of our approximations. The initial unstable solution branch corresponds to the phase portrait 'd', where the primary system is completely stabilized. Note that the supercritical branch turns around and becomes unstable via a turning point bifurcation. Thus, unbounded solutions might exist for large amplitude initial conditions for parameters in the stable regime, indicating bistability. Further, because of this turning point bifurcation, only unbounded solutions exist for large detuning. The present multiple-scale analyses have not captured these aspects. However, solutions above red stars show loss of contact, i.e., negative depth of cut or $x - x_\tau < -\frac{5}{12}$. Before those red stars, where the present analysis is valid, Fig. 4.10 indicates supercritical bifurcation for all cases as indicated by the multiple scales results. As discussed earlier, the solutions above the red star are not correct for the physical system and self-interruption is required to capture the correct behavior which has been left for future work. We next discuss this in detail.

4.7.2 Practical stability boundary for tool chatter along the second lobe

Amplitude evolution equations corresponding to all cases comprising the second stability lobe take the form similar to Eqs. (4.70) and (4.71) obtained for case-1, where supercriticality requires $c_2 > 0$. Interestingly, these equations for cases 3a, 3b and 3c possess $c_2 = 1$; see section 4.7.1. Therefore, the bifurcation is supercritical at corresponding boundaries. Because we have already demonstrated supercriticality for case-1, our analysis establishes supercritical bifurcation along the complete second lobe of Fig. 4.2. Because of the supercriticality, the loss of contact occurs mainly after the Hopf bifurcation. Hence, bistability in the linearly stable regime is completely eliminated. This is an improvement since our current cutting force model is based on the $3/4^{\text{th}}$ power law for which Molnar *et al.* [117] reported bistability till 6.5% below the linear stability boundary. Earlier, Habib *et al.* [62] using NLTVA found supercritical bifurcation for some range of rotational speed and not throughout the stability curve in their study. Their study, however, has the advantage of a higher minimum p for the lobe since the secondary system is tuned and positively damped. In the present study, the advantage gained is the supercriticality over the complete second lobe. For a tuned absorber, cases corresponding to ω close to unity require a separate investigation because the present analysis is not valid when ω is close to ω_p. We discuss this regime later in this chapter using results from DDE-BIFTOOL. Before that, we discuss the stability boundary for our system corresponding to conditional and unconditional appearance of tool chatter which can be viewed as the practical stability boundary of the primary system.

We have shown in Fig. 4.9 that $c_1 < 0$ for case-1. For cases 3a and 3b, $c_1 = -\frac{4}{\beta} < 0$. For case-3c, $\bar{p} = 0.1, 0.2, 0.3$ yield $c_1 = -3.70, -3.373, -3.023$, respectively, for the parameter set considered in the present work with $\bar{\tau} = 4\pi$. This indicates $c_1 < 0$ for case-3c as well. Hence, $c_1 < 0$ for the complete second lobe. Therefore, the bifurcation structure is explained by the second quadrant of the c_1-c_2 plane (Fig. 4.8). Figure 4.12 shows bifurcation boundaries in the τ-p plane for segments of the second lobe corresponding to different cases. Note that we have plotted $\mathcal{O}(\varepsilon^2)$ approximation for the linear stability

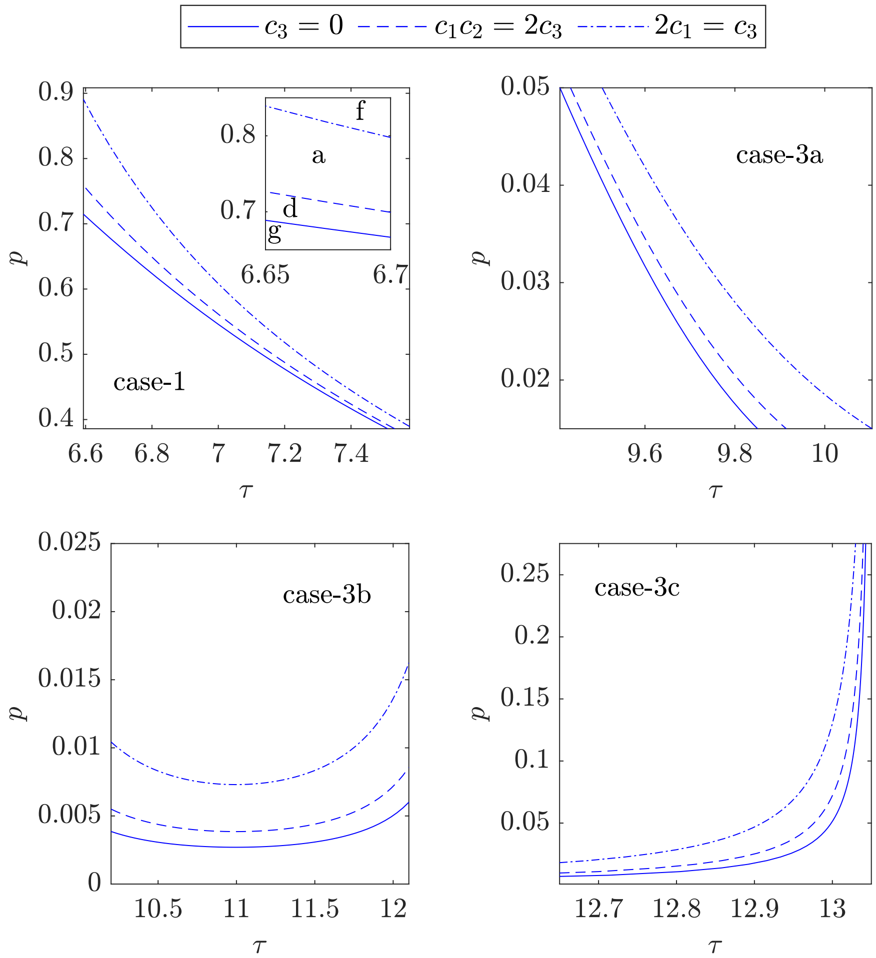

FIGURE 4.12: Bifurcation boundaries near different segments of the second lobe. Labels in the subfigure of case-1 represent phase portraits shown in Fig. 4.8. Other cases follow the identical bifurcation structure. Here, $c_3 = 0$ represents linear stability boundary, where $\mathcal{O}(\varepsilon^2)$ approximations are plotted. Parameter values are $\varepsilon = 0.05, m = 1, c = 2, c_v = 2, \beta = 1, \omega_p = 1.573$.

boundary, i.e., $c_3 = 0$ curve shown by solid line. Labels in the subfigure of case-1 relate to the corresponding phase portraits in Fig. 4.8. $c_1c_2 = 2c_3$ and $2c_1 = c_3$ represent the bifurcation boundaries for the changing tool chatter dynamics for different values of the detuning parameter δ. As mentioned earlier, the bifurcation structure is identical for the other cases, where corresponding boundaries are $c_1 = 2c_3$ and $2c_1 = c_3$ because $c_2 = 1$. We emphasize that after crossing the $c_3 = 0$ curve, the equilibrium of the primary system loses stability but chatter vibrations do not last and the primary system remains stable. In contrast, the uncoupled primary system starts exhibiting large amplitude chatter vibrations immediately after crossing $c_3 = 0$. With a further increase in δ, c_3 becomes more negative and only when we cross the $c_1 c_2 = 2c_3$ boundary, the unstable primary limit cycle becomes stable with the appearance of an unstable (saddle) quasiperiodic solution. Hence, chatter vibrations might appear depending on the initial disturbance and the primary system has conditional stability. Finally, with an even further increase in δ, the $2c_1 = c_3$ boundary is crossed wherein the unstable quasiperiodic solution merges with the stable secondary limit cycle and makes it unstable. This results in the appearance of tool chatter vibrations for any initial disturbance. Note that because of the turning point bifurcation which is not captured in our slow flow equations, unbounded solutions exist for very large detuning requiring incorporation of self-interruption for bounded solutions.

4.7.3 Effect of absorber parameters on criticality of bifurcation

For a supercritical bifurcation, the condition is $c_2 > 0$ which by Eq. (4.68) implies that

$$\frac{9\left(\omega^2-\omega_p^2\right)^4 \bar{\tau}\,\left(\omega^2-1\right)^2}{10\,m\gamma\,\beta\omega^{10}} < 1. \tag{4.89}$$

Recalling that $m\gamma = c_v$, we can note from the above that the linear and nonlinear damping coefficients of the absorber, c_v and βc_v, should be kept high to ensure supercriticality. For higher lobes, i.e., high $\bar{\tau}$, c_v and β required is high as well. Here, higher β helps to use lower c_v denoting lower input energy because c_v is the coefficient of negative damping in the secondary oscillator. Higher β indicates a smaller amplitude limit cycle for the secondary oscillator because the amplitude of the uncoupled secondary oscillator is inversely proportional to $\sqrt{\beta}$. The effect of β on the observed dynamics is best visualized through the $2c_3 = c_1c_2$ boundary. Raising this boundary increases the unconditionally stable regime for the primary system. However, the limit of stabilization of the primary system is decided by the other boundary $2c_1 = c_3$ that turns out to be independent of β.

Figure 4.13 shows regimes of $c_2 > 0$ in the ω_p-ω plane for different parameters. For ω close to unity, Fig. 4.13 recommends low values of ω_p to ensure supercriticality. However, that yields $c_2 < 0$ for large ω. We note that a large ω corresponds to a large p and small

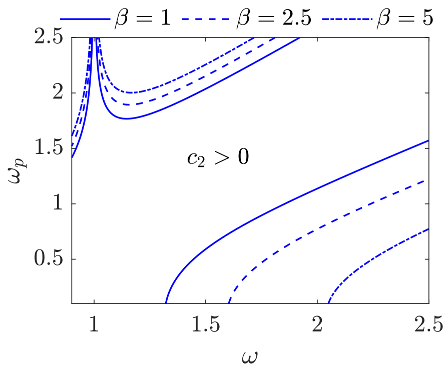

(a)

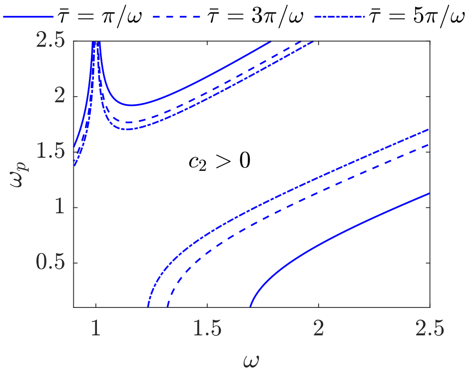

(b)

FIGURE 4.13: Effect of (a) β and (b) $\bar{\tau}$ in ensuring supercriticality ($c_2 > 0$). Other parameter values are $m = 1$, $c = 2$, $c_v = 2$, $\beta = 1$ (for (b)), $\bar{\tau} = 3\pi/\omega$ (for (a)). By the expression of c_2, we understand that m and γ have a similar effect as β.

τ segment of the first stability lobe, i.e., stable high-speed operation. A large ω_p provides $c_2 > 0$ for large ω. However, for the range of ω corresponding to the second stability lobe, i.e., approximately $1 < \omega < 1.5$, a large ω_p yields $c_2 < 0$ for a large portion of the stability boundary and hence, not recommended. Here, the band of ω_p close to 1.4 is the most appropriate to obtain supercriticality over the complete second lobe. Figure 4.13(a) shows that an increase in β enlarges the regime for $c_2 > 0$, indicating an increase in the bandwidth of permissible ω_p. Recalling the expression for c_2 in Eq. (4.68), m and γ have a similar effect as β. Hence, to allow a wider bandwidth of ω_p, m and γ can be increased as well. Figure 4.13(b) shows the effect of $\bar{\tau}$. For the higher lobe, the $c_2 > 0$ regime shrinks. However, the corresponding range of ω for the higher stability lobes also decreases. By Fig. 4.13(b), ω_p close to 1.4 or slightly lower than that will continue to provide supercriticality over the complete boundary for higher lobes as well.

For completeness, we present contours of $c_1 = 0$ for case-1 in Fig. 4.14 to observe the effect of various parameters on regimes of positive and negative c_1. Here, $\omega_p = \omega$ is a common boundary independent of other parameters. Figure 4.14(a) shows that new regimes of $c_1 > 0$ emerge with an increase in m. Figure 4.14(b) shows that an increase in γ shrinks the regime near $\omega_p = \omega$ with a new loop emerging near $\omega = 1.5$. Finally, Fig. 4.14(c) shows $c_1 > 0$ regimes for different lobes. We observe that, for higher lobes, $c_1 > 0$ regime near $\omega_p = \omega$ shrinks slightly differently than in subplot (b), and new branches have emerged as

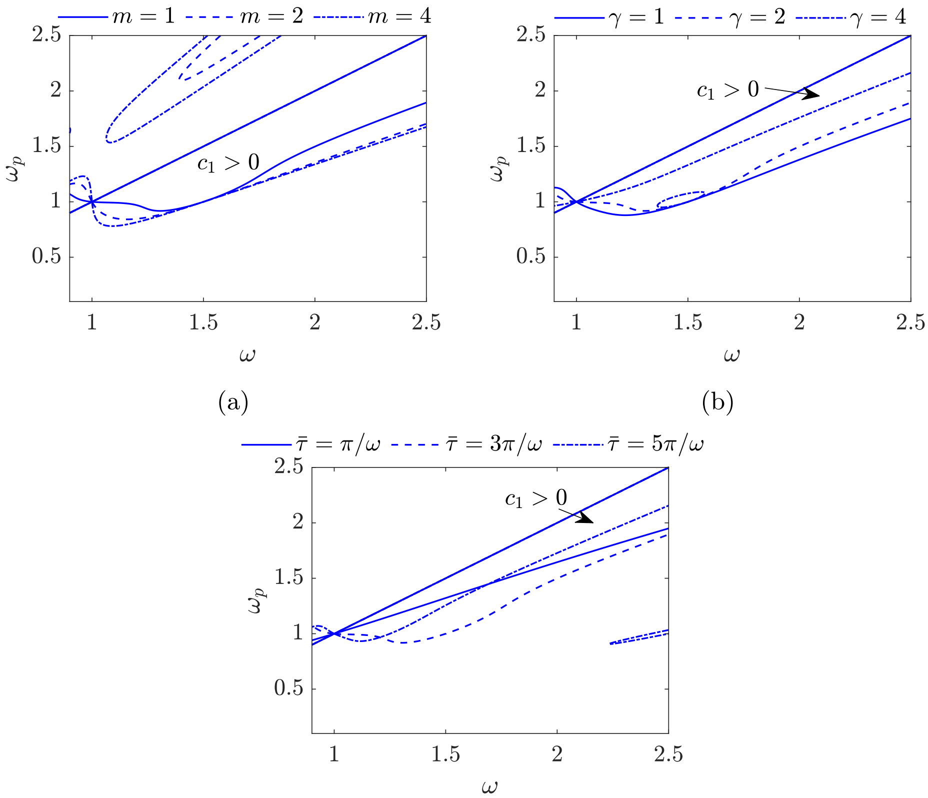

(c)

FIGURE 4.14: Effect of (a) m, (b) γ and (c) $\bar{\tau}$ on c_1. Other parameter values are $m = 1$, $c = 2$, $c_v = 2$, $\beta = 1$, $\bar{\tau} = 3\pi/\omega$ wherever kept constant.

well. Finally, by Eq. (4.67), $c_1 = 0$ contours are independent of β. Figures 4.13 and 4.14 are useful to associate parameter regimes with different dynamics presented in the c_1-c_2 plane in Fig. 4.8.

Finally, the expression for c_2 in terms of dimensional parameters is worth mentioning. Using Eqs. (4.7) and (4.10), Eq. (4.68) can be written as

$$c_2 = 1 - \left(\frac{5(2N+1)\pi M \left(\Omega^2 - \Omega_p^2\right)^4 \left(\Omega^2 - \omega_n^2\right)^2}{32 f_0^2 \bar{\beta}\, \bar{c}_v \Omega^{11}} \right), \tag{4.90}$$

where Ω and Ω_p denote the (dimensional) Hopf frequency and the secondary oscillator's (dimensional) natural frequency, respectively. From the above equation, a higher value of the product $\bar{\beta}\bar{c}_v$ is recommended to obtain supercriticality. Further, for lower M and N (lobe number) and higher f_0, the requirement on the product is lighter. Finally, the effect of Ω_p is the same as that of the nondimensional frequency ω_p because of the identical form in the expression.

4.7.4 Tuning and other regimes of operation

In the preceding sections, we have elaborated dynamics for a nonresonant absorber with a stable limit cycle response, and demonstrated supercriticality over the complete second lobe. However, as shown in Fig. 4.15, a tuned absorber offers a significantly larger minimum p in the linear stability curve. Here, ω and ω_p are close to unity, which makes the presented multiple scales analysis invalid. Therefore, we present numerical results for the machine tool system with a nonlinear tuned absorber.

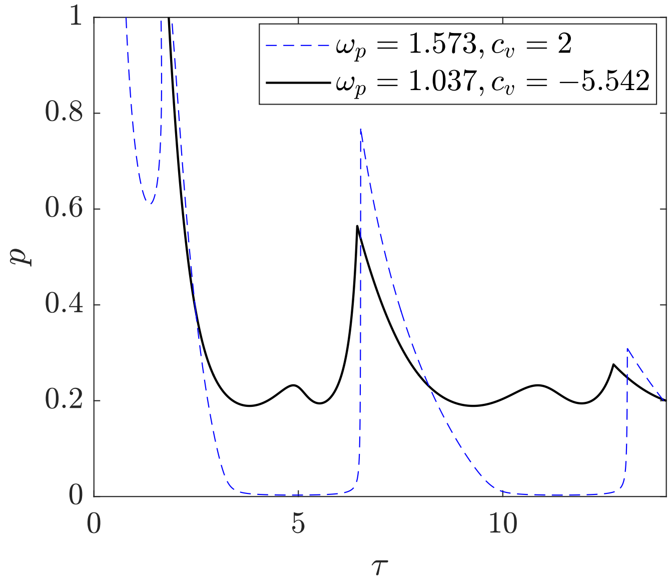

FIGURE 4.15: Stability curves for the system with tuned positively damped (solid black) and untuned negatively damped (dotted blue) absorbers. $c_v < 0$ denotes a positively damped absorber. Parameter values are $\varepsilon = 0.05, m = 1, c = 2$.

A nonlinear tuned absorber is linearly positively damped, i.e., $c_v < 0$. Depending on the sign of nonlinear damping coefficient β, the absorber provides different responses:

1. c_v and β both positive: stable limit cycle response,

2. c_v negative and β positive: unstable limit cycle response,

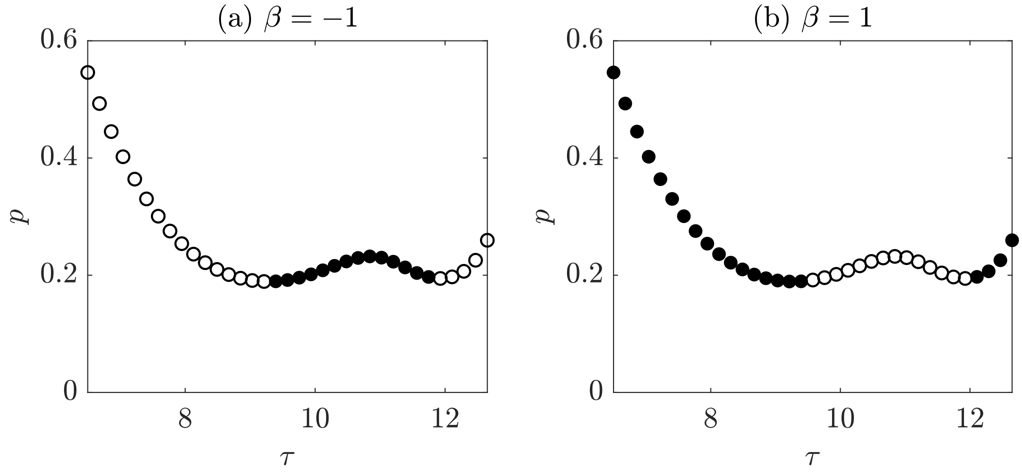

FIGURE 4.16: Nature of bifurcation along the second lobe for a nonlinear tuned absorber: open circles denote supercritical bifurcation and solid circles denote subcritical bifurcation. Parameter values are $\varepsilon = 0.05, m = 1, c = 2, c_v = -5.542, \omega_p = 1.037$.

3. c_v and β both negative: globally stable origin,

4. c_v positive and β negative: unstable origin and destabilizing nonlinear damping.

We explore bifurcation scenarios for the tuned absorber with positive or negative β, hence, exhibiting an unstable limit cycle or globally stable origin. Figure 4.16(a) shows the nature of bifurcation along the second stability lobe with stabilizing nonlinear damping, i.e., $\beta < 0$ or globally stable origin. We generated the figure using the DDE-BIFTOOL package by observing a small-amplitude periodic solution near the Hopf point. If the solution occurs beyond the Hopf point, the bifurcation is supercritical. In the figure, open circles denote supercritical bifurcation, and solid circles denote subcritical bifurcation. By Fig. 4.16(a), we observe that a segment in the middle of the lobe exhibits subcritical bifurcation. Figure 4.16(b) shows that $\beta > 0$ yields supercritical bifurcation for that segment, where $\beta > 0$ denotes destabilizing nonlinear damping or unstable limit cycle response of the secondary oscillator. Thus, the present system, when tuned, can offer supercriticality using stabilizing or destabilizing nonlinear damping. Further, we numerically observe that small $\beta > 0$ helps to eliminate bistability in the case of an unstable limit cycle oscillator. Here, a large amplitude stable limit cycle can be added surrounding the unstable limit cycle to limit unbounded responses, forming a double limit cycle oscillator as our nonlinear vibration absorber. Further, for negative β, varying ω_p shifts the subcritical segment of the tuned stability lobe as shown in Fig. 4.17, where increasing (decreasing) ω_p from the tuned value shifts that segment to the left (right). Hence, for ω_p far away from the tuned frequency, that segment can be shifted beyond the corresponding double Hopf point, resulting in supercritical bifurcation for the complete second lobe. Note that varying $\beta < 0$ does not shift that segment as we have used $\beta = -2$ in Fig. 4.17 and $\beta = -1$ in Fig. 4.16(a). Further, by Fig. 4.17, the effect of frequency ratio on the stability lobe is clearly seen, i.e., the second lobe shifts to the right with an increase in ω_p.

To summarize, the untuned case can offer supercriticality for the complete second lobe, and the tuned positively damped case can offer a better linear stability boundary with different requirements for supercriticality along the curve. Thus, an optimization problem can be set up to find the absorber parameters that yield a larger minimum p in the stability curve and supercritical bifurcation along the complete lobe. We leave that analysis for future work.

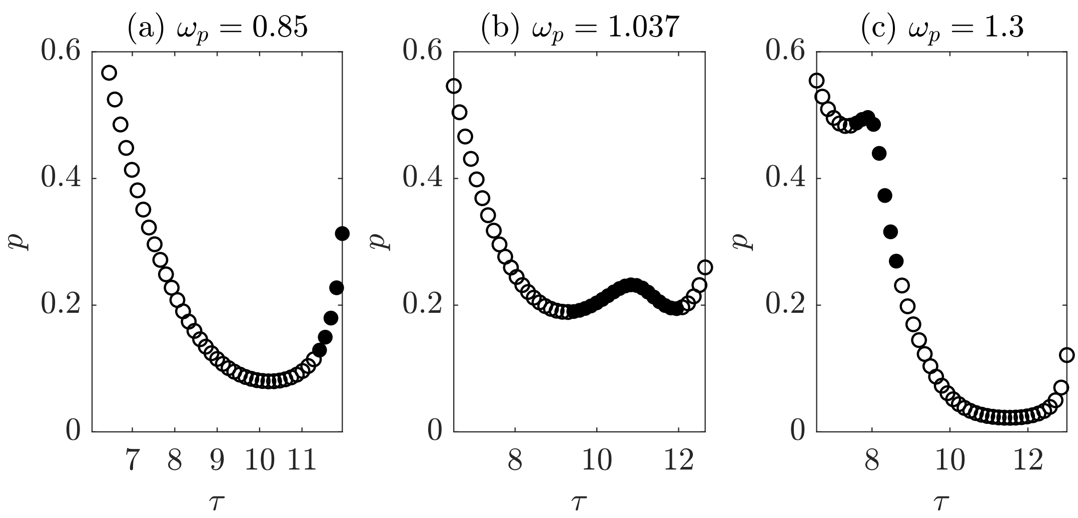

FIGURE 4.17: Nature of bifurcation along the second lobe for absorbers with different ω_p. Open circles denote supercritical bifurcation, and solid circles denote subcritical bifurcation. Parameter values are $\varepsilon = 0.05, m = 1, c = 2, c_v = -5.542, \beta = -2$.

We note that a friction-induced vibration oscillator (with an exponential friction model) can offer the above-mentioned regimes of operation, namely, stable limit cycle response, globally stable trivial solution and a double limit cycle response. Such *potential* limit cycle oscillators can be used to realize the results revealed in this study. We close the discussion by pointing out that $\mathcal{O}(\varepsilon^2)$ solution X_1 in a stable regime may cause slight dissatisfaction with the surface finish of a machined product. Future studies may shed some light on such aspects. In view of the present study, the possibility of supercriticality eliminating bistability in the linearly stable regime, offered by the use of a light, untuned limit cycle oscillator, may attract the research community working on chatter suppression.

4.8 Conclusions

In light of suppressing regenerative chatter vibrations, we have studied the nonlinear dynamics of a primary machine tool system coupled with a secondary light and nonresonant limit cycle oscillator. The attached system does not require precise tuning because of the nonresonant characteristic. Using numerics, we demonstrated post-bifurcation bounded responses of the primary oscillator, indicating supercritical bifurcation. Using the DDE-BIFTOOL Matlab package, we showed that the present system with a typical parameter set shows supercritical bifurcation compared to subcritical bifurcation for a system with a TMD. To understand the complete bifurcation scenario, we used a second-order approximation of a Hopf point and applied the method of multiple scales. Amplitude evolution equations decouple from the relative phase because of the nonresonant characteristic. Therefore, the analysis is reduced to that of a two-dimensional ODE from that of the infinite-dimensional delay differential equation. That system of ODEs is further simplified using a transformation where we find that essentially three parameters, c_1, c_2 and c_3, govern the system dynamics. These parameters are functions of system parameters, including the frequency ω corresponding to a Hopf bifurcation. We explore the final simplified system and find corresponding fixed points, their stability and twelve feasible phase portraits. The bifurcation scenario is pictured by observing the phase portraits and corresponding conditions. We find that $c_2 > 0$ provides supercritical bifurcation. For the frequency ratio $\omega_p = 1.573$, a nonresonant value, we find that supercriticality ($c_2 > 0$) is offered for the complete second lobe. The expression for c_2 shows that a higher negative damping parameter c_v helps in attaining $c_2 > 0$. The parameter governing nonlinear damping β plays an important role in raising the unconditional stability limit post-bifurcation. However, the final boundary indicating supercritical bifurcation is found to be independent of β. Finally, we note that the stable branch emerged by supercritical bifurcation turns around via turning point bifurcation, resulting in a larger amplitude unstable branch and leaving no stable solution for higher detuning. However, loss of contact may occur before the turned branch enters the stable regime. That will completely eliminate the bistability in the linearly stable regime.

We note that the limit cycle oscillator operating in regime-2 possessing a double limit cycle might provide an even richer set of possible system behavior and that study has been left for future work. Instead, we now focus on an alternate case of a nonresonant interaction in a parametrically excited system where the frequency of excitation and the natural frequency of the system are nonresonant. Note that such a situation is encountered in a real quadrupole ion trap, where two frequencies involved are: a parametric forcing frequency and an ion's secular frequency.

Chapter 5

Quadrupole ion trap with dipolar DC excitation: Motivation, nonlinear dynamics, and simple formulas

In this chapter, we study nonresonant interactions relevant to the dynamics of a trapped ion in a mass spectrometer under the action of both the usual quadrupolar RF as well as dipolar DC excitation. The relevant governing equation, derived from electrostatic field calculations for realistic geometries, is an inhomogeneous Mathieu equation with a constant along with a quadratic term on the right hand side. Here, two frequencies involved are the frequency of the parametric forcing and the secular frequency characterizing the ion. When these frequencies have no special rational relationship, a nonresonant scenario arises, which is the primary interest in this thesis.

An early paper by Plass [7] examined the case without the quadratic term using variation of parameters. Here we note a significantly simpler particular solution than used by Plass, include the quadratic term, and develop a second order averaging based approximation, where we do not assume any resonance and consider (nondimensional) secular frequencies away from 1, 2/3, etc. The averaging results show that a particular underlying simple periodic solution is stable. We then show that a two-frequency approximation matches that solution well for practical purposes. Finally, we present and validate an easy iterative calculation for obtaining that two-frequency solution, and quantify the effect of the quadratic nonlinearity. This study has been published as [85].

I acknowledge Prof. A. K. Mohanty for his contributions to this chapter. Specifically, for writing sections 5.1, 5.2 and 5.4; performing BEM and other calculations; and preparing figures in these sections. These portions are included in this thesis for completeness, because they also appear in [85]. My own academic contribution to this work is given primarily in section 5.3.

5.1 Introduction

In this chapter, we study ion dynamics in an ion trap mass spectrometer with hyperboloid shaped electrodes with a combination of quadrupolar RF and dipolar DC excitation. In particular, the addition of dipolar excitation introduces interesting and useful new behavior in the ion dynamics.

The earliest ion trap mass spectrometers [124, 125] used only quadrupolar excitation. Both the endcaps of the quadrupole ion trap were grounded in such instruments. Subsequently, dipolar AC excitation [124] was used for resonance ejection. This resulted in higher resolution in the mass spectrum. More recently, dipolar DC excitation (DDC) has been used to provide enhanced functionalities in ion trap mass spectrometers. The two main uses of dipolar DC excitation are collision induced dissociation (CID) and DC tomography [7, 126–128].

In CID, as demonstrated by Lammert, Cooks, and coworkers, a dipolar DC voltage is used to move the trapped ion cloud away from the trapping centre, thereby increasing significantly the amplitude of micromotion and the kinetic energy of each ion. This allows the collisions involving the trapped ions to cause greater dissociation of the ions and neutral molecules into ion fragments that are of analytical interest. More recently McLuckey and coworkers [129–134] have used CID for detailed mass analysis of biomolecules.

In DC tomography, the increased amplitude of micromotion caused by a dipolar DC field raises the effective temperature of ions. This allows the selective ejection of certain species [135–137] of ions to enhance the sensitivity of ion detection.

A mathematical treatment of dipolar DC excitation has been given by Plass [7] using Mathieu functions. The present work aims to add to the mathematical understanding of dipolar DC excitation in two ways. First, Plass only examines the case of a constant dipolar field. In reality, the dipolar field has a significant quadratic component which is explicitly taken into account in the present work. Second, even for a constant dipolar field, which results in a Mathieu equation with a constant right hand side, there is a simple periodic solution that has no secular frequency component. Plass does not notice this simpler choice of particular solution. This periodic solution leads to simplified formulae for practical DDC calculations.

5.2 Governing equation from ion trap theory

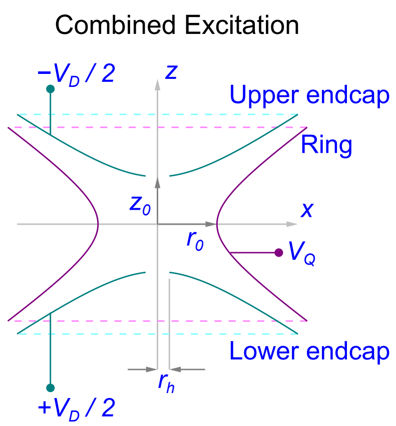

FIGURE 5.1: Cross section of an axisymmetric QIT with combined quadrupolar and dipolar excitations.

A truncated Quadrupole Ion Trap (QIT) [124, 125] is shown in Fig. 5.1. There are holes in the endcaps for the introduction of the analyte and the exit of the ions. The parameters r_0 and z_0 determine the size of the trap. The hole radius r_h is small compared to r_0. Even though a practical QIT must be truncated and must have holes in the endcaps, for simplest understanding the QIT can be regarded as being defined by the two distances r_0, and z_0. It is often the case that $z_0 = r_0/\sqrt{2}$, but as Knight [138] has pointed out, this is not strictly necessary. The quantity $\mathcal{A} = z_0/r_0$ is called the *aspect ratio* of the QIT in the present work. In addition to the usual quadrupolar excitation required for trapping, there is provision for DC dipolar excitation.

5.2.1 Quadrupolar field

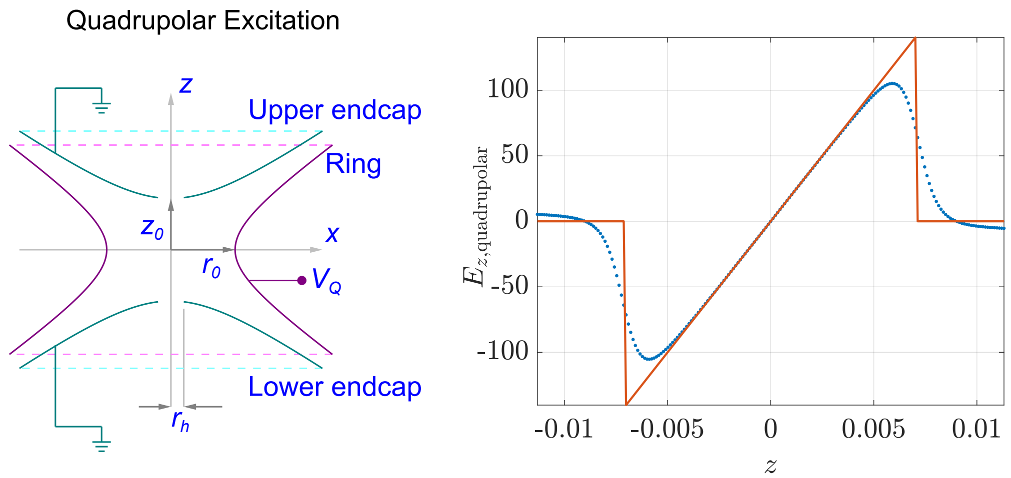

(a) (b)

FIGURE 5.2: (a) Outline of a QIT with quadrupolar excitation. (b) E_z in a QIT with unit quadrupolar excitation.

For the quadrupolar excitation shown in Fig. 5.2(a), the z component of the electric field on the z axis is of the form

$$E_{z,\mathrm{Q}}(z) = V_{\mathrm{Q}} e_{z,\mathrm{Q}}(z), \tag{5.1}$$

where $e_{z,\mathrm{Q}}$ for the QIT with hole has been computed numerically using the Boundary Element Method (BEM) [139]. It is plotted as the dotted curve in Fig. 5.2(b). In the absence of the hole, and with no truncation, it would have been of the form [124]

$$e_{z,\mathrm{Q}}(z) = \begin{cases} \dfrac{4z}{r_0^2 + 2z_0^2} & \text{if } |z| < z_0, \\ 0 & \text{if } |z| > z_0. \end{cases} \tag{5.2}$$

The *ideal* $e_{z,\mathrm{Q}}$ is plotted as the solid curve in Fig. 5.2(b).

The quadrupolar excitation is of the form

$$V_\mathrm{Q} = U_\mathrm{DC} + V_\mathrm{RF}\cos(\omega t).$$

Here $\omega = 2\pi f$, f being the quadrupolar drive frequency.

5.2.2 Dipolar field

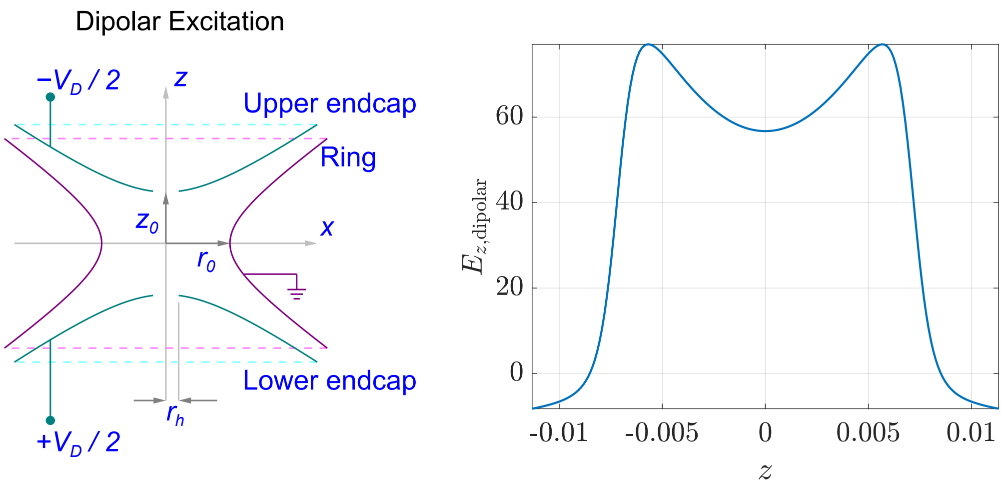

(a) (b)

FIGURE 5.3: (a) Outline of a QIT with dipolar excitation. (b) E_z in a QIT with unit dipolar excitation.

Unlike Eq. (5.2) which describes the E_z due to quadrupolar excitation, there is no simple formula for the E_z due to dipolar excitation. A numerical investigation using the BEM is used to characterize the dipolar field. For a QIT with $r_0 = 1$ cm, and $z_0 = r_0/\sqrt{2}$, Fig. 5.3(b) shows the dipolar field per unit potential. It shows that the dipolar field is not

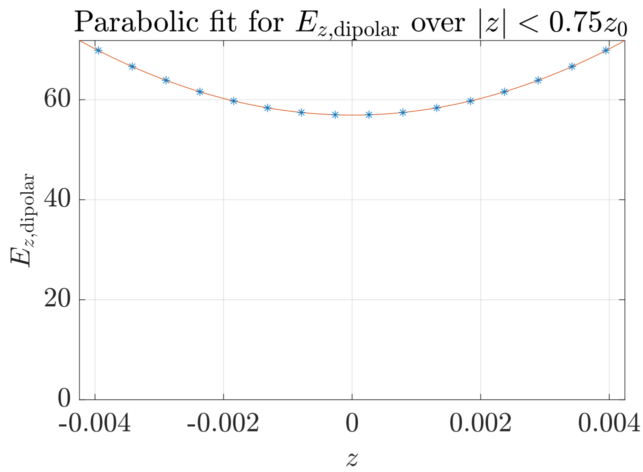

FIGURE 5.4: Comparison of the quadratic fit of Eq. (5.3) with the original dipolar E_z over $|z| < 0.75z_0$.

constant as z changes. Close to the trapping centre, the field has approximately parabolic variation. As Fig. 5.4 shows, for $|z| < 0.75z_0$, the dipolar field per unit potential can be approximated very well by a quadratic in z,

$$E_{z,\mathrm{D}}(z) = V_{\mathrm{D}} e_{z,\mathrm{D}}(z),$$

where dimensional analysis shows that $e_{z,\mathrm{D}}(z)$, the dipolar field per unit potential, must be of the form

$$e_{z,\mathrm{D}}(z) \approx \frac{\psi}{2z_0}\left[1 + \kappa\left(\frac{z}{z_0}\right)^2\right], \tag{5.3}$$

where again, ψ and κ are dimensionless numbers that depend only on the aspect ratio $\mathcal{A} = z_0/r_0$. For the commonly used aspect ratio $\mathcal{A} = z_0/r_0 = 1/\sqrt{2}$, a least-squares fit over $|z| \leq 0.75z_0$ yields $\psi = 0.80527$ and $\kappa = 0.72939$. For other aspect ratios the same process can be used to determine ψ and κ.

For the range of aspect ratios $0.4 \leq \mathcal{A} \leq 1.0$, which is likely to cover all practical QITs, ψ and κ can be calculated with error magnitudes less than 10^{-4} by the following expressions that were obtained by degree least-squares fits:

$$\psi \approx -0.029372\mathcal{A}^4 + 0.328635\mathcal{A}^3 - 0.761063\mathcal{A}^2 + 0.364329\mathcal{A} + 0.819347,$$

and

$$\kappa \approx 0.1279\mathcal{A}^4 - 1.1164\mathcal{A}^3 + 3.2222\mathcal{A}^2 - 1.7530\mathcal{A} + 0.7206.$$

Figures 5.5(a) and 5.5(b) show the validity of these fits against ψ and κ values obtained by accurate BEM calculations.

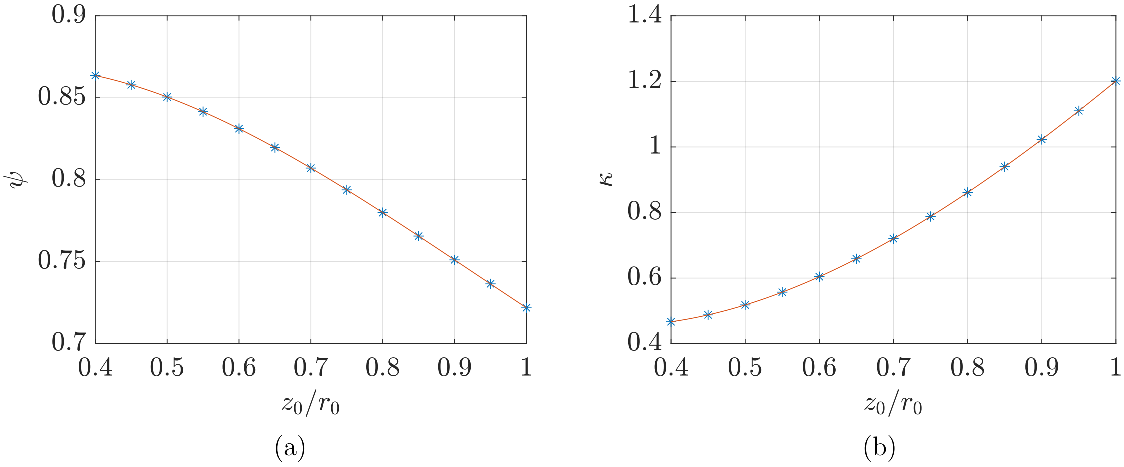

FIGURE 5.5: (a) ψ as a function of the aspect ratio z_0/r_0. (b) κ as a function of the aspect ratio z_0/r_0.

5.2.3 Governing equation

For completeness, and for the interest of a general reader, the governing equation for axial motion of an ion in a trap is now presented.

The equation of motion for an ion on the z axis is

$$m\frac{\mathrm{d}^2 z}{\mathrm{d}t^2} = QE_z(z) = Q\left(V_{\mathrm{Q}}e_{z,\mathrm{Q}}(z) + V_{\mathrm{D}}e_{z,\mathrm{D}}(z)\right), \tag{5.4}$$

where m is the mass of the ion and Q its charge. $E_z(z)$, the electric field on the z axis, can be expressed as a sum of the quadrupolar and dipolar contributions. In the interval

$|z| < 0.75z_0$, we use the quadratic approximation for the dipolar field.

$$E_z(z) = V_{\mathrm{Q}} e_{z,\mathrm{Q}}(z) + V_{\mathrm{D}} e_{z,\mathrm{D}}(z) = \left[U_{\mathrm{DC}} + V_{\mathrm{RF}}\cos(\omega t)\right] \frac{4z}{r_0^2 + 2z_0^2} + V_{\mathrm{D}} \frac{\psi}{2z_0}\left[1 + \kappa\left(\frac{z}{z_0}\right)^2\right]. \quad (5.5)$$

Substituting Eq. (5.5) in Eq. (5.4), dividing both sides by m, and moving the quadrupolar, i.e., linear part to the left hand side, we obtain

$$\frac{\mathrm{d}^2 z}{\mathrm{d}t^2} - \frac{Q}{m}\left[U_{\mathrm{DC}} + V_{\mathrm{RF}}\cos(\omega t)\right]\frac{4z}{r_0^2 + 2z_0^2} = \frac{Q}{m} V_{\mathrm{D}} \frac{\psi}{2z_0}\left[1 + \kappa\left(\frac{z}{z_0}\right)^2\right]. \quad (5.6)$$

To transform the left hand side to the Mathieu form, we use the independent variable

$$\xi = \frac{\omega t}{2},$$

yielding

$$\frac{\mathrm{d}^2 z}{\mathrm{d}\xi^2} + \left[-\frac{16QU_{\mathrm{DC}}}{m(r_0^2 + 2z_0^2)\omega^2} - 2\frac{8QV_{\mathrm{RF}}}{m(r_0^2 + 2z_0^2)\omega^2}\cos(2\xi)\right] z = \frac{2QV_{\mathrm{D}}}{m z_0 \omega^2}\psi\left[1 + \kappa\left(\frac{z}{z_0}\right)^2\right]. \quad (5.7)$$

The coefficient of z in the LHS can be written in the form $(a - 2q\cos(2\xi))$, if one uses

$$a = -\frac{16QU_{\mathrm{DC}}}{m(r_0^2 + 2z_0^2)\omega^2}$$

and

$$q = \frac{8QV_{\mathrm{RF}}}{m(r_0^2 + 2z_0^2)\omega^2}.$$

Then Eq. (5.7) can be written in terms of the Mathieu parameters a and q as

$$\frac{\mathrm{d}^2 z}{\mathrm{d}\xi^2} + [a - 2q\cos(2\xi)]z = \frac{2QV_{\mathrm{D}}}{m z_0 \omega^2}\psi\left[1 + \kappa\left(\frac{z}{z_0}\right)^2\right]. \quad (5.8)$$

The LHS is now in the form of a standard Mathieu equation. The RHS has a quadratic dependence on z. Since the LHS has the dimension of length, the term $\dfrac{2QV_{\mathrm{D}}}{mz_0\omega^2}$ on the RHS also has the dimension of length. Dividing both sides of Eq. (5.8) by z_0, one obtains,

$$\frac{\mathrm{d}^2\zeta}{\mathrm{d}\xi^2} + [a - 2q\cos(2\xi)]\zeta = \frac{2QV_{\mathrm{D}}}{mz_0^2\omega^2}\psi(1+\kappa\zeta^2), \tag{5.9}$$

where

$$\zeta = \frac{z}{z_0}.$$

Now the term $\dfrac{2QV_{\mathrm{D}}}{mz_0^2\omega^2}$ is dimensionless. Let

$$\mu = \frac{2QV_{\mathrm{D}}}{mz_0^2\omega^2}\psi,$$

so that

$$\frac{\mathrm{d}^2\zeta}{\mathrm{d}\xi^2} + [a - 2q\cos(2\xi)]\zeta = \mu(1+\kappa\zeta^2). \tag{5.10}$$

We now have a nonlinear inhmogeneous Mathieu equation with a quadratic right hand side (RHS). All quantities appearing in this equation, namely ζ, ξ, a, q, μ, and κ, are dimensionless. While it may be possible to discuss Eq. (5.10) for $|\zeta| > 1$, only the range $|\zeta| < 1$, or even $|\zeta| < 0.75$, is of practical interest in connection with DC dipolar excitation. This is because the holes in the endcaps weaken the field significantly beyond $|\zeta| > 0.75$.

With this motivation, we proceed with an analysis of Eq. (5.10).

5.3 Analytical treatment

As mentioned earlier, the two foregoing sections were primarily written by Prof. A. K. Mohanty. My own contribution to this work begins here.

We will examine the dynamics of Eq. (5.10) using the method of higher order averaging [140]. Technically, because we work out the solutions using truncated series at each order, this is an approximate implementation of higher order averaging. However, because the series expansions converge rapidly, it will be seen that the approximation is very good and numerical solutions will show an excellent match.

For reasons of familiarity, we replace the nonlinearity coefficient κ with a small bookkeeping parameter ε. We then introduce an even smaller damping term, of $\mathcal{O}(\varepsilon^2)$, through an $\mathcal{O}(1)$ parameter η to obtain

$$\zeta'' + \varepsilon^2 \eta \zeta' - 2q\cos(2\xi)\zeta = \mu\left(1 + \varepsilon\zeta^2\right), \tag{5.11}$$

where prime ($'$) denotes differentiation with respect to ξ. Here, we consider $a = 0$ and take q to be $\mathcal{O}(1)$ and nonresonant (the meaning of “nonresonant” will be clear below). Selection of the other parameter μ will be presented later in this section. At this point, we observe that the $\varepsilon = 0$ or unperturbed equation is an inhomogeneous Mathieu equation with a constant right hand side; at first order in ε there is a quadratic nonlinearity that is not parametrically forced; and at second order in ε we have a small amount of damping intended to reveal steady state behavior.

5.3.1 Relevant literature

Perturbation analyses of weakly nonlinear homogeneous Mathieu equations have regularly appeared in nonlinear vibrations literature. We review some related articles below, and point out ways in which our analysis has new elements.

If the amplitude of the parametric term in the Mathieu equation is small, i.e., q is small, then direct application of perturbation methods is routine [70–72]. Notable among such papers, using the method of multiple scales, Zavodney and Nayfeh [70] studied a damped single-degree-of-freedom (SDOF) system with a small parametric term and quadratic and cubic nonlinearities near the fundamental parametric resonance. They found that the parametric excitation and the damping should be higher and lower than their respective threshold values to excite the resonance; some other aspects of the dynamics were studied and bifurcation diagrams were provided. In the MEMS area, Rhoads *et al.* [71] studied a damped, parametrically excited system with a cubic nonlinearity. Averaged equations near the principal parametric resonance were found, and stability and bifurcations of steady state solutions were examined using frequency response curves. Younesian *et al.* [72] listed several studies of the Mathieu equation published between 1993 to 2003, and not all of those papers had small q; the papers therein which had large q will be discussed separately below. Here we note that Younesian *et al.*'s own study of periodic solutions was of a generalized Mathieu equation with small q.

The above studies deal with nonlinear and homogeneous, or *unforced*, Mathieu equations. Nonlinear inhomogeneous Mathieu equations arise due to external forcing. For example, the effects of external periodic forcing, with various nonlinearities and resonant interactions, were studied in [73–75]. We note that these studies also consider small q, and the unperturbed equation was a simple harmonic oscillator in [74] and a periodically but nonresonantly forced harmonic oscillator in [73, 75].

In contrast to the abovementioned studies with periodic excitation, our system has a constant inhomogeneous term. In that context, we note [76] and [77]. In [76], there was an inhomogeneous term, the system was piecewise linear, and the amplitude of parametric excitation was small (i.e., small q again). Li *et al.* [77] presented an offbeat approximation technique, a variant of the usual variation of parameters, for the linear Mathieu equation with external periodic plus constant forcing. Their approach is difficult to generalize to nonlinear systems. Moreover, it struggles when the magnitude of the parametric excitation (i.e., our q) is large.

We now consider situations where the parametric forcing amplitude (our q) is not small. Considering periodic solutions alone, Sevugarajan and Menon [78] used harmonic balance approximations to seek transition curves of a nonlinear homogeneous Mathieu equation wherein q is not small. We also mention here the work of Esmailzadeh and Nakhaie-jazar [79], from the references given in [72]. This work [79] focused on periodic solutions of the Mathieu-Duffing oscillator. In contrast to these two works, studies of the transient dynamics of such weakly nonlinear systems typically use some version of either averaging or multiple scales. Expansions using periodic functions can be used for developing good approximations in such cases, as initially presented in [80]. Applications to parameter regimes relevant to mass spectrometers were presented before in [81–83]. In [81, 82], the approximate averaging calculation was carried out to first order only; attention was paid to near-resonant situations; q was not small; and the nonlinearity was small. In [81], external periodic forcing was included as well. Rajanbabu *et al.* [83] applied similar series-aided multiple scales calculations up to second order to elucidate ion dynamics near a stability boundary (i.e., near-resonant) [141]. In their work the nonlinearity was small, but q was not small; and the unperturbed equation was homogeneous.

We mention the works of Mahmoud [142, 143], of which the first paper studies small q, but the second one treats a homogeneous but strongly nonlinear Mathieu equation (i.e., large q) to obtain periodic solutions using a modified version of his generalized averaging[1] method [144]. As emphasized above, we include nonhomogeneous terms, have weak nonlinearity, and study transient motions.

We close this literature review by noting two more papers, [145] and [146]. In these works, an externally forced, damped Mathieu oscillator with, respectively, cubic and quadratic plus cubic nonlinearities, was examined using the method of varying amplitudes (see footnote 1). The method is similar to the harmonic balance method except that the coefficients therein are considered time-dependent. Additionally, in [145], q was assumed small within perturbation solutions that were used to compare with the corresponding "new" solutions proposed in the paper.

As is clear from the foregoing survey of the literature, there is no formal averaging-based or similar analysis of a weakly nonlinear Mathieu equation with a constant inhomogeneous term and large q. In [81, 82], there was analysis that is similar to ours, except we have the inhomogeneous term with a specific mass-spectrometric application in mind; and we carry the calculation out to more terms in the expansion and up to second order in the expansion parameter. As will be seen below, the final approximation results we obtain

[1] Such methods, which do not require the expansion parameter to be small, can sometimes give very good results although they are not asymptotic methods.

yield an extremely good qualitative match with full numerical solutions: no comparable match of such a system has been presented in the literature before.

We now begin our analytical treatment of Eq. (5.11), where we use the software package Maple to handle lengthy intermediate expressions. In a later section, we will also develop simpler approximate working formulas for practicing mass-spectrometry researchers.

5.3.2 Solution of the unperturbed equation

By Eq. (5.11), the unperturbed equation is

$$\zeta'' - 2q\cos(2\xi)\zeta = \mu. \tag{5.12}$$

We represent the general solution of Eq. (5.12) as

$$\zeta = A\phi_1(\xi) + B\phi_2(\xi) + \chi(\xi), \tag{5.13}$$

where $\phi_1(\xi)$, $\phi_2(\xi)$ and $\chi(\xi)$ are functions to be determined, and A and B are constants determined from initial conditions. Functions $\phi_1(\xi)$ and $\phi_2(\xi)$ constitute a complementary solution; and $\chi(\xi)$ represents a particular integral. For compact presentation, we suppress ξ-dependence of the functions in further calculations. We first find ϕ_1 and ϕ_2. We know that ϕ_1 and ϕ_2 satisfy

$$\phi_1'' - 2q\cos(2\xi)\phi_1 = 0 \quad \text{and} \quad \phi_2'' - 2q\cos(2\xi)\phi_2 = 0. \tag{5.14}$$

Following [81], we consider

$$\phi_1 = \sum_{j=-N}^{j=N} C_j \cos((\beta + 2j)\xi) \quad \text{and} \quad \phi_2 = \sum_{j=-N}^{j=N} S_j \sin((\beta + 2j)\xi), \tag{5.15}$$

where the coefficients C_j and S_j and the frequency β are functions of q, and converge rapidly with increasing N within the approximation. Although we technically require $N \to \infty$, rapid convergence allows us to use an intermediate value of N [81, 82, 147, 148].

We substitute ϕ_1 from Eq. (5.15) in the first equation of Eq. (5.14). The resulting left hand side is then simplified, and the coefficients of $\cos((\beta + 2j)\xi)$ with $-N \leq j \leq N$, are set to zero. The obtained system of $2N+1$ equations is arranged in matrix form, $Mx = 0$, where M_{ij} is the coefficient of C_j in the ith equation, and the column matrix x contains the unknowns C_j. For a non-trivial solution of x, we require $\det(M) = 0$, which results in a characteristic equation in terms of q and β. We solve the characteristic equation numerically and obtain a fit[2] for q in terms of β as

$$q = 0.9060864 \sin\left(\frac{\beta\pi}{2}\right) - 0.0019439 \sin\left(\frac{3\beta\pi}{2}\right). \tag{5.16}$$

The excellent match of the numerical solution of the characteristic equation with the

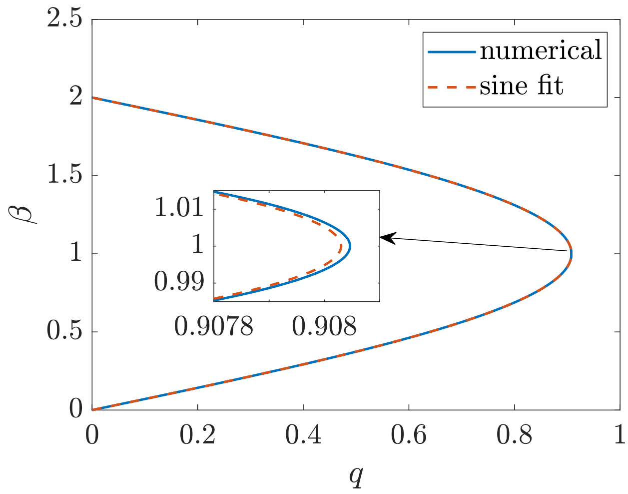

FIGURE 5.6: Comparison of numerical solution of the characteristic equation ($\det(M) = 0$ for $N = 5$) and the fitted Eq. (5.16). The error is about 0.00002.

fitted (5.16) is shown in Fig. 5.6. We observe that multiple β exist for a given q. However, we consider $\beta \in (0, 1)$ because the infinite series underlying the assumed solution of (5.15) remains unchanged upon replacing β with $\pm\beta \pm 2k$ for any integer k. With the approximation (5.16), we henceforth treat β as our free parameter instead of q.

[2]Physically, e.g., in a laboratory, we set q and β is determined as a result. For analytical work, it is simpler to choose a β of interest and then compute the required q. In terms of results obtained, there is no difference.

Having determined q as a function of β, in the interest of shorter expressions, we henceforth use $N = 4$ instead of $N = 5$. Accuracy remains very high. Next, we temporarily set $C_0 = 1$ in the new system $Mx = 0$ (i.e., for $N = 4$); ignore the row corresponding to $\cos(\beta\xi)$, and solve for the remaining C_j. The expressions of C_j at this point are provided in Appendix F. Since the coefficients C_j vary quite a lot with β, we finally normalize these coefficients such that $\|C\|_2 = 1$, i.e.,

$$\sum_{j=-N}^{j=N} C_j^2 = 1.$$

Finally, for ϕ_2, we note that the system of equations $Mx = 0$ remains the same with x containing S_j. Therefore, $S_j = C_j$. We have now determined the complementary solution to high accuracy using our truncated series.

By Eq. (5.12), the particular integral χ satisfies

$$\chi'' - 2q\cos(2\xi)\chi = \mu. \tag{5.17}$$

As mentioned earlier, Plass [7] did not notice the simple particular integral we use below. He used the method of variation of parameters to compute a formally valid, but less transparent, particular integral. Here, we directly use the Fourier series-based approximation

$$\chi = \mu \sum_{k=0}^{k=N} D_k \cos(2k\xi), \tag{5.18}$$

where the coefficients D_k are, again, functions of β. We substitute Eq. (5.18) in (5.17), and simplify the resulting equation. The coefficients of the trigonometric terms $\cos(2k\xi)$ with $1 \le k \le N$, are then set to zero, and a constant term in the expression is equated to unity (to be subsequently scaled by the constant μ that we will choose). We thus obtain $N + 1$ equations, which can be easily solved for D_k. The expressions of D_k are provided in Appendix F for $N = 4$. Having obtained D_k, we will adjust μ such that $\mu\|D\|_2 = 0.5$. This choice of μ is appropriate as $|\zeta| < 0.75$ is of practical interest.

At this point, we have obtained functions $\phi_1(\xi)$, $\phi_2(\xi)$ and $\chi(\xi)$ explicitly, and thus a general solution (5.13). We next proceed with the method of higher order averaging.

5.3.3 Higher order averaging

Following the general solution (5.13) of the unperturbed equation, we express the solution of the nonlinear Eq. (5.11) as

$$\zeta = A(\xi)\phi_1(\xi) + B(\xi)\phi_2(\xi) + \chi(\xi). \tag{5.19}$$

We further adopt the constraint equation

$$\zeta' = A(\xi)\phi_1'(\xi) + B(\xi)\phi_2'(\xi) + \chi'(\xi), \tag{5.20}$$

which is a routine step in the method of variation of parameters. For brevity of presentation, we again suppress the ξ-dependence of various quantities in further calculations. By Eqs. (5.19) and (5.20), we obtain

$$A'\phi_1 + B'\phi_2 = 0. \tag{5.21}$$

Substituting Eqs. (5.19) and (5.20) in (5.11), we obtain

$$\begin{aligned} A\phi_1'' + B\phi_2'' + \chi'' + A'\phi_1' + B'\phi_2' + \varepsilon^2\eta\left(A\phi_1' + B\phi_2' + \chi'\right) \\ - 2q\cos(2\xi)\left(A\phi_1 + B\phi_2 + \chi\right) = \mu + \varepsilon\mu\left(A\phi_1 + B\phi_2 + \chi\right)^2, \end{aligned} \tag{5.22}$$

where Eq. (5.21) is imposed. Recalling Eqs. (5.14) and (5.17), Eq. (5.22) reduces to

$$A'\phi_1' + B'\phi_2' + \varepsilon^2\eta\left(A\phi_1' + B\phi_2' + \chi'\right) = \varepsilon\mu\left(A\phi_1 + B\phi_2 + \chi\right)^2. \tag{5.23}$$

Solving Eqs. (5.21) and (5.23) for A' and B', we obtain equations ready for averaging,

$$A' = -\frac{\varepsilon\phi_2}{\Delta}\left[\mu(A\phi_1 + B\phi_2 + \chi)^2 - \varepsilon\eta(A\phi_1' + B\phi_2' + \chi')\right] \tag{5.24}$$

and

$$B' = \frac{\varepsilon\phi_1}{\Delta}\left[\mu(A\phi_1 + B\phi_2 + \chi)^2 - \varepsilon\eta(A\phi_1' + B\phi_2' + \chi')\right], \tag{5.25}$$

where $\Delta = \phi_1\phi_2' - \phi_2\phi_1'$ turns out to be a β-dependent constant, independent of ξ. We introduce the near-identity transformation (NIT)

$$\begin{aligned} A &= \bar{A}(\xi) + \varepsilon W_1(\bar{A}, \bar{B}, \xi) + \varepsilon^2 W_2(\bar{A}, \bar{B}, \xi), \\ B &= \bar{B}(\xi) + \varepsilon V_1(\bar{A}, \bar{B}, \xi) + \varepsilon^2 V_2(\bar{A}, \bar{B}, \xi), \end{aligned} \tag{5.26}$$

where the W's and V's are to be determined successively as the calculation proceeds, such that rapid oscillatory behavior in $\bar{A}$ and $\bar{B}$ are eliminated. In the calculations, for brevity of presentation, we suppress the dependency of the W's and V's on $\bar{A}$, $\bar{B}$ and ξ. Differentiating the NIT (5.26) with respect to time ξ, we obtain

$$\begin{aligned} A' &= \bar{A}' + \varepsilon\left(\frac{\partial W_1}{\partial \xi} + \frac{\partial W_1}{\partial \bar{A}}\bar{A}' + \frac{\partial W_1}{\partial \bar{B}}\bar{B}'\right) + \varepsilon^2\left(\frac{\partial W_2}{\partial \xi} + \frac{\partial W_2}{\partial \bar{A}}\bar{A}' + \frac{\partial W_2}{\partial \bar{B}}\bar{B}'\right), \\ B' &= \bar{B}' + \varepsilon\left(\frac{\partial V_1}{\partial \xi} + \frac{\partial V_1}{\partial \bar{A}}\bar{A}' + \frac{\partial V_1}{\partial \bar{B}}\bar{B}'\right) + \varepsilon^2\left(\frac{\partial V_2}{\partial \xi} + \frac{\partial V_2}{\partial \bar{A}}\bar{A}' + \frac{\partial V_2}{\partial \bar{B}}\bar{B}'\right). \end{aligned} \tag{5.27}$$

By Eqs. (5.24), (5.25) and (5.27), we conclude that $\bar{A}'$ and $\bar{B}'$ are $\mathcal{O}(\varepsilon)$. Therefore, we write

$$\begin{aligned} \bar{A}' &= \varepsilon X_1 + \varepsilon^2 X_2, \\ \bar{B}' &= \varepsilon Y_1 + \varepsilon^2 Y_2, \end{aligned} \tag{5.28}$$

where X_1, X_2, Y_1 and Y_2 are yet to be determined functions of $\bar{A}$ and $\bar{B}$. Substituting Eqs. (5.28) in (5.27), we obtain

$$A' = \varepsilon\left(X_1 + \frac{\partial W_1}{\partial \xi}\right) + \varepsilon^2\left(X_2 + \frac{\partial W_2}{\partial \xi} + \frac{\partial W_1}{\partial \bar{A}}X_1 + \frac{\partial W_1}{\partial \bar{B}}Y_1\right) + \mathcal{O}(\varepsilon^3) \tag{5.29}$$

and

$$B' = \varepsilon\left(Y_1 + \frac{\partial V_1}{\partial \xi}\right) + \varepsilon^2\left(Y_2 + \frac{\partial V_2}{\partial \xi} + \frac{\partial V_1}{\partial \bar{A}}X_1 + \frac{\partial V_1}{\partial \bar{B}}Y_1\right) + \mathcal{O}(\varepsilon^3). \tag{5.30}$$

By the NIT (5.26) and Eqs. (5.29) and (5.30), we eliminate A, B, A' and B' from Eqs. (5.24) and (5.25). The resulting equations are now ready to be treated in successive orders of the small parameter ε.

The $\mathcal{O}(\varepsilon)$ equations are

$$X_1 + \frac{\partial W_1}{\partial \xi} = -\frac{\mu\phi_2}{\Delta}\left(\bar{A}^2\phi_1^2 + \bar{B}^2\phi_2^2 + \chi^2 + 2\bar{A}\bar{B}\phi_1\phi_2 + 2\bar{A}\phi_1\chi + 2\bar{B}\phi_2\chi\right) \tag{5.31}$$

and

$$Y_1 + \frac{\partial V_1}{\partial \xi} = \frac{\mu\phi_1}{\Delta}\left(\bar{A}^2\phi_1^2 + \bar{B}^2\phi_2^2 + \chi^2 + 2\bar{A}\bar{B}\phi_1\phi_2 + 2\bar{A}\phi_1\chi + 2\bar{B}\phi_2\chi\right). \tag{5.32}$$

The trick now is to note that W_1 and V_1 involve only partial derivatives with respect to ξ. Therefore, for addressing Eqs. (5.31) and (5.32), we can effectively think of $\bar{A}$ and $\bar{B}$ as variables that are independent of ξ. X_1 and Y_1 can now be chosen to balance the non-zero ξ-averages of the right hand sides of Eqs. (5.31) and (5.32), respectively; and the zero-mean oscillating parts of these right hand sides can be assigned to $\dfrac{\partial W_1}{\partial \xi}$ and $\dfrac{\partial V_1}{\partial \xi}$. This determines W_1 and V_1; but at the next order, similar simplifying steps can be applied using W_2 and V_2. In this way, the averaging calculation can in principle be extended to any desired order.

On computing the non-zero ξ-averages of the right hand sides of Eqs. (5.31) and (5.32), we find that $\phi_2^2\chi$ and $\phi_1^2\chi$ are the only terms that make any contributions. We thus obtain, at first order in ε,

$$X_1 = \mu c_1 \bar{B} \quad \text{and} \quad Y_1 = \mu c_2 \bar{A}, \tag{5.33}$$

where c_1 and c_2 depend on β alone, and are plotted in Fig. 5.7. Expressions for c_1 and c_2 are provided in Appendix G. Observing those expressions and recalling $S_j = C_j$, we confirm that $c_1 = -c_2$. We further note that these coefficients, being bounded for β away from 0 and 1, do not indicate any role of resonance. First order averaging is now complete. The role of resonance will be seen at the next order in ε.

We now substitute Eq. (5.33) in Eqs. (5.31) and (5.32), and obtain expression for $\dfrac{\partial W_1}{\partial \xi}$ and $\dfrac{\partial V_1}{\partial \xi}$. We analytically integrate those expressions with respect to ξ treating $\bar{A}$ and $\bar{B}$ as constants, because of the partial derivative. That integration yields the zero-mean oscillating parts W_1 and V_1. Because the expressions for W_1 and V_1 are lengthy, and

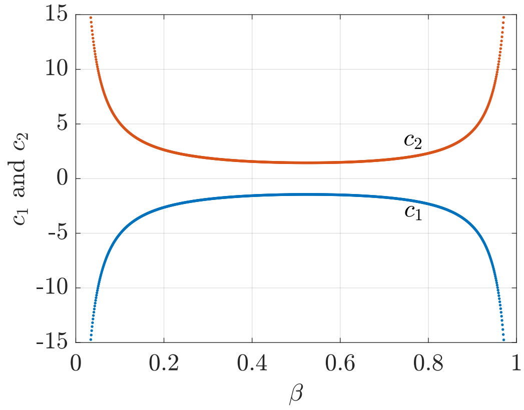

FIGURE 5.7: Variation of the $\mathcal{O}(\varepsilon)$ slow flow coefficients c_1 and c_2 with β.

because these quantities themselves only play an intermediate role in the calculation, we avoid writing them out in the interest of brevity. We do mention, however, that W_1 and V_1 both depend on $\bar{A}$, $\bar{B}$, β, ξ, as well as the quantity μ which has previously been determined as a function of β (recall the discussion following Eq. (5.18)).

We are now ready for second order averaging. We proceed with the $\mathcal{O}(\varepsilon^2)$ equations

$$X_2 + \frac{\partial W_2}{\partial \xi} + \frac{\partial W_1}{\partial \bar{A}} X_1 + \frac{\partial W_1}{\partial \bar{B}} Y_1 = -\frac{\mu \phi_2}{\Delta}\Big(2\bar{A} W_1 \phi_1^2 + 2(\bar{A} V_1 + \bar{B} W_1)\phi_1 \phi_2 + 2\bar{B} V_1 \phi_2^2 + 2W_1 \phi_1 \chi + 2V_1 \phi_2 \chi \Big) + \frac{\phi_2}{\Delta}\Big(\bar{A}\eta\phi_1' + \bar{B}\eta\phi_2' \Big) \tag{5.34}$$

and

$$Y_2 + \frac{\partial V_2}{\partial \xi} + \frac{\partial V_1}{\partial \bar{A}} X_1 + \frac{\partial V_1}{\partial \bar{B}} Y_1 = \frac{\mu \phi_1}{\Delta}\Big(2\bar{A} W_1 \phi_1^2 + 2(\bar{A} V_1 + \bar{B} W_1)\phi_1 \phi_2 + 2\bar{B} V_1 \phi_2^2 + 2W_1 \phi_1 \chi + 2V_1 \phi_2 \chi \Big) - \frac{\phi_1}{\Delta}\Big(\bar{A}\eta\phi_1' + \bar{B}\eta\phi_2' \Big). \tag{5.35}$$

In the above two equations, we recall that left hand side terms involving partial derivatives of W_1 and V_1 have zero-mean oscillating components only. X_2 and Y_2 above must balance the non-zero averages of the right hand sides of Eqs. (5.34) and (5.35), respectively. Substituting the already-known W_1 and V_1, and finding averages of all the terms individually (using Maple), we finally obtain

$$\begin{aligned} X_2 &= \mu^2\big(\alpha_1\bar{A}^2\bar{B}+\alpha_2\bar{B}^3+\alpha_3\bar{B}\big)-\alpha_4\eta\bar{A},\\ Y_2 &= \mu^2\big(\gamma_1\bar{B}^2\bar{A}+\gamma_2\bar{A}^3+\gamma_3\bar{A}\big)-\gamma_4\eta\bar{B}, \end{aligned} \tag{5.36}$$

where α_i and γ_i, with $1 \le i \le 4$, depend on β and are plotted in Fig. 5.8. We note that

$$\alpha_1 = \alpha_2 = -\gamma_1 = -\gamma_2, \quad \alpha_3 = -\gamma_3, \quad \text{and} \quad \alpha_4 = \gamma_4 = 0.5. \tag{5.37}$$

Thus, there are only two new functions of β in Eq. (5.36). In what follows, we will write, for simplicity,

$$c_1 = c, \quad \alpha_1 = \alpha, \quad \text{and} \quad \gamma_3 = \gamma. \tag{5.38}$$

We note also that Fig. 5.8 further indicates a resonance point, $\beta = 2/3$. This resonance was studied before in [81, 82], but only to first order[3] and without the inhomogeneous term; we will explore the resonant point in section 5.3.6. But we will first address in detail the nonresonant case, i.e., β away from $2/3$. The nonlinear nonresonant case has not been discussed in the literature at all.

By Eqs. (5.28), (5.33) and (5.36), we obtain the slow flow (recall Eqs. (5.37) and (5.38))

$$\begin{aligned} \bar{A}' &= \varepsilon(\mu c\bar{B})+\varepsilon^2\left(\mu^2\{\alpha(\bar{A}^2+\bar{B}^2)-\gamma\}\bar{B}-0.5\eta\bar{A}\right),\\ \bar{B}' &= -\varepsilon(\mu c\bar{A})+\varepsilon^2\left(-\mu^2\{\alpha(\bar{A}^2+\bar{B}^2)-\gamma\}\bar{A}-0.5\eta\bar{B}\right). \end{aligned} \tag{5.39}$$

We now demonstrate its match with a corresponding response by the original equation.

5.3.4 Numerical validation

We consider the arbitrarily chosen $\beta = 0.542$, a nonresonant value, to illustrate the validity of the slow flow, Eqs. (5.39). We first find $q = 0.6804671$ by Eq. (5.16). Unscaled coefficients C_j are then found using the expressions in Appendix F. Normalizing them such

[3]With parametric excitation of the quadratic nonlinear term, which we do not have here, the resonance is felt at first order.

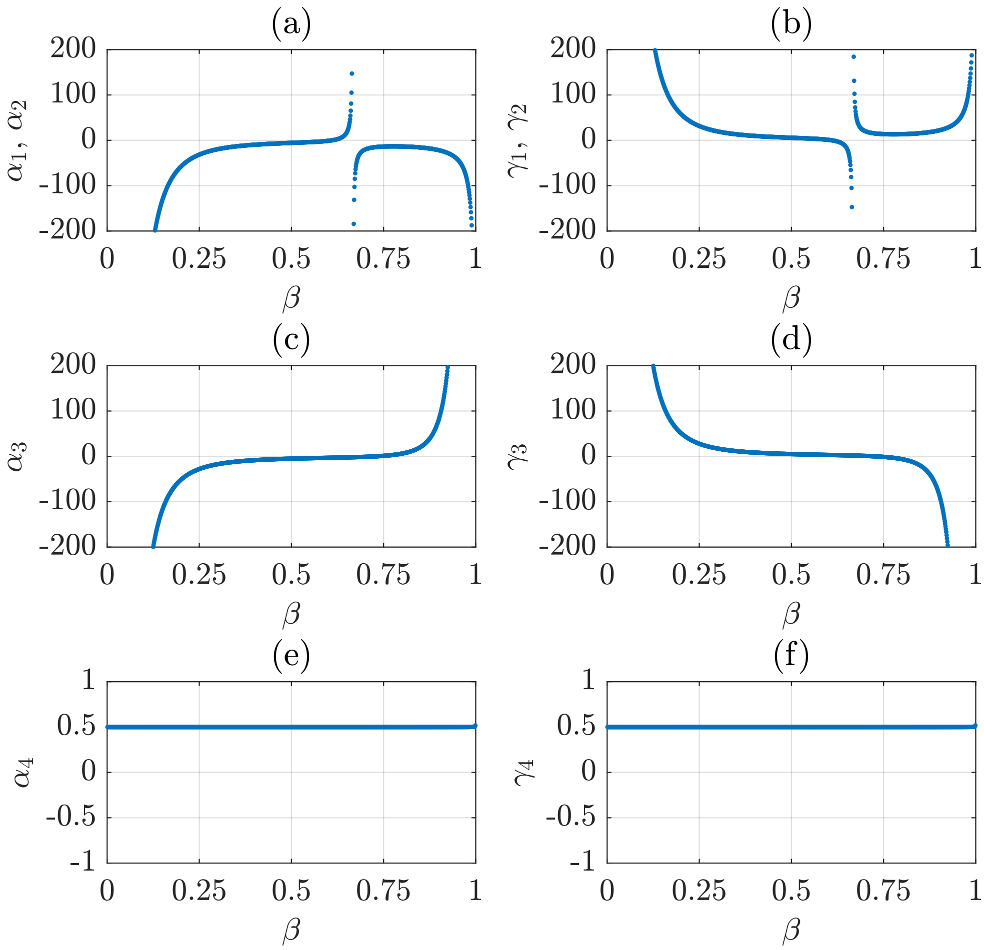

FIGURE 5.8: Variation of the $\mathcal{O}(\varepsilon^2)$ slow flow coefficients α_i and γ_i with β, where $1 \leq i \leq 4$.

that $\|C\|_2 = 1$, we obtain

$$C_{-4} = 0.0000049, \quad C_{-3} = -0.0004015, \quad C_{-2} = 0.0175720, \quad C_{-1} = -0.3083887,$$
$$C_0 = 0.9458276, \quad C_1 = -0.0999338, \quad C_2 = 0.0032980, \quad C_3 = -0.0000524,$$
$$C_4 = 0.0000005.$$

We recall $S_j = C_j$. By Eq. (5.15), the homogeneous solutions ϕ_1 and ϕ_2 are now known. By expressions for D_k in Appendix F, we obtain

$$D_0 = 4.2880482, \quad D_1 = -1.4695787, \quad D_2 = 0.0625503, \quad D_3 = -0.0011825,$$
$$D_4 = 0.0000126.$$

We then adjust the particular solution amplitude to 0.5, i.e., $\mu\|D\|_2 = 0.5$, which yields $\mu = 0.1103$. With that, we now have integral χ given by Eq. (5.18). Finally, the coefficients in the slow flow, Eq. (5.39), are found to be

$$c = -1.4484907, \quad \alpha = -4.2500961, \quad \text{and} \quad \gamma = 4.1775115.$$

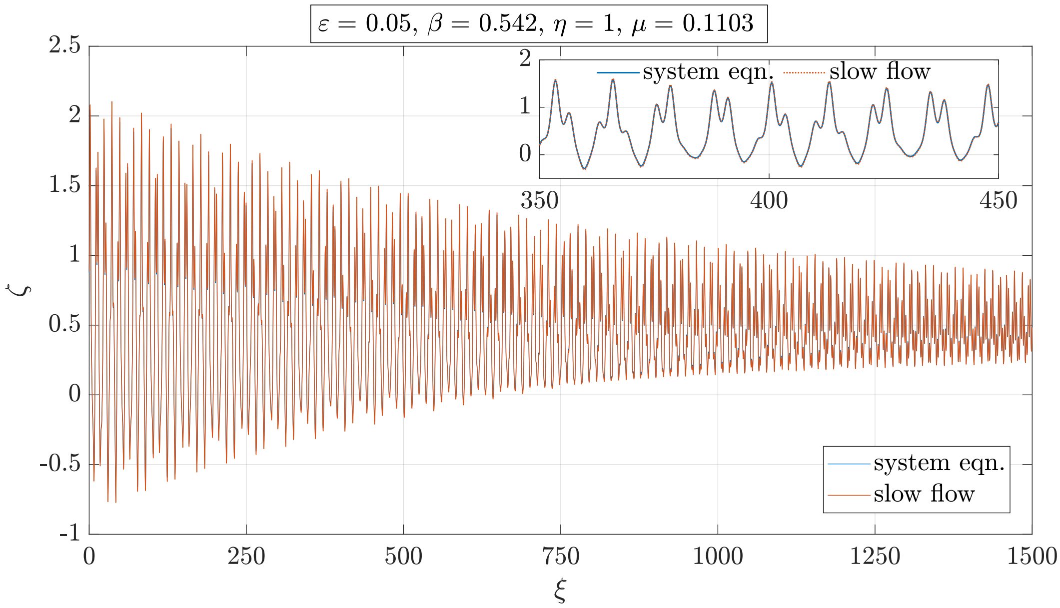

FIGURE 5.9: Comparison of numerical solution of the system equation (5.11) and the slow flow (5.39) with the change in coordinates according to Eqs. (5.19) and (5.26).

Figure 5.9 compares the response obtained from numerical integration of the system equation (5.11) and the slow flow (5.39) with Eq. (5.19) and the NIT (5.26). The match is excellent. Figure 5.10 shows A-B phase portraits obtained from the numerical integration of the slow flow (5.39) (left subplot), and that from the system equation (5.11) followed by the change of coordinates as per Eqs. (5.19) and (5.20) (right subplot). We observe that even in the A-B coordinates, the match is very good. Moreover, we see how the rapid oscillations in A and B have been averaged out and the mean inward spiralling behavior has been accurately captured. It is clear that the response finally goes to the origin in the A-B plane, i.e., the solution eventually settles down to the particular solution χ. In other words, the particular solution χ is stable. In this was, our choice of particular solution is more useful than that proposed by Plass [7]. This stability of χ holds at other values of β

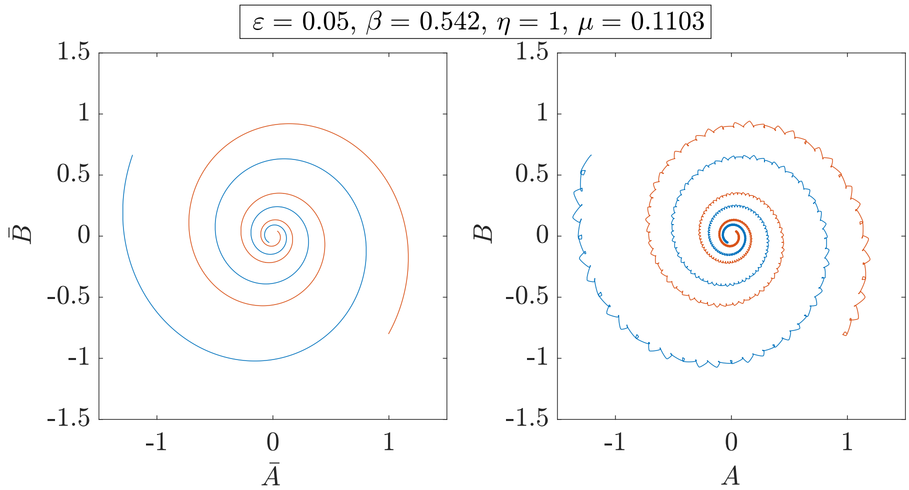

FIGURE 5.10: Comparison of A-B phase portraits. The left subplot is obtained from numerical integration of the slow flow (5.39), and the right subplot is obtained from that of the system equation (5.11) followed by the coordinate change according to Eqs. (5.19) and (5.20). Note that the trajectories are spiralling inward.

and for somewhat larger nonlinearity as well, e.g., see Fig. 5.11, where β is different, and ε and μ are both larger. The corresponding numerical values are

$$
\begin{array}{llll}
q = 0.8448727, & C_{-4} = 0.0000200, & C_{-3} = -0.0012399, & C_{-2} = 0.0402283, \\
C_{-1} = -0.4976745, & C_0 = 0.8611218, & C_1 = -0.0956910, & C_2 = 0.0035661, \\
C_3 = -0.0000659, & C_4 = 0.0000007, & D_0 = 2.7705774, & D_1 = -1.1836102, \\
D_2 = 0.0625776, & D_3 = -0.0014691, & D_4 = 0.0000194, & \\
c = -2.0210604, & \alpha = -13.4060727, & \gamma = -2.0854362. &
\end{array}
$$

We now turn to an analysis of the slow flow for general nonresonant β.

5.3.5 Response for a general β

We introduce the transformation

$$\bar{A} = R\cos\theta \quad \text{and} \quad \bar{B} = R\sin\theta,$$

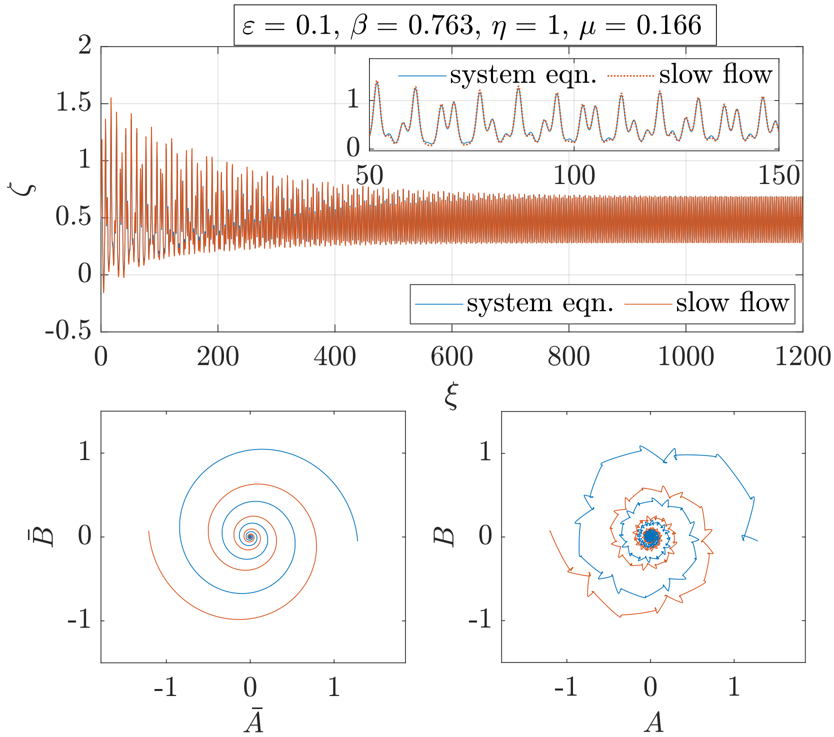

FIGURE 5.11: Comparison of numerical solution of the system equation (5.11) and the slow flow (5.39). The top figure compares the response as that in Fig. 5.9 and the bottom figures compare the phase portraits as that in Fig. 5.10.

where R and θ are new coordinates that are functions of ξ. Equation (5.39) then yields

$$R' = -\frac{\varepsilon^2 \eta R}{2}, \tag{5.40}$$

$$\theta' = -\varepsilon\mu \left(c + \varepsilon\mu \left(\alpha R^2 - \gamma\right)\right). \tag{5.41}$$

By Eq. (5.40), R decays to zero irrespective of the value of β, provided the averaged equations are valid, i.e., whenever ε is small enough and β is away from 0, 1, and 2/3. This shows our particular solution χ is stable for β away from 0, 1, and 2/3. For mass spectrometric applications, a significant practical insight is that the shifted ion motion under dipolar excitation has no components involving the secular frequency β. The motion, although not purely harmonic, has the same period as the quadrupolar excitation.

We now recall that Fig. 5.8 indicated a resonance at $\beta = 2/3$, and turn to examine that resonance.

5.3.6 The resonance at $\beta = 2/3$

To perform the averaging analysis near the resonance frequency $\beta = 2/3$, we replace q in Eq. (5.11) by $(q^* + \varepsilon\delta)$ to obtain

$$\zeta'' + \varepsilon^2\eta\zeta' - 2(q^* + \varepsilon\delta)\cos(2\xi)\zeta = \mu\left(1 + \varepsilon\zeta^2\right), \tag{5.42}$$

where $q^* = 0.7846938$ by Eq. (5.16), and δ denotes a detuning parameter. The averaging calculation closely follows section 5.3.3, except that finding the nonzero averages of oscillating quantities is now simpler because oscillations are periodic. The final slow flow takes the form

$$\begin{aligned}\bar{A}' = \varepsilon\left(\mu c_{11}\bar{A}\bar{B} + (\delta c_{12} + \mu c_{13})\bar{B}\right) + \varepsilon^2\Big(\mu^2(\alpha_{11}\bar{A}^2\bar{B} + \alpha_{12}\bar{A}\bar{B} + \alpha_{11}\bar{B}^3 \\ +\alpha_{15}\bar{B}) + \mu\delta(\alpha_{13}\bar{A}\bar{B} + \alpha_{16}\bar{B}) + \delta^2\alpha_{17}\bar{B} - 0.5\eta\bar{A}\Big)\end{aligned} \tag{5.43}$$

and

$$\begin{aligned}\bar{B}' = \varepsilon\left(\mu c_{21}\bar{A}^2 - \mu c_{21}\bar{B}^2 - (\delta c_{12} + \mu c_{13})\bar{A}\right) + \varepsilon^2\Big(\mu^2(-\alpha_{11}\bar{A}^3 - \alpha_{11}\bar{A}\bar{B}^2 \\ +\gamma_{24}\bar{A}^2 - \gamma_{24}\bar{B}^2 - \alpha_{15}\bar{A}) + \mu\delta(\gamma_{23}\bar{A}^2 - \alpha_{16}\bar{A} - \gamma_{23}\bar{B}^2) - \delta^2\alpha_{17}\bar{A} - 0.5\eta\bar{B}\Big),\end{aligned} \tag{5.44}$$

where the numerical coefficients are found to be

$$\begin{array}{llll} c_{11} = -1.5733095, & c_{12} = 1.3871189, & c_{13} = -1.6107711, & c_{21} = -0.7866547, \\ \alpha_{11} = -5.2040858, & \alpha_{12} = 5.1857743, & \alpha_{13} = -7.4965634, & \alpha_{15} = -1.9020383, \\ \alpha_{16} = 0.2835549, & \alpha_{17} = 2.5831053, & \gamma_{23} = -3.7482817, & \gamma_{24} = 2.5928871. \end{array} \tag{5.45}$$

Figure 5.12 compares the response obtained from the numerical integration of Eq. (5.42) and the slow flow (5.43) and (5.44), where relevant coordinate changes follow Eqs. (5.19)

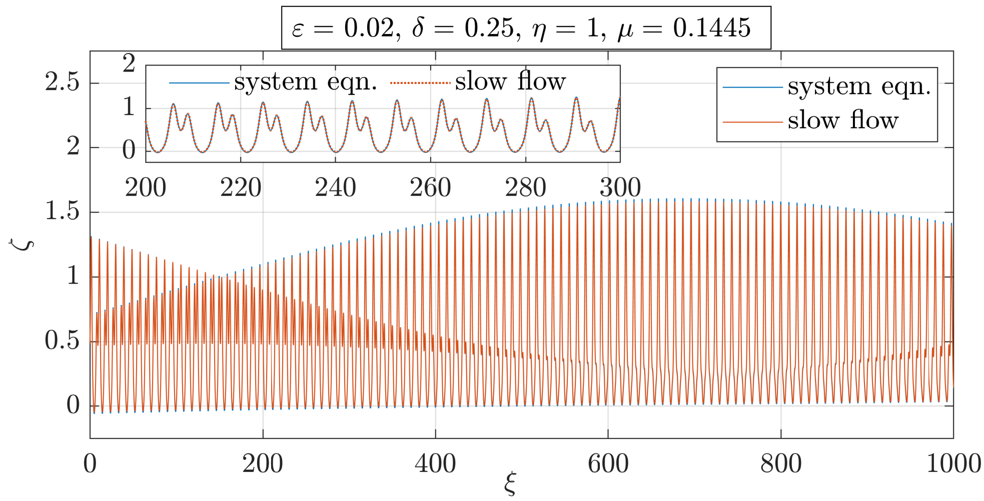

FIGURE 5.12: Numerical solution obtained from (i) Eq. (5.42) and (ii) from Eqs. (5.43) and (5.44) followed by use of Eqs. (5.19) and (5.26).

and (5.26). We know that $\mathcal{O}(\varepsilon)$ terms in the slow flow dominate. Therefore, to understand the qualitative dynamics of the system, we drop $\mathcal{O}(\varepsilon^2)$ terms and study the first-order system

$$\bar{A}' = \varepsilon\left(\mu c_{11}\bar{A}\bar{B} + (\delta c_{12} + \mu c_{13})\bar{B}\right) + \mathcal{O}(\varepsilon^2),$$
$$\bar{B}' = \varepsilon\left(\mu c_{21}\bar{A}^2 - \mu c_{21}\bar{B}^2 - (\delta c_{12} + \mu c_{13})\bar{A}\right) + \mathcal{O}(\varepsilon^2).$$

We find the fixed points $(\bar{A}, \bar{B})$ as

$$(0,0), \quad \left(\frac{2\,(\delta c_{12} + \mu c_{13})}{\mu c_{11}}, 0\right) \quad \text{and} \quad \left(-\frac{\delta c_{12} + \mu c_{13}}{\mu c_{11}}, \pm\frac{\sqrt{3}(\delta c_{12} + \mu c_{13})}{\mu c_{11}}\right), \tag{5.46}$$

where we have used $2c_{21} = c_{11}$ from Eq. (5.45). Here, $(0,0)$ is a center which turns into a stable spiral when damping is included. The other fixed points are saddles. All four fixed points are marked using red solid circles in the phase portraits presented in Fig. 5.13, wherein the left and right subplots correspond to the slow flow Eqs. (5.43) and (5.44) and to the original Eq. (5.42), respectively. In Fig. 5.13, we observe a stable region around the origin, whose size is determined by the locations of the saddles. The closer the saddles are to the origin, the smaller is the stable region. By Eq. (5.46), at $\delta^* = -\mu c_{13}/c_{12}$, all the fixed points are at the origin, leaving no stable region. For detuning values increasingly far away from this δ^*, an increasingly larger nonzero stable region exists. This explains why, in the preceding nonresonant analysis, all solutions were observed to be stable as per Eqs. (5.40) and (5.41).

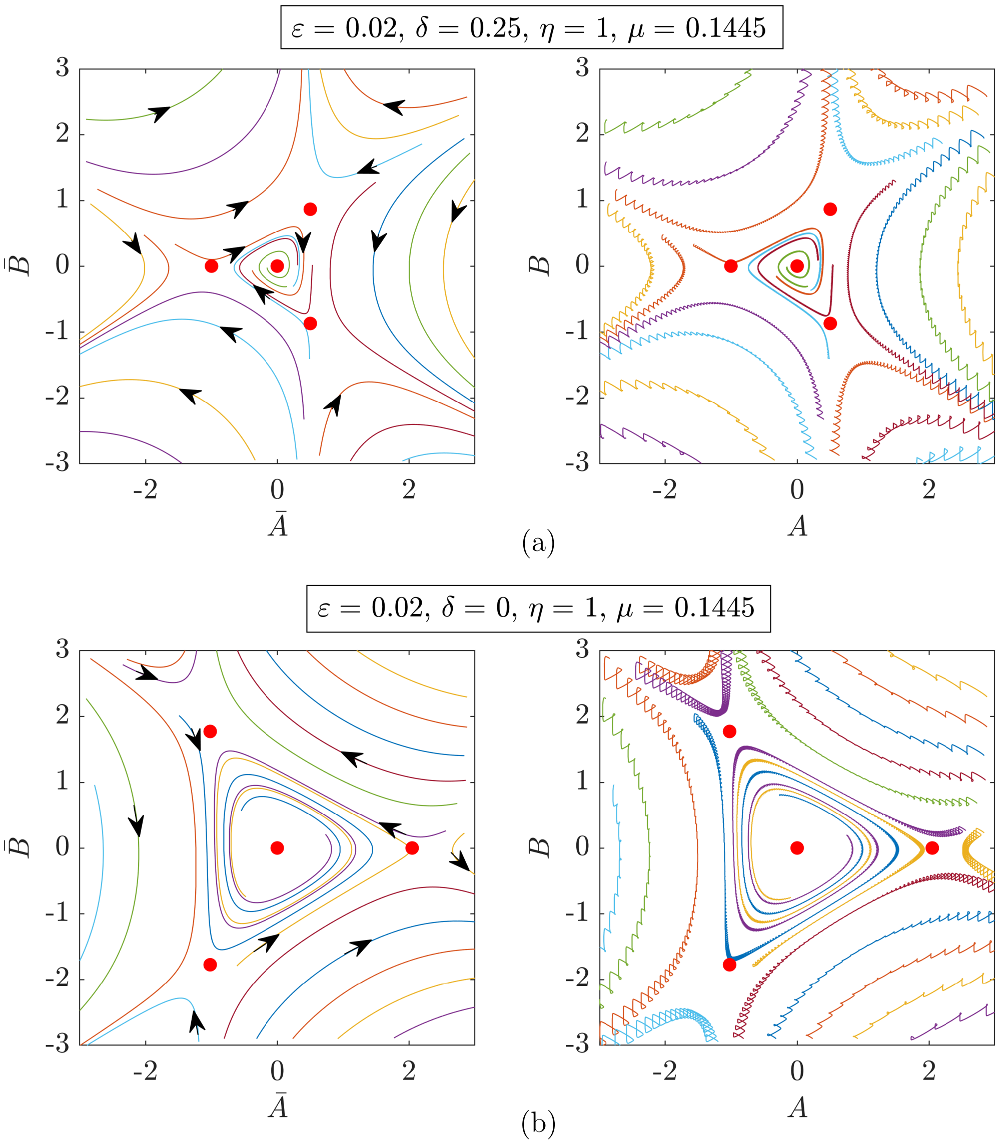

FIGURE 5.13: Phase portraits (left) for two different detuning values δ, and corresponding full numerical solutions (right). Subplot (b) shows a larger stable region because the distance $|\delta - \delta^*|$ is larger.

Figures 5.13(a) and 5.13(b) consider $\delta = 0.25$ and $\delta = 0$, respectively. With $\delta^* = 0.1677785$ in the present analysis, subplot (b) shows a larger stable regime as the magnitude of $(\delta - \delta^*)$

is higher than that in subplot (a), as anticipated. We recall that the origin, $\bar{A} = \bar{B} = 0$, corresponds to the nonzero solution χ as in Eq. (5.18).

Finally, we note that the resonant behavior depicted in Fig. 5.13 resembles phase portraits presented in [81]. However, in [81], a quadratic nonlinearity was present in the parametric term only, and the unperturbed equation was homogeneous. In other words, there was no dipolar excitation. Moreover, our results for the nonresonant case are new.

We close the section by acknowledging that a nonresonant case can also show unbounded solutions for large enough initial conditions, as seen in Fig. 5.14. Such large solutions cannot be studied by the present analytical strategy. Fortunately for our application, such large initial conditions are not relevant to practical traps.

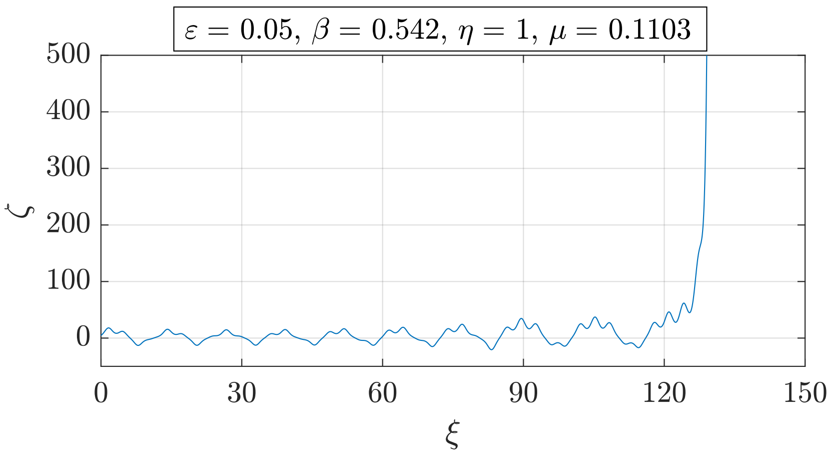

FIGURE 5.14: Unbounded solutions do exist in the nonresonant situation. However, the required initial conditions are too large to be relevant to ion traps.

This concludes our formal, and relatively more rigorous, analysis of Eq. (5.10). We now turn to the task of obtaining simpler approximations that may be more useful to practitioners of mass spectrometry. As mentioned earlier, the following section is primarily due to Prof. A. K. Mohanty, and is included here for completeness and consistency with [85].

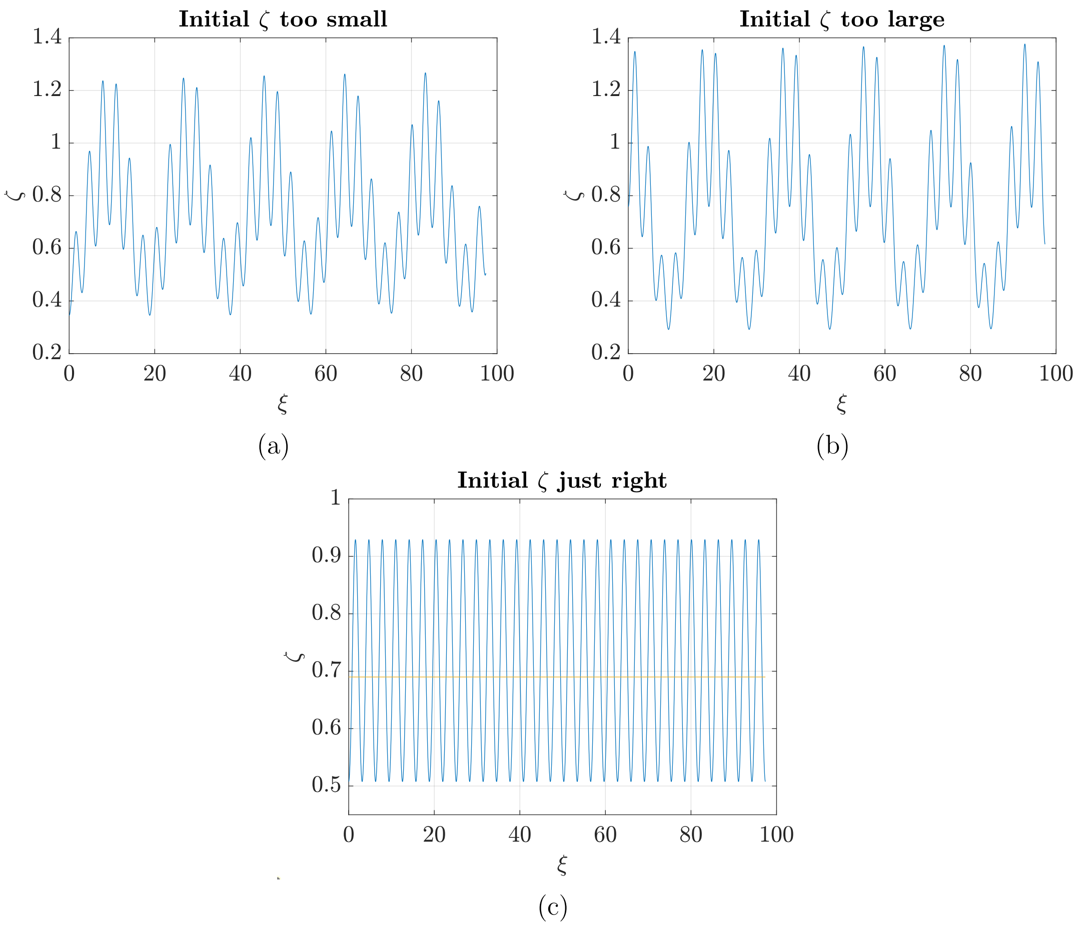

FIGURE 5.15: (a) Solution for initial ζ that is too small for having a periodic solution. (b) Solution for initial ζ that is too large for having a periodic solution. (c) Solution for initial ζ that is just right for having a periodic solution.

5.4 Simpler working formulas

In general, the solution of Eq. (5.10) contains slow secular oscillations due to the parametric forcing in the Mathieu differential operator on the left hand side. In general, also, the period of the secular motion is not a rational multiple of π, so the solution is not periodic. Example solutions having slow secular oscillations are shown in Figs. 5.15(a) and 5.15(b).

However, as already seen above, there is a special solution that is free from the secular oscillations, and has period π. Such a solution is plotted in Fig. 5.15(c). In addition to being the simplest solution in some sense, as well as being an attractor in the presence of damping as shown by the foregoing analysis, this solution is also important in dipolar DC applications. For the analytical chemist, the maximum kinetic energy of an ion associated with this periodic solution provides a guaranteed minimum dissociation capability.

In this section we present simple formulae and iterative methods for approximating the periodic solution. These are based on harmonic balance. The Mathieu Equation with a constant RHS is discussed first. Then the results obtained are used to develop approximate formulae for the determination of the periodic solution.

5.4.1 Periodic solutions of Eq. (5.10) using numerical harmonic residue

A numerical method for the accurate determination of the periodic solution of Eq. (5.10) will now be described. This section may be viewed as working with an alternative and in some ways simpler approach to find approximations motivated by Eq. (5.18) above. Note that Eq. (5.10) does not contain damping; a small amount of damping was introduced in the averaging analysis to demonstrate how, even with a little damping, the periodic solution becomes an attractor.

In general, a solution of the undamped Eq. (5.10) will have slow secular oscillations. However, for a specific initial condition $\zeta_0 = \zeta_{0,p}$ and $\dot{\zeta}_0 = 0$, the secular frequency components vanish and we have a periodic solution. A direct numerical approach, which provides a conceptually simpler alternative to the earlier analytically obtained truncated Fourier series approximation, is described first. The periodic solutions thus obtained for the undamped case will be used as a reference for the subsequently presented approximations.

For any initial value ζ_0, and initial derivative equal to 0, Eq. (5.10) can be solved numerically over an interval $(0, \xi_{\max})$. For practical computation, $\xi_{\max}$ can be a number that is greater than a secular period of the homogeneous Mathieu equation with the given a and q. Let this solution be called $\zeta(\xi; \zeta_0)$. Using the usual linear least-squares technique, one can compute coefficients $d_0, d_1, \ldots, d_N$ so that the 2-norm of $\zeta(\xi; \zeta_0) - \sum_{k=0}^{N} d_k \cos(2k\xi)$ over the interval $(0, \xi_{\max})$ is minimized. It is possible to get a reasonably good representation even for $N = 2$. The minimum 2-norm so obtained, which is the error in the least squares fit, is a function of ζ_0. Let it be denoted as $r(\zeta_0)$; this is the *harmonic residue*. The value of ζ_0 that minimizes $r(\zeta_0)$ provides a good approximation to the desired periodic solution. For example, the solution shown in Fig. 5.15(c) was generated using $N = 2$, $\xi_{\max} = 31\pi$, $a = 0$, $q = 0.6$, $\mu = 0.1$, and $\kappa = 0.5$.

5.4.2 Periodic solution of the Mathieu equation with a constant RHS

In Eq. (5.10), if κ is set to 0, the RHS becomes the constant μ. A solution for the RHS equal to 1 is first obtained. Then multiplication of this solution by μ provides the solution for RHS equal to μ. In what follows, since we seek a specific π-periodic solution, we do not have to consider β (recall Fig. 5.6) and we can work directly with q, which will be useful for practitioners.

The Mathieu Equation with RHS equal to 1 is

$$\frac{\mathrm{d}^2\zeta}{\mathrm{d}\xi^2} + [a - 2q\cos(2\xi)]\zeta = 1. \tag{5.47}$$

As was seen in Eq. (5.18) and the subsequent analysis, a β-independent periodic solution exists which is expressible as

$$\zeta_p(\xi) = D_0 + \sum_{k=1}^{\infty} D_k \cos(2k\xi). \tag{5.48}$$

Since we are no longer interested in higher order analysis and only seek a good approximation to the periodic solution, we can take $N = 2$. This yields our *two-frequency approximation.*

$$\begin{bmatrix} a & -q & 0 \\ 2q & 4-a & q \\ 0 & q & 16-a \end{bmatrix} \begin{bmatrix} D_0 \\ D_1 \\ D_2 \end{bmatrix} = \begin{bmatrix} 1 \\ 0 \\ 0 \end{bmatrix}$$

The solutions are

$$\mathcal{D} = a(4-a)(16-a) + q^2(32-3a),$$

$$D_0 = \frac{(4-a)(16-a) - q^2}{\mathcal{D}}, \tag{5.49}$$

$$D_1 = \frac{-2q(16-a)}{\mathcal{D}}, \tag{5.50}$$

and

$$D_2 = \frac{2q^2}{\mathcal{D}}. \tag{5.51}$$

Moreover, if $a = 0$, then

$$D_{0,a=0} = \frac{2}{q^2} - \frac{1}{32},$$

$$D_{1,a=0} = -\frac{1}{q},$$

and

$$D_{2,a=0} = \frac{1}{16}.$$

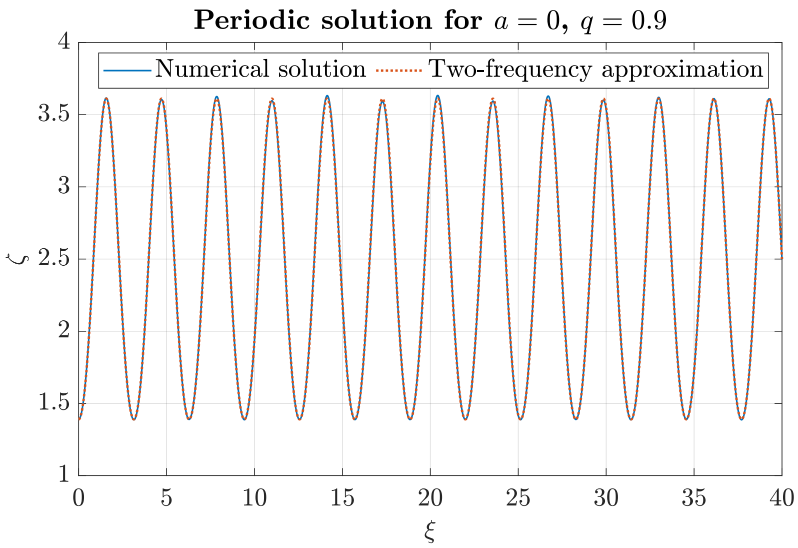

FIGURE 5.16: Periodic solution of Eq. (5.47) using the two-frequency approximation, compared with the numerical solution obtained by minimizing the harmonic residue.

As Fig. 5.16 shows, the two-frequency approximation works quite well even for q as high as 0.9. When the RHS of Eq. (5.47) is μ instead of 1, we use $\mu\left(D_0 + D_1\cos(2\xi) + D_2\cos(4\xi)\right)$.

5.4.3 Simple iterative calculation for the nonlinear case

If $\kappa = 0$ in Eq. (5.10) then D_0, given by Eq. (5.49), is the gain factor by which the RHS is multiplied to obtain the *average* ion displacement.

Now we let κ be nonzero but not too large, and assume a two-frequency approximate periodic solution of the form

$$\zeta_p(\xi) = A_0 + A_1 \cos(2\xi) + A_2 \cos(4\xi). \tag{5.52}$$

These A's will be the same as μ times the foregoing D's if $\kappa = 0$. Otherwise, they will differ.

In foregoing sections, we have presented a somewhat complicated second order averaging calculation to show that the approximations we propose are valid in principle. Now we present a simple two-frequency approximation for the nonlinear problem that can be implemented using a few lines of code.

Two frequency harmonic balance yields the nonlinear set of simultaneous equations

$$\begin{bmatrix} a & -q & 0 \\ 2q & 4-a & q \\ 0 & q & 16-a \end{bmatrix} \begin{bmatrix} A_0 \\ A_1 \\ A_2 \end{bmatrix} = \mu \begin{bmatrix} 1 + \kappa\left(A_0^2 + \frac{1}{2}(A_1^2 + A_2^2)\right) \\ -\kappa(2A_0A_1 + A_1A_2) \\ -\kappa(2A_0A_2 + \frac{1}{2}A_1^2) \end{bmatrix} \tag{5.53}$$

Equation (5.53) can in principle be solved in any way we like. For example, it could be solved using Newton-Raphson iterations. For small κ, it could be solved using a perturbation expansion in κ as well. However, conceptually and algorithmically, the simplest approach we know is iterative. The iteration is:

$$\begin{bmatrix} A_0 \\ A_1 \\ A_2 \end{bmatrix}_{k+1} = \mu \begin{bmatrix} a & -q & 0 \\ 2q & 4-a & q \\ 0 & q & 16-a \end{bmatrix}^{-1} \begin{bmatrix} 1 + \kappa\left(A_0^2 + \frac{1}{2}(A_1^2 + A_2^2)\right) \\ -\kappa(2A_0A_1 + A_1A_2) \\ -\kappa(2A_0A_2 + \frac{1}{2}A_1^2) \end{bmatrix}_k \tag{5.54}$$

The initial values to be used in the iteration need to be specified. The simplest choice seems to be the $\kappa = 0$ or linear case; however, that choice is in turn simply one iteration away from the choice $A_0 = A_1 = A_2 = 0$. Therefore, the starting guess for the iterations can be simply $A_0 = A_1 = A_2 = 0$. Note that due to quadratic terms on the right hand side, large initial guesses and/or large κ can lead to divergence in the iterations. However, for physically relevant parameter values and zero initial guesses, the iterations have converged quickly in our numerical experiments. Additionally, since both this iteration and our foregoing perturbation analysis are both based on a small-κ assumption, this iterative method is expected to work as well, or as poorly, as our perturbation solution.

Finally, a nonlinear enhancement factor may be defined as

$$g = \frac{A_0}{\mu D_0}.$$

This factor indicates the extent to which the nonlinear term retained in the ion dynamics affects the average ion position, as compared to simply retaining a constant on the right hand side of Eq. (5.10) (with $\kappa = 0$). If g differs significantly from unity, we conclude that the quadratic nonlinear term is indeed significant. Some numerical values of g obtained using the iterative method (which converged in all cases) are reported in Table 5.1. It is seen that the quadratic nonlinearity can play a significant role (up to about 40 percent for reasonable parameter values).

TABLE 5.1: Parameter values a, q, μ, and κ, and the nonlinear enhancement factor g.

a	q	μ	κ	Nonlinear enhancement factor g
0	0.1	0.003	0.5	1.3099
0	0.3	0.026	0.5	1.2834
0	0.6	0.1	0.5	1.2862
0.1	0.6	0.15	0.5	1.2424
−0.1	0.8	0.125	0.5	1.4128
0	0.9	0.13	0.5	1.0761

We hope that the approximate periodic solution of Eq. (5.10) developed using the iterative method proposed in this section will appeal to the mass spectrometry research community.

5.5 Concluding remarks

In this chapter we began with a specific mass spectrometry application, namely DC dipolar excitation in Paul traps. Electrostatic field calculations were used to demonstrate that the relevant governing equation for ion dynamics is an inhomogeneous Mathieu equation with a constant as well as a quadratic term on the right hand side.

A small parameter was identified and used to develop a second order averaging calculation, which was validated by comparison with direct numerical solution. The averaging calculation yielded slow flows that showed how, in the presence of a small amount of damping, and for general parameter values including the important *nonresonant* case, a simple periodic particular solution is an attractor, i.e., stable.

Subsequently, much simpler two-term harmonic balance equations were found to yield good approximations to that same periodic solution. Solution of the two-term harmonic balance equations in the presence of nonlinearity was then set up for easy iterative solution. These two-term approximations may be attractive to users who do not wish to delve into the tedious intermediate details of the averaging calculation. Given that the averaging calculation has been shown to predict a single stable periodic solution of practical interest, it is useful to have such quick approximations for that stable periodic solution.

The iterative approach for the two-term approximation was found to work well and quickly. A simple estimate of the importance of the nonlinear term, in form of an enhancement factor, showed effects of up to about 40 percent for reasonable parameter values. Thus, the practical utility of retaining the quadratic term in our analyses was justified.

We hope that this chapter will be of interest and use both to academicians interested in the nonlinear dynamics of ions in Paul traps as well as to practitioners interested in using such traps with DC dipolar excitation.

This concludes the studies of nonresonant interactions undertaken in this thesis.

Chapter 6

Concluding Remarks

This thesis has presented four studies on nonresonant interactions. These studies have relevance to practical applications and contain new academic components as well.

Chapters 2, 3 and 4 present nonresonant interaction studies in relevance to untuned vibration suppression in mechanical systems. In these studies, we have demonstrated stabilization of an unstable mode using a light, nonresonant, secondary limit cycle oscillator. The second order perturbation analyses yielded amplitude slow-flows that are independent of phases, reducing the analyses to lower order. Novel analytical understanding has emerged from the simplified amplitude evolution equations. Further, a finite number of phase portraits depict unifying dynamics of the nonresonant nonlinear systems studied in this thesis.

In Chapter 2, the primary system representing an unstable mode of a structure is modeled using a negatively damped single degree of freedom spring-mass system. The attached secondary light limit cycle oscillator is modelled using the van der Pol oscillator. We achieved conditional stabilization of the primary oscillator under the criterion that a single nondimensional governing parameter is within a particular range (between 0 and 4). Two phase portraits summarized the nonresonant dynamics of the system.

In light of the available models of limit cycle oscillations using a mass on a moving belt system, we introduced a quartic nonlinearity in the secondary oscillator in Chapter 3. This models some additional responses of that system, i.e., double limit cycle and globally stable equilibrium. Following the multiple scales treatment of Chapter 2, we found that two nondimensional parameters govern the system dynamics. We identified bifurcation boundaries in the parameter plane and detailed the dynamics using amplitude phase portraits. We identified parameter domains which can provide conditional or unconditional stabilization of the primary system.

In Chapter 4, the primary system is a regenerative delay model of machine tool vibrations, and the secondary system is a light, nonresonant, limit cycle oscillator. Using the method of multiple scales, we found that three nondimensional parameters govern the system dynamics. We pictured feasible phase portraits and found the criterion for supercritical bifurcation along the linear stability boundary. We establish supercriticality for the complete second lobe, whereas earlier studies, in our knowledge, have reported supercriticality for limited segments of the lobe. We noted the existence of a turning point bifurcation using DDE-BIFTOOL. This chapter provides useful insights on the efficacy of a nonresonant limit cycle absorber to suppress machine tool vibrations.

Chapter 5 explores nonresonant interactions relevant to dipolar DC excitation in Paul traps. The major contribution of this chapter lies in a proposed simple steady state solution that was unnoticed earlier. A nonresonant averaging analysis establishes the asymptotic stability of that simple solution. The important takeaway for an analyst is that the simple solution has a frequency the same as that of excitation, independent of the secular frequency characterizing the ion. Finally, for practitioners, an enhancement factor helps to estimate the effect of the quadratic nonlinearity.

We hope that this thesis will prompt further research interest in nonresonant interactions in nonlinear dynamical systems.

Appendix A

Expressions from multiple scale analysis of Chapter 2

The solution for Z_1 is

$$
\begin{aligned}
Z_1(T_0, T_1, T_2) = -\frac{1}{4(1-{\omega_p}^2)^4}\big(&(2\gamma{\omega_p}^4 - 4\gamma{\omega_p}^2 + 2\gamma)RQ^2 - (4\gamma{\omega_p}^4 \\
&-8\gamma{\omega_p}^2 + 4\gamma - \gamma R^2)R\big)\cos(T_0+\phi) + \frac{m{\omega_p}^4 R}{(1-{\omega_p}^2)^3}\sin(T_0+\phi) \\
&+\frac{\gamma R^3}{4(9-{\omega_p}^2)(1-{\omega_p}^2)^3}\cos(3T_0+3\phi) - \frac{\gamma Q^3}{32\omega_p}\cos(3\omega_p T_0 + 3\psi) \\
&+\frac{(1-2\omega_p)\gamma Q^2 R}{4(1-3\omega_p)(1+\omega_p)(1-\omega_p)^2}\cos(T_0 - 2\omega_p T_0 + \phi - 2\psi) \\
&+\frac{(1+2\omega_p)\gamma Q^2 R}{4(1+3\omega_p)(1-\omega_p)(1+\omega_p)^2}\cos(T_0 + 2\omega_p T_0 + \phi + 2\psi) \\
&+\frac{\gamma(2-\omega_p)QR^2}{16(1-\omega_p)(1-{\omega_p}^2)^2}\cos(2T_0 - \omega_p T_0 + 2\phi - \psi) \\
&-\frac{\gamma(2+\omega_p)QR^2}{16(1+\omega_p)(1-{\omega_p}^2)^2}\cos(2T_0 + \omega_p T_0 + 2\phi + \psi). \qquad \text{(A.1)}
\end{aligned}
$$

Recall Eq. (2.27), the expressions are

$$
\begin{aligned}
L_1 = \frac{\partial^2 X_2}{\partial {T_0}^2} + X_2 - \left(\frac{m^2 {\omega_p}^4 (1+3{\omega_p}^2) R}{4(1-{\omega_p}^2)^3} + 2R \frac{\partial \phi}{\partial T_2} \right) \sin(T_0+\phi) \\
+ \left(cR + \frac{m\gamma \left(2(Q^2-2)(1-{\omega_p}^2)^2 + R^2 \right) R}{4(1-{\omega_p}^2)^4} + 2\frac{\partial R}{\partial T_2} \right) \cos(T_0+\phi) \\
- \frac{m\gamma\omega_p \left((Q^2-4)(1-{\omega_p}^2)^2 + 2R^2 \right) Q}{4(1-{\omega_p}^2)^3} \cos(\omega_p T_0 + \psi) \\
+ \frac{m^2 {\omega_p}^6 Q}{(1-{\omega_p}^2)^2} \sin(\omega_p T_0+\psi) + \frac{9m\gamma\omega_p Q^3}{32} \cos(3\omega_p T_0 + 3\psi) \\
- \frac{9m\gamma R^3}{4(9-{\omega_p}^2)(1-{\omega_p}^2)^3} \cos(3T_0+3\phi) \\
- \frac{m\gamma(1+2\omega_p)^3 Q^2 R}{4(1+3\omega_p)(1-\omega_p)(1+\omega_p)^2} \cos(T_0 + 2\omega_p T_0 + \phi + 2\psi) \\
- \frac{m\gamma(1-2\omega_p)^3 Q^2 R}{4(1-3\omega_p)(1+\omega_p)(1-\omega_p)^2} \cos(T_0 - 2\omega_p T_0 + \phi - 2\psi) \\
+ \frac{m\gamma(2+\omega_p)^3 Q R^2}{16(1+\omega_p)(1-{\omega_p}^2)^2} \cos(2T_0 + \omega_p T_0 + 2\phi + \psi) \\
- \frac{m\gamma(2-\omega_p)^3 Q R^2}{16(1-\omega_p)(1-{\omega_p}^2)^2} \cos(2T_0 - \omega_p T_0 + 2\phi - \psi), \quad \text{(A.2)}
\end{aligned}
$$

and

$$L_2 = \frac{\partial^2 Z_2}{\partial {T_0}^2} + {\omega_p}^2 Z_2 + \frac{\partial^2 X_2}{\partial {T_0}^2} + \frac{{\omega_p}^2}{8(1-{\omega_p}^2)^5}\Big(m\gamma(6{\omega_p}^6 - 10{\omega_p}^4 + 2{\omega_p}^2$$
$$+ 2)Q^2R + m\gamma(-12{\omega_p}^6 + 20{\omega_p}^4 - 4{\omega_p}^2 - 4 + 7{\omega_p}^2R^2 + R^2)R + (-16{\omega_p}^8 + 64{\omega_p}^6$$
$$- 96{\omega_p}^4 + 64{\omega_p}^2 - 16)\frac{\partial R}{\partial T_2}\Big)\cos(T_0+\phi) + \frac{1}{16(9-{\omega_p}^2)(1-9{\omega_p}^2)(1-{\omega_p}^2)^6}$$
$$\Big((-45{\omega_p}^{10} + 518{\omega_p}^8 - 1110{\omega_p}^6 + 864{\omega_p}^4 - 245{\omega_p}^2 + 18)\gamma^2R^2Q^2 + (-18{\omega_p}^{14}$$
$$+ 264{\omega_p}^{12} - 1150{\omega_p}^{10} + 2356{\omega_p}^8 - 2574{\omega_p}^6 + 1504{\omega_p}^4 - 418{\omega_p}^2 + 36)\gamma^2Q^4$$
$$+ (18{\omega_p}^4 - 92{\omega_p}^2 + 10)\gamma^2R^4 + (72{\omega_p}^{14} - 1016{\omega_p}^{12} + 4072{\omega_p}^{10} - 7640{\omega_p}^8 + 7640{\omega_p}^6$$
$$- 4072{\omega_p}^4 + 1016{\omega_p}^2 - 72)\gamma^2Q^2 + (-72{\omega_p}^8 + 800{\omega_p}^6 - 1456{\omega_p}^4 + 800{\omega_p}^2 - 72)\gamma^2R^2$$
$$+ m^2(-36{\omega_p}^{16} + 292{\omega_p}^{14} + 472{\omega_p}^{12} - 1784{\omega_p}^{10} + 1164{\omega_p}^8 - 108{\omega_p}^6) + \gamma^2(144{\omega_p}^{12}$$
$$- 1888{\omega_p}^{10} + 6256{\omega_p}^8 - 9024{\omega_p}^6 + 6256{\omega_p}^4 - 1888{\omega_p}^2 + 144) + (-288{\omega_p}^{16}$$
$$+ 4064{\omega_p}^{14} - 16288{\omega_p}^{12} + 30560{\omega_p}^{10} - 30560{\omega_p}^8 + 16288{\omega_p}^6 - 4064{\omega_p}^4$$
$$+ 288{\omega_p}^2)\frac{\partial \phi}{\partial T_2}\Big)R\sin(T_0+\phi) + \frac{\omega_p}{4(1-{\omega_p}^2)^4}\Big(({\omega_p}^8 - 3{\omega_p}^6 + 3{\omega_p}^4 - {\omega_p}^2)m\gamma Q^3$$
$$+ (-2{\omega_p}^4 - 2{\omega_p}^2)m\gamma R^2Q + (-4{\omega_p}^8 + 12{\omega_p}^6 - 12{\omega_p}^4 + 4{\omega_p}^2)m\gamma Q + (8{\omega_p}^8 - 32{\omega_p}^6$$
$$+ 48{\omega_p}^4 - 32{\omega_p}^2 + 8)\frac{\partial Q}{\partial T_2}\Big)\cos(\omega_pT_0+\psi) - \frac{1}{128(1-9{\omega_p}^2)(1-{\omega_p}^2)^5}\Big((336{\omega_p}^8$$
$$- 896{\omega_p}^6 + 800{\omega_p}^4 - 256{\omega_p}^2 + 16)\gamma^2R^2Q^2 + (63{\omega_p}^{12} - 322{\omega_p}^{10} + 665{\omega_p}^8 - 700{\omega_p}^6$$
$$+ 385{\omega_p}^4 - 98{\omega_p}^2 + 7)\gamma^2Q^4 + (108{\omega_p}^4 - 84{\omega_p}^2 + 8)\gamma^2R^4 + (-288{\omega_p}^{12} + 1472{\omega_p}^{10}$$
$$- 3040{\omega_p}^8 + 3200{\omega_p}^6 - 1760{\omega_p}^4 + 448{\omega_p}^2 - 32)\gamma^2Q^2 + (-288{\omega_p}^8 + 896{\omega_p}^6$$
$$- 960{\omega_p}^4 + 384{\omega_p}^2 - 32)\gamma^2R^2 + m^2(-864{\omega_p}^{14} + 2688{\omega_p}^{12} - 2880{\omega_p}^{10} + 1152{\omega_p}^8$$
$$- 96{\omega_p}^6) + \gamma^2(288{\omega_p}^{12} - 1472{\omega_p}^{10} + 3040{\omega_p}^8 - 3200{\omega_p}^6 + 1760{\omega_p}^4 - 448{\omega_p}^2 + 32)$$
$$+ (2304{\omega_p}^{13} - 11776{\omega_p}^{11} + 24320{\omega_p}^9 - 25600{\omega_p}^7 + 14080{\omega_p}^5 - 3584{\omega_p}^3$$
$$+ 256\omega_p)\frac{\partial \psi}{\partial T_2}\Big)Q\sin(\omega_pT_0+\psi) + \frac{m\gamma{\omega_p}^2(7{\omega_p}^4 - 46{\omega_p}^2 - 9)R^3}{8(9-{\omega_p}^2)(1-{\omega_p}^2)^5}\cos(3T_0+3\phi)$$
$$- \frac{3\gamma^2R^3}{16(9-{\omega_p}^2)(1-{\omega_p}^2)^6}\big(({\omega_p}^8 - 17{\omega_p}^6 + 69{\omega_p}^4 - 91{\omega_p}^2 + 38)Q^2$$
$$+(-3{\omega_p}^2 + 11)R^2 + 8{\omega_p}^6 - 56{\omega_p}^4 + 88{\omega_p}^2 - 40\big)\sin(3T_0+3\phi) - \frac{5m\gamma{\omega_p}^3Q^3}{32(1-{\omega_p}^2)}$$
$$\cos(3\omega_pT_0+3\psi) + \frac{\gamma^2Q^3}{128(1-9{\omega_p}^2)(1-{\omega_p}^2)^3}\big((9{\omega_p}^8 - 28{\omega_p}^6 + 30{\omega_p}^4 - 12{\omega_p}^2$$
$$+1)Q^2 + (540{\omega_p}^4 - 152{\omega_p}^2 - 4)R^2 + 72{\omega_p}^8 - 224{\omega_p}^6 + 240{\omega_p}^4 - 96{\omega_p}^2 + 8\big)$$
$$\sin(3\omega_pT_0 + 3\psi) + \frac{5\gamma^2R^5}{16(9-{\omega_p}^2)(1-{\omega_p}^2)^5}\sin(5T_0 + 5\phi) - \frac{5\gamma^2Q^5}{128}\sin(5\omega_pT_0 + 5\psi)$$

$$
\begin{aligned}
&- \frac{m\gamma{\omega_p}^2(22{\omega_p}^4+3{\omega_p}^3-3{\omega_p}^2+\omega_p+1)RQ^2}{8(1+3\omega_p)(1-{\omega_p}^2)^3}\cos(T_0 + 2\omega_p T_0 + \phi + 2\psi)\\
&- \frac{m\gamma{\omega_p}^2(22{\omega_p}^4-3{\omega_p}^3-3{\omega_p}^2-\omega_p+1)RQ^2}{8(1-3\omega_p)(1-{\omega_p}^2)^3}\cos(T_0 - 2\omega_p T_0 + \phi - 2\psi)\\
&+ \frac{m\gamma{\omega_p}^2({\omega_p}^4+7{\omega_p}^3+14{\omega_p}^2-2\omega_p+4)QR^2}{16(1-{\omega_p}^2)^4}\cos(2T_0 + \omega_p T_0 + 2\phi + \psi)\\
&- \frac{m\gamma{\omega_p}^2({\omega_p}^4-7{\omega_p}^3+14{\omega_p}^2+2\omega_p+4)QR^2}{16(1-{\omega_p}^2)^4}\cos(2T_0 - \omega_p T_0 + 2\phi - \psi)\\
&+ \frac{\gamma^2(4+\omega_p)({\omega_p}^3+2{\omega_p}^2-17\omega_p-26)QR^4}{64(9-{\omega_p}^2)(1+\omega_p)(1-{\omega_p}^2)^4}\sin(4T_0 + \omega_p T_0 + 4\phi + \psi)\\
&+ \frac{\gamma^2(4-\omega_p)({\omega_p}^3-2{\omega_p}^2-17\omega_p+26)QR^4}{64(9-{\omega_p}^2)(1-\omega_p)(1-{\omega_p}^2)^4}\sin(4T_0 - \omega_p T_0 + 4\phi - \psi)\\
&+ \frac{\gamma^2(1+4\omega_p)(11{\omega_p}^2+8\omega_p+1)Q^4R}{64\omega_p(1+3\omega_p)(1+\omega_p)(1-{\omega_p}^2)}\sin(T_0 + 4\omega_p T_0 + \phi + 4\psi)\\
&- \frac{\gamma^2(1-4\omega_p)(11{\omega_p}^2-8\omega_p+1)Q^4R}{64\omega_p(1-3\omega_p)(1-\omega_p)(1-{\omega_p}^2)}\sin(T_0 - 4\omega_p T_0 + \phi - 4\psi)\\
&+ \frac{\gamma^2RQ^2}{64\omega_p(1-9{\omega_p}^2)(1-{\omega_p}^2)^3}\big((5{\omega_p}^2+54{\omega_p}^7+135{\omega_p}^6-186{\omega_p}^5-141{\omega_p}^4\\
&+146{\omega_p}^3-14\omega_p+1)Q^2+(-36{\omega_p}^4+78{\omega_p}^3-2{\omega_p}^2-4\omega_p)R^2+48{\omega_p}^7-32{\omega_p}^2\\
&-224{\omega_p}^6+112{\omega_p}^5+256{\omega_p}^4-176{\omega_p}^3+16\omega_p\big)\sin(T_0 - 2\omega_p T_0 + \phi - 2\psi)\\
&+ \frac{\gamma^2RQ^2}{64\omega_p(1-9{\omega_p}^2)(1-{\omega_p}^2)^3}\big((-5{\omega_p}^2+54{\omega_p}^7-135{\omega_p}^6-186{\omega_p}^5+141{\omega_p}^4\\
&+146{\omega_p}^3-14\omega_p-1)Q^2+(36{\omega_p}^4+78{\omega_p}^3+2{\omega_p}^2-4\omega_p)R^2+48{\omega_p}^7+224{\omega_p}^6\\
&+112{\omega_p}^5-256{\omega_p}^4-176{\omega_p}^3+32{\omega_p}^2+16\omega_p\big)\sin(T_0 + 2\omega_p T_0 + \phi + 2\psi)\\
&- \frac{\gamma^2QR^2}{32(1-3\omega_p)(9-{\omega_p}^2)(1-{\omega_p}^2)^5}\big((3{\omega_p}^{10}-18{\omega_p}^9-48{\omega_p}^8+283{\omega_p}^7\\
&+193{\omega_p}^6-1277{\omega_p}^5+7{\omega_p}^4+1777{\omega_p}^3-416{\omega_p}^2-765\omega_p+261)Q^2\\
&+(-6{\omega_p}^5-22{\omega_p}^4+116{\omega_p}^3+84{\omega_p}^2-334\omega_p+98)R^2+12{\omega_p}^9+44{\omega_p}^8-256{\omega_p}^7\\
&-448{\omega_p}^6+1592{\omega_p}^5+440{\omega_p}^4-2464{\omega_p}^3+288{\omega_p}^2+1116\omega_p-324\big)\\
&\sin(2T_0 - \omega_p T_0 + 2\phi - \psi) + \frac{\gamma^2QR^2}{32(1+3\omega_p)(9-{\omega_p}^2)(1-{\omega_p}^2)^5}\\
&\big((3{\omega_p}^{10}+18{\omega_p}^9-48{\omega_p}^8-283{\omega_p}^7+193{\omega_p}^6+1277{\omega_p}^5+7{\omega_p}^4\\
&-1777{\omega_p}^3-416{\omega_p}^2+765\omega_p+261)Q^2+(6{\omega_p}^5-22{\omega_p}^4-116{\omega_p}^3+84{\omega_p}^2+334\omega_p\\
&+98)R^2-12{\omega_p}^9+44{\omega_p}^8+256{\omega_p}^7-448{\omega_p}^6-1592{\omega_p}^5+440{\omega_p}^4\\
&+2464{\omega_p}^3+288{\omega_p}^2-1116\omega_p-324\big)\sin(2T_0 + \omega_p T_0 + 2\phi + \psi)
\end{aligned}
$$

$$
\begin{aligned}
&- \frac{\gamma^2(2+3\omega_p)(6{\omega_p}^3+49{\omega_p}^2+24\omega_p+1)R^2Q^3}{128\omega_p(1+3\omega_p)(1+\omega_p)(1-{\omega_p}^2)^2}\sin(2T_0+3\omega_pT_0+2\phi+3\psi)\\
&\quad + \frac{\gamma^2(2-3\omega_p)(6{\omega_p}^3-49{\omega_p}^2+24\omega_p-1)R^2Q^3}{128\omega_p(1-3\omega_p)(1-\omega_p)(1-{\omega_p}^2)^2}\sin(2T_0-3\omega_pT_0+2\phi-3\psi)\\
&\quad - \frac{\gamma^2(3+2\omega_p)(3{\omega_p}^4+11{\omega_p}^3-29{\omega_p}^2-107\omega_p-38)R^3Q^2}{32(1+3\omega_p)(9-{\omega_p}^2)(1+\omega_p)(1-{\omega_p}^2)^3}\sin(3T_0+2\omega_pT_0\\
&\qquad +3\phi+2\psi) - \frac{\gamma^2(3-2\omega_p)(3{\omega_p}^4-11{\omega_p}^3-29{\omega_p}^2+107\omega_p-38)}{32(1-3\omega_p)(9-{\omega_p}^2)(1-\omega_p)(1-{\omega_p}^2)^3}\\
&\qquad R^3Q^2\sin(3T_0-2\omega_pT_0+3\phi-2\psi). \qquad (A.3)
\end{aligned}
$$

The solution for X_2 is

$$
\begin{aligned}
X_2(T_0,T_1,T_2) = {}& \frac{((Q^2-4)(1-{\omega_p}^2)^2+2R^2)m\gamma Q\omega_p}{4(1-{\omega_p}^2)^4}\cos(\omega_pT_0+\psi)\\
& -\frac{Qm^2{\omega_p}^6}{(1-{\omega_p}^2)^3}\sin(\omega_pT_0+\psi) - \frac{9m\gamma\omega_pQ^3}{32(1-9{\omega_p}^2)}\cos(3\omega_pT_0+3\psi)\\
& - \frac{9m\gamma R^3}{32(9-{\omega_p}^2)(1-{\omega_p}^2)^3}\cos(3T_0+3\phi)\\
& - \frac{(1+2\omega_p)^3m\gamma RQ^2}{16\omega_p(1+3\omega_p)(1-\omega_p)(1+\omega_p)^3}\cos(T_0+\phi+2\omega_pT_0+2\psi)\\
& + \frac{(1-2\omega_p)^3m\gamma RQ^2}{16\omega_p(1-3\omega_p)(1+\omega_p)(1-\omega_p)^3}\cos(T_0+\phi-2\omega_pT_0-2\psi)\\
& + \frac{(2+\omega_p)^3m\gamma R^2Q}{16(3+\omega_p)(1-\omega_p)^2(1+\omega_p)^4}\cos(2T_0+2\phi+\omega_pT_0+\psi)\\
& - \frac{(2-\omega_p)^3m\gamma R^2Q}{16(3-\omega_p)(1+\omega_p)^2(1-\omega_p)^4}\cos(2T_0+2\phi-\omega_pT_0-\psi) \qquad (A.4)
\end{aligned}
$$

Appendix B

Expressions for p_1, p_2, τ_1 and τ_2 of case-2 in Chapter 4

$$
\begin{aligned}
p_1 = \Big(\omega_p\,\big(&-\gamma^2 m^3 {\omega_p}^7 - 3\,m^3 {\omega_p}^7 {\omega_2}^2 + 20\,m^2 {\omega_p}^6 {\omega_2}^3 + \gamma^4 m {\omega_p}^5 - 5\,\gamma^2 m {\omega_p}^5 {\omega_2}^2 \\
&- 44\,m{\omega_p}^5{\omega_2}^4 + 2\,\gamma^4{\omega_p}^4\omega_2 - 2\,\gamma^2 m^2{\omega_p}^4\omega_2 + 16\,\gamma^2{\omega_p}^4{\omega_2}^3 - 12\,m^2{\omega_p}^4{\omega_2}^3 \\
&+ 32\,{\omega_p}^4{\omega_2}^5 - 2\,\gamma^4 m{\omega_p}^3 + 2\,\gamma^2 m{\omega_p}^3{\omega_2}^2 + 56\,m{\omega_p}^3{\omega_2}^4 - 4\,\gamma^4{\omega_p}^2\omega_2 \\
&- 32\,\gamma^2{\omega_p}^2{\omega_2}^3 - 64\,{\omega_p}^2{\omega_2}^5 + \gamma^4 m\omega_p + 3\,\gamma^2 m\omega_p\,{\omega_2}^2 \\
&- 12\,m\omega_p\,{\omega_2}^4 + 2\,\gamma^4\omega_2 + 16\,\gamma^2{\omega_2}^3 + 32\,{\omega_2}^5\big)\Big)\Big/\Big(2\,\big(-2\,m{\omega_p}^3\omega_2 + \gamma^2{\omega_p}^2 \\
&+4\,{\omega_p}^2{\omega_2}^2 - \gamma^2 - 4\,{\omega_2}^2\big)^2\Big),
\end{aligned}
$$

$$
\tau_1 = -\frac{\omega_2}{\omega_1}\bar{\tau} + \frac{2\Big(\gamma\, m\omega_p\,\big(\gamma^2 m{\omega_p}^3 + 5\,m{\omega_p}^3{\omega_2}^2 - \gamma^2{\omega_p}^2\omega_2 - 8\,{\omega_p}^2{\omega_2}^3 + 3\,\gamma^2\omega_2 + 16\,{\omega_2}^3\big)\Big)}{\Big(\big(\gamma^2 + 4\,{\omega_2}^2\big)\big(m^2{\omega_p}^6 - 4\,m{\omega_p}^5\omega_2 + \gamma^2{\omega_p}^4 + 4\,{\omega_p}^4{\omega_2}^2 + 4\,m{\omega_p}^3\omega_2 - 2\,\gamma^2{\omega_p}^2 - 8\,{\omega_p}^2{\omega_2}^2 + \gamma^2 + 4\,{\omega_2}^2\big)\Big)},
$$

$$
\begin{aligned}
p_2 = -\Big(& -\gamma^4 m^4 {\omega_p}^{10} - 10\,\gamma^2 m^4 {\omega_p}^{10} {\omega_2}^2 - m^4 {\omega_p}^{10} {\omega_2}^4 + 8\,c\gamma\, m^3 {\omega_p}^{10} {\omega_2}^2 \\
& + 4\,\gamma^4 m^3 {\omega_p}^9 \omega_2 + 20\,\gamma^2 m^3 {\omega_p}^9 {\omega_2}^3 + 14\, m^3 {\omega_p}^9 {\omega_2}^5 - 8\,c\gamma^3 m^2 {\omega_p}^9 \omega_2 \\
& - 32\,c\gamma\, m^2 {\omega_p}^9 {\omega_2}^3 + 6\,\gamma^4 m^2 {\omega_p}^8 {\omega_2}^2 + 14\,\gamma^2 m^2 {\omega_p}^8 {\omega_2}^4 - 60\, m^2 {\omega_p}^8 {\omega_2}^6 \\
& + 2\,c\gamma^5 m {\omega_p}^8 + 16\,c\gamma^3 m {\omega_p}^8 {\omega_2}^2 + 32\,c\gamma\, m {\omega_p}^8 {\omega_2}^4 - 2\,\gamma^6 m {\omega_p}^7 \omega_2 \\
& - 8\,\gamma^4 m^3 {\omega_p}^7 \omega_2 - 14\,\gamma^4 m {\omega_p}^7 {\omega_2}^3 - 42\,\gamma^2 m^3 {\omega_p}^7 {\omega_2}^3 - 6\,\gamma^2 m {\omega_p}^7 {\omega_2}^5 \\
& - 6\, m^3 {\omega_p}^7 {\omega_2}^5 + 104\, m {\omega_p}^7 {\omega_2}^7 + 8\,c\gamma^3 m^2 {\omega_p}^7 \omega_2 + 32\,c\gamma\, m^2 {\omega_p}^7 {\omega_2}^3 \\
& - \gamma^6 {\omega_p}^6 {\omega_2}^2 - 7\,\gamma^4 m^2 {\omega_p}^6 {\omega_2}^2 - 12\,\gamma^4 {\omega_p}^6 {\omega_2}^4 - 4\,\gamma^2 m^2 {\omega_p}^6 {\omega_2}^4 \\
& - 48\,\gamma^2 {\omega_p}^6 {\omega_2}^6 + 72\, m^2 {\omega_p}^6 {\omega_2}^6 - 64\, {\omega_p}^6 {\omega_2}^8 - 4\,c\gamma^5 m {\omega_p}^6 \\
& - 32\,c\gamma^3 m {\omega_p}^6 {\omega_2}^2 - 64\,c\gamma\, m {\omega_p}^6 {\omega_2}^4 + 6\,\gamma^6 m {\omega_p}^5 \omega_2 + 48\,\gamma^4 m {\omega_p}^5 {\omega_2}^3 \\
& + 66\,\gamma^2 m {\omega_p}^5 {\omega_2}^5 - 216\, m {\omega_p}^5 {\omega_2}^7 + 3\,\gamma^6 {\omega_p}^4 {\omega_2}^2 - 3\,\gamma^4 m^2 {\omega_p}^4 {\omega_2}^2 \\
& + 36\,\gamma^4 {\omega_p}^4 {\omega_2}^4 - 26\,\gamma^2 m^2 {\omega_p}^4 {\omega_2}^4 + 144\,\gamma^2 {\omega_p}^4 {\omega_2}^6 - 12\, m^2 {\omega_p}^4 {\omega_2}^6 \\
& + 192\, {\omega_p}^4 {\omega_2}^8 + 2\,c\gamma^5 m {\omega_p}^4 + 16\,c\gamma^3 m {\omega_p}^4 {\omega_2}^2 + 32\,c\gamma\, m {\omega_p}^4 {\omega_2}^4 \\
& - 6\,\gamma^6 m {\omega_p}^3 \omega_2 - 54\,\gamma^4 m {\omega_p}^3 {\omega_2}^3 - 114\,\gamma^2 m {\omega_p}^3 {\omega_2}^5 + 120\, m {\omega_p}^3 {\omega_2}^7 \\
& - 3\,\gamma^6 {\omega_p}^2 {\omega_2}^2 - 36\,\gamma^4 {\omega_p}^2 {\omega_2}^4 - 144\,\gamma^2 {\omega_p}^2 {\omega_2}^6 - 192\, {\omega_p}^2 {\omega_2}^8 \\
& + 2\,\gamma^6 m \omega_p\, \omega_2 + 20\,\gamma^4 m \omega_p\, {\omega_2}^3 + 54\,\gamma^2 m \omega_p\, {\omega_2}^5 - 8\, m \omega_p\, {\omega_2}^7 \\
& + \gamma^6 {\omega_2}^2 + 12\,\gamma^4 {\omega_2}^4 + 48\,\gamma^2 {\omega_2}^6 + 64\, {\omega_2}^8 \Big) \\
& \qquad \Big/ \Big(2\left(-2\, m {\omega_p}^3 \omega_2 + \gamma^2 {\omega_p}^2 + 4\, {\omega_2}^2 {\omega_p}^2 - \gamma^2 - 4\, {\omega_2}^2\right)^3 \Big),
\end{aligned}
$$

$$\tau_2 = \frac{\omega_2^2}{\omega_1^2}\bar{\tau} + 2\Big(- 2\,\gamma^3 m^4 {\omega_p}^9 {\omega_2}^3 - 6\,\gamma\, m^4 {\omega_p}^9 {\omega_2}^5 - 2\,c\gamma^4 m^3 {\omega_p}^9 \omega_2 - 16\,c\gamma^2 m^3 {\omega_p}^9 {\omega_2}^3$$
$$- 32\,cm^3 {\omega_p}^9 {\omega_2}^5 - \gamma^7 m^3 {\omega_p}^8 - 8\,\gamma^5 m^3 {\omega_p}^8 {\omega_2}^2 + 48\,\gamma\, m^3 {\omega_p}^8 {\omega_2}^6 + c\gamma^6 m^2 {\omega_p}^8$$
$$+ 20\,c\gamma^4 m^2 {\omega_p}^8 {\omega_2}^2 + 112\,c\gamma^2 m^2 {\omega_p}^8 {\omega_2}^4 + 192\,cm^2 {\omega_p}^8 {\omega_2}^6 - 2\,\gamma^5 m^2 {\omega_p}^7 {\omega_2}^3 - 44\,\gamma^3 m^2 {\omega_p}^7 {\omega_2}^5$$
$$- 112\,\gamma\, m^2 {\omega_p}^7 {\omega_2}^7 - 6\,c\gamma^6 m {\omega_p}^7 \omega_2 - 72\,c\gamma^4 m {\omega_p}^7 {\omega_2}^3 - 288\,c\gamma^2 m {\omega_p}^7 {\omega_2}^5 - 384\,cm {\omega_p}^7 {\omega_2}^7$$
$$+ \gamma^7 m^3 {\omega_p}^6 + \gamma^7 m {\omega_p}^6 {\omega_2}^2 + 9\,\gamma^5 m^3 {\omega_p}^6 {\omega_2}^2 + 17\,\gamma^5 m {\omega_p}^6 {\omega_2}^4 + 8\,\gamma^3 m^3 {\omega_p}^6 {\omega_2}^4$$
$$+ 72\,\gamma^3 m {\omega_p}^6 {\omega_2}^6 - 32\,\gamma\, m^3 {\omega_p}^6 {\omega_2}^6 + 80\,\gamma\, m {\omega_p}^6 {\omega_2}^8 + c\gamma^8 {\omega_p}^6 - c\gamma^6 m^2 {\omega_p}^6$$
$$+ 16\,c\gamma^6 {\omega_p}^6 {\omega_2}^2 - 20\,c\gamma^4 m^2 {\omega_p}^6 {\omega_2}^2 + 96\,c\gamma^4 {\omega_p}^6 {\omega_2}^4 - 112\,c\gamma^2 m^2 {\omega_p}^6 {\omega_2}^4 + 256\,c\gamma^2 {\omega_p}^6 {\omega_2}^6$$
$$- 192\,cm^2 {\omega_p}^6 {\omega_2}^6 + 256\,c {\omega_p}^6 {\omega_2}^8 - 4\,\gamma^7 m^2 {\omega_p}^5 \omega_2 - 28\,\gamma^5 m^2 {\omega_p}^5 {\omega_2}^3 + 24\,\gamma^3 m^2 {\omega_p}^5 {\omega_2}^5$$
$$+ 224\,\gamma\, m^2 {\omega_p}^5 {\omega_2}^7 + 12\,c\gamma^6 m {\omega_p}^5 \omega_2 + 144\,c\gamma^4 m {\omega_p}^5 {\omega_2}^3 + 576\,c\gamma^2 m {\omega_p}^5 {\omega_2}^5 + 768\,cm {\omega_p}^5 {\omega_2}^7$$
$$- 6\,\gamma^7 m {\omega_p}^4 {\omega_2}^2 - 79\,\gamma^5 m {\omega_p}^4 {\omega_2}^4 - 296\,\gamma^3 m {\omega_p}^4 {\omega_2}^6 - 304\,\gamma\, m {\omega_p}^4 {\omega_2}^8 - 3\,c\gamma^8 {\omega_p}^4$$
$$- 48\,c\gamma^6 {\omega_p}^4 {\omega_2}^2 - 288\,c\gamma^4 {\omega_p}^4 {\omega_2}^4 - 768\,c\gamma^2 {\omega_p}^4 {\omega_2}^6 - 768\,c {\omega_p}^4 {\omega_2}^8 + 4\,\gamma^7 m^2 {\omega_p}^3 \omega_2$$
$$+ 38\,\gamma^5 m^2 {\omega_p}^3 {\omega_2}^3 + 84\,\gamma^3 m^2 {\omega_p}^3 {\omega_2}^5 + 16\,\gamma\, m^2 {\omega_p}^3 {\omega_2}^7 - 6\,c\gamma^6 m {\omega_p}^3 \omega_2 - 72\,c\gamma^4 m {\omega_p}^3 {\omega_2}^3$$
$$- 288\,c\gamma^2 m {\omega_p}^3 {\omega_2}^5 - 384\,cm {\omega_p}^3 {\omega_2}^7 + 5\,\gamma^7 m {\omega_p}^2 {\omega_2}^2 + 59\,\gamma^5 m {\omega_p}^2 {\omega_2}^4 + 184\,\gamma^3 m {\omega_p}^2 {\omega_2}^6$$
$$+ 112\,\gamma\, m {\omega_p}^2 {\omega_2}^8 + 3\,c\gamma^8 {\omega_p}^2 + 48\,c\gamma^6 {\omega_p}^2 {\omega_2}^2 + 288\,c\gamma^4 {\omega_p}^2 {\omega_2}^4 + 768\,c\gamma^2 {\omega_p}^2 {\omega_2}^6$$
$$+ 768\,c {\omega_p}^2 {\omega_2}^8 + 3\,\gamma^5 m {\omega_2}^4 + 40\,\gamma^3 m {\omega_2}^6 + 112\,\gamma\, m {\omega_2}^8 - c\gamma^8$$
$$- 16\,c\gamma^6 {\omega_2}^2 - 96\,c\gamma^4 {\omega_2}^4 - 256\,c\gamma^2 {\omega_2}^6 - 256\,c {\omega_2}^8\Big)$$
$$\Big/\Big(\left(\gamma^2 + 4\,{\omega_2}^2\right)^2 \big(m^2 {\omega_p}^6 - 4\,m {\omega_p}^5 \omega_2 + \gamma^2 {\omega_p}^4$$
$$+4\,{\omega_p}^4 {\omega_2}^2 + 4\,m {\omega_p}^3 \omega_2 - 2\,\gamma^2 {\omega_p}^2 - 8\,{\omega_p}^2 {\omega_2}^2 + \gamma^2 + 4\,{\omega_2}^2\big)^2 \Big).$$

Appendix C

Expressions for p_2, τ_1 and τ_2 of case-3a in Chapter 4

$$
\begin{aligned}
p_2 &= \frac{\omega_3\,\left(2\,m{\omega_p}^4+{\omega_p}^4\omega_3-2\,{\omega_p}^2\omega_3+\omega_3\right)}{2\left(\omega_p^2-1\right)^2},\\
\tau_1 &= -\omega_3\bar{\tau}+\frac{2\left(c{\omega_p}^4-2\,c{\omega_p}^2-\gamma\,m+c\right)}{\left(\omega_p^2-1\right)\left(m{\omega_p}^2+2\,{\omega_p}^2\omega_3-2\,\omega_3\right)},\\
\tau_2 &= \omega_3^2\bar{\tau}-\frac{2\gamma\omega_3\,m\left(2\,m{\omega_p}^4+7\,{\omega_p}^4\omega_3-6\,{\omega_p}^2\omega_3-\omega_3\right)}{\left(\omega_p^2-1\right)^2\left(m{\omega_p}^2+2\,{\omega_p}^2\omega_3-2\,\omega_3\right)^2}\\
&\qquad -\frac{2\omega_3\,c\left(2\,m{\omega_p}^4+{\omega_p}^4\omega_3-2\,{\omega_p}^2\omega_3+\omega_3\right)}{\left(m{\omega_p}^2+2\,{\omega_p}^2\omega_3-2\,\omega_3\right)^2}.
\end{aligned}
$$

Appendix D

Expression for Z_1 in Chapter 4

$$
\begin{aligned}
Z_1 = \frac{1}{E_1} \big[& -R^3 \cos(\omega T_0 + \phi)\, \beta\, \gamma\, \omega^7 \bar{p}^2 \bar{\tau}^2 - 2\, R\, Q^2 \cos(\omega T_0 + \phi)\, \beta\, \gamma\, \omega^7 \bar{p}^2 \bar{\tau}^2 \\
& +4\, R\, Q^2 \cos(\omega T_0 + \phi)\, \beta\, \gamma\, \omega^5 {\omega_p}^2 \bar{p}^2 \bar{\tau}^2 - 2\, R\, Q^2 \cos(\omega T_0 + \phi)\, \beta\, \gamma\, \omega^3 {\omega_p}^4 \bar{p}^2 \bar{\tau}^2 \\
& -4\, R^3 \cos(\omega T_0 + \phi)\, \beta\, \gamma\, \omega^9 - 8\, R\, Q^2 \cos(\omega T_0 + \phi)\, \beta\, \gamma\, \omega^9 \\
& +16\, R\, Q^2 \cos(\omega T_0 + \phi)\, \beta\, \gamma\, \omega^7 {\omega_p}^2 - 8\, R\, Q^2 \cos(\omega T_0 + \phi)\, \beta\, \gamma\, \omega^5 {\omega_p}^4 \\
& +4\, R \cos(\omega T_0 + \phi)\, \gamma\, \omega^7 \bar{p}^2 \bar{\tau}^2 - 8\, R \cos(\omega T_0 + \phi)\, \gamma\, \omega^5 {\omega_p}^2 \bar{p}^2 \bar{\tau}^2 \\
& +4\, R \cos(\omega T_0 + \phi)\, \gamma\, \omega^3 {\omega_p}^4 \bar{p}^2 \bar{\tau}^2 - 8\, R \cos(\omega T_0 + \phi)\, m \omega^5 {\omega_p}^4 \bar{p}\, \bar{\tau} \\
& +8\, R \cos(\omega T_0 + \phi)\, m \omega^3 {\omega_p}^6 \bar{p}\, \bar{\tau} + 16\, \sin(\omega T_0 + \phi)\, R m \omega^6 {\omega_p}^4 \\
& -16\, \sin(\omega T_0 + \phi)\, R m \omega^4 {\omega_p}^6 + 16\, R \cos(\omega T_0 + \phi)\, \gamma\, \omega^9 \\
& -32\, R \cos(\omega T_0 + \phi)\, \gamma\, \omega^7 {\omega_p}^2 + 16\, R \cos(\omega T_0 + \phi)\, \gamma\, \omega^5 {\omega_p}^4 \\
& -16\, R \cos(\omega T_0 + \phi)\, \omega^5 {\omega_p}^2 p_1\, \bar{p}\, \bar{\tau} + 32\, R \cos(\omega T_0 + \phi)\, \omega^3 {\omega_p}^4 p_1\, \bar{p}\, \bar{\tau} \\
& -16\, R \cos(\omega T_0 + \phi)\, \omega\, {\omega_p}^6 p_1\, \bar{p}\, \bar{\tau} + 32\, \sin(\omega T_0 + \phi)\, R \omega^6 {\omega_p}^2 p_1 \\
& -64\, \sin(\omega T_0 + \phi)\, R \omega^4 {\omega_p}^4 p_1 + 32\, \sin(\omega T_0 + \phi)\, R \omega^2 {\omega_p}^6 p_1 \big] \\
+ \frac{1}{E_2} \big[& \left(-440\, R Q^2 \beta\, \gamma\, \omega^7 {\omega_p}^3 - 48\, R Q^2 \beta\, \gamma\, \omega^2 {\omega_p}^8\right) \cos(\omega T_0 - 2\, \omega_p T_0 + \phi - 2\, \psi) \\
& +8\, R^3 \cos(3\, \omega T_0 + 3\, \phi)\, \beta\, \gamma\, \omega^9 \omega_p - 72\, R^3 \cos(3\, \omega T_0 + 3\, \phi)\, \beta\, \gamma\, \omega^7 {\omega_p}^3 \\
& + \left(72\, R Q^2 \beta\, \gamma\, \omega^9 \omega_p + 144\, R Q^2 \beta\, \gamma\, \omega^8 {\omega_p}^2\right) \cos(\omega T_0 - 2\, \omega_p T_0 + \phi - 2\, \psi)
\end{aligned}
$$

$$
\begin{aligned}
&+ \left(-592\, RQ^2\beta\,\gamma\,\omega^6{\omega_p}^4 + 408\, RQ^2\beta\,\gamma\,\omega^5{\omega_p}^5\right)\cos\left(\omega\, T_0 - 2\,\omega_p\, T_0 + \phi - 2\,\psi\right) \\
&\quad + \left(496\, RQ^2\beta\,\gamma\,\omega^4{\omega_p}^6 - 40\, RQ^2\beta\,\gamma\,\omega^3{\omega_p}^7\right)\cos\left(\omega\, T_0 - 2\,\omega_p\, T_0 + \phi - 2\,\psi\right) \\
&\quad + \left(48\, RQ^2\beta\,\gamma\,\omega^2{\omega_p}^8 + 72\, RQ^2\beta\,\gamma\,\omega^9\omega_p\right)\cos\left(\omega\, T_0 + 2\,\omega_p\, T_0 + \phi + 2\,\psi\right) \\
&\quad + \left(-144\, RQ^2\beta\,\gamma\,\omega^8{\omega_p}^2 - 440\, RQ^2\beta\,\gamma\,\omega^7{\omega_p}^3\right)\cos\left(\omega\, T_0 + 2\,\omega_p\, T_0 + \phi + 2\,\psi\right) \\
&\quad + \left(592\, RQ^2\beta\,\gamma\,\omega^6{\omega_p}^4 + 408\, RQ^2\beta\,\gamma\,\omega^5{\omega_p}^5\right)\cos\left(\omega\, T_0 + 2\,\omega_p\, T_0 + \phi + 2\,\psi\right) \\
&\quad + \left(-496\, RQ^2\beta\,\gamma\,\omega^4{\omega_p}^6 - 40\, RQ^2\beta\,\gamma\,\omega^3{\omega_p}^7\right)\cos\left(\omega\, T_0 + 2\,\omega_p\, T_0 + \phi + 2\,\psi\right) \\
&\quad + \left(-9\, Q^3\beta\,\gamma\,\omega^{10} + 109\, Q^3\beta\,\gamma\,\omega^8{\omega_p}^2 - 282\, Q^3\beta\,\gamma\,\omega^6{\omega_p}^4\right)\cos\left(3\,\omega_p\, T_0 + 3\,\psi\right) \\
&\quad + \left(282\, Q^3\beta\,\gamma\,\omega^4{\omega_p}^6 - 109\, Q^3\beta\,\gamma\,\omega^2{\omega_p}^8 + 9\, Q^3\beta\,\gamma\,{\omega_p}^{10}\right)\cos\left(3\,\omega_p\, T_0 + 3\,\psi\right)\Big] \\
&\quad + \frac{1}{E_3}\Big[\left(-160\, R^2Q\beta\,\gamma\,\omega^9 + 80\, R^2Q\beta\,\gamma\,\omega^8\omega_p\right)\cos\left(2\,\omega\, T_0 + 2\,\phi + \omega_p\, T_0 + \psi\right) \\
&\quad + \left(120\, R^2Q\beta\,\gamma\,\omega^7{\omega_p}^2 - 20\, R^2Q\beta\,\gamma\,\omega^6{\omega_p}^3\right)\cos\left(2\,\omega\, T_0 + 2\,\phi + \omega_p\, T_0 + \psi\right) \\
&\quad + \left(-20\, R^2Q\beta\,\gamma\,\omega^5{\omega_p}^4 - 30\, R^2Q\beta\,\gamma\,\omega^5{\omega_p}^2\right)\cos\left(2\,\omega\, T_0 + 2\,\phi + \omega_p\, T_0 + \psi\right) \\
&\quad + \left(80\, R^2Q\beta\,\gamma\,\omega^8\omega_p - 120\, R^2Q\beta\,\gamma\,\omega^7{\omega_p}^2\right)\cos\left(2\,\omega\, T_0 + 2\,\phi - \omega_p\, T_0 - \psi\right) \\
&\quad + \left(-20\, R^2Q\beta\,\gamma\,\omega^6{\omega_p}^3 + 20\, R^2Q\beta\,\gamma\,\omega^5{\omega_p}^4\right)\cos\left(2\,\omega\, T_0 + 2\,\phi - \omega_p\, T_0 - \psi\right) \\
&\quad + \left(40\, R^2Q\beta\,\gamma\,\omega^7 - 20\, R^2Q\beta\,\gamma\,\omega^6\omega_p\right)\cos\left(2\,\omega\, T_0 + 2\,\phi + \omega_p\, T_0 + \psi\right) \\
&\quad + \left(5\, R^2Q\beta\,\gamma\,\omega^4{\omega_p}^3 + 5\, R^2Q\beta\,\gamma\,\omega^3{\omega_p}^4\right)\cos\left(2\,\omega\, T_0 + 2\,\phi + \omega_p\, T_0 + \psi\right) \\
&\quad + \left(-40\, R^2Q\beta\,\gamma\,\omega^7 - 20\, R^2Q\beta\,\gamma\,\omega^6\omega_p\right)\cos\left(2\,\omega\, T_0 + 2\,\phi - \omega_p\, T_0 - \psi\right) \\
&\quad + \left(30\, R^2Q\beta\,\gamma\,\omega^5{\omega_p}^2 + 5\, R^2Q\beta\,\gamma\,\omega^4{\omega_p}^3\right)\cos\left(2\,\omega\, T_0 + 2\,\phi - \omega_p\, T_0 - \psi\right) \\
&\quad + \left(-5\, R^2Q\beta\,\gamma\,\omega^3{\omega_p}^4 + 160\, R^2Q\beta\,\gamma\,\omega^9\right)\cos\left(2\,\omega\, T_0 + 2\,\phi - \omega_p\, T_0 - \psi\right) \\
&+ \left(-192\, R^2\omega^8\bar{p} + 576\, R^2\omega^6{\omega_p}^2\bar{p} - 576\, R^2\omega^4{\omega_p}^4\bar{p} + 192\, R^2\omega^2{\omega_p}^6\bar{p}\right)\cos\left(2\,\omega\, T_0 + 2\,\phi\right)\Big]\,,
\end{aligned}
$$

where

$$
\begin{aligned}
E_1 \quad = \quad & 4\,\omega^8\bar{p}^2\bar{\tau}^2 \;-\; 16\,\omega^6{\omega_p}^2\bar{p}^2\bar{\tau}^2 \;+\; 24\,\omega^4{\omega_p}^4\bar{p}^2\bar{\tau}^2 \;-\; 16\,\omega^2{\omega_p}^6\bar{p}^2\bar{\tau}^2 \;+\; 4\,{\omega_p}^8\bar{p}^2\bar{\tau}^2 \\
& + 16\,\omega^{10} - 64\,\omega^8{\omega_p}^2 + 96\,\omega^6{\omega_p}^4 - 64\,\omega^4{\omega_p}^6 + 16\,\omega^2{\omega_p}^8
\end{aligned}
$$

$$E_2 = 288\,\omega^{10}\omega_p - 3488\,\omega^8{\omega_p}^3 + 9024\,\omega^6{\omega_p}^5 - 9024\,{\omega_p}^7\omega^4 + 3488\,\omega 1^9\omega^2 - 288\,{\omega_p}^{11}$$

$$
\begin{aligned}
E_3 = {} & 1280\,\omega^{10} - 4160\,\omega^8{\omega_p}^2 + 4800\,\omega^6{\omega_p}^4 - 2240\,\omega^4{\omega_p}^6 + 320\,\omega^2{\omega_p}^8 - 320\,\omega^8 \\
& + 1040\,\omega^6{\omega_p}^2 - 1200\,\omega^4{\omega_p}^4 + 560\,\omega^2{\omega_p}^6 - 80\,{\omega_p}^8.
\end{aligned}
$$

Appendix E

Reasoning for four phase portraits with two fixed points in Chapter 4

We first consider cases when $(-c_1, 0)$ exists. Here, $(0, -c_3/c_2)$ does not exist when c_2 and c_3 have the same sign. First considering both to be positive, non-existence of (S^*, P^*) leads to the following sub-cases:

1. $S^* < 0$ and $P^* > 0$

   We obtain phase portrait 'g' of Fig. 4.8.

2. $S^* > 0$ and $P^* < 0$

   $2c_1 > c_3$ contradicts $c_1 < 0, c_3 > 0$. Hence, this case is infeasible.

Now, considering c_2 and c_3 to be negative, we find the following:

1. $S^* < 0$ and $P^* > 0$

   $2c_3 > c_1c_2$ contradicts $c_1 < 0, c_2 < 0, c_3 < 0$. Hence, this case is infeasible.

2. $S^* > 0$ and $P^* < 0$

   We obtain phase portrait 'h' of Fig. 4.8.

Next, we consider cases when $(0, -c_3/c_2)$ exists: (a) $c_2 > 0, c_3 < 0$ and (b) $c_2 < 0, c_3 > 0$. Here, $c_1 > 0$. Considering case (a), we find the following:

1. $S^* < 0$ and $P^* > 0$

   $2c_3 > c_1c_2$ contradicts $c_1 > 0, c_2 > 0, c_3 < 0$. Hence, this case is infeasible.

2. $S^* > 0$ and $P^* < 0$

   We obtain phase portrait 'i' of Fig. 4.8.

Finally, we consider the case (b), i.e., $c_2 < 0, c_3 > 0$, and follow the procedure.

1. $S^* < 0$ and $P^* > 0$

   We obtain phase portrait 'j' of Fig. 4.8.

2. $S^* > 0$ and $P^* < 0$

   $2c_3 < c_1c_2$ contradicts $c_1 > 0, c_2 < 0, c_3 > 0$. Hence, this case is infeasible.

With that, we obtain four phase portraits (g-h-i-j) with two fixed points.

Appendix F

Expressions for C_j and D_k in Chapter 5

Recall that q is given by Eq. (5.16). The expressions for C_j, before normalization, are

$$C_{-4} = q^4/(\beta^8 - 40\beta^7 + 680\beta^6 - 3\beta^4q^2 - 6400\beta^5 + 60\beta^3q^2 + 36368\beta^4 - 476\beta^2q^2 + q^4 - 127360\beta^3 + 1760\beta q^2 + 267520\beta^2 - 2624q^2 - 307200\beta + 147456),$$

$$C_{-3} = -((\beta - 8)^2q^3)/(\beta^8 - 40\beta^7 + 680\beta^6 - 3\beta^4q^2 - 6400\beta^5 + 60\beta^3q^2 + 36368\beta^4 - 476\beta^2q^2 + q^4 - 127360\beta^3 + 1760\beta q^2 + 267520\beta^2 - 2624q^2 - 307200\beta + 147456),$$

$$C_{-2} = q^2(\beta^2 - 14\beta + q + 48)(\beta^2 - 14\beta - q + 48)/(\beta^8 - 40\beta^7 + 680\beta^6 - 3\beta^4q^2 - 6400\beta^5 + 60\beta^3q^2 + 36368\beta^4 - 476\beta^2q^2 + q^4 - 127360\beta^3 + 1760\beta q^2 + 267520\beta^2 - 2624q^2 - 307200\beta + 147456),$$

$$
\begin{aligned}
C_{-1} = -q(&\beta^6 - 36\beta^5 + 532\beta^4 - 2\beta^2q^2 - 4128\beta^3 + 24\beta q^2 + 17728\beta^2 - 80q^2 \\
&- 39936\beta + 36864)/(\beta^8 - 40\beta^7 + 680\beta^6 - 3\beta^4q^2 - 6400\beta^5 + 60\beta^3q^2 \\
&+ 36368\beta^4 - 476\beta^2q^2 + q^4 - 127360\beta^3 + 1760\beta q^2 + 267520\beta^2 \\
&- 2624q^2 - 307200\beta + 147456),
\end{aligned}
$$

$C_0 = 1,$

$$
\begin{aligned}
C_1 = -(&\beta^{10} - 40\beta^9 + 680\beta^8 - 4\beta^6q^2 - 6400\beta^7 + 96\beta^5q^2 + 36368\beta^6 - 1008\beta^4q^2 \\
&+ 3\beta^2q^4 - 127360\beta^5 + 5888\beta^3q^2 - 24\beta q^4 + 267520\beta^4 - 20352\beta^2q^2 + 80q^4 \\
&- 307200\beta^3 + 39936\beta q^2 + 147456\beta^2 - 36864q^2)/(q(\beta^8 - 40\beta^7 \\
&+ 680\beta^6 - 3\beta^4q^2 - 6400\beta^5 + 60\beta^3q^2 + 36368\beta^4 - 476\beta^2q^2 + q^4 \\
&- 127360\beta^3 + 1760\beta q^2 + 267520\beta^2 - 2624q^2 - 307200\beta + 147456)),
\end{aligned}
$$

$$
\begin{aligned}
C_2 = (&\beta^2 + 14\beta + q + 48)(\beta^2 + 14\beta - q + 48)(\beta^{10} - 40\beta^9 + 680\beta^8 - 4\beta^6q^2 - 6400\beta^7 \\
&+ 96\beta^5q^2 + 36368\beta^6 - 1008\beta^4q^2 + 3\beta^2q^4 - 127360\beta^5 + 5888\beta^3q^2 - 24\beta q^4 \\
&+ 267520\beta^4 - 20352\beta^2q^2 + 80q^4 - 307200\beta^3 + 39936\beta q^2 + 147456\beta^2 \\
&- 36864q^2)/((\beta^6 + 36\beta^5 + 532\beta^4 - 2\beta^2q^2 + 4128\beta^3 - 24\beta q^2 + 17728\beta^2 \\
&- 80q^2 + 39936\beta + 36864)(\beta^8 - 40\beta^7 + 680\beta^6 - 3\beta^4q^2 - 6400\beta^5 \\
&+ 60\beta^3q^2 + 36368\beta^4 - 476\beta^2q^2 + q^4 - 127360\beta^3 + 1760\beta q^2 \\
&+ 267520\beta^2 - 2624q^2 - 307200\beta + 147456)),
\end{aligned}
$$

$$
\begin{aligned}
C_3 = -(\beta+8)^2 q(&\beta^{10} - 40\beta^9 + 680\beta^8 - 4\beta^6 q^2 - 6400\beta^7 + 96\beta^5 q^2 + 36368\beta^6 \\
&- 1008\beta^4 q^2 + 3\beta^2 q^4 - 127360\beta^5 + 5888\beta^3 q^2 - 24\beta q^4 + 267520\beta^4 - 20352\beta^2 q^2 \\
&+ 80q^4 - 307200\beta^3 + 39936\beta q^2 + 147456\beta^2 - 36864q^2)/((\beta^6 + 36\beta^5 + 532\beta^4 \\
&- 2\beta^2 q^2 + 4128\beta^3 - 24\beta q^2 + 17728\beta^2 - 80q^2 + 39936\beta + 36864)(\beta^8 - 40\beta^7 \\
&+ 680\beta^6 - 3\beta^4 q^2 - 6400\beta^5 + 60\beta^3 q^2 + 36368\beta^4 - 476\beta^2 q^2 + q^4 \\
&- 127360\beta^3 + 1760\beta q^2 + 267520\beta^2 - 2624q^2 - 307200\beta + 147456)),
\end{aligned}
$$

and

$$
\begin{aligned}
C_4 = q^2(&\beta^{10} - 40\beta^9 + 680\beta^8 - 4\beta^6 q^2 - 6400\beta^7 + 96\beta^5 q^2 + 36368\beta^6 - 1008\beta^4 q^2 \\
&+ 3\beta^2 q^4 - 127360\beta^5 + 5888\beta^3 q^2 - 24\beta q^4 + 267520\beta^4 - 20352\beta^2 q^2 - 307200\beta^3 \\
&+ 80q^4 + 39936\beta q^2 + 147456\beta^2 - 36864q^2)/((\beta^6 + 36\beta^5 + 532\beta^4 - 2\beta^2 q^2 \\
&+ 4128\beta^3 - 24\beta q^2 + 17728\beta^2 - 80q^2 + 39936\beta + 36864)(\beta^8 - 40\beta^7 \\
&+ 680\beta^6 - 3\beta^4 q^2 - 6400\beta^5 + 60\beta^3 q^2 + 36368\beta^4 - 476\beta^2 q^2 + q^4 \\
&- 127360\beta^3 + 1760\beta q^2 + 267520\beta^2 - 2624q^2 - 307200\beta + 147456)).
\end{aligned}
$$

The expressions of D_k are

$$
\begin{aligned}
&D_0 = -\frac{(q^4 - 2624q^2 + 147456)}{32q^2(5q^2 - 2304)}, \quad D_1 = -\frac{1}{q}, \quad D_2 = \frac{(q^2 - 2304)}{16(5q^2 - 2304)}, \\
&D_3 = \frac{4q}{(5q^2 - 2304)}, \quad D_4 = \frac{q^2}{16(5q^2 - 2304)}.
\end{aligned}
$$

Appendix G

Expressions for c_1 and c_2 in Chapter 5

The expressions of $\mathcal{O}(\varepsilon)$ coefficients c_1 and c_2 are

$$
\begin{aligned}
c_1 = \frac{-1}{\Delta}\Big(&{S_{-4}}^2D_0 + S_{-4}S_{-3}D_1 + S_{-4}S_{-2}D_2 + S_{-4}S_{-1}D_3 + S_{-4}S_0D_4 + {S_{-3}}^2D_0 \\
&+ S_{-3}S_{-2}D_1 + S_{-3}S_{-1}D_2 + S_{-3}S_0D_3 + S_{-3}S_1D_4 + {S_{-2}}^2D_0 + S_{-2}S_{-1}D_1 \\
&+ S_{-2}S_0D_2 + S_{-2}S_1D_3 + S_{-2}S_2D_4 + {S_{-1}}^2D_0 + S_{-1}S_0D_1 + S_{-1}S_1D_2 \\
&+ S_{-1}S_2D_3 + S_{-1}S_3D_4 + {S_0}^2D_0 + S_0S_1D_1 + S_0S_2D_2 + S_0S_3D_3 \\
&+ S_0S_4D_4 + {S_1}^2D_0 + S_1S_2D_1 + S_1S_3D_2 + S_1S_4D_3 + {S_2}^2D_0 \\
&+ S_2S_3D_1 + S_2S_4D_2 + {S_3}^2D_0 + S_3S_4D_1 + {S_4}^2D_0\Big),
\end{aligned}
$$

and

$$c_2 = \frac{1}{\Delta}\Big(C_{-4}{}^2 D_0 + C_{-4}C_{-3}D_1 + C_{-4}C_{-2}D_2 + C_{-4}C_{-1}D_3 + C_{-4}C_0D_4 + C_{-3}{}^2 D_0$$
$$+ C_{-3}C_{-2}D_1 + C_{-3}C_{-1}D_2 + C_{-3}C_0D_3 + C_{-3}C_1D_4 + C_{-2}{}^2 D_0 + C_{-2}C_{-1}D_1$$
$$+ C_{-2}C_0D_2 + C_{-2}C_1D_3 + C_{-2}C_2D_4 + C_{-1}{}^2 D_0 + C_{-1}C_0D_1 + C_{-1}C_1D_2$$
$$+ C_{-1}C_2D_3 + C_{-1}C_3D_4 + C_0{}^2 D_0 + C_0C_1D_1 + C_0C_2D_2 + C_0C_3D_3$$
$$+ C_0C_4D_4 + C_1{}^2 D_0 + C_1C_2D_1 + C_1C_3D_2 + C_1C_4D_3 + C_2{}^2 D_0$$
$$+ C_2C_3D_1 + C_2C_4D_2 + C_3{}^2 D_0 + C_3C_4D_1 + C_4{}^2 D_0\Big).$$

Bibliography

[1] How Swings Work - Sixty Symbols, YouTube video. https://www.youtube.com/watch?v=UXo6WvHRs_I (accessed March 2025)

[2] Nandakumar, K., and Chatterjee, A., 2005, Resonance, Parameter Estimation, and Modal Interactions in a Strongly Nonlinear Benchtop Oscillator, *Nonlinear Dynamics*, 40: 149-167.

[3] Singla, S., and Chatterjee, A., 2020, Nonlinear responses of an SDOF structure with a light, whirling, driven, untuned pendulum, *International Journal of Mechanical Sciences*, 168: 105305.

[4] Shirude, Ashutosh, Vyasarayani, C. P., Chatterjee, A., 2021, Towards design of a nonlinear vibration stabilizer for suppressing single-mode instability, *Nonlinear Dynamics*, 103: 1563-1583.

[5] Bartos, M., and Habib, G., 2023, Hybrid vibration absorber for self-induced vibration suppression: exact analytical formulation for acceleration feedback control, *Meccanica*, 58: 2269-2289.

[6] Quadrupole Ion Trap (QIT), MASS SPEC PRO. http://www.massspecpro.com/technology/mass-analyzers/quadrupole-ion-trap-qit (accessed March 2025)

[7] Plass, Wolfgang R., 2000, Theory of dipolar DC excitation and DC tomography in the rf quadrupole ion trap, *International Journal of Mass Spectrometry*, 202: 175-197.

[8] Farid Ullah Khan, 2016, Review of non-resonant vibration based energy harvesters for wireless sensor nodes, *Journal of Renewable and Sustainable Energy*, 8: 044702.

[9] Tiwari, S., Dangi, A., Pratap, R., 2023, A tip-coupled, two-cantilever, non-resonant microsystem for direct measurement of liquid viscosity, *Microsystems & Nanoengineering*, 9: 34.

[10] Gattulli, V., Di Fabio, F., Luongo, A., 2004, Nonlinear Tuned Mass Damper for self-excited oscillations, *Wind and Structures*, 7(4): 251-264.

[11] Storti, D. W., and Rand, R. H., 1982, Dynamics of two strongly coupled van der Pol oscillators, *International Journal of Non-Linear Mechanics*, 17(3): 143-152.

[12] Natsiavas, S., 1994, Free vibration of two coupled nonlinear oscillators, *Nonlinear Dynamics*, 6: 69-86.

[13] Rand, R. H., and Holmes, P. J., 1980, Bifurcation of periodic motions in two weakly coupled van der Pol oscillators, *International Journal of Non-Linear Mechanics*, 15(4-5): 387-399.

[14] Storti, D. W., and Rand, R. H., 1986, Dynamics of two strongly coupled relaxation oscillators, *SIAM Journal on Applied Mathematics*, 46(1): 56-67.

[15] Chakraborty, T., and Rand, R. H., 1988, The transition from phase locking to drift in a system of two weakly coupled van der Pol oscillators, *International Journal of Non-Linear Mechanics*, 23(5-6): 369-376.

[16] Storti, D. W., and Reinhall, P. G., 1997, Stability of in-phase and out-of-phase modes for a pair of linearly coupled van der Pol oscillators, Guran, A. (Ed.), Nonlinear Dynamics: The Richard Rand 50th Anniversary Volume, 1-23, World Scientific, Singapore.

[17] Storti, D. W., and Reinhall, P. G., 2000, Phase-locked mode stability for coupled van der Pol oscillators, *ASME Journal of Vibration and Acoustics*, 122(3): 318-323.

[18] Wirkus, S., and Rand, R., 2002, The dynamics of two coupled van der Pol oscillators with delay coupling, *Nonlinear Dynamics*, 30: 205-221.

[19] Low, L. A., Reinhall, P. G., Storti, D. W., 2003, An investigation of coupled van der Pol oscillators, *ASME Journal of Vibration and Acoustics*, 125(2): 162-169.

[20] Ivanchenko, M. V., Osipov, G. V., Shalfeev, V. D., Kurths, J., 2004, Synchronization of two non-scalar-coupled limit-cycle oscillators, *Physica D: Nonlinear Phenomena*, 189(1-2): 8-30.

[21] Camacho, E., Rand, R., Howland, H., 2004, Dynamics of two van der Pol oscillators coupled via a bath, *International Journal of Solids and Structures*, Special Issue in Honour of Prof. Bruno Boley, 41(8): 2133-2143.

[22] Tang, J., Han, F., Xiao, H., Wu, X., 2009, Amplitude control of a limit cycle in a coupled van der Pol system, *Nonlinear Analysis: Theory, Methods & Applications*, 71(7-8): 2491-2496.

[23] Zhang, J., and Gu, X., 2010, Stability and bifurcation analysis in the delay-coupled van der Pol oscillators, *Applied Mathematical Modelling*, 34(9): 2291-2299.

[24] Kulikov, D. A., 2022, Dynamics of Coupled Van der Pol Oscillators, *Journal of Mathematical Sciences*, 262: 817-824.

[25] Poliashenko, M., McKay, S. R., Smith, C. W., 1991, Hysteresis of synchronous-asynchronous regimes in a system of two coupled oscillators, *Physical Review A*, 43(10): 5638-5641.

[26] Chunbiao, G., Qishao, L., Kelei, H., 1991, Strongly resonant bifurcations of nonlinearly coupled van der Pol-Duffing Oscillator, *Applied Mathematics and Mechanics*, 20: 68-75.

[27] Zang, H., Zhang, T., Zhang, Y., 2014, Stability and bifurcation analysis of delay coupled Van der Pol-Duffing oscillators, *Nonlinear Dynamics*, 75: 35-47.

[28] Gattulli, V., Di Fabio, F., Luongo, A., 2003, One to one resonant double Hopf bifurcation in aeroelastic oscillators with tuned mass dampers, *Journal of Sound and Vibration*, 262(2): 201-217.

[29] Habib, G., and Kerschen, G., July 2014, Stability and bifurcation analysis of a Van der Pol-Duffing oscillator with a nonlinear tuned vibration absorber, Proceedings of the Eighth European Nonlinear Dynamics Conference, Vienna, Austria.

[30] Mansour, W. M., 1972, Quenching of limit cycles of a Van der Pol oscillator, *Journal of Sound and Vibration*, 25(3): 395-405.

[31] Suchorsky, M. K., and Rand, R. H., 2012, A pair of van der Pol oscillators coupled by fractional derivatives, *Nonlinear Dynamics*, 69: 313–324.

[32] Pastor, I., Pérez-García, V. M., Encinas-Sanz, F., Guerra, J. M., 1993, Ordered and chaotic behavior of two coupled van der Pol oscillators, *Physical Review E*, 48(1): 171-182.

[33] Teufel, A., Steindl, A., Troger, H., 2006, Synchronization of two flow excited pendula, *Communications in Nonlinear Science and Numerical Simulation*, 11(5): 577-594.

[34] Kuznetsov, A. P., and Roman, J. P., 2009, Properties of synchronization in the systems of non-identical coupled van der Pol and van der Pol–Duffing oscillators. Broadband synchronization, *Physica D: Nonlinear Phenomena*, 238(16): 1499-1506.

[35] Paccosi, R. G., Figliola, A., Galán-Vioque, J., 2014, A bifurcation approach to the synchronization of coupled Van der Pol oscillators, *SIAM Journal on Applied Dynamical Systems*, 13(3): 1152-1167.

[36] Li, X., Ji, J. C., Hansen, C. H., 2006, Dynamics of two delay coupled van der Pol oscillators, *Mechanics Research Communications*, 33(5): 614-627.

[37] Woafo, P., Chedjou, J. C., Fotsin, H. B., 1996, Dynamics of a system consisting of a van der Pol oscillator coupled to a Duffing oscillator, *Physical Review E*, 54(6): 5929-5934.

[38] Rajasekar, S., and Murali, K., 2004, Resonance behaviour and jump phenomenon in a two coupled Duffing–van der Pol oscillators, *Chaos, Solitons & Fractals*, 19(4): 925-934.

[39] Kuznetsov, A. P., Stankevich, N. V., Turukina, L. V., 2009, Coupled van der Pol–Duffing oscillators: Phase dynamics and structure of synchronization tongues, *Physica D: Nonlinear Phenomena*, 238(14): 1203-1215.

[40] Chatterjee, S., and Dey, S., 2013, Nonlinear dynamics of two harmonic oscillators coupled by Rayleigh type self-exciting force, *Nonlinear Dynamics*, 72: 113-128.

[41] Gendelman, O. V., and Bar, T., 2010, Bifurcations of self-excitation regimes in a Van der Pol oscillator with a nonlinear energy sink, *Physica D: Nonlinear Phenomena*, 239(3-4): 220-229.

[42] Domany, E., and Gendelman, O. V., 2013, Dynamic responses and mitigation of limit cycle oscillations in Van der Pol–Duffing oscillator with nonlinear energy sink, *Journal of Sound and Vibration*, 332(21): 5489-5507.

[43] Natsiavas, S., Bouzakis, K. D., Aichouh, P., 1997, Free vibration in a class of self-excited oscillators with 1:3 internal resonance, *Nonlinear Dynamics*, 12: 109-128.

[44] Natsiavas, S., and Metallidis, P., 1997, External primary resonance of self-excited oscillators with 1:3 internal resonance, *Journal of Sound and Vibration*, 208(2): 211-224.

[45] El-Badawy, A. A., and Nasr El-Deen, T. N., 2007, Quadratic nonlinear control of a self-excited oscillator, *Journal of Vibration and Control*, 13(4): 403-414.

[46] Verros, G., and Natsiavas, S., 1998, Self-excited oscillators with asymmetric nonlinearities and one-to-two internal resonance, *Nonlinear Dynamics*, 17: 325-346.

[47] Kengne, J., Chedjou, J. C., Kom, M., Kyamakya, K., Kamdoum Tamba, V., 2014, Regular oscillations, chaos, and multistability in a system of two coupled van der Pol oscillators: numerical and experimental studies, *Nonlinear Dynamics*, 76: 1119-1132.

[48] Chedjou, J. C., Fotsin, H. B., Woafo, P., Domngang, S., 2001, Analog simulation of the dynamics of a van der Pol oscillator coupled to a Duffing oscillator, *IEEE Transactions on Circuits and Systems I: Fundamental Theory and Applications*, 48(6): 748-757.

[49] Ngamsa Tegnitsap, J. V., Fotsin, H. B., Kamdoum Tamba, V., Megam Ngouonkadi, E. B., 2020, Dynamical study of VDPCL oscillator: antimonotonicity, bursting oscillations, coexisting attractors and hardware experiments, *European Physical Journal Plus*, 135: 591.

[50] Kalmár-Nagy, T., Stépán, G., Moon, F. C., 2001, Subcritical Hopf Bifurcation in the Delay Equation Model for Machine Tool Vibrations, *Nonlinear Dynamics*, 26: 121-142.

[51] Tarng, Y. S., Kao, J. Y., Lee, E. C., 2000, Chatter suppression in turning operations with a tuned vibration absorber, *Journal of Materials Processing Technology*, 105(1-2): 55-60.

[52] Sims, N. D., 2007, Vibration absorbers for chatter suppression: A new analytical tuning methodology, *Journal of Sound and Vibration*, 301(3-5): 592-607.

[53] Miguélez, M. H., Rubio, L., Loya, J. A., Fernández-Sáez, J., 2010, Improvement of chatter stability in boring operations with passive vibration absorbers, *International Journal of Mechanical Sciences*, 52(10): 1376-1384.

[54] Rubio, L., Loya, J. A., Miguélez, M. H., Fernández-Sáez, J., 2013, Optimization of passive vibration absorbers to reduce chatter in boring, *Mechanical Systems and Signal Processing*, 41(1-2): 691-704.

[55] Patel, A., Talaviya, D., Law, M., Wahi, P., 2022, Optimally tuning an absorber for a chatter-resistant rotating slender milling tool holder, *Journal of Sound and Vibration*, 520: 116594.

[56] Moradi, H., Bakhtiari-Nejad, F., Movahhedy, M. R., 2008, Tuneable vibration absorber design to suppress vibrations: An application in boring manufacturing process, *Journal of Sound and Vibration*, 318(1-2): 93-108.

[57] Patel, A., Yadav, A., Law, M., Bhattacharya, B., Wahi, P., 2023, Damped Chatter Resistant Boring Bar Integrated with an Absorber Working in Conjunction with an Eddy Current Damper, *Journal of Vibration Engineering & Technologies*, 11: 2013-2024.

[58] Dogan, H., Sims, N. D., Wagg, D. J., 2019, Investigation of the inerter-based dynamic vibration absorber for machining chatter suppression, *Journal of Physics: Conference Series*, 1264(1): 012030.

[59] Dogan, H., Sims, N. D., Wagg, D. J., 2023, Implementation of Inerter-Based Dynamic Vibration Absorber for Chatter Suppression, *ASME Journal of Manufacturing Science and Engineering*, 145(8): 084502.

[60] Gourc, E., Seguy, S., Michon, G., Berlioz, A., 2013, Chatter Control in Turning Process with a Nonlinear Energy Sink, *Advanced Materials Research*, hal-01808190, 698: 89-98.

[61] Nankali, A., Lee, Y. S., Kalmár-Nagy, T., 2017, Targeted Energy Transfers for Suppressing Regenerative Machine Tool Vibrations, *ASME Journal of Computational and Nonlinear Dynamics*, 12(1): 011010.

[62] Habib, G., Kerschen, G., Stepan, G., 2017, Chatter mitigation using the nonlinear tuned vibration absorber, *International Journal of Non-Linear Mechanics*, 91: 103-112.

[63] Edhi, E., and Hoshi, T., 2001, Stabilization of high frequency chatter vibration in fine boring by friction damper, *Precision Engineering*, 25(3): 224-234.

[64] Wang, M., Zan, T., Yang, Y., Fei, R., 2010, Design and implementation of nonlinear TMD for chatter suppression: An application in turning processes, *International Journal of Machine Tools and Manufacture*, 50(5): 474-479.

[65] Wang, M., 2011, Feasibility study of nonlinear tuned mass damper for machining chatter suppression, *Journal of Sound and Vibration*, 330(9): 1917-1930.

[66] Gourc, E., Seguy, S., Michon, G., Berlioz, A., Mann, B. P., 2015, Quenching chatter instability in turning process with a vibro-impact nonlinear energy sink, *Journal of Sound and Vibration*, 355: 392-406.

[67] Iklodi, Z., Barton, David A. W., Dombovari, Z., 2022, Bi-stability induced by motion limiting constraints on boring bar tuned mass dampers, *Journal of Sound and Vibration*, 517: 116538.

[68] Tewani, S. G., Rouch, K. E., Walcott, B. L., 1995, A study of cutting process stability of a boring bar with active dynamic absorber, *International Journal of Machine Tools and Manufacture*, 35(1): 91-108.

[69] Sahu, G. N., Vashisht, S., Wahi, P., Law, M., 2020, Validation of a hardware-in-the-loop simulator for investigating and actively damping regenerative chatter in orthogonal cutting, *CIRP Journal of Manufacturing Science and Technology*, 29: 115-129.

[70] Zavodney, L. D., and Nayfeh, A. H., 1988, The response of a single-degree-of-freedom system with quadratic and cubic non-linearities to a fundamental parametric resonance, *Journal of Sound and Vibration*, 120(1): 63-93.

[71] Rhoads, Jeffrey F., Shaw, Steven W., Turner, Kimberly L., Moehlis, Jeff, DeMartini, Barry E., Zhang, Wenhua, 2006, Generalized parametric resonance in electrostatically actuated microelectromechanical oscillators, *Journal of Sound and Vibration*, 296(4): 797-829.

[72] Younesian, D., Esmailzadeh, E., Sedaghati, R., 2005, Existence of Periodic Solutions for the Generalized Form of Mathieu Equation, *Nonlinear Dynamics*, 39: 335-348.

[73] Kim, C. H., Lee, C., Perkins, N. C., 2005, Nonlinear Vibration of Sheet Metal Plates Under Interacting Parametric and External Excitation During Manufacturing, *ASME Journal of Vibration and Acoustics*, 127(1): 36-43.

[74] Pandey, M., Rand, R. H., Zehnder, A. T., 2008, Frequency locking in a forced Mathieu-van der Pol-Duffing system, *Nonlinear Dynamics*, 54: 3-12.

[75] Ramakrishnan, V., and Feeny, B. F., 2012, Resonances of a Forced Mathieu Equation With Reference to Wind Turbine Blades, *ASME Journal of Vibration and Acoustics*, 134(6): 064501.

[76] Natsiavas, S., Theodossiades, S., Goudas, I., 2000, Dynamic analysis of piecewise linear oscillators with time periodic coefficients, *International Journal of Non-Linear Mechanics*, 35(1): 53-68.

[77] Li, Xianghong, Hou, Jingyu, Chen, Jufeng, 2016, An analytical method for Mathieu oscillator based on method of variation of parameter, *Communications in Nonlinear Science and Numerical Simulation*, 37: 326-353.

[78] Sevugarajan, S., and Menon, A. G., 2002, Transition curves and *iso*-β_u lines in nonlinear Paul traps, *International Journal of Mass Spectrometry*, 218(2): 181-196.

[79] Esmailzadeh, E., and Nakhaie-jazar, G., 1997, Periodic solution of a Mathieu-Duffing type equation, *International Journal of Non-Linear Mechanics*, 32(5): 905-912.

[80] Chatterjee, Anindya, 2003, Harmonic balance based averaging: Approximate realizations of an asymptotic technique, *Nonlinear Dynamics*, 32: 323-343.

[81] Abraham, Glomin Thomas, and Chatterjee, Anindya, 2003, Approximate asymptotics for a nonlinear Mathieu equation using harmonic balance based averaging, *Nonlinear Dynamics*, 31: 347-365.

[82] Abraham, Glomin Thomas, Chatterjee, Anindya, Menon, A. G., 2004, Escape velocity and resonant ion dynamics in Paul trap mass spectrometers, *International Journal of Mass Spectrometry*, 231(1): 1-16.

[83] Rajanbabu, N., Marathe, Amol, Chatterjee, Anindya, Menon, A. G., 2007, Multiple scales analysis of early and delayed boundary ejection in Paul traps, *International Journal of Mass Spectrometry*, 261(2): 170-182.

[84] Tandel, D. D., Wahi, P., Chatterjee, A., 2023, Vibration stabilization by a nonresonant secondary limit cycle oscillator, *Nonlinear Dynamics*, 111: 6043-6062.

[85] Tandel, D. D., Chatterjee, A., Mohanty, A. K., 2023, Quadrupole ion trap with dipolar DC excitation: motivation, nonlinear dynamics, and simple formulas, *Nonlinear Dynamics*, 111: 15837-15852.

[86] Frahm, Hermann, April 1911, Device for damping vibrations of bodies, US Patent 989958.

[87] Ibrahim, R. A., 2008, Recent advances in nonlinear passive vibration isolators, *Journal of Sound and Vibration*, 314(3-5): 371-452.

[88] Ding, Hu, and Chen, Li Qun, 2020, Designs, analysis, and applications of nonlinear energy sinks, *Nonlinear Dynamics*, 100: 3061-3107.

[89] Gatti, Gianluca, 2018, Fundamental insight on the performance of a nonlinear tuned mass damper, *Meccanica*, 53: 111-123.

[90] Starosvetsky, Y., and Gendelman, O. V., 2009, Vibration absorption in systems with a nonlinear energy sink: Nonlinear damping, *Journal of Sound and Vibration*, 324(3-5): 916–939.

[91] Zhu, S. J., Zheng, Y. F., Fu, Y. M., 2004, Analysis of non-linear dynamics of a two-degree-of-freedom vibration system with non-linear damping and non-linear spring, *Journal of Sound and Vibration*, 271(1-2): 15-24.

[92] Verhulst, Ferdinand, 2005, Quenching of self-excited vibrations, *Journal of Engineering Mathematics*, 53: 349-358.

[93] Lee, Young S., Vakakis, Alexander F., Bergman, Lawrence A., McFarland, D. Michael, 2006, Suppression of limit cycle oscillations in the van der Pol oscillator by means of passive non-linear energy sinks, *Structural Control and Health Monitoring*, 13: 41-75.

[94] Habib, Giuseppe, and Kerschen, Gaëtan, 2015, Suppression of limit cycle oscillations using the nonlinear tuned vibration absorber, *Proceedings of the Royal Society A: Mathematical, Physical and Engineering Sciences*, 471(2176): 20140976.

[95] Wang, Js., Fan, Dixia, Lin, Ke, 2020, A review on flow-induced vibration of offshore circular cylinders, *Journal of Hydrodynamics*, 32: 415-440.

[96] Nasrabadi, M., Sevbitov, A. V., Maleki, V. A., Akbar, N., Javanshir, I., 2022, Passive fluid-induced vibration control of viscoelastic cylinder using nonlinear energy sink, *Marine Structures*, 81: 103116.

[97] Guo, Hulun, Liu, Bin, Yu, Yangyang, Cao, Shuqian, Chen, Yushu, 2017, Galloping suppression of a suspended cable with wind loading by a nonlinear energy sink, *Archive of Applied Mechanics*, 87: 1007-1018.

[98] Qin, Zhaohong, Chen, Yushu, Zhan, Xueping, Liu, Bin, Zhu, Kuanjun, 2012, Research on the galloping and anti-galloping of the transmission line, *International Journal of Bifurcation and Chaos*, 22(02): 1250038.

[99] Dai, H. L., Abdelkefi, A., Wang, L., 2016, Usefulness of passive non-linear energy sinks in controlling galloping vibrations, *International Journal of Non-Linear Mechanics*, 81: 83-94.

[100] Chatterjee, S., 2011, On the efficacy of an active absorber with internal state feedback for controlling self-excited oscillations, *Journal of Sound and Vibration*, 330(7): 1285-1299.

[101] Mondal, Joy, and Chatterjee, S., 2021, Controlling self-excited vibration of a nonlinear beam by nonlinear resonant velocity feedback with time-delay, *International Journal of Non-Linear Mechanics*, 131: 103684.

[102] Gattulli, V., Di Fabio, F., Luongo, A., 2001, Simple and double Hopf bifurcations in aeroelastic oscillators with tuned mass dampers, *Journal of the Franklin Institute*, 338(2-3): 187-201.

[103] Nayfeh, Ali H., 2000, *Perturbation Methods*, Wiley, New York.

[104] Nayfeh, Ali H., and Mook, Dean T., 1979, *Nonlinear Oscillations*, Wiley, New York.

[105] Cartmell, M. P., Ziegler, S., Khanin, R., Forehand, D., 2003, Multiple scales analyses of the dynamics of weakly nonlinear mechanical systems, *Applied Mechanics Reviews*, 56(5): 455-492.

[106] Yamashita, Kiyotaka, Yagyu, Takahiro, Yabuno, Hiroshi, 2019, Nonlinear interactions between unstable oscillatory modes in a cantilevered pipe conveying fluid, *Nonlinear Dynamics*, 98: 2927-2938.

[107] Guckenheimer, John, and Holmes, Philip, 1983, *Nonlinear Oscillations, Dynamical systems, and Bifurcations of Vector Fields*, Springer-Verlag, New York.

[108] Link for the animations in Chapter 3 of the present thesis. `https://drive.google.com/drive/folders/1Zwhrt_D7gSO74EFWzjagMEBnTBAYVrA8?usp=sharing`

[109] Saha, A., Bhattacharya, B., Wahi, P., 2010, A comparative study on the control of friction-driven oscillations by time-delayed feedback, *Nonlinear Dynamics*, 60: 15-37.

[110] Hu, Jia Lin, Habib, Giuseppe, 2020, Friction-Induced Vibration Suppression via the Tuned Mass Damper: Optimal Tuning Strategy, *Lubricants*, 8(11): 100.

[111] Nayfeh, A. H., Nayfeh, N. A., 2011, Analysis of the cutting tool on a lathe, *Nonlinear Dynamics*, 63: 395-416.

[112] Mohanty, S., and Dwivedy, S. K., 2019, Nonlinear dynamics of piezoelectric-based active nonlinear vibration absorber using time delay acceleration feedback, *Nonlinear Dynamics*, 98: 1465-1490.

[113] Mondal, J., and Chatterjee, S., 2021, Controlling self-excited vibration of a nonlinear beam by nonlinear resonant velocity feedback with time-delay, *International Journal of Non-Linear Mechanics*, 131: 103684.

[114] Wahi, P., and Chatterjee, A., 2008, Self-interrupted regenerative metal cutting in turning, *International Journal of Non-Linear Mechanics*, 43(2): 111-123.

[115] Engelborghs, K., Luzyanina, T., Samaey, G., 2001, DDE-BIFTOOL v. 2.00: a Matlab package for bifurcation analysis of delay differential equations, Technical Report TW-330, Department of Computer Science, K.U.Leuven, Leuven, Belgium.

[116] Engelborghs, K., Luzyanina, T., Roose, D., 2002, Numerical bifurcation analysis of delay differential equations using DDE-BIFTOOL, *ACM Transactions on Mathematical Software*, 28(1): 1-21.

[117] Molnar, T. G., Insperger, T., Stepan, G., 2019, Closed-form estimations of the bistable region in metal cutting via the method of averaging, *International Journal of Non-Linear Mechanics*, 112: 49-56.

[118] Das, S. L., and Chatterjee, A., 2002, Multiple Scales without Center Manifold Reductions for Delay Differential Equations near Hopf Bifurcations, *Nonlinear Dynamics*, 30: 323-335.

[119] Saha, A., and Wahi, P., 2011, Delayed feedback for controlling the nature of bifurcations in friction-induced vibrations, *Journal of Sound and Vibration*, 330(25): 6070-6087.

[120] Subramanian, P., Sujith, R. I., Wahi, P., 2013, Subcritical bifurcation and bistability in thermoacoustic systems, *Journal of Fluid Mechanics*, 715: 210-238.

[121] Saha, A., and Wahi, P., 2014, An analytical study of time-delayed control of friction-induced vibrations in a system with a dynamic friction model, *International Journal of Non-Linear Mechanics*, 63: 60-70.

[122] Wahi, P., and Chatterjee, A., 2005, Regenerative Tool Chatter Near a Codimension 2 Hopf Point Using Multiple Scales, *Nonlinear Dynamics*, 40: 323-338.

[123] Wahi, P., 2005, A study of delay differential equations with applications to machine tool vibrations, Ph.D. Thesis, Indian Institute of Science, Bangalore.

[124] March, R. E., and Todd, J. F. J., 2005, *Quadrupole Ion Trap Mass Spectrometry*, 2nd ed., John Wiley & Sons Inc., Hoboken, NJ.

[125] Dawson, Peter H., 1976, *Quadrupole Mass Spectrometry and its Applications*, 2nd ed., Elsevier, Amsterdam.

[126] Lammert, Stephen A., and Cooks, R. Graham, 1991, Surface-induced Dissociation of Molecular Ions in a Quadrupole Ion Trap Mass Spectrometer, *Journal of the American Society for Mass Spectrometry*, 2: 487-491.

[127] Lammert, Stephen A., and Cooks, R. Graham, 1992, Pulsed axial activation in the ion trap: A new method for performing tandem mass spectroscopy (MS/MS), *Rapid Communications in Mass Spectrometry*, 6: 528-530.

[128] Lammert, Stephen A., Cleven, Curtis D., Cooks, R. Graham, 1994, Determination of Ion Frequencies in a Quadrupole Ion Trap By Using a Fast Direct Current Pulse as Pump and a Laser Probe, *Journal of the American Society for Mass Spectrometry*, 5: 29-36.

[129] Webb, Ian K., Londry, Frank A., McLuckey, Scott A., 2011, Implementation of dipolar direct current (DDC) collision-induced dissociation in storage and transmission modes on a quadrupole/time-of-flight tandem mass spectrometer, *Rapid Communications in Mass Spectrometry*, 25: 2500-2510.

[130] Prentice, Boone M., Xu, Wei, Ouyang, Zheng, McLuckey, Scott A., 2011, DC potentials applied to an end-cap electrode of a 3D ion trap for enhanced MS^n functionality, *International Journal of Mass Spectrometry*, 306: 114-122.

[131] Prentice, Boone M., Santini, Robert E., McLuckey, Scott A., 2011, Adaptation of a 3-D Quadrupole Ion Trap for Dipolar DC Collisional Activation, *Journal of the American Society for Mass Spectrometry*, 22: 1486-1492.

[132] Prentice, Boone M., and McLuckey, Scott A., 2011, Dipolar DC Collisional Activation in a “Stretched” 3-D Ion Trap: The Effect of Higher Order Fields on rf-Heating, *Journal of the American Society for Mass Spectrometry*, 23: 736-744.

[133] Shih, Mack, and McLuckey, Scott A., 2019, Ion/ion charge inversion/attachment in conjunction with dipolar DC collisional activation as a selective screen for sulfo- and phosphopeptides, *International Journal of Mass Spectrometry*, 444: 116181.

[134] Adhikari, Sarju, Dziekonski, Eric T., Londry, Frank A., McLuckey, Scott A., 2019, Dipolar DC induced collisional activation of non-dissociated electron-transfer products, *Journal of Mass Spectrometry*, 54: 459-465.

[135] Weil, Carsten, Wells, J. Mitchell, Wollnik, H., Cooks, R. Graham, 2000, Axial ion motion within the quadrupole ion trap elucidated by dc pulse tomography, *International Journal of Mass Spectrometry*, 194: 225-234.

[136] Plass, Wolfgang R., Gill, Lynn A., Bui, Huy A., Cooks, R. Graham, 2000, Ion Mobility Measurement by Dc Tomography in an Rf Quadrupole Ion Trap, *Journal of Physical Chemistry A*, 104(21): 5059-5065.

[137] Webb, Ian K., Gao, Yang, Londry, Frank A., McLuckey, Scott A., 2013, Trapping mode dipolar DC collisional activation in the RF-only ion guide of a linear ion trap/time-of-flight instrument for gaseous bio-ion declustering, *Journal of Mass Spectrometry*, 48: 1059-1065.

[138] Knight, Randall D., 1983, The General Form of the Quadrupole Ion Trap Potential, *International Journal of Mass Spectrometry and Ion Physics*, 51: 127-131.

[139] Wang, Y., and Franzen, J., 1994, The non-linear ion trap. Part 3. Multipole components in three types of practical ion trap, *International Journal of Mass Spectrometry and Ion Processes*, 132: 155-172.

[140] Rand, R. H., and Armbruster, D., 1987, *Perturbation Methods, Bifurcation Theory and Computer Algebra*, Springer, Berlin.

[141] Das, S. L., and Chatterjee, A., 2003, Multiple Scales via Galerkin Projections: Approximate Asymptotics for Strongly Nonlinear Oscillations, *Nonlinear Dynamics*, 32: 161-186.

[142] Mahmoud, Gamal M., 1997, Stability regions for coupled Hill's equations, *Physica A: Statistical Mechanics and its Applications*, 242(1): 239-249.

[143] Mahmoud, Gamal M., 1997, Periodic solutions of strongly non-linear Mathieu oscillators, *International Journal of Non-Linear Mechanics*, 32(6): 1177-1185.

[144] Mahmoud, Gamal M., 1993, On the generalized averaging method of a class of strongly nonlinear forced oscillators, *Physica A: Statistical Mechanics and its Applications*, 199(1): 87-95.

[145] Aghamohammadi, M., Sorokin, V., Mace, B., 2022, Dynamic analysis of the response of Duffing-type oscillators subject to interacting parametric and external excitations, *Nonlinear Dynamics*, 107: 99–120.

[146] Neumeyer, S., Sorokin, V. S., Thomsen, J. J., 2017, Effects of quadratic and cubic nonlinearities on a perfectly tuned parametric amplifier, *Journal of Sound and Vibration*, 386: 327-335.

[147] Bhattacharjee, Arindam, Shah, Kushal, Chatterjee, Anindya, 2019, Unifying averaged dynamics of the Fokker-Planck equation for Paul traps, *Physics of Plasmas*, 26(1): 012302.

[148] McLachlan, Norman William, 1947, *Theory and Applications of Mathieu Functions*, Oxford University Press, Oxford.